



Uptake, Cellular Fate and Toxicity of Engineered Gold Nanoparticles in A549 cells.

By

Abiola Nneka Dosumu

A thesis submitted to the University of Birmingham for the degree of
DOCTOR OF PHILOSOPHY

School of Biosciences
College of Life and Environmental Sciences
University of Birmingham
August 2017

UNIVERSITY OF
BIRMINGHAM

University of Birmingham Research Archive

e-theses repository

This unpublished thesis/dissertation is copyright of the author and/or third parties. The intellectual property rights of the author or third parties in respect of this work are as defined by The Copyright Designs and Patents Act 1988 or as modified by any successor legislation.

Any use made of information contained in this thesis/dissertation must be in accordance with that legislation and must be properly acknowledged. Further distribution or reproduction in any format is prohibited without the permission of the copyright holder.

Abstract

Engineered gold nanoparticles (AuNPs) can be modified to produce functionalized AuNPs with potential biomedical applications. However, prior to medical use, an understanding of cellular uptake and fate is critical to assess their potential toxicity.

This thesis studied 20 nm AuNPs coated with a luminescent ruthenium complex (RuS12) to form RuS12·AuNP20, which were fully characterised prior to cellular studies in A549 cells treated for 2-72 hours.

The size of internalised particles as quantified by transmission electron microscopy (TEM) was in agreement with characterisation data of particles in solution and particle size remained unchanged after up to 72hours treatment indicating non-aggregation of internalised RuS12·AuNP20. Particle number increased over time, and this was confirmed by quantitative analysis of confocal images, TEM and inductively coupled plasma mass spectrometry.

Macropinocytosis and clathrin-mediated endocytosis were shown to be the route of uptake, with particles trafficked via the endo-lysosomal pathway as confirmed by co-localisation with fluorescent markers of early endosomes, lysosomes and autophagosomes in a time-dependent manner that, ultimately involved autophagy as confirmed by western blotting of LC3 protein.

Cellular accumulation of RuS12·AuNP20 also caused cellular changes related to oxidative stress including depletion of glutathione and DNA-strand breaks, but the mechanism of action remains to be elucidated.

*This thesis is dedicated to my
amazing parents
Mr and Col. (Mrs) Dosumu for
giving me the best legacy.*

Acknowledgement

The journey of four years was made easier with the support of my two supervisors Dr Nik Hodges and Prof Zoe Pikramenou. I humbly acknowledge their wealth of knowledge and the time spent in patiently overseeing my PhD from the laboratory stage to the writing up period. I consider myself fortunate and privileged to have been under their supervisory guidance, and I would not have wanted any other supervisory team.

I am also grateful to the past and present members of the Hodges and Pikramenou group. I specially thank Sunil, who together with Shani, Chris and Siobhan took the time to teach me all I know about microscopy and imaging as well as guiding me through the pathway of nanoparticle synthesis. The advice and support of my biosciences laboratory mates and office mates especially: Lorna, Louise, Zahra, Racheal, Noor, Israa, Shrikant are well appreciated as well as colleagues on the 4th floor. I am also grateful to Steve for his help with my real time PCR and Theresa for her painstaking help with the transmission electron microscopy.

I really appreciate my old friends from back home and the wonderful friends made during this journey. I want to say thank you for always looking out for me by calling and messaging, praying for me, cooking for me, listening to me complain about my cells and nanoparticles acting up and saying don't worry you would be fine. Your presence and impact in my life these last four years cannot be quantified; it provided the right balance for this PhD.

Words fail me in expressing my gratitude to my parents who provided not just the funds, but have also been emotionally supportive, believed in me, prayed for me, encouraged me and has been my backbone and rock. My success story is not complete without them. Also, my amazing brothers: Olamide, Opeyemi and my sweet sister Blessing that says I have always been in school. Just to let you know, I am done acquiring degree certificates for now. I am grateful for all the support from you people. In the wholeness of all I am and have, I thank God Almighty who not only made it possible for me to start the PhD but also enabled me to complete it, and surrounded me with these people and others too numerous to mention I bless you all from the depth of my heart.

Table of Contents

Table of Contents	i
List of Figures	v
List of Tables	ix
List of Abbreviations.....	x

Chapter 1

Introduction and Background Literature Review	1
1.1. Engineered Nanoparticles	2
1.1.1.Engineered Nanoparticles and Medicine.	6
1.1.1.1. Therapeutic Engineered Nanoparticles.	6
1.1.1.2.Diagnostic Engineered Nanoparticles.	9
1.2.Gold Nanoparticles (AuNP)	10
1.2.1.Cellular Uptake of Gold Nanoparticles.....	14
1.2.2. Intracellular Localisation and Cellular Fate of Gold Nanoparticles.	19
1.2.3. Cytotoxicity of Gold Nanoparticles.	23
1.3. Functionalization of Gold Nanoparticles with Metal Complex.	29
1.4. Hypothesis and Objectives.	32

Chapter 2

Materials and Methods	34
Chemicals and Consumables.....	35
2.1. Nanoparticle Synthesis.	35
2.1.1 RuS12·AuNP20 Synthesis.....	35
2.1.1.1. AuNP Colloid Preparation.	35
2.1.1.2. Coating of AuNP Colloid with RuS12 and Characterisation.....	36
2.2 Cell Culture.	38
2.2.1. Cell Type.	38
2.2.2. Cell Culture Technique.	38
2.2.2.1. Sub-culturing.	38
2.2.2.2. Cell Counting by Haemocytometer.	39
2.3. Uptake of RuS12·AuNP20 in A549 cells.....	39
2.3.1 Confocal Microscopy.....	39

2.3.1.1 Live Cell Imaging.	40
2.3.1.2. Fixed Cell Imaging.	40
2.3.2. Transmission Electron Microscopy.....	41
2.3.3. Inductively Coupled Plasma Mass Spectrometry (ICP-MS).....	41
2.4. Organelle Localisation Studies Using Fluorescent Probes	42
2.4.1. Golgi: GOLGI ID® Green assay:.....	42
2.4.2. Mitochondria: MitoGreen.	43
2.4.3. Endoplasmic reticulum: ER-Tracker™ Green.	43
2.5. Organelle Localisation by Transfection of A549 Cell Line with Tagged Organelle Specific Markers.	43
2.5.1 Preparation of Luria-Bertani (LB) Broth and Agar Plates.....	44
2.5.2 Bacteria Recovery.	45
2.5.3. Plasmid Mini-Prep.....	45
2.5.4. Transient Transfection.	46
2.6. Protein Extraction.....	46
2.6.1 Protein Quantification by Bradford Assay.....	47
2.6.2 Western Blotting.....	47
2.7. Ribonucleic Acid (RNA) Extraction and Quantification.	48
2.7.1. Complementary DNA (cDNA) Synthesis	49
2.7.2. Quantitative real-time PCR (RT-PCR).	49
2.8. Cytotoxicity Assay of RuS12·AuNP20 in A549 cells.....	50
2.8.1. 3-(4, 5-dimethylthiazol-2-yl)-2, 5 diphenyltetrazolium bromide) MTT Assay.....	50
2.8.2. Crystal Violet Staining.	51
2.8.3 Dichloro-dihydro-fluorescein Assay.	52
2.8.4 Glutathione Assay.....	53
2.8.4.1. Glutathione Standard Curve.	53
2.8.5 Alkaline Comet Assay.....	54
2.8.5.1. Slide Preparation.	54
2.9. Statistics.....	55
Chapter 3	
Characterization of RuS12·AuNP20 and Uptake in A549 cells.....	56
3.1. Introduction	57
3.2. Results.....	60

3.2.1 Characterisation of RuS12·AuNP20.....	60
3.2.2.1. Confocal Microscopy	64
3.2.2.2. Transmission Electron Microscopy Imaging	71
3.2.2.3. Inductively coupled plasma mass spectrometry (ICP-MS).....	74
3.3. Discussion.....	77

Chapter 4

Localisation and Cellular Fate of RuS12·AuNP20 in A549 cells.....	82
4.1 Introduction	83
4.2 Results.....	85
4.2.1. Co-localisation by Confocal Imaging	85
4.2.1.1. Golgi Apparatus	86
4.2.1.2. Mitochondria	89
4.2.2.3. Endoplasmic reticulum	91
4.2.2.4. RAB4: Early endosomes.....	93
4.2.2.5. LAMP1: Lysosomes.....	95
4.2.2.6. LC3: Autophagosome	97
4.2.2.7. Summary of the co-localisation by confocal imaging based on Pearson's Coefficient of Correlation.....	100
4.2.2. Cellular Localisation by Transmission Electron Microscopy Imaging	102
4.2.3. Western blotting of Microtubule-associated proteins 1A/1B light chain 3 (LC3).....	105
4.2.4. Quantitative real-time PCR (RT-PCR)	107
4.3 Discussion.....	109

Chapter 5

Cytotoxicity of RuS12·AuNP20 on A549 cells	116
5.1. Introduction	117
5.2. Results.....	119
5.2.1. MTT Assay.	119
5.2.2. Crystal Violet Assay.....	121
5.2.3. Dichloro-dihydro-fluorescein diacetate (H ₂ DCFDA Assay)	123
5.2.4. Glutathione Assay.....	125
5.2.5. Alkaline Comet Assay	127
5.3 Discussion.....	130

Chapter 6

General Discussion and Conclusion	135
6.1. General Discussion.....	136
6.2 Conclusion	142
6.3 Future Work/ Recommendations	143
References..	144

Appendix

Chapter 2: Materials and Method	162
Chapter 3: Characterization of RuS12·AuNP20 and Uptake in A549 cells.....	165
Chapter 4: Localisation and Cellular Fate of RuS12·AuNP20 in A549 cells.....	176
Chapter 5: Cytotoxicity of RuS12·AuNP20 on A549 cells.	185

List of Figures

Figure 1: Rosace nord stained glass in the Cathédrale Notre-Dame de Chartres (France). -----	2
Figure 2: Natural processes leading to the formation of nanoparticles in the environment-----	3
Figure 3: Representative types of ENPs (in green) and their origins (red).-----	4
Figure 4: Schematic illustration of Surface Plasmon Resonance -----	11
Figure 5: Images of aqueous solutions of gold nanoparticles (AuNP) -----	12
Figure 6: Schematic representation of electrostatic and steric stabilization in metal nanoparticles.-----	13
Figure 7: Multiple portals of entry into the mammalian cell. -----	15
Figure 8: Endosomal trafficking. -----	20
Figure 9: Possible ROS mediated mechanism of toxicity. -----	28
Figure 10 : A schematic representation of coating of AuNP colloid with zonyl and Ruthenium complex (RuS12) to give RuS12·AuNP20.-----	37
Figure 11 Schematic of the pCMV6-AC-GFP expression vectors -----	44
Figure 12: Uv-vis absorption spectra coating of citrate stabilised AuNP with RuS12. -----	62
Figure 13: TEM image of RuS12.AuNP20 in water. -----	63
Figure 14: Luminescence emission spectra of RuS12.AuNP20 in water -----	63
Figure 15: Representative merged confocal images of major time points of fixed A549 treated with 0.9 nM RuS12·AuNP20 and Hoechst.-----	67
Figure 16: Representative confocal images of live cell imaging of A549 treated with 0.9 nM RuS12.AuNP20 -----	68
Figure 17: Steps in quantification of confocal images -----	69
Figure 18: Quantification of acquired images of A549 cells treated with 0.9 nM RuS12·AuNP20 -----	70
Figure 19: TEM image of A549 cells treated with 0.9 nM RuS12·AuNP20 for 2 hours. -----	72

Figure 20: TEM image of A549 cells treated with 0.9 nM RuS12·AuNP20 for 4 hours.	73
Figure 21: TEM image of A549 cells treated with RuS12·AuNP20 for 72 hours.	73
Figure 22: ICP-MS measurement of uptake of 0.9 nM RuS12·AuNP20 in A549 cells.	75
Figure 23: Linear fit of count by microscopy and concentration of Au by ICP-MS.	76
Figure 24: Pathway of macropinocytosis	80
Figure 25: Representative image of fixed A549 control cells stained with Golgi ID 86	
Figure 26 Representative image of fixed A549 treated with 0.9nM RuS12·AuNP20 for 24 hours and stained with Golgi ID	88
Figure 27: Representative image of fixed A549 treated with 0.9nM RuS12·AuNP20 for 24 hours and stained with MitoGreen	90
Figure 28: Representative image of fixed A549 treated with 0.9 nM RuS12·AuNP20 for 24 hours and stained with ER-tracker green.	92
Figure 29: Representative image of fixed A549 transiently transfected with GFP-RAB4.	94
Figure 30: Representative image of fixed A549 transiently transfected with GFP-LAMP1.	96
Figure 31: Representative image of fixed A549 transiently transfected with GFP-LC3.	99
Figure 32: Pearson's Coefficient of Correlation value of A549 organelles treated with 0.9nM RuS12·AuNP20 at 37 ⁰ C	101
Figure 33: TEM image of A549 cells treated with 0.9nM RuS12·AuNP20 for 4 hours at 37 ⁰ C	103
Figure 34: TEM image of A549 cells treated with 0.9nM RuS12·AuNP20 for 24 hours at 37 ⁰ C	103
Figure 35: TEM image of A549 cells treated with 0.9 nM RuS12·AuNP20 for 48 hours at 37 ⁰ C	104
Figure 36: Detection of LC3 protein by western blotting.	106
Figure 37: RT-PCR of A549 cells treated with 0.9 nM RuS12·AuNP20 over 0-24 hours	107
Figure 38: Intracellular trafficking of ENPS	111

Figure 39: Process of Autophagy-----	113
Figure 40: MTT Assay on A549 treated with RuS12·AuNP20 for 24, 48 and 72 hours -----	120
Figure 41: CVS on A549 treated with RuS12·AuNP20 for 24, 48 and 72 hours----	122
Figure 42: DCFH-DA Assay on A549 treated with RuS12·AuNP20 for 24, 48 and 72 hours -----	124
Figure 43: GSH Assay on A549 treated with RuS12·AuNP20 for 24, 48 and 72 hours -----	126
Figure 44: Representative images of cell nuclei of A549 assessed for DNA strand break by Comet Assay. Arrows indicate comet-like structure.-----	128
Figure 45: Median Tail intensity of A549 cells treated with RuS12·AuNP20-----	129
Figure 46: Steps in quantification of confocal images by ImageJ-----	164
Figure 47: Representative merged confocal images of major time points of fixed A549 treated with 0.9 nM RuS12·AuNP20 and Hoechst.-----	168
Figure 48: A549 cells treated with 0.63 nM RuS12 alone for 4 hours -----	169
Figure 49: Standard curve of Au and Ru used for ICP-MS-----	170
Figure 50: ICP-MS measurement of uptake of 0.9 nM RuS12·AuNP20 in A549 cells	171
Figure 51: Cell viability of A549 cells treated with endocytic inhibitors -----	174
Figure 52: FITC fluorescence of positive control of endocytic inhibitors -----	175
Figure 53: Representative image of fixed A549 treated with 0.9 nM RuS12·AuNP20 and stained with Golgi ID-----	177
Figure 54: Representative image of fixed A549 treated with 0.9nM RuS12·AuNP20 and stained with with MitoGreen -----	178
Figure 55: Representative image of fixed A549 treated with 0.9nM RuS12·AuNP20 and stained with ER-tracker green. -----	179
Figure 56 Representative image of fixed A549 transiently transfected with GFP- RAB4 and treated with 0.9 nm of RuS12·AuNP20.-----	180
Figure 57: Representative image of fixed A549 transiently transfected with GFP- LAMP1.-----	182
Figure 58: Representative image of fixed A549 transiently transfected with GFP- LC3. -----	183

Figure 59: MTT Assay on A549 treated with RuS12·AuNP20 for 24, 48 and 72 hours -----	185
Figure 60: MTT Assay on A549 treated with RuS12 alone for 24 hours-----	185
Figure 61: CVS on A549 treated with RuS12·AuNP20 for 24, 48 and 72 hours----	186
Figure 62: DCFH-DA Assay on A549 treated with RuS12·AuNP20 for 24, 48 and 72 hours -----	186
Figure 63: Standard curve of GSH used for GSH Assay.-----	187
Figure 64: GSH Assay on A549 treated with RuS12·AuNP20 for 24, 48 and 72 hours -----	187
Figure 65: Median Tail intensity of A549 cells on exposure to RuS12·AuNP20 ---	188

List of Tables

Table 1: Summary of in vitro gold nanoparticle toxicity results based on surface coating -----	26
Table 2: Gene used in RT-PCR -----	50
Table 3: Summary of AuNP SPR shift upon coating. -----	62
Table 4: Dynamic light scattering (DLS) sizing data of AuNP in water. -----	63
Table 5: Summary of the trafficking of RuS12·AuNP20 in A549 cell from 2-72hrs.	138
Table 6: Summary of intracellular fate and toxicity of A549 treated with RuS12·AuNP20 -----	141

List of Abbreviations

A549:	Adenocarcinoma epithelial cell line
ANOVA:	Analysis of Variance
CAT:	Catalase
CVS:	Crystal violet staining
DLS:	Dynamic light scattering
EM:	Emission
ENP:	Engineered Nanoparticles
EXC:	Excitation
FITC:	Florescein isothiocyanate
GFP:	Green fluorescent protein
GSH:	Glutathione
GSR:	Glutathione reductase
H2DCF-DA:	2',7'-dichlorodihydrofluorescein diacetate
HSP:	Heat shock protein
ICP-MS:	Inductively Coupled Plasma Mass Spectroscopy
LAMP1:	Lysosomal-associated membrane protein 1
LC3:	light chain 3 ptotein
MTT:	3-(4,5-dimethylthiazol-2-yl)-2,5-diphenyltetrazolium bromide
RAB4:	Ras-related protein
ROS:	Reactive oxygen species
RT-PCR:	Real time-polymerase chain reaction
RuS12·AuNP20:	Ruthenium bipyridine SS. Gold Nanoparticles
SEM:	Standard error of mean
TEM:	Transmission electron microscopy
Uv-vis:	ultraviolet-visible spectrophotometry

Chapter 1

Introduction and Background Literature Review

1.1. Engineered Nanoparticles

Nanoparticles are particles within the 1-100 nanometer (nm) scale, showing properties different from bulk samples of the same material (Auffan *et al.*, 2009; Nel *et al.*, 2006; Uboldi *et al.*, 2009). The key point in defining nanoparticles lies in its dimensions; that is all three dimension of the particle are within the nanoscales (Murthy, 2007).

The existence of nanomaterials can be traced back to Roman times. In Medieval Europe, what is now believed to be nanoparticles were used in stained glass currently observed in ancient churches (an example depicted in

Figure 1) and nanotubes were also found in blades of swords made in Damascus used during the crusader war (Colomban *et al.*, 2009; Horikoshi & Serpone, 2013; Jin *et al.*, 2001; Reibold *et al.*, 2006). However, the term nanoparticle was yet to be coined.

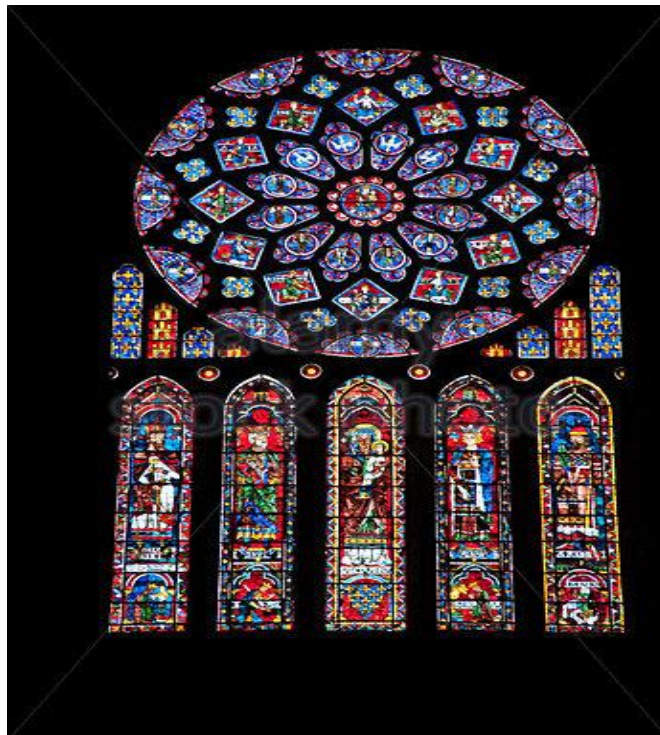


Figure 1: Rosace nord stained glass in the Cathédrale Notre-Dame de Chartres (France).

Color changes depend on the size and shape of particles, which were made up of either gold (Au) or silver (Ag). Red triangle: $\sim 100\text{nm Ag}$; Yellow sphere: $\sim 100\text{nm Au}$; Green spheres: $\sim 50\text{nm Ag}$; Light blue sphere: $\sim 90\text{nm Ag}$ and Blue spheres: $\sim 40\text{nm Ag}$. Figure adapted from (Horikoshi & Serpone, 2013).

The renowned physicist Richard Feynman in 1959 during a talk titled “There is plenty room at the bottom” first raised the scientific potential of nanoparticles and suggested engineers should go down to the bottom (nanoscale) and start from there (Appenzeller, 1991; Fitzpatrick *et al.*, 2014). This talk is widely seen as the beginning of the study of nanoparticles, which became fully possible after the invention of powerful microscopes to enable the imaging of particles at nanoscale.

Nanoparticles may occur naturally in soil, ground and surface water (Sharma *et al.*, 2015). They can also be formed by naturally occurring activities such as wind erosion, weathering, volcanic activity, chemical-precipitation of naturally occurring chemicals and biomass combustion (in favorable conditions of temperature and oxygen) as shown in Figure 2 (Hochella *et al.*, 2015; Wang *et al.*, 2013) however, most nanoparticles are man-made.

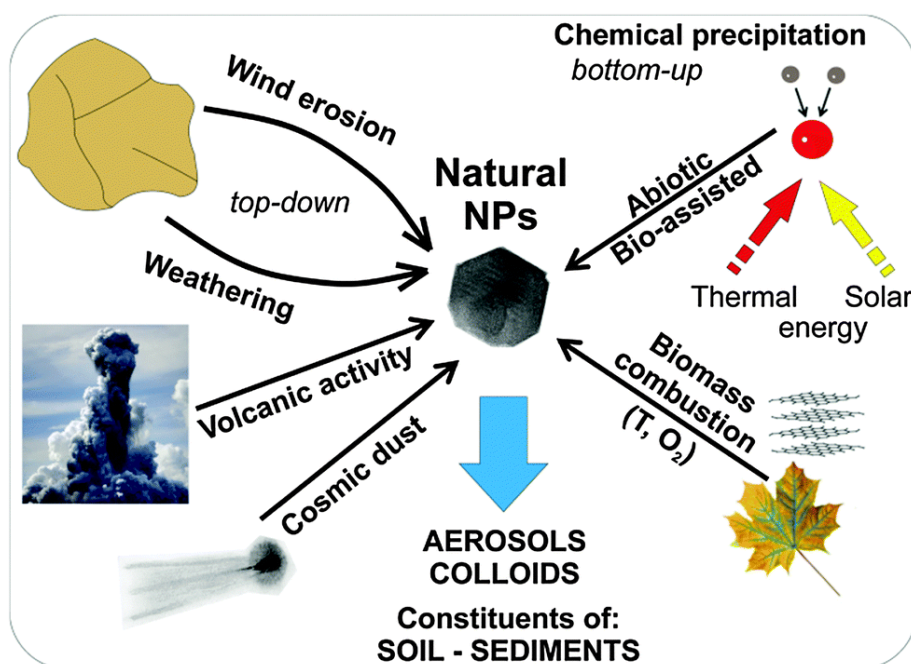


Figure 2: Natural processes leading to the formation of nanoparticles in the environment (Natural NPs – natural nanoparticles; T – temperature; O₂ – oxygen) bottom-up approach starts from molecular/ionic species while the top-down approach starts from larger precursors. Figure taken from (Sharma *et al.*, 2015).

Man-made nanoparticles are referred to as anthropogenic nanoparticles and can be classified into two groups: non-engineered nanoparticles and engineered nanoparticles. Non-

engineered nanoparticles are incidental by-products of human activities such as running diesels, fuels, erosions, welding, large-scale mining and combustion products (Handy & Shaw, 2007; Reinert *et al.*, 2006). Non-engineered nanoparticles generally have widely distributed sizes and shapes and are a mixture of different elements (Contado, 2015) therefore they are heterogeneous in nature. In contrast, engineered nanoparticles (ENPs) are specifically synthesized usually by chemical reactions (Oberdorster *et al.*, 2005). The design and synthesis of ENPs varies, and is dependent on its final applications (Kessler, 2011a). ENPs usually range in design and structure from solid spheres to tubes, rods, hollows and complex strands (Provenzale & Silva, 2009). ENPs are often polymers, carbon based, non-metal, metals or metal oxide as shown in Figure 3. ENPs can also be made from biological molecules like phospholipids, lactic acid and dextran (De Jong & Borm, 2008; Maurer-Jones *et al.*, 2013; Sharma *et al.*, 2015; Tiede *et al.*, 2008).

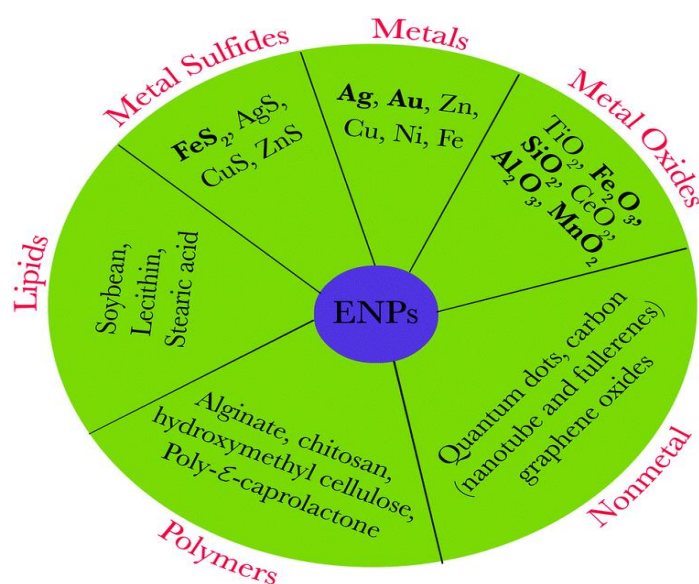


Figure 3: Representative types of ENPs (in green) and their origins (red).

The origin of ENPs determines the type of ENPs. Example: ENPs made of metals are referred to as metallic ENPs with Ag and Au been the most common. Figure adapted from (Sharma *et al.*, 2015).

The increase in the synthesis of ENPs over the last decade is linked to the desire to take advantage of their unique electrical, optical, magnetic and catalytic properties associated with their nanoscale dimensions (Limbach *et al.*, 2007; Sanvicens & Marco, 2008; Tonga *et*

al., 2014). The remarkable properties of ENPs are responsible for their various applications especially their unique large surface area to volume ratio (Auffan *et al.*, 2008; Auffan *et al.*, 2009; Chen and Zhang, 1998; Dick *et al.*, 2002; Kalantzi and Biskos, 2014). ENPs are currently being developed to target specific applications in various economic sectors: most notably: the chemical industry, structural engineering, textiles, electronics, consumer products and medical sciences (Bhatt & Tripathi, 2011; Linkov *et al.*, 2009; Mazzola, 2003). ENPs can be either a final product or a component of a final product. Specific commercial applications of ENPS includes sporting goods, tyres, stain-resistant clothing, sunscreens, sanitary ware coatings, toothpaste, food products and electronics (Heiligtag & Niederberger, 2013; Hoet *et al.*, 2004; Kessler, 2011b; Nel *et al.*, 2006; Tsuji *et al.*, 2006; Zhang *et al.*, 2015). In addition to these commercial applications, intensive research is geared towards the potential application and inherent risks associated with the use of ENPs in the health sector, which is discussed in details in this literature review.

1.1.1. Engineered Nanoparticles and Medicine.

Engineered nanoparticles have remarkable potential in almost every branch of medicine ranging from oncology, cardiology, immunology, neurology, endocrinology, ophthalmology, pulmonary, orthopedics, to dentistry (Jain, 2008; Murthy, 2007). Recent investigation into specific use of ENPs in medicine includes:

- Diagnosis,
- Fluorescence biological imaging,
- Probing of DNA structure,
- Detection of proteins/gene,
- Tumour destruction via heating (Hyperthermia),
- Tissue engineering,
- Gene and Drug Delivery (Cao *et al.*, 2003; Giljohann *et al.*, 2010; Nel *et al.*, 2006; Pantarotto *et al.*, 2004; Salata, 2004; Sanvicens & Marco, 2008).

Therefore, the role of ENPs in medicine can broadly be classified into therapeutic and diagnostic roles (Kim & Hyeon, 2014; Zhang *et al.*, 2008). As a therapeutic agent ENPs have great potential for targeted delivery of drugs and genes to help overcome problems of drug safety and toxicity as well as crossing biological barriers (Burgess *et al.*, 2010; Davis *et al.*, 2008). ENPs as a diagnostic agent, allows detection at molecular scale, example is the identification of precancerous cells and disease markers that are difficult to detect via traditional diagnostic methods (Alharbi & Al-Sheikh, 2014; Solano-Umaña *et al.*, 2015).

1.1.1.1. Therapeutic Engineered Nanoparticles.

Targeted delivery is one of the most important therapeutic application of ENPs. ENP can act as a delivery system that allows targeted delivery and controlled release (Caruthers *et al.*,

2007; De Jong & Borm, 2008; Zhang *et al.*, 2008). The rationale behind ENPs being a good delivery system lies in their physiochemical properties listed below.

- i. Ability to improve pharmaceutical and pharmacological property of drug, without causing drug degradation while ensuring reduced side effects (Peer *et al.*, 2007; Singh & Lillard, 2009; Wilczewska *et al.*, 2012).
- ii. Ability to cross (because of its nano-size) a range of biological barriers. Examples: fenestration of epithelial lining, endothelial and blood brain barrier as well as ability to penetrate deep into tissues through fine capillaries, accumulate in angiogenic tumour tissue to deliver drugs to target tissue/organ (Sung *et al.*, 2007; Upadhyay, 2014; Voigt *et al.*, 2014).
- iii. Ability to deliver multiple types of therapeutics with different physiochemical properties (Kamaly *et al.*, 2012; Panyam & Labhasetwar, 2003).
- iv. Ability to deliver a combination of imaging and therapeutic agents for real-time monitoring of therapeutic efficacy (Jo *et al.*, 2016; Kamaly *et al.*, 2012; Zhang *et al.*, 2008).

Therapeutic ENPs are usually delivered to site of action, which in many cases are tumor by either active or passive targeting. In passive targeting, the ENPs accumulate preferentially to the tumor and inflammation sites via the enhanced permeability and retention (EPR) effect (Bazak *et al.*, 2014). The EPR effect occurs when there is a disruption in the normal vasculature causing leaky blood vessels. Tumors, sites of inflammation, and diseased tissues are usually where EPR effects are observed, because of the compromise in their blood vessels compared to a normal blood vessels, thereby causing increased permeability due to openings which are absent in healthy tissues (Kobayashi *et al.*, 2013). The EPR effect allows therapeutic ENPs to reach and persist in their target tissue/sites by passing readily from the blood vessels into tumor or inflamed tissue (Burgess *et al.*, 2010) as shown in Figure 4:

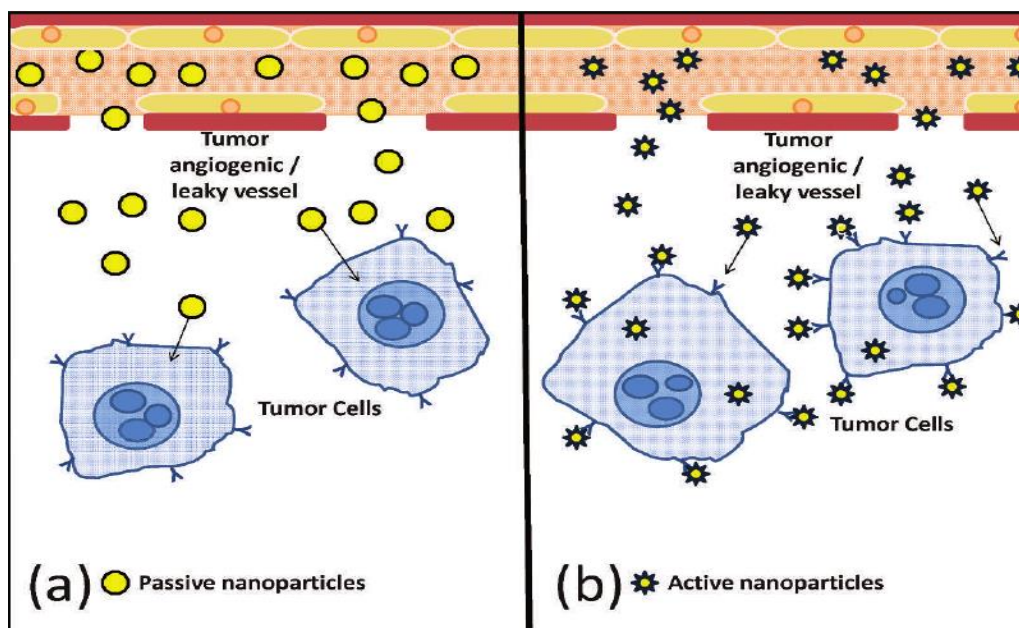


Figure 4: Schematic illustration of nanoparticle accumulation in tumors

A: passive mechanism via the EPR effect that allows preferential accumulation of nanoparticles near tumor tissue using leaky vasculature. B: Site-specific active tumor targeting through ligand-tumor cell surface receptor interactions. Figure taken from (Patel *et al.*, 2012)

In active targeting (also known as ligand-mediated targeting), bio-recognition molecules are attached to the surface of ENPs to target specific markers such as sugars or lipids or receptors that are overly expressed on the surface of the tumors usually and absent in healthy tissue (des Rieux *et al.*, 2013; Yu *et al.*, 2010). Bio-recognition molecules could be antibodies, proteins, peptides, nucleic acids, sugars or small molecules (Saha *et al.*, 2010). This method of targeting tends to exhibit higher specificity, efficacy with decrease toxicity (Byrne *et al.*, 2008; Singh & Lillard, 2009).

1.1.1.2. Diagnostic Engineered Nanoparticles.

Although most of the applications of ENPs in medicine are directed towards therapeutic use, ENPs can also function as diagnostic agent specifically in imaging as nanoprobes. ENPs aim to improve the sensitivity and specificity in medical testing because they are well suited as a label for early diagnosis of diseases and biological testing (Rosi & Mirkin, 2005).

Imaging has the ability to detect, quantify, and display molecular and cellular changes *in vitro* and *in vivo* non-invasively (Weissleder, 2006). The use of ENPs as nanoprobes offers them an advantage over routinely used fluorescent markers for diagnostic purpose. These advantages includes less photo-bleaching, better contrast enhancement and increased sensitivity (Chapman *et al.*, 2013; Mirabello *et al.*, 2015; Sahoo & Labhasetwar, 2003). The most commonly used ENPs for imaging are quantum dots (QD), magnetic nanoparticles and metallic nanoparticles such as gold and silver (Biju *et al.*, 2008; Edmundson *et al.*, 2014; Mirabello *et al.*, 2015). For the purpose of this thesis, only gold nanoparticles (metallic nanoparticles) will be thoroughly discussed because they have demonstrated enormous feasibility in diagnosis and therapy of various different types of cancers (Huang & El-Sayed, 2010) and are the subject of this research.

1.1. Gold Nanoparticles (AuNP)

The discovery of AuNP was initiated by Michael Faraday when he wrote “gold is reduced to exceedingly fine particles which becoming diffused, produces a beautiful fluid of different colours” (Faraday, 1857). What Faraday observed 159 years ago is currently regarded as colloidal gold because they exhibited different characteristic from elemental gold. Colloidal gold, also known as gold nanoparticles (AuNP), is a suspension (or colloid) of nanometer-sized particles of gold (Mody *et al.*, 2010).

AuNP have unique chemical and physical properties making them suitable as optical markers for medical diagnosis and drug delivery (Duncan *et al.*, 2010; Gibson *et al.*, 2007; Mieszawska *et al.*, 2013; Paciotti *et al.*, 2006). Certain characteristics of AuNP such as: ease of synthesis in the lab, stability, Surface Plasmon Resonance (SPR), ability to scatter light, facile bio-conjugation and ability to incorporate selectively with recognition molecules such as proteins, makes them attractive for biomedical applications specifically cancer diagnosis and therapeutic drug delivery (Hu *et al.*, 2006; Jain *et al.*, 2008; Sokolov *et al.*, 2003).

The SPR of AuNP is responsible for most of its attractive properties. The SPR arises from free oscillating electrons on the surface of AuNPs, which can be excited by light of a specific wavelength. This excitation produces a collective coherent oscillation of the free electrons from the metal and a dipole oscillation along the direction of the field of light (Huang & El-Sayed, 2010). SPR is achieved when the amplitude of the dipole oscillating reaches a maximum at a specific frequency (Huang & El-Sayed, 2010; Huang *et al.*, 2007).

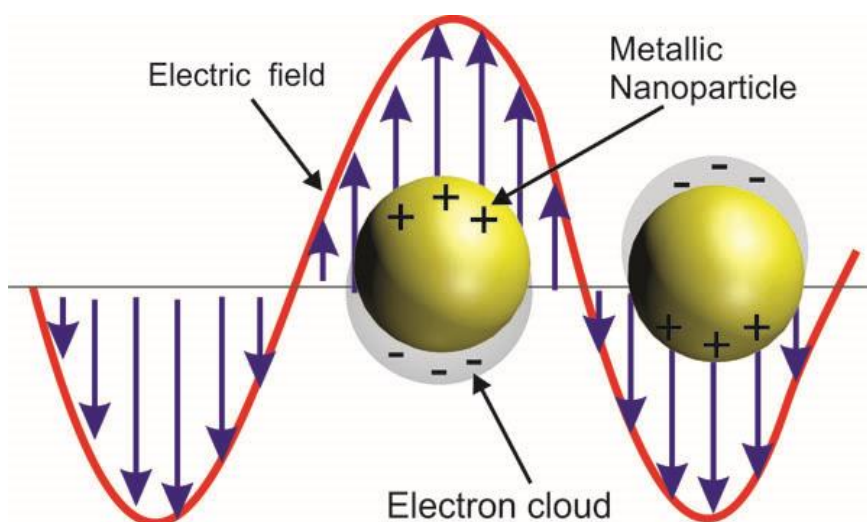


Figure 4: Schematic illustration of Surface Plasmon Resonance

The interaction of light of a specific wavelength with free electrons on the surface of metallic nanoparticles causes them to oscillate collectively in the direction of the electric field. Figure adapted from (Camacho, 2015).

As the size of AuNP increases, the wavelength of the SPR also increases and there is a change in colour from red to purple as observed in the upper panel of Figure 5 (Murphy *et al.*, 2008). SPR induces a strong absorption of incident light and thus can be measured using a UV-Vis absorption spectrometer. Therefore, modification of SPR by varying the size and shape of AuNP is useful in the synthesis of functionalised AuNPs with specific optical properties for different biomedical applications (Amendola *et al.*, 2017).

The SPR also strongly affects the aspect ratio of nanoparticles. Aspect ratio is defined as the length of the major axis divided by the width of the minor axis, therefore nanoparticles that are spherical have an aspect ratio of 1 (Murphy & Jana, 2002). When the shape of AuNP changes from spheres to rod, the SPR produces a strong band in the near-infrared region, which corresponds to the amplitude of the oscillating electrons (Huang & El-Sayed, 2010). This band (which is usually in the visible region), shifts largely from visible region to near-infrared region and results in increased aspect ratio as well as colour change as observed in lower panel of

Figure 5 (Huang & El-Sayed, 2010). An example of aspect ratio effect is a change in shape: Gold nanorods can be formed by asymmetric growth of spherical AuNPs in the presence of shape-forming surfactants, weak reducing agents and catalysts (Huang & El-Sayed, 2010; Ward *et al.*, 2014).

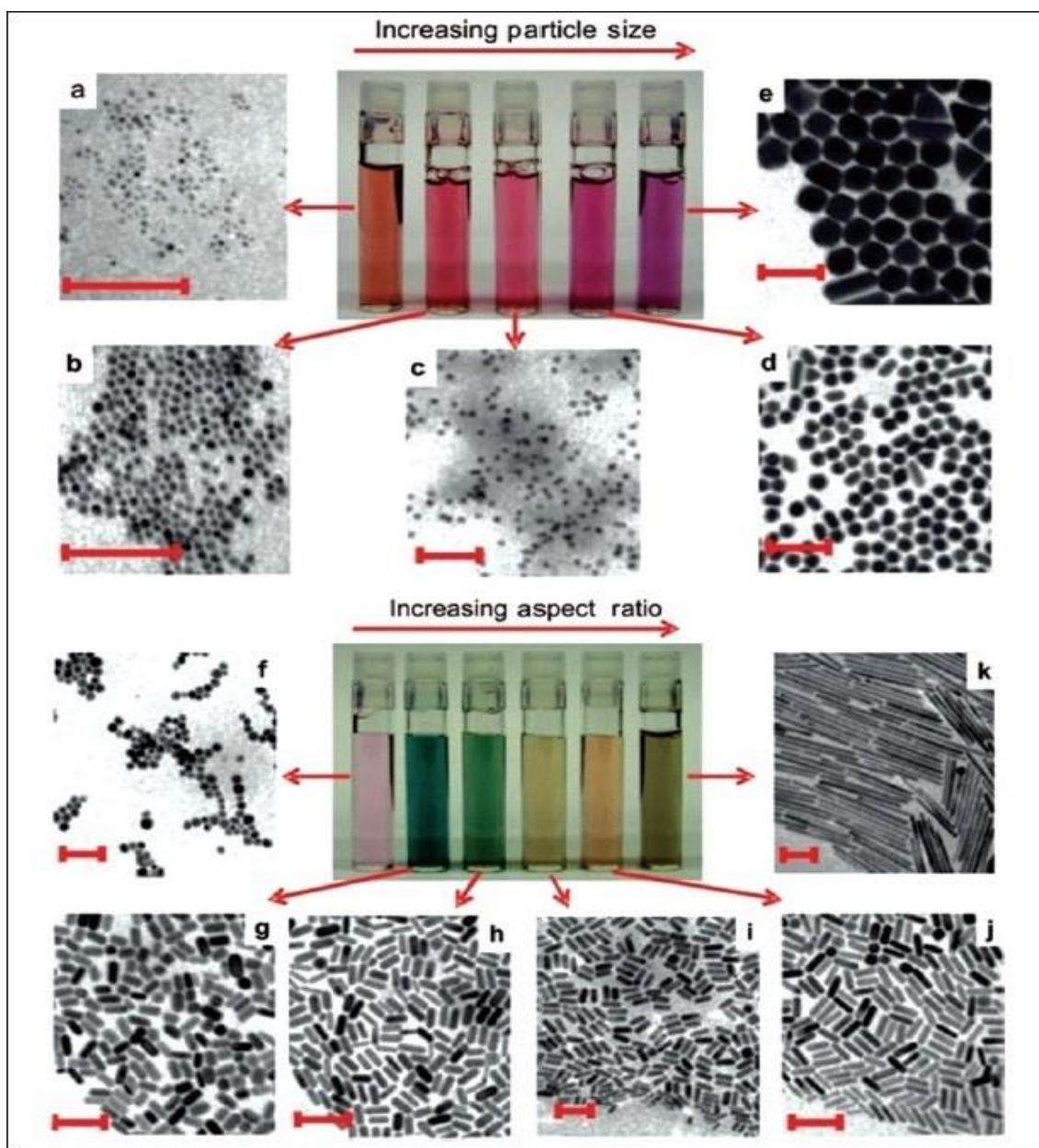


Figure 5: Images of aqueous solutions of gold nanoparticles (AuNP)

Nanospheres (upper panels) and gold nanorods (lower panels). The AuNP and their corresponding transmission electron microscopy images are shown with a scale bar representing 100 nm. Sphere (upper panel a-e) showed a less change in colour with increasing size compared to the rods (lower panel f-k). The difference in colour is because of plasmon band, which has greater effect on rods compared to spheres. Image adapted from (Murphy *et al.*, 2008).

The most common method for the synthesis of monodisperse spherical AuNP was pioneered by Turkevich *et al.* (1951) and later refined by Frens (1973). It involves the chemical reduction of gold salts such as hydrogen tetrachloraurate (HAuCl₄) in aqueous, organic or mixed solvent systems. Aggregation tends to occur because of the high reactivity of gold surface, which results in collision of colloidal particles with each other due to Brownian motion, gravity and similar forces present in the colloidal suspension (Hotze *et al.*, 2010). The main reason for aggregation of particles in colloidal suspension is van der Waals forces that attracts particles in close proximity and causes destabilization (Zhou *et al.*, 2007). It is essential for AuNP to be stably dispersed in biological fluid for most of its biomedical applications. To avoid the issue of aggregation; AuNP are regularly reduced in the presence of stabilisers, which bind to its surface and prevents aggregation via cross-linking and charge properties (Castro & Kumar, 2013). The stabiliser aims to introduce repulsive forces between particles to prevent particles from aggregating as shown in Figure 6.

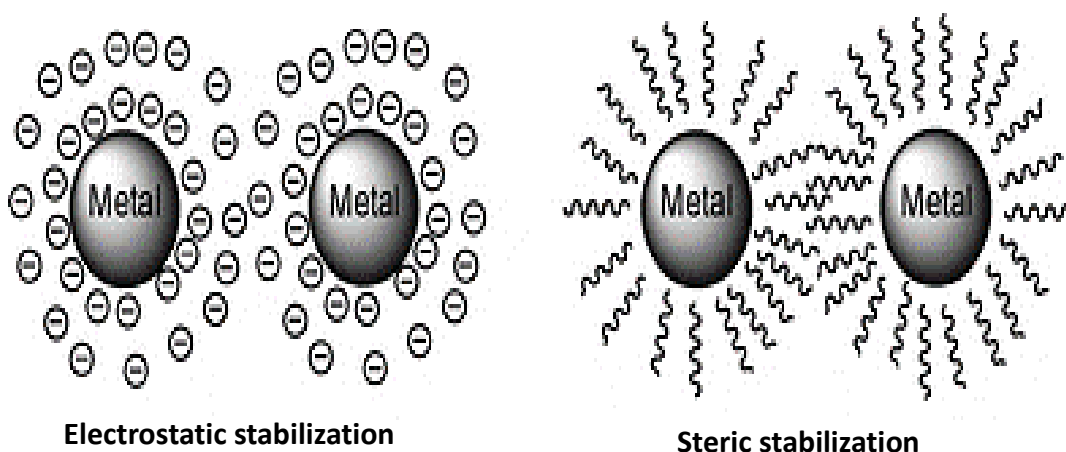


Figure 6: Schematic representation of electrostatic and steric stabilization in metal nanoparticles.

*Electrostatic stabilization of positively charged nanoparticles produced double layer of negative charge around it, preventing aggregation between the particles in solution. While, in steric stabilization polymer forms a coating around metal nanoparticles. Image adapted from (Gual *et al.*, 2010).*

The major methods of stabilization of colloidal AuNP are electrostatic stabilization and steric stabilization (Babu & Dhamodharan, 2009; Lin *et al.*, 2004). Electrostatic stabilization is a kinetic mechanism based on the generation of an electrical double layer of ions around the particles. The double layer causes repulsion between particles by counterbalancing the van der Waals force by repulsive Coulomb force that acts between the charged colloidal particles and provides stability (Brown *et al.*, 2016; Kraynov & Müller, 2011; Polte, 2015). Steric stabilization is a thermodynamic mechanism based on the coordination of sterically bulky organic macromolecules such as polymers and surfactants. They act as a protective shield on metallic surface of particle preventing attractive force between particles (Polte, 2015; Zhou *et al.*, 2009). Because steric stabilization is a thermodynamic stabilization, particles are re-dispersible when slightly aggregated unlike particles with electrostatic stabilization (Babu & Dhamodharan, 2009; Chow & Zukoski, 1994). Citrate stabilization is a form of electrostatic stabilization as it provides a repulsive force; this method of stabilization was employed during the synthesis of AuNP used in this research for cellular studies.

1.1.1. Cellular Uptake of Gold Nanoparticles.

Cellular uptake of AuNPs occurs via several pathways that are dependent on particle physiochemical properties such as size, shape and surface coatings (Chithrani *et al.*, 2006; Kunzmann *et al.*, 2011; Nativo *et al.*, 2008). Cellular uptake of AuNPs into cells is necessary in exerting specific function/target in the cells; therefore, it is necessary to understand the mechanism of cellular uptake.

For cellular uptake to occur, particles must cross the barrier of the plasma membrane, which is selectively permeable to control the entry and exist of molecules in and out of the cell. Smaller molecules such as amino acids, sugars and ions move across the membrane by

diffusion, osmosis and mediated-transport system; active transport and facilitated diffusion (Conner & Schmid, 2003). While molecules too large to pass through the cell membrane like AuNP move across the membrane by endocytosis (Levy *et al.*, 2010).

Endocytosis is a form of active transport where uptake occurs by cells engulfing the molecule aimed at internalization. Endocytosis is broadly classified into phagocytosis (cell eating) and pinocytosis (cell drinking) (Steinman *et al.*, 1983) as shown in Figure 7.

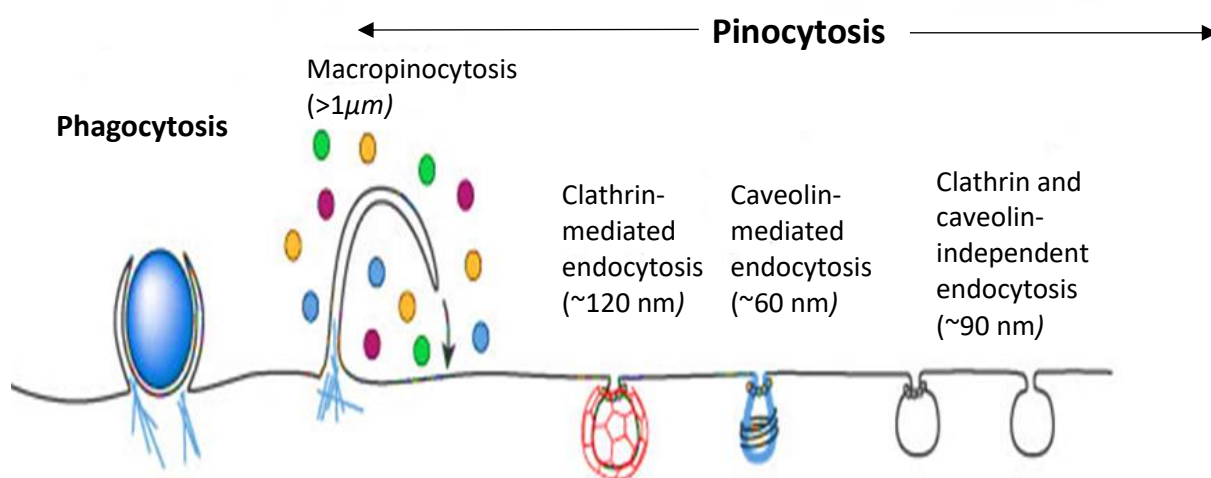


Figure 7: Multiple portals of entry into the mammalian cell.

The endocytic pathway differs with regard to the size of the endocytic vesicle, the nature of the cargo and the mechanism of vesicle formation. Pinocytosis is the general mode of uptake in non-phagocytic cell. Image adapted from (Conner & Schmid, 2003)

Phagocytosis involves cells engulfing large particles (> 0.5 µm) such as bacteria or cell debris and is restricted to specialised phagocytic cells such as cells involved in immune response for example: macrophages (Stow & Condon, 2016). Pinocytosis involves the uptake of fluids and solutes and is the most common form of uptake in eukaryotes (Conner & Schmid, 2003). The two major types of pinocytosis are macropinocytosis and receptor-mediated endocytosis (RME) that is further divided into clathrin, and caveolin mediated endocytosis (Gao *et al.*, 2005). Macropinocytosis is highly dependent on actin cytoskeleton because it involves the reorganisation of the cell membrane to form a macropinosome that

protrudes from the plasma membrane and re-joins the plasma membrane after engulfing solutes (Doherty & McMahon, 2009). Clathrin-mediated endocytosis is the most studied and best understood form of receptor-mediated endocytosis. It occurs by an inward budding of the plasma membrane and formation of clathrin-coated vesicles (Johannes *et al.*, 2015). Caveolin mediated endocytosis involves the formation of a flask shaped invagination composed of lipids rafts from the plasma membrane and their mechanism is poorly understood (Andrews *et al.*, 2014; Kirkham & Parton, 2005). Clathrin and Caveolin-independent endocytosis are methods of cellular uptake that do not fall into aforementioned categories. They do not involve the use of actin filaments, clathrin coated pits or caveolae flask (Damm *et al.*, 2005; Mayor & Pagano, 2007). They are the least understood mode of cellular uptake.

The exact mechanism by which AuNPs enters cells is still the subject of much debate; typically, delivery of ENPs into cells involves attachment to receptor on the cell surface plasma membrane, followed by internalization due to endocytosis (Treuel *et al.*, 2013). Various researchers have confirmed via TEM images, that the internalization of AuNPs in common cell line models such as HeLa, A549, Caco-2 cells, HEK 293 occurs by endocytosis (Giljohann *et al.*, 2010; Oh & Park, 2014; Park *et al.*, 2009; Tlotleng *et al.*, 2016). According to Chithrani *et al.* (2006), they hypothesize and demonstrated RME to be the major mechanism of cellular uptake of spherical shaped citrate capped AuNP by using transferrin-coated AuNP. Similar study have shown using AuNP of ≤ 100 nm to be internalised by RME (Chithrani & Chan, 2007; Nativo *et al.*, 2008; Shukla *et al.*, 2005).

In RME, the receptor recycles back to the plasma membrane surface after cellular internalization of ENPs (Chithrani *et al.*, 2006; Xu *et al.*, 2013). Cells have a maximum receptor density (the number of receptors per cell surface area on the membrane) therefore, the availability of receptors affects the cellular uptake of particle in terms of quantity

(Chithrani *et al.*, 2006). Cellular uptake of ENPs leads to the localisation within vesicles usually endosomes (Kou *et al.*, 2013; Yameen *et al.*, 2014). The endosomes are formed from the invagination of the membrane after the uptake of particles and undergoes fusion with other organelles in the cells usually the lysosome (Panariti *et al.*, 2012). The fusion of the endosome and the acidic lysosome can result in degradation of nanoparticles by lysosomal enzymes (Sabella *et al.*, 2014; Stern *et al.*, 2012).

Efficient endocytosis of AuNP is dependent on physiochemical properties such as particle shape, size and surface properties (Alkilany & Murphy, 2010; Chithrani, 2011; Kou *et al.*, 2013; Levy *et al.*, 2010; Wang *et al.*, 2015). AuNP can be synthesised to various shapes: spherical, rod, star or triangular plate and the shape affects the way is taken up by the cells. Chithrani *et al.* (2006) demonstrated that spherical AuNPs were more rapidly internalised in cells by RME (clathrin-mediated endocytosis) compared to gold nanorods. HeLa cells were treated with spherical AuNPs with diameter of 14, 30, 50, 74 and 100 nm and gold nanorods with length by width of 40 x14 nm and 74 x14 nm were for 6 hours. Their result showed cellular uptake measured quantitatively by ICP-ACES to be greater in spherical AuNPs of 74 and 14 nm diameter compared to rod-shaped AuNP of 74x14 nm. They attributed the differences in uptake to the curvature of the different-shaped nanoparticles and the surfactant used during synthesis. They propose that the rod-shaped AuNPs have more contact area to interact with the cell membrane receptors than the spherical, thereby reducing the number of available receptor sites for binding. They also propose that the surfactant used cetyltrimethylammonium bromide (CTAB) during synthesis is adsorbed onto the rod-shaped nanoparticles and if not properly purified can interfere with the serum protein that normally binds to AuNPs and aids cellular uptake (Chithrani *et al.*, 2006).

The cell plasma membrane has a strong negative charge because of phosphate groups attached to the lipid bilayer. Therefore, the charge of AuNP also affects its interaction with

plasma membrane. Studies have shown that positively charged AuNPs are more readily internalised (Gong *et al.*, 2015), this can be attributed to differences in charge of particle and plasma membrane thereby causing an attraction observed as cellular uptake. *In vitro*, when particles are dispersed in cell culture media, the media can influence their surface charge, which then affects their cellular uptake (Strojan *et al.*, 2017).

Cell culture media is a complex aqueous mixture of electrolytes, serum proteins, nutrients, antibiotics and metabolites and the various components can interact with nanoparticles and have an effect on cellular uptake. Serum proteins present in media are capable of being adsorbed onto the surface of nanoparticles and form a protein corona, which is a nanoparticle-protein complex (Fleischer & Payne, 2014; Piella *et al.*, 2017). Protein corona formation is dependent on various factors such as size, surface coating of nanoparticles and composition of the media (Rahman *et al.*, 2013; Strojan *et al.*, 2017). The composition of the media used for the dilution of ENPs is very important in the protein corona formation and ultimately the uptake. This was demonstrated by Maiorano *et al.* (2010) using AuNPs in two commonly used cell culture media; Dulbecco Modified Eagle's medium (DMEM) and Roswell Park Memorial Institute medium (RPMI) both supplemented with 10% fetal bovine serum (FBS) and mixed with different sizes of spherical citrate-capped AuNPs in two cell lines HeLa and U937 (human lymphoblast cell line). They observed that protein-gold nanoparticles formed in RPMI were abundantly internalised in cells compared to DMEM evident from their absorption spectra of AuNPs in different media. However, DMEM formed large time-dependent protein corona compared to RPMI. They attributed the differences found in the cellular uptake of AuNPs to differences in protein corona formation to be a co-operative mechanism of different parameters such as protein-AuNP interaction, protein-protein interaction, protein-media components and AuNPs-media components (Maiorano *et al.*, 2010). There is a lot to understand about protein corona because its dynamic

and changes with time and environment (Hamad-Schifferli, 2015). It is worth noting that AuNP is plausible of getting a new biological identity when mixed with media, which the cells recognises during cellular uptake. In addition, there is a tendency of nanoparticles to aggregate in the media (Moore *et al.*, 2015) which in turn influences their cellular uptake and cellular fate.

The effect of AuNP aggregation on cellular uptake and toxicity was demonstrated by Albanese and Chan (2011) using transferrin-coated AuNP aggregates of different sizes in A549, HeLa and MDA-MB 435 cell line. Interestingly, their result showed no difference in toxicity response between aggregated and single particles but the uptake patterns between the aggregated and single particles were different. Aggregated particles showed an increased uptake in HeLa and A549 cells compared to single particle. This study shows the importance of considering aggregation when studying the uptake of particle because; uptake influences intracellular trafficking and understanding the cellular uptake mechanism helps determine subsequent molecular response of the cell.

1.2.2. Intracellular Localisation and Cellular Fate of Gold Nanoparticles.

The localisation of AuNP within the cell is important for understanding their mechanism of interaction with sub-cellular components and hence their potential toxicity. Most studies on localisation involve fluorescent-labelled nanoparticles and the use of confocal microscopy. The limited resolution of confocal microscopy makes it hard to determine the exact position/location of the particle in the cell (Iversen *et al.*, 2011; Stefancikova *et al.*, 2014). To resolve the issue, Transmission electron microscopy (TEM) technique is widely used as a supplement for the study of cellular fate of nanoparticles in addition to characterization of shape and size of nanoparticles (Weir *et al.*, 2008). TEM has a resolution of about 0.2 nm (Chapman *et al.*, 2012) and the electron density of gold atoms gives it a high contrast upon

biology matrix enabling a better study of sub cellular localisation of AuNPs (Chen *et al.*, 2013).

As mentioned earlier, the proposed mechanism of cellular uptake of AuNP is via endocytosis, which involves the formation of vesicles. These formed vesicles traffic their content to early endosomes first irrespective of the type of endocytosis (Kou *et al.*, 2013; Panariti *et al.*, 2012; Xu *et al.*, 2013). The early endosomes, considered to be the main sorting station can then transfer it content to the late endosomes and lysosomes via endocytic trafficking (Liu *et al.*, 2013). During endocytic trafficking, there is a decrease in pH in vesicles from the endosomes (6.5) to the lysosomes (4.5) that is the organelles become acidified as shown in Figure 8.

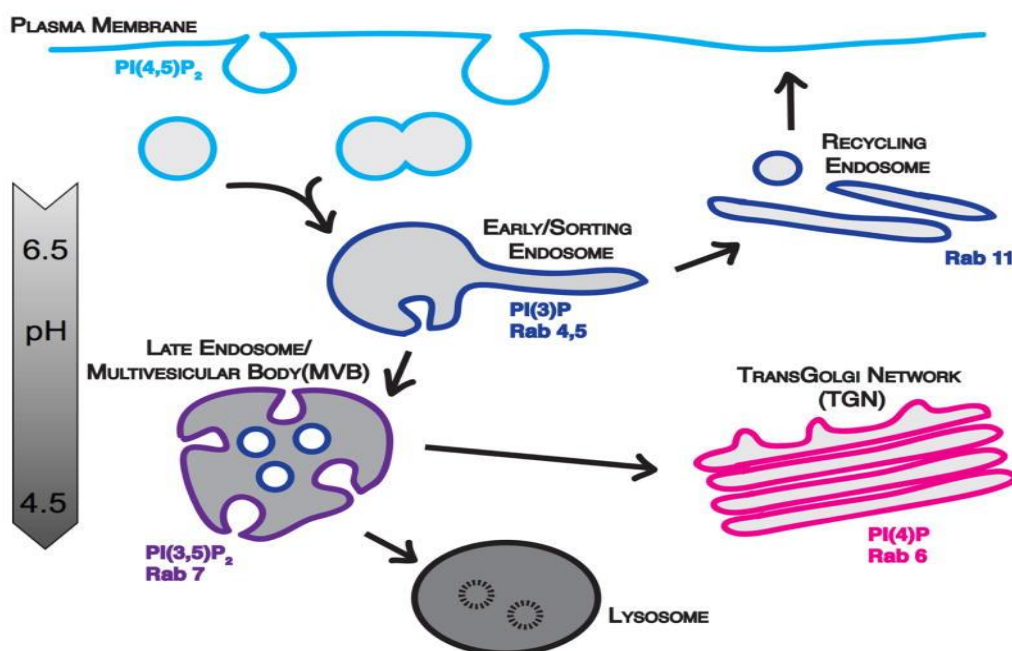


Figure 8: Endosomal trafficking.

Formed vesicles from the plasma membrane, transports it content to early/sorting endosomes, where sorting takes places. AUNPs are transported to either the recycling membrane, Golgi or late endosome/multivesicular bodies and finally to the lysosome for degradation. Image taken from (Elkin *et al.*, 2016).

Therefore, it is expected to observe particles in the early endosome, late endosome, multi-vesicular bodies (MVB), golgi network and lysosome and this was proven by several

studies, showing AuNP within these organelles (Kim *et al.*, 2015; Levy *et al.*, 2010; Ma *et al.*, 2011; Wang & Petersen, 2013).

However, AuNP have also being reported to be localised in other organelles not associated with endosomal trafficking, organelles such as mitochondria (Karatas *et al.*, 2009; Kodiha *et al.*, 2015) or even free in the cytosol (Verma *et al.*, 2008). Gu *et al.* (2009) showed AuNP modified with poly (ethylene glycol) (PEG) and 3-mercaptopropionic acid (MPA) studied in HeLa cells penetrated into the nucleus of mammalian cells after a 24-hour treatment. This is a good evidence of localisation in organelles not involved in endosomal trafficking, as well as a possibility of nuclear localisation, thereby, increasing the potential of AuNP for nuclear targeted drug delivery.

In endosomal trafficking, the lysosome is often viewed as the last target for internalised particles (Yameen *et al.*, 2014). This is because; the lysosome is the digesting or recycling components of the cell machinery (Shukla *et al.*, 2005; Yameen *et al.*, 2014). Trafficked AuNPs in the late endosomes vesicles fuses with the primary lysosomes of the cells (originates from the golgi) to form secondary lysosomes (Huotari & Helenius, 2011; Taylor *et al.*, 2016). However, the cellular fate of AuNPs in the lysosome is inconclusive. Most studies reports AuNPs remains in membrane bounded vesicles (Kim *et al.*, 2015) arranged in a perinuclear fashion (Shukla *et al.*, 2005) with a possibility of exocytosis of AuNPs from the cell (Chithrani *et al.*, 2006). A suggested rationale of AuNP persistence in the lysosome could be that, the digestive enzymes of the lysosomes is not designed to digest metals but are capable of forming complex with the metals (Pernodet *et al.*, 2006).

In summary, AuNP generally has a nonspecific subcellular localisation, as it moves between organelles but its most often concentrated in endosome/lysosomes (Dykman & Khlebtsov, 2012; Kodiha *et al.*, 2015; Levy *et al.*, 2010). However, with specific targeting

like attaching peptides or antibodies onto AuNP surface, this helps to achieve targeted subcellular organelle localisation.

One of such targeted subcellular organelles localisation *in vitro* was to the nucleus of HepG2 cells using peptide-modified AuNPs complex, the modification was with nuclear localisation signals and adenovirus receptor-mediated endocytosis peptide attached to the AuNPs as two separate pieces by Tkachenko *et al.* (2003). Their differential interference contrast (DIC) imaging result showed nuclear localisation and the ability of functionalizing AuNPs for targeted subcellular localisation. Worth noting from their experiment was the mix of two different peptide to achieve nuclear localisation, they reported NLS peptide modified AuNPs alone showed no internalisation and adenovirus receptor-mediated endocytosis peptide modified AuNPs does not achieve nuclear localisation. It is clear that physio-chemical properties of AuNP affect the uptake, which then affects its subcellular localisation. Therefore, uptake mechanisms evading endocytic trafficking would decrease its endosome/lysosome concentrations and increase its intracellular concentration in other organelles especially the nucleus. Hence, the emphasises on understanding the mechanism of uptake and trafficking of AuNPs to determine subcellular localisation and cellular fate would be beneficial for its biomedical applications.

Although the ultimate cellular fate of AuNPs is not clear, there are two likely possibilities: passing on AuNP to daughter cell during cell division (Mironava *et al.*, 2010) or exocytosis (Oh & Park, 2014), with more research focus on the later. Chithrani and Chan (2007) demonstrated the exocytosis of transferrin coated AuNPs (14 nm and 74 nm) following cellular internalization by clathrin-mediated endocytosis. Smaller AuNPs (14 nm) underwent exocytosis two times faster compared to larger AuNPs (74 nm) implying that exocytosis is size dependent. They concluded that although exocytosis was size dependent, size alone does not influence exocytosis other parameters should be considered as well.

Interestingly, they also observed exocytosis occurred when vesicles with entrapped AuNPs moves towards the cellular membrane, fuses with it and then releases its content (entrapped AuNPs) to the external cellular environment. Using the study above as a case study of cellular localisation with a bit of exocytosis occurring, it is assumed that most of the particle are still internalised, with only a few undergoing exocytosis. Therefore, it is necessary to study the toxic effects of the internalised AuNPs to the cells.

1.2.3. Cytotoxicity of Gold Nanoparticles.

The cellular internalization of AuNPs leads to potential interactions with cellular organelles such as mitochondria, golgi, nucleus or lysosomes. These interactions can produce toxic effects such as organelle or DNA damage, oxidative stress, apoptosis, mutagenesis and dysregulation of protein (Aillon *et al.*, 2009; Manke *et al.*, 2013; Nel *et al.*, 2006; Pan *et al.*, 2009; Rim *et al.*, 2013; Unfried *et al.*, 2007). Although bulk gold has been found to be generally safe and inert, AuNPs are regarded to have some toxic potential (Arvizo *et al.*, 2010). The toxicity of AuNPs has been investigated at cellular levels focusing on the various properties such as surface characteristic, concentrations, size, shape, and as well as composition of exposure medium (Boisselier & Astruc, 2009; Murphy *et al.*, 2008; Wang *et al.*, 2015). Contradictory results about the cytotoxicity have been reported and further research is therefore required.

Using 14 nm citrate-capped AuNP at various concentrations (0.2, 0.4, 0.6, 0.8 mg/mL), Pernodet *et al.* (2006) investigated the effect of concentration and exposure time (2, 4 and 6 days) on human dermal fibroblast. Their results showed that greatest accumulation of AuNPs in the cell occurred at the highest concentration and that cellular uptake was concentration and time dependent. AuNPs were observed to accumulate in vacuoles in cells; surprisingly

they did not identify the vacuoles. Also, observed was damage to actin filaments compared to their control evident from their fluorescence imaging.

This damage affected the motility, proliferative and adhesive abilities of cells. After 6 days, they observed the largest inhibition on the proliferation of cells suggesting that 14 nm citrate capped AuNPs entry to cell is not immediately detrimental to cell function but rather the formation of an unusual large number of vacuoles that triggers a series of secondary events such as cell growth and protein synthesis. This study showed the long-term effect of AuNPs exposure to cells, which most studies have not shown because of their short exposure time of 24 hours or less. A similar study by Mironava *et al.* (2010) using 13 nm and 45 nm AuNPs on human dermal fibroblast also showed similar result of decreased proliferation, cytoskeleton disruption and induction of apoptosis. They attributed their result to the number of vacuoles rather than the concentration of the particle within the cells. Wei *et al.* (2007) study the effect of 25 ± 3.5 nm spherical AuNPs on human hepatoma HepG2 cells a cancer cell line and their result showed AuNP had a low effect on proliferation but disrupted cell adhesion. It should be noted that although these experiment used similar AuNPs, which were spherical citrate AuNPs on different cell lines, the outcomes were different. Therefore, the toxicity observed on AuNPs exposure cannot be generalised without considering other parameters discussed below as well as examining toxicity of AuNPs on a case-case basis.

The charge and surface coating of AuNPs can influence its cytotoxicity potential (Zhang *et al.*, 2012). Interaction of ENPs generally with the plasma membrane also influences its toxicity (Wang *et al.*, 2015). The plasma membrane carries a negative charge, therefore AuNP coated with cationic ligand such as cetytrimethyammonium bromide (CTAB) disrupts the plasma membrane which increases cytotoxicity compared to AuNP conjugated with biotin, cysteine, citrate, glucose and polyethylene glycol (PEG) (Alkilany & Murphy, 2010; Boisselier & Astruc, 2009; Murphy *et al.*, 2008; Verma & Stellacci, 2010). Goodman *et al.*

(2004) designed spherical AuNPs, which were either cationic or anionic and studied their toxicity *in vitro*. They observed that although both particles interacted with cells in a passive process, cationic AuNPs interacted strongly with the negatively charged plasma membrane compared to the anionic AuNPs. This strong electrostatic attraction of cationic AuNP with the plasma membrane caused a membrane disruption capable of inducing a variety of further interactions, which could be linked to observed toxicity of cationic AuNPs. In addition, the observed toxicity was found to be concentration dependent. An identical research by Connor *et al.* (2005) demonstrated the effect of surface modification with several ligands; citrate, biotin and CTAB. Citrate and biotin modified AuNP were non-toxic up to concentration of 250 μM whereas CTAB coated AuNP were already toxic at 0.05 μM , interestingly when CTAB coated AuNP were centrifuged and washed to remove unbound CTAB, the particles lost their toxic properties. CTAB is a commonly used cationic surfactant to stabilise AuNP and CTAB alone has been found to be quite toxic to the cells at sub-micromolar dose (Alkilany *et al.*, 2009). Clearly surface modification impacts on cytotoxicity of AuNP and the toxicity observed could originate from either the AuNP, its surface coating or functionalised AuNP (Connor *et al.*, 2005). Table 1 shows a summary of *in vitro* AuNPs toxicity results based on surface coating.

Cell Line	AuNP characteristics (size, shape and surface coating)	Toxicity Conclusion	Ref
COS-1, Red blood cells and <i>E. coli</i>	2 nm Sphere. Coating: Quaternary ammonium, carboxylic acid	Cationic nanoparticles found to be toxic and anionic not toxic.	(Goodman <i>et al.</i> , 2004)
K562	4, 12 and 18 nm Sphere. Coating: CTAB, citrate, cysteine, glucose, biotin	All nanoparticles were not toxic, although the surface coating may be toxic	(Connor <i>et al.</i> , 2005)
HeLa	65 × 11 nm Rods. Coating: CTAB, PEG	Replacing CTAB with PEG on the surface of nanorods reduced the toxicity	(Takahashi <i>et al.</i> , 2006)
Human dermal fibroblast	13.1 nm Sphere. Coating: Citrate	Nanoparticles decreased cell proliferation rate, adhesion, and motility	(Pernodet <i>et al.</i> , 2006)
Hep2G, BHK21 and A549	33 nm Spheres. Coating: CTAB and citrate	Non-toxic to Hep2G and BHK21 but to A549 cell line	(Patra <i>et al.</i> , 2007)
HeLa	18 nm Sphere. Coating: Citrate	Non-toxic and no change in gene-expression patterns	(Khan <i>et al.</i> , 2007)
HeLa	3.7 nm Sphere. Coating: PEG	Nanoparticles entered nucleus and did not induce toxicity	(Gu <i>et al.</i> , 2009)
Microglia neural cells, transgenic mouse	10–80 nm sphere, rod and urchin. Coating: PEG and CTAB	Autophagy and phagocytosis	(Hutter <i>et al.</i> , 2010)
HaCaT	1.5 nm Sphere. Coating: Positively charged (trimethylammoniummethanethiol), negatively charged (mercaptoethanesulfonate) and neutral (mercaptoethoxyethoxyethanol)	Cell morphology was disrupted by all three NPs in a dose-dependent manner; charged NPs induced cell death through apoptosis while neutral NPs via necrosis	(Schaeublin <i>et al.</i> , 2011)
A549, 16HBE MSC cells	55.6 × 13.3 nm Rod. Coating: serum protein-coated	Selective lysosomal membranes and actin damage	(Wang <i>et al.</i> , 2011)
A549, 16HBE	55 rod Coating: CTAB	Oxidative stress, mitochondria damage	(Zhang <i>et al.</i> , 2013)
Vero, NIH3T3 and MRC-5 cells.	nano-rod structure with an average length of 10–40 nm	Decreased cell growth associated with apoptosis induction in Vero cells and autophagy in NIH3T3 cells. cDNA microarray analyses of MRC-5 cells showed involvement of DNA damage and repair responses, cell-cycle regulation, and oxidative stress.	(Chueh <i>et al.</i> , 2014)
A549 cells	25 × 52 nm rod, Coating Citrate.	Decreased cell viability and increases ROS production	(Tang <i>et al.</i> , 2015)

Table 1: Summary of in vitro gold nanoparticle toxicity results based on surface coating
Selected references were chosen based on experiment that focused on cytotoxicity of surface modified AuNPs in mammalian cell lines, which are relevant to this research.

From Table 1, AuNP mediated toxicity are often associated with oxidative stress, mitochondria damage, apoptosis, necrosis, autophagy, genotoxicity and inhibition of cell division and proliferation. The most common and studied mechanism involved in AuNP toxicity is the production of reactive oxygen species (ROS) (Fard *et al.*, 2015; Oo *et al.*, 2012; Schaeublin *et al.*, 2011). ROS are highly reactive oxygen radical formed upon the incomplete reduction of molecular oxygen (Nordberg & Arner, 2001).

ROS are generated within the cells by normal cellular activities such as mitochondria respiration and are involved in cell signalling and homeostasis (Bolisetty & Jaimes, 2013). In addition, exogenous generation of ROS could be by pollutant, ENPs, chemicals and ionizing radiation (Minai *et al.*, 2013; Valko *et al.*, 2006). When the production of ROS is not counterbalanced by antioxidant production, this leads to oxidative stress (Manke *et al.*, 2013). Oxidative stress results in mitochondria membrane damage thereby disrupting electron transport chain and other downstream effects such as DNA damage, apoptosis, lipid peroxidation and activation of signalling networks linked with cell cycle (Ott *et al.*, 2007). These changes have been observed in cells exposed to AuNPs (Alkilany & Murphy, 2010; Kovacic & Somanathan, 2013; Madl *et al.*, 2014; Pan *et al.*, 2009), therefore the emphasises on AuNP-mediated ROS generation. As mentioned above, ROS generation and its effects have been reported on cell lines exposed to AuNPs the exact underlying cellular mechanism is still elusive. A proposed mechanism of intracellular ROS generation is the direct or indirect interaction of AuNPs with the mitochondria because mitochondria is the main source of ROS (Dayem *et al.*, 2017). Interaction with the mitochondria leads to a cascade of events plausible of inducing oxidative stress and cytotoxicity as shown in Figure 9.

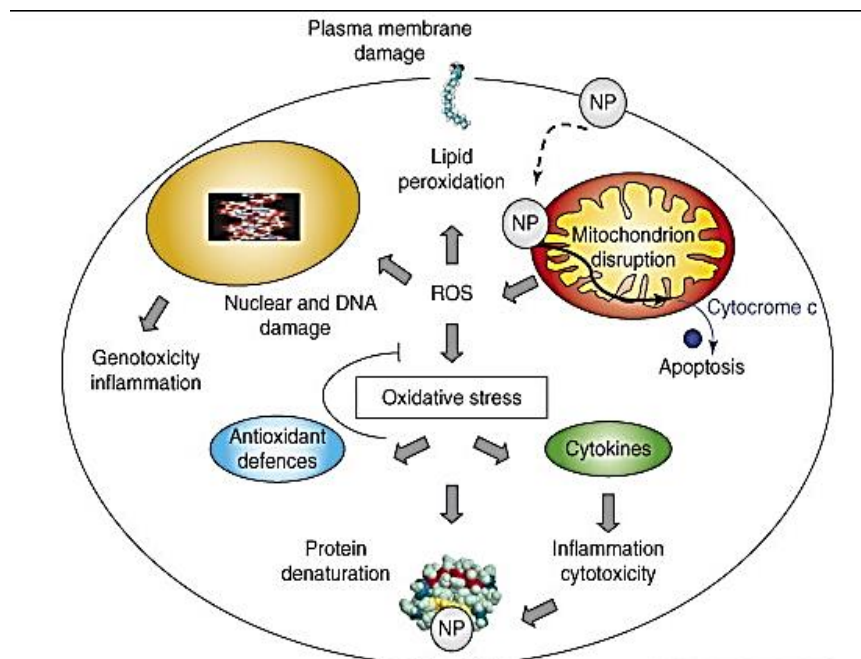


Figure 9: Possible ROS mediated mechanism of toxicity.

Nanoparticles are capable of interacting with mitochondria, disrupting its function and leading to production of ROS. ROS production can cause a cascade of events such as nuclear damage, lipid peroxidation and oxidative stress. Oxidative stress causes a reduction in antioxidant, release of cytokines, protein denaturation. All this results in cytotoxicity. Images adapted from (Sanvicens & Marco, 2008)

Nanoparticles have also been proposed to interact with enzymes involved in maintaining cellular redox potential and activation of intracellular signalling pathways that induces ROS generation (Auffan *et al.*, 2009). The activated pathway is the stress-dependent signalling pathway such as mitogen-activated protein kinase (MAPK) or I κ B kinase, which ultimately alters the gene expression of the antioxidant response element by activating transcription factors, such as AP-1, NF- κ B, or Nrf2, and finally leading to ROS generation. (Feng *et al.*, 2015; Soenen *et al.*, 2011). *In vitro* studies have demonstrated an increase in oxidative stress and lipid peroxidation by western blotting of autophagic protein (LC3) and malondialdehyde (a by-product of lipid peroxidation) (Li *et al.*, 2010). In addition, the measurement of glutathione (GSH) an antioxidant that deactivates intracellular ROS has been demonstrated to diminish on exposure of AuNPs (Zhang *et al.*, 2013). All these evidences links the observed cytotoxicity on exposure to AuNPs to the generation of ROS which can arise from either the gold core, its surface coating or the functionalised AuNP itself.

1.3. Functionalization of Gold Nanoparticles with Metal Complex.

Functionalization is the process of adding new functions or modifying the characteristics of a material by changing its surface chemistry. Functionalization of ENPs aims to give it a tailored property or function. Functionalization of ENPs surface can be after the synthesis of the particle by the addition of thiols, disulphides, amines, nitriles and biomolecule group which bind to the surface of the particle or enable secondary binding of other functional groups/probe (Roux *et al.*, 2005; Woehrle & Hutchison, 2005; Zhou *et al.*, 2009). Functionalization of ENPs can be direct or post-functionalization. In direct approach, the functional ligand is a bi-functional compound, with one of the functional group attaching to ENP surface while the other functional group contains the required active functionality i.e. the desired properties to be added to the ENP (Subbiah *et al.*, 2010). In post-functionalization approach, a binding chelating group is used to produce a coupling site, where the final functional group is attached (Subbiah *et al.*, 2010).

AuNP can be easily functionalised because of its large surface to mass ratio that acts as a scaffold to enable attachment of multiple probes onto its surface (Rogers *et al.*, 2014). The attachment of probes onto AuNP surface modifies the fluorescence signal usually generated from AuNP alone, therefore functionalised AuNP acts as a nanoprobe with unique optical properties, large Stokes shift and high photo stability (Osborne & Pikramenou, 2015). The type of probes usually attached to AuNP includes; metal complex, ions or bio-molecules (Lewis & Pikramenou, 2014; Lo *et al.*, 2012). For the purpose of this thesis, only metal complex coating would be discussed.

Metal complex consist of a central metal surrounded by molecules or ions known as ligands and the metal complex acts as a Lewis base (electron donor). The biomedical application of metal complex is usually as a chemotherapeutic agent such as cisplatin or as a diagnostic

tool for medical imaging such as Magnetic resonance imaging (MRI), Positron emission tomography (PET), Single-photon emission computed tomography (SPECT) and fluorescence cell imaging (Arrowsmith *et al.*, 2012; Fernandez-Moreira *et al.*, 2010; Tanaka & Fukase, 2008).

The most biologically used metal complexes for imaging are transition metals and lanthanides because of their high photo-stability compared to organic dyes (Lewis & Pikramenou, 2014). Transition metals are elements with partially filled d orbital while lanthanides are f block elements of the periodic table. Both transition metals and lanthanides have been reported to be functionalised onto AuNPs surface for imaging purposes (Comby *et al.*, 2014; Zhang *et al.*, 2016). Transition-metal complex is prepared in fewer steps, which are easily modifiable and also their variable oxidation state can coordinate ligands to form different geometries as well as participate in various biological redox reactions (Ma *et al.*, 2013a). Transition-metal complex produces strong and sufficiently long-lived phosphorescence emission that allows the imaging of biological events (Demas & DeGraff, 2001; Ma *et al.*, 2013b). Hence, their ability to modify the fluorescence nature of AuNPs and making functionalised AuNPs attractive as a nanoprobe for bio-imaging. Labelling of AuNPs with transition metal complexes assigns it, unique optical properties of luminescence (Lewis & Pikramenou, 2014). These properties includes long emission half-life, photo-stability, and emission spectra within the visible region (Rogers *et al.*, 2014). These properties confer them with the ability for application in time-resolved emission imaging microscopy (TREM), fluorescence lifetime imaging microscopy (FLIM) and continuous monitoring of biological events (Botchway *et al.*, 2008; Svensson *et al.*, 2011).

Transition metal complexes of ruthenium (II), iridium (III) have been reported to coat the surface of AuNPs (Adams *et al.*, 2014; Elmes *et al.*, 2011; Glomm *et al.*, 2005; Huang & Murray, 2002; Jebb *et al.*, 2007; Rogers *et al.*, 2014) and has been used for cellular studies

(Elmes *et al.*, 2011; Rogers *et al.*, 2014). Only a few studies have functionalised AuNP with ruthenium metal complex for cellular studies, however the most used ruthenium complex ruthenium trisbipyridine $[\text{Ru}(\text{bpy})_3]^{2+}$ photophysical properties is well documented (Juris *et al.*, 1988; McCusker, 2003). Our lab has successfully coated ruthenium complex onto AuNP surface and used it for cellular studies (Rogers *et al.*, 2014). Luminescence imaging of this ruthenium functionalised AuNP by confocal microscopy was possible and also observed was the stability of the ruthenium complex on AuNP even after 24 hours incubation (Rogers *et al.*, 2014). The preliminary result gotten in our lab that showed the potential of these particles to be used as nanoprobe without been toxic, led to the recent synthesis of a more luminescent ruthenium functionalised AuNP published in Osborne and Pikramenou (2015). Although previous ruthenium functionalised AuNPs showed cellular internalization and no cytotoxicity in A549 cells, the mechanism of cellular uptake, and fate was not studied. Upon synthesizing a more luminescent ruthenium functionalised AuNP (Osborne & Pikramenou, 2015) which has a potential as a nanoprobe, this current research was carried out to fill the knowledge gaps about the mechanism of uptake, cellular fate and plausible toxicity of this functionalised AuNP in A549 cells. A549 cells was chosen based on preliminary data on cellular uptake of nanoparticle obtained in our lab. A549 cells are human cell line gotten from lung tissue, epithelial in nature and grow as a monolayer adherent cell line (Foster *et al.*, 1998) They are mostly used for enzymatic studies because it is a very transfection host, cell proliferation studies and the mechanism involved and recently in the study of nanoparticle toxicity (De Marzi *et al.*, 2014).

1.4. Hypothesis and Objectives.

The therapeutic and diagnostic potential of AuNPs generally has been established from the review above, however various challenges limits the clinical translation of AuNP. The lack of understanding of the mechanism of cellular uptake, localisation and possible toxicity that needs further careful evaluation both *in vitro* and *in vivo*. Various AuNPs can be synthesised with different characteristic for different purposes, therefore the study of AuNP should be treated on a unique case-by-case basis.

This research is aimed at critically understanding the mechanism of uptake of functionalised AuNP coated with ruthenium bipyridine SS, (a luminescent transition metal complex), as toxic effects, sub-cellular localisation and cellular fate are dependent on uptake mechanism. The functionalized AuNP would be referred to as RuS12·AuNP20 throughout this thesis. *Human lung adenocarcinoma* epithelial cell line (A549 cells) were used for this study because of preliminary data on the uptake of ruthenium coated gold nanoparticle in our lab.

We hypothesized based on preliminary data and literature review that internalised RuS12·AuNP20 in A549 do not cause toxicity up to 72 hours but induces cellular stress due to accumulation in vesicles upon cellular uptake by endocytosis.

Specific objectives:

1. Investigate the mechanism of cellular uptake of RuS12·AuNP20 in A549 cells and quantify internalised RuS12·AuNP20.
2. Investigate the sub-cellular localisation and cellular fate of internalised RuS12·AuNP20 by different imaging modalities. Molecular probes as well as transiently transfected cells expressing GFP-tagged organelle marker would be used as model for investigating sub-cellular localisation.
3. Investigate the ultimate cellular fate of RuS12·AuNP20 in A549 cells by trafficking particles over a 72 hours period.
4. Investigate the toxic potential of RuS12·AuNP20 in A549 cells by cytotoxicity testing and change in gene expression associated with stress response.

Chapter 2

Materials and Methods

Chemicals and Consumables.

Unless otherwise stated, all chemicals and consumables were purchased from Sigma-Aldrich-UK and were of the highest quality available.

2.1. Nanoparticle Synthesis.

2.1.1 RuS12·AuNP20 Synthesis.

The colloids (AuNP) were prepared first and coated with Zonyl[®] FSA fluorosurfactant followed by final coating with transition metal complex; ruthenium-bipyridine-SS (RuS12), which was prepared, characterised as described previously and published by Osborne and Pikramenou (2015). Details of ruthenium complex synthesizes is provided in appendix 2A. I acknowledge Shani Osbourne for providing all the ruthenium complexes used for this research. Coating with the fluorosurfactant was to enable high loading of ruthenium-bipyridine-SS onto AuNP surface as well as stabilizing the nanoparticle. Schematic of the synthesis is shown in **Error! Reference source not found.**

2.1.1.1. AuNP Colloid Preparation.

Synthesis of Au colloid was performed according to procedure described by Schulz *et al.* (2014). All glassware used in this preparation were initially washed with freshly prepared aqua regia (3:1 HCl/HNO₃), then distilled water and followed by drying in an oven. The preparation was as followed: In a 250 ml round bottom flask attached to a condenser on a heater plate, the following compounds (60.0 mg, 0.2 mmol of trisodium citrate; 13.3 mg, 0.7 mmol citric acid and 1.0 mg, 0.004 mmol ethylenediaminetetraacetic acid (EDTA)) were dissolved in 100 ml of deionised water, heated to 150⁰C and refluxed for 15 minutes. 8.0 mg, 0.022 mmol of H₂AuCl₄·3H₂O (Alfa Aesar) was dissolved in 25 ml deionised water and gently heated in a 120⁰C oven for about 10 minutes, and then rapidly added to the content of round bottom flask and refluxed for 10 minutes with vigorous stirring. A change in colour

from pale yellow to wine red was observed indicating the reduction of gold salts and formation of nanoparticles. Heating was removed but stirring was continued for an additional 30 minutes to enable slow cooling to room temperature.

The resulting solution of colloids (1.6 nM) was characterised by determining the surface plasmon resonance (SPR) by collecting UV-VIS spectra using a 1 cm path length quartz cuvettes on Varian Cary 50 spectrophotometer. λ_{\max} (H₂O) = 516 nm (SPR), Diameter = 12 ± 3 nm (DLS number distribution), PDI = 0.1, ζ -potential = -46 ± 16 mV.

2.1.1.2. Coating of AuNP Colloid with RuS12 and Characterisation.

The concentration of the AuNP colloid was changed from 1.6 nM to 9 nM by centrifugation at 13,000 g for 30 minutes and re-dispersing pellet in 350 μ l of deionised water. 10 μ l of 10% Zonyl FSO fluorosurfactant (v/v) was used to coat 1 ml of 9 nM AuNP colloid and coating was monitored by measuring the SPR. Once fully coated the solution was centrifuged at 13,000 g for 30 minutes and the pellet re-suspended in 1 ml of water to give Zonyl coated AuNP (AuNP.Z). λ_{\max} (H₂O) = 518 nm (SPR), Diameter = 16 ± 5 nm (DLS number distribution), PDI = 0.3, ζ -potential = -50 ± 8 mV. 1 ml of AuNP.Z was coated with 20 μ l of 0.87 mM RuS12 using 2 μ l aliquots and sonicating solution frequently, full coating was again monitored by a shift in SPR to ensure a full coating of metal complex onto AuNPs to give RuS12·AuNP20. The final step was purification of RuS12·AuNP20 by size-exclusion chromatography on Sephadex G25 and RuS12·AuNP20 was eluted with distilled water. A full characterization of RuS12·AuNP20 was performed. TEM and Dynamic Light scattering (DLS) was used for characterization by size. λ_{\max} (H₂O) = 520 nm (SPR), Diameter: 22 ± 9 nm (DLS number distribution), PDI = 0.3, ζ -potential = -42 ± 15 mV. Stability of RuS12·AuNP20 was carried out by measuring the luminescence lifetime decay

as described previously and published by Osborne and Pikramenou, 2015 (I acknowledge Shani Osborne for carrying out the experiment on the luminescence lifetime decay, data shown in appendix 2B). An emission scan of RuS12·AuNP20 at excitation wavelength of 488 nm was done to prove its luminescence property. Fully characterised RuS12·AuNP20 were then used for cell work.

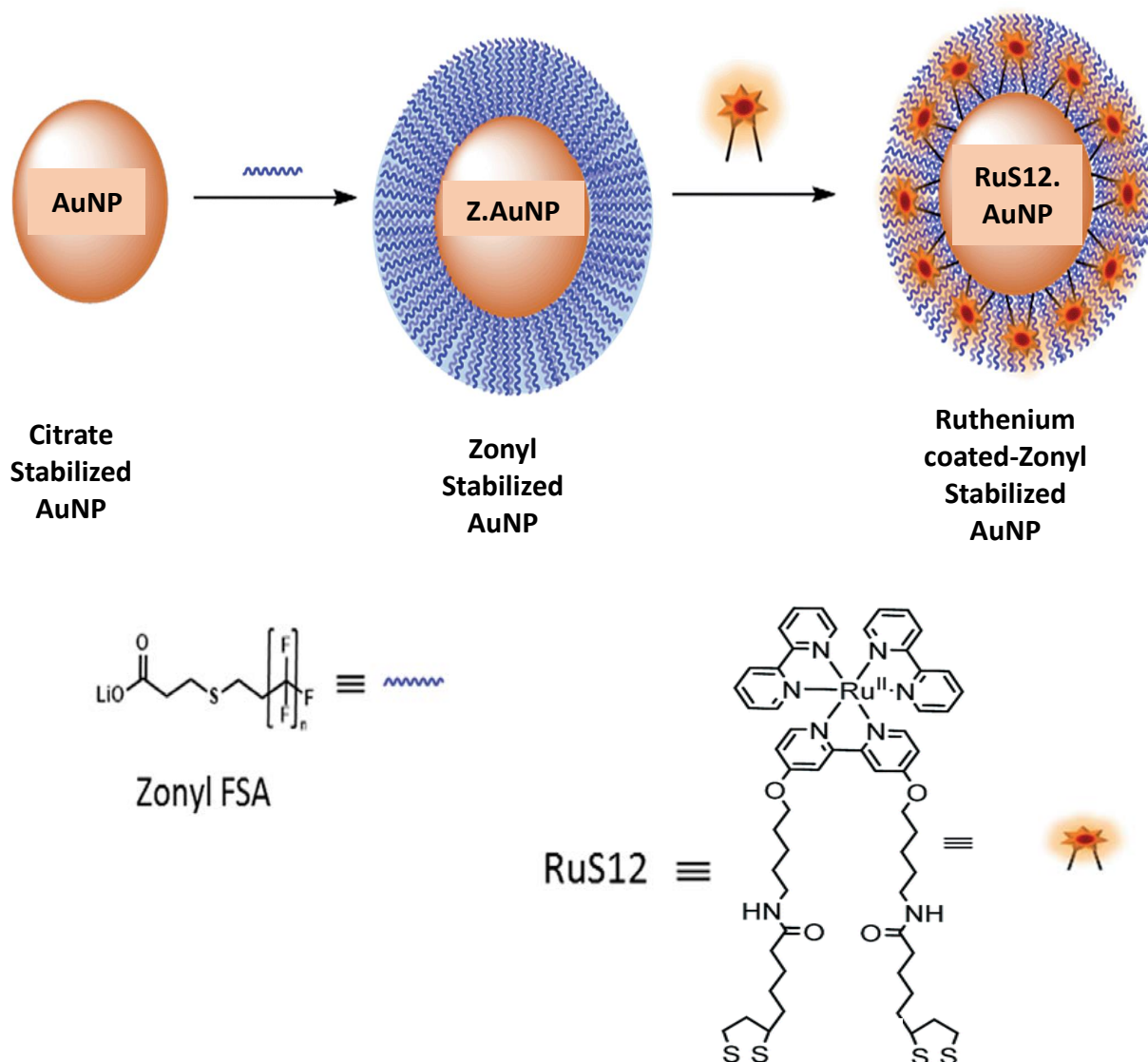


Figure 10 : A schematic representation of coating of AuNP colloid with zonyl and Ruthenium complex (RuS12) to give RuS12·AuNP20.

AuNP colloid was synthesized from the reduction of gold salt in the presence of citrate. The citrate stabilized AuNP was firstly coated with 10% Zonyl FSA (a fluorosurfactant) and finally RuS12 (I acknowledge Shani Osborne for synthesizing ruthenium complex). Image adapted from (Osborne & Pikramenou, 2015)

2.2 Cell Culture.

2.2.1. Cell Type.

The A549 cells are *Human lung adenocarcinoma* epithelial cell line initiated by Giard *et al.* (1973) through explant culture of lung carcinomatous tissue from a 58-year-old Caucasian male. A549 cell line is grown in the lab as a monolayer adherent cell attached to culture flask and its acts very well as a transfection host (Marzbali *et al.*, 2016; Mu *et al.*, 2016) and also it is a well suited model for study of AuNP cellular uptake mechanism and trafficking (Capel *et al.*, 2016). The A549 cell line is a widely used cell line for the study of nanoparticles uptake, localisation and toxicity (Chang *et al.*, 2011; De Marzi *et al.*, 2014; Kim *et al.*, 2012) therefore making it a good model cell line for this current study.

2.2.2. Cell Culture Technique.

A549 cells which were cryopreserved at a very low passage of 3 in our laboratory were thawed and used throughout this project. Thawed cells were cultured in aseptic environment using a lamina flow hood and grown in a humidified atmosphere (5% CO₂ incubator; 95% air) at 37°C.

2.2.2.1. Sub-culturing.

Cells were maintained by growing in a vented cap T₇₅ flask at 37°C in Dulbecco's modified Eagle medium (DMEM) supplemented with 10% fetal bovine serum (FBS), 2 mM L-glutamine, 100 U/ml penicillin and 100 µg/ml streptomycin, hereafter called complete media. Media was replaced every 3-4 days and cells sub-cultured once they had reached approximately 70% confluence using a standardised trypsin-ethylenediaminetetraacetic acid (EDTA) protocol. Briefly, cells are washed twice with 10 ml of phosphate buffer saline Solution (PBS), detached with 3 ml of trypsin-EDTA and harvested with 9 ml of complete

media. Cells were then centrifuged at 1500 g for 5 minutes, the supernatant discarded and the pellet re-suspended in 1 ml of complete media. The cell suspension was then sub-cultured at a ratio of 1:4 into a 15 ml complete media in new T₇₅ culture flask.

2.2.2.2. Cell Counting by Haemocytometer.

Cells used in all experiments were counted using a haemocytometer. After centrifugation and re-suspension of the cell pellet in 1 ml of complete media, a 15 μ l aliquot is diluted 1:1 with 0.4 % trypan blue and cells counted using a 10X magnification of light microscope. Only cells in the middle grid are counted and they are counted in duplicate. The average count was then used to calculate the number of cell in the 1ml suspension and cells are seeded at the appropriate density for the experiments as described in subsequent sections.

2.3. Uptake of RuS12·AuNP20 in A549 cells.

Uptake of RuS12·AuNP20 into A549 cells was studied over a period of 2-72 hours using multiple techniques (confocal imaging, transmission electron microscopy and inductively coupled plasma-mass spectrometry). The concentration used (0.9 nM of RuS12·AuNP20, which is equivalent to 10% dilution of 9 nM RuS12·AuNP20 with complete media) was based on previously published result (Rogers *et al.*, 2014) in our lab that gave best ratio of nanoparticles to media dilution without being toxic to the cells.

2.3.1 Confocal Microscopy.

Uptake of RuS12·AuNP20 into A549 cells by confocal microscopy was investigated using a Leica SP2 confocal system with 63X and 100X oil immersion objective lens. Images were acquired in fluorescence, reflectance and transmission mode. Fluorescence channels were acquired with the following excitation and emission:

- Hoechst (Thermofisher) (blue channel): $\lambda_{exc} = 405 \text{ nm}$ (75%), $\lambda_{em} = 410\text{-}455 \text{ nm}$.

- Nanoparticle luminescence (red channel): $\lambda_{exc} = 458 \text{ nm}$ (100 %), 476 nm (100%), 488 nm (100%) 496 nm (100%) and 514 nm (57%), $\lambda_{em} = 620 - 800 \text{ nm}$
- GFP (green channel) 488 nm , $em = 502 \text{ nm}$.

Reflection images were acquired at $\lambda_{exc} = 488 \text{ nm}$ (67%), $\lambda_{em} = 478 - 498 \text{ nm}$ and transmission images were acquired using the default transmission setup of the microscope with beam intensity 1-3 %. Images were acquired on both live cell and fixed cell. All images acquired were processed by imaging software (ImageJ Version 1.43M) details in Appendix 2C. Confocal imaging were carried out in biological triplicate and controls were cells not treated with nanoparticles. The first and second duplicate for confocal imaging were used to optimize the conditions for the experiments and imaging, only the result of the third triplicate were reported.

2.3.1.1 Live Cell Imaging.

Cells were seeded at a density of 100,000 into a 35 mm dish with a 10 mm glass diameter insert and allowed to attach overnight. The next day, cells were rinsed with PBS and then treated with 3 ml of media containing 0.9 nM RuS12·AuNP20 for 2, 4, 8, 12, 24, 48 and 72 hours. At the end of each time point, spent media was aspirated and cells rinsed three times with PBS followed by 30 minutes treatment with 2.5 $\mu\text{g/ml}$ Hoechst 33258. Cells were finally rinsed three times with PBS and imaged in live cell imaging solution (Thermofisher).

2.3.1.2. Fixed Cell Imaging.

Cells were seeded at a density of 100,000 onto a sterilised 22 mm diameter cover-glass in a 6-well plate and allowed to attach overnight. The next day cells were rinsed with PBS and then treated with 3 ml of media containing 0.9 nM RuS12·AuNP20 for 2, 4, 8, 12, 16, 24, 32, 40, 48, 56, 64 and 72 hours. At the end of each time point, spent media was aspirated and cells rinsed three times with PBS followed by fixation with 4% paraformaldehyde (4% PFA) for 15 minutes at room temperature. After fixing, cells were further rinsed two times

with PBS and stained with 1 $\mu\text{g/ml}$ Hoechst 33258 for 10 minutes. Cells were then rinsed twice with PBS followed by mounting to glass slide with a drop of Hydromount media (National diagnostics). Slides were stored for 24 hours at 4°C before imaging. For each time points, 10 random different images were acquired per slides and used for image processing.

2.3.2. Transmission Electron Microscopy.

Cells were seeded at a density of 100,000 on to a sterilised 13 mm diameter coverglass in a 6-well plate and allowed to attach overnight. The next day cells were rinsed with PBS and then treated with 0.9 nM RuS12·AuNP20 for 2, 4, 8, 24, 48 and 72 hours. At the end of each time point, spent media was aspirated and cells rinsed three times with PBS followed by fixation with 2.5% glutaraldehyde for 24 hours at 4°C. Samples were taken for processing at Centre for Electron Microscopy (University of Birmingham). Ultrathin sections of between 70-90 nm were cut parallel to cover-glass and mounted onto formvar-coated 200 mesh copper grids. Images were acquired with Jeol 1200 EX transition electron micrograph operated at 80kV in imaging mode. Images were acquired using Digital Micrograph Version 1.83.842. TEM imaging was carried out as a biological duplicate, the first duplicate was used to optimize the settings of the microscope, while the second duplicate were prepared as technical duplicate and the result were reported.

2.3.3. Inductively Coupled Plasma Mass Spectrometry (ICP-MS).

Cells were seeded at a density of 100,000 cells per well in a 6-well plate and left overnight for attachment to occur. Spent media was aspirated and replaced with 3 ml of complete media containing 0.9 nM, RuS12·AuNP20 and treated for 2, 4, 8, 12, 16, 24, 32, 40,48, 56, 64 and 72 hours. At the end of each time point, spent media was removed and cells washed three times with 1 ml of PBS. Cells were detached by treating with 1 ml of trypsin for 10 minutes and pelleted by centrifuging for 10 minutes at 1500 g. The cell pellets were dissolved in 300

μl of ultra-pure aqua regia (3 HCl: 1 HNO₃) and left to digest overnight at room temperature. The next day, digested samples were diluted with 4% HNO₃ to reduce the aqua regia content to less than 4% and samples were analysed at analytical chemistry lab at the University of Warwick. ICP-MS experiment was done as a biological triplicate with three technical triplicate. A series of standard solutions (0, 0.2, 0.5, 1, 2, 5, 10, 20 ppb) containing metals to be detected (gold and ruthenium) was used for calibration and determining metal content taken up by cells in each sample.

2.4. Organelle Localisation Studies Using Fluorescent Probes

2.4.1. Golgi: GOLGI ID® Green assay:

Co-localisation of RuS12·AuNP20 with golgi was studied with A549 cells grown on cover slips in a 6-well plate and treated for 4, 8, 12, 16 and 24 hours with 0.9 nM RuS12·AuNP20. The preparation and staining method followed, was according to manufacturer protocol with slight modification. Briefly, 1 X assay solution was prepared by the addition of 1 ml of 10 X assay buffer 1 to 0.2 ml 50 X assay buffer 2 into 8.8 ml of distilled water. 100 μl of 1X assay solution was added to a vial containing lyophilised GOLGI-ID® green detection reagent (50 nM) to give 100 X GOLGI-ID® green dye solution. Dual detection reagent was prepared using Hoechst 33342 nuclear stain included in the kit by 1:100 dilution with 100X GOLGI-ID® green dye solution. At the end of each time point, cells were rinsed three times with 1 X assay solution and treated with dual detection reagent for 30 minutes at 4°C. Stained cells were washed with ice-cold media, treated in complete media for a further 30 minutes and followed by final rinsing, fixing and mounting of cover slip to slide for imaging. The experiment was done as a biological duplicate. The first duplicate was used to optimize the conditions for the experiments and imaging, only the result of the second duplicate was reported.

2.4.2. Mitochondria: MitoGreen.

Co-localisation of RuS12·AuNP20 with mitochondria was studied with A549 cells grown on cover slips in a 6–well plate and treated for 4, 8, 12, 16 and 24 hours with 0.9 nM RuS12·AuNP20. 200 µM stock solution of dye was prepared from lyophilised product using DMSO according to manufacturer instructions. To optimise the concentration and duration of staining various concentrations between 20–200 nM and 5–30 minutes respectively was tested. At the end of each time point, cells were rinsed, fixed with 4% PFA for 10 minutes and stained with 200 µM MitoGreen for 10 minutes (optimised conditions), followed by additional staining with 1 µg/ml Hoechst 33258 for 10 minutes before mounting and imaging. The experiment was done as a biological duplicate. The first duplicate was used to optimize the conditions for imaging, only the result of the second duplicate was reported.

2.4.3. Endoplasmic reticulum: ER-Tracker™ Green.

Co-localisation of RuS12·AuNP20 with endoplasmic reticulum was studied with A549 cells grown on cover slips in a 6–well plate and treated for 4, 8, 12, 16 and 24 hours with 0.9 nM RuS12·AuNP20. 1mM stock solution of dye was prepared from lyophilised product using DMSO according to manufacturer instructions. At the end of each time point, cells were rinsed three times, and stained with 1 µM of ER-Tracker™ Green diluted with Hank's Balanced Salt Solution (HBSS) followed by 30 minutes treatment at 37°C. Cells were fixed using 4% PFA for 2 minutes at 37°C and stained with 1 µg/ml Hoechst 33258 for 5 minutes before mounting and imaging. The first duplicate was used to optimize the conditions for imaging, only the result of the second duplicate was reported.

2.5. Organelle Localisation by Transfection of A549 Cell Line with Tagged Organelle Specific Markers.

GFP-tagged organelle specific markers were visualised by transiently transfecting plasmid DNA into A549 cells. Plasmids were isolated from frozen glycerol stocks of *E.*

coli previously transformed in our laboratory. The organelle marker plasmid used for this research were; human lysosomal associated membrane protein (LAMP1) representing lysosome; human RAB4A, member RAS oncogene family (RAB4A) representing early endosome; human microtubule associated protein (LC3) representing autophagosomes in transfected cells. Each of these organelle marker plasmids allows direct visualization of organelles without additional staining procedure. The expression vector for all organelle markers was pCMV6-AC-GFP vector shown in Figure 11 and all organelle markers are turboGFP tagged.

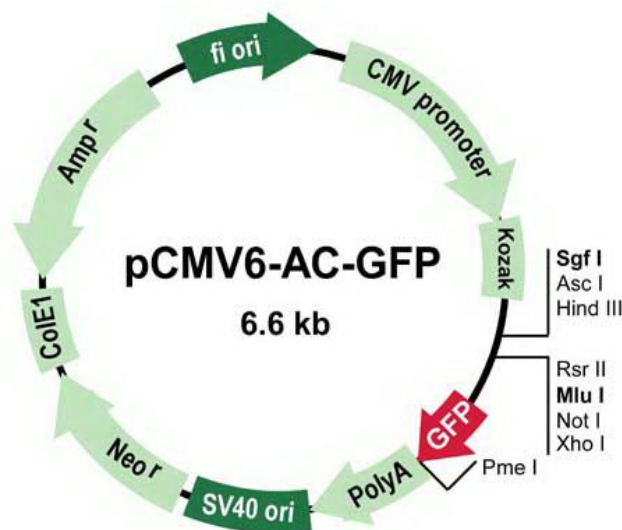


Figure 11 Schematic of the pCMV6-AC-GFP expression vectors

This vector contains the **CMV promoter**, which can be used to express the cloned cDNA. The **Kozak** sequence that drives protein expression in mammalian cell. The **C-terminal tGFP** tag. The **PolyA** signal located downstream of the signal. The **SV40 ori** allows the replication in mammalian cells, The **Neo^r** that confers the selection of plasmid in mammalian cell. The **ColE1** is the bacterial origin of replication. The **Amp^r** gene that confers the selection of the plasmids in *E. coli* and the **fi ori** is the filamentous phage origin of replication, allowing the recovery of single-stranded plasmids. **Image taken from origene.com**

2.5.1 Preparation of Luria-Bertani (LB) Broth and Agar Plates.

LB broth and agar plates were used to grow bacteria recovered from frozen bacteria stock.

LB broth was prepared by dissolving 10 g of LB broth medium into 500 ml of deionised water while 1.2% LB agar was prepared by dissolving 6 g of agar and 10 g of broth into 500 ml of deionised water, both media were sterilised by autoclaving at 120°C for 20 minutes.

Both LB broth and agar plates were poured in a sterile environment, which was cleaned with 70% ethanol and loop flamed with Bunsen burner.

2.5.2 Bacteria Recovery.

A sterile pipette tip was used to scrape the top of frozen bacteria from glycerol stock, while avoiding thawing of bacteria. The sterile tips were then placed into tubes containing LB Broth (5 ml) with appropriate antibiotic; ampicillin (100 µg/ml) for LAMP1 and RAB4 or kanamycin (25 µg/ml) for LC3. Bacteria cultures were incubated at 37°C with shaking (270 RPM) overnight. Overnight cultures of bacteria were plated on LB agar plate at various dilutions of broth (1, 1:10, 1:100, and 1:1000) on agar plates, which were inverted and incubated at 37°C overnight. The 1:1000 dilution of LB broth and bacteria gave the best density of colony with less background lawn and was therefore used to make up a new set of glycerol stock (40% glycerol to 60% autoclave dH₂O). Well-isolated colonies were picked at random using a pipette tip and placed in tube containing 5 ml of antibiotic containing Broth. Bacterial cultures were incubated in a shaker overnight at 37°C and 270 RPM to amplify colonies for plasmid mini-prep.

2.5.3. Plasmid Mini-Prep.

Mini-prep on overnight bacteria culture was carried out using QIAprep Spin Miniprep Kit (Qiagen). Overnight bacteria cultures were centrifuged for 10 minutes at maximum speed of 13,000 RPM with a bench top centrifuge to pellet cells. Pellets were re-suspended in 250 µl re-suspension buffer, 250 µl lysis buffer, 350 µl neutralization buffer and centrifuged for 10 minutes at 13,000 RPM. Supernatants were transferred to a spin column placed in a collection tube, centrifuged for 1 minute. 500 µl of wash buffer A and 700 µl of wash buffer B was added to spin column, centrifuged at maximum speed to remove all traces of ethanol. Spin column was placed in a new elution tube and 50 µl of elution buffer was used to elute

plasmid DNA. DNA quantification was done on isolated plasmid DNA to determine purity and concentration by NanoDrop ND1000 spectrophotometer. Isolated plasmid was stored at -80°C until needed.

2.5.4. Transient Transfection.

A549 cells were seeded at a density of 60,000 in a 6- well plate and left to attach overnight. Confluence was about 50 % the next day and cells were transfected according to manufacturer instructions (Origene). Briefly, 9 μl of Turbofectin 8.0 (Origene) was added to 300 μl of serum free DMEM followed by the addition of 3 μg of isolated plasmid DNA and gently pipetting of mixture. The transfection mixture was incubated at room temperature for 25 minutes followed by drop-wise addition to cells. Plates were gently shaken to ensure homogenous transfection and left to incubate at 37°C for 48 hours. 48 hours post-transfection, cells were treated with 0.9 nM RuS12·AuNP20 for 4-72 hours for study of co-localisation with specific organelle marker. At the end of each time points, cells were fixed with 4% PFA and mounted on a glass slide for confocal imaging. Images are acquired as described in section 2.3.1 above and analysed for co-localisation using JACoP plugin (Just Another Co-localisation Plugin) for ImageJ software.

2.6. Protein Extraction.

Cells were seeded at a density of 400,000 in a T₂₅ flask and allowed to achieve approximately 60% confluence before treatment with 0.9 nM RuS12·AuNP20 for 2, 4, 8, 12, 16 and 24 hours. At the end of each time point, cells were washed three times with PBS and trypsinised with 0.5 ml of trypsin for 5 minutes at 37°C . The supernatant was discarded and the pellet stored at -80°C until required. Frozen pellets were thawed and incubated on ice with regular vortexing and pipetting for 20 minutes with 250 μl of radioimmunoprecipitation (RIPA) buffer (1 M Tris-HCl pH 7.4, 150 mM NaCl, 1% Triton X-100, 0.5 M EDTA, 10% w/v

sodium deoxycholate and 10% SDS) supplemented with 0.01 % mammalian protease inhibitor cocktail (PhI) added just before use. After 20 minutes, cells were centrifuged for 15 minutes at 14,000 RPM and 4⁰C. Supernatant (2 µl) containing protein was used for protein quantification by Bradford assay and the remaining, stored at -80⁰C for western blotting.

2.6.1 Protein Quantification by Bradford Assay.

BioRad sterilised Bradford reagent (1ml of 1X filtered solution) was added to all cuvettes (standard and sample). To the standard cuvette, 0, 1, 2, 4, 6, 8 and 10 µl of 1 mg/ml bovine serum albumin (BSA) was added and to the sample, 2µl of sample (supernatant containing protein) was added. The cuvettes were gently mixed to ensure a homogenous solution and absorbance measured at 595 nm using 1 ml of Bradford reagent as blank. Protein concentration of samples were read from the standard curve obtained.

2.6.2 Western Blotting

Total protein (40 µg) was mixed with an equal volume of 2X Laemelli sample buffer and denatured by heating at 95⁰C for 5 minutes. Samples were then loaded into wells made with 4 % stacking gel (4% acrylamide, 125 mM Tris-HCl pH 6.8, 0.1% SDS, 1 µl/ml TEMED and 10 µl/ml ammonium persulfate) and 12.5% resolving gel (12.5% acrylamide, 375 mM Tris-HCl pH 8.8, 0.1% SDS, 1.5 µl/ml TEMED and 15 µl/ml ammonium persulfate) and samples ran for 90 minutes at 120V. Separated proteins were transferred onto 0.2 µm PVDF membrane (Bio-rad Trans-Blot[®] Turbo[™] Mini PVDF) using a Trans-Blot[®] Turbo[™] transfer starter system (Bio-rad). The PVDF membrane was blocked with blocking buffer 5% (w/v) BSA in [0.1% TBST (Tris buffer Saline and 0.1% Tween-20)] for 1 hour on rocker at room temperature to stop any non-specific binding. This was followed by overnight incubation with primary antibody LC3 raised in rabbit (cell signalling technology) diluted

with blocking buffer 1:1000 and β -actin raised in mouse (used as housekeeping control genes) diluted with blocking buffer 1:10,000 all at 4⁰C with gentle shaking. Membranes were washed three times for 10 minutes each, with 0.1% TBST on a rocker at room temperature, before incubating with secondary antibody. Secondary antibodies used were all *horseradish peroxidase* (HRP) conjugated and diluted with blocking buffer 1:5000 with sheep anti-rabbit antibody (Bio-Rad) for LC3 primary protein and 1:1000 with goat anti-mouse for β -actin (Life technologies) and incubate at room temperature for 1 hour on a rocker. Membranes were washed twice for 10 min with TBST and once with TBS before protein detection using SignalFire™ ECL Reagent (Cell Signalling Technology) and Amersham Hyperfilm (GE healthcare). The film was exposed for 5 minutes and developed using a XoGraph machine (AGFA Curix 60).

2.7. Ribonucleic Acid (RNA) Extraction and Quantification.

Cells were seeded at a density of 100,000 in a 6-well plate and left to attach overnight before treatment with 0.9 nM RuS12·AuNP20 for 4, 8, 16, 24, 48 and 72 hours. At the end of each time point, cells were washed three times with PBS, trypsinised for 5 minutes and centrifuged for 5 minutes at 1500 g. Cell pellet were stored in 500 μ l RNAlater until required.

RNA extraction was done using an RNA extraction kit (Qiagen) according to the manufacturer instructions. Briefly, cell pellets were thawed on ice and centrifuged to get rid of RNAlater and to obtain solid cell pellets. Next pellets were lysed with 350 μ l of buffer RLT and 350 μ l of 70% ethanol (dissolved in RNAase-free water), and the solution was pipetted up and down to lyse the cells. The solution 700 μ l of was transferred to a spin column in a 2 ml collection tube and centrifuged for 8,000 RPM on a bench-top centrifuge for 1 minute followed by the addition of 700 μ l of buffer RW1 to the spin column (flow through was discarded) and further centrifuged for 1 minute at 8,000g (flow through

discarded). Buffer RBE of 500 μ l of was added to spin column and centrifuged for 2 minutes and flow through discarded. Spin column was placed in a 1.5 ml collection tube (RNAase-free water) and RNA was eluted using 40 μ l of RNAase-free water added directly to the column, allowed to stand for 1 minute and centrifuged for 1 minute. Concentration and purity of extracted RNA was determined by Nanodrop ND1000 spectrophotometer and stored at -80⁰C until needed.

2.7.1. Complementary DNA (cDNA) Synthesis

cDNA was synthesised from extracted RNA using a Tetro cDNA synthesis kit (Bioline). All solutions used were briefly vortexed and all preparation were done on ice. Extracted RNA of 500 ng was added to the premix solution. The Premix was made by the addition of 1 μ l of oligo (dT) primer, 1 μ l of 10 mM dNTP mix, 4 μ l 5X RT buffer, 1 μ l RiboSafe RNase inhibitor and 1 μ l of Tetro Reverse Transcriptase. Premix solution containing RNA was mixed gently by pipetting. The solution was then incubated at 45⁰C for 30 minutes and the reaction terminated by incubating at 85⁰ C for 5 minutes. Samples were then chilled on ice before storing at -20⁰C until needed.

2.7.2. Quantitative real-time PCR (RT-PCR).

RT-PCR was done using 250 ng of cDNA, 1 μ l TaqMan[®] Gene Expression Assay primer (Applied Biosystems,) and 10 μ l of TaqMan[®] Fast Advanced Master Mix (Applied Biosystems) made up to 20 μ l with RNAse-free water. The RT -PCR run, consisted of one cycle (polymerase activation) at 95⁰C for 20 seconds, then 40 cycles of denaturing at 95⁰C for 1 second and annealing at 60⁰C for 20 seconds. The data was collected at the annealing stage. All primers (TaqMan[®] Gene Expression Assay) used were FAM labelled and from human species, β -actin was chosen as the housekeeping genes based on result of western blot. All experiments were done using three biological replicate for each

time points and included three technical replicates. Data analysis was by $\Delta\Delta\text{Ct}$ method (Pfaffl, 2001).

Gene	Symbol	UniGene ID
Microtubule associated protein 1 light chain 3 alpha	MAP1LC3A	Hs.632273
Heat shock protein family A (Hsp 70) member 1A	HSPA1A	Hs.274402
Glutathione-disulfide reductase	GSR	Hs.271510
Catalase	CAT	Hs.502302

Table 2: Gene used in RT-PCR

2.8. Cytotoxicity Assay of RuS12·AuNP20 in A549 cells.

The biochemical effect of RuS12·AuNP20 on A549 cells was investigated by assessing cell viability (MTT and crystal violet) generation of ROS (H₂DCF-DA assay), oxidative stress (glutathione assay) and single strand DNA damage by (comet assay) at different concentrations and different exposure times. RuS12·AuNP20 (9 nM) was diluted 1:10 with media to make a stock solution (0.9 nM) and stock solution was serially diluted 1:2, 1:4, and 1:8 with media to give 0.45 nM, 0.225 nM and 0.1125 nM respectively. Each assay had a negative control (A549 cells grown in complete media and not exposed to any nanoparticles) and an appropriate positive control. All assays were done in biologically triplicates.

2.8.1. 3-(4, 5-dimethylthiazol-2-yl)-2, 5 diphenyltetrazolium bromide) MTT Assay.

Cell viability was measured by the MTT assay, a metabolic assay that measures mitochondria activity. MTT powder was made to a stock solution of 5 mg/ml in PBS and used at a final concentration of 0.5 mg/ml in media. The presence of mitochondrial

dehydrogenase in viable cells allows the reduction of MTT to a purple formazan precipitate, which upon addition of DMSO can be quantified colorimetrically.

Cells were seeded at a density of 8,000 cells per well in a flat clear bottom 96-well plate and left overnight for attachment to occur. Spent media was aspirated and replaced with 100 μ l of complete media containing 0.9 nM, 0.45 nM, 0.225 nM and 0.1125 nM of RuS12·AuNP20 and incubated for 24, 48 and 72 hours at 37°C. One hour before the end of the time points, positive control cells were treated with 0.15 % (v/v) Triton X-100. At the end of each time point, cells were washed three times with PBS and incubated for 3 hours at 37°C with 100 μ l of media containing 0.5 mg/ml MTT. Media was removed and formazan precipitate was dissolved with 200 μ l of DMSO. The absorbance of dissolved formazan was determined at 590 nm in a plate reader (Tecan Infinite® 200 PRO) Cell viability was expressed as a percentage control of (average mean- DMSO blank) \pm SEM.

2.8.2. Crystal Violet Staining.

Crystal violet staining (CVS) is a quantitative assay used to determine cellular viability by staining the DNA of adherent cells, which are then solubilised with acetic acid. Cells were seeded at a density of 15,000 cells per well in a 24-well plate and left overnight for attachment to occur. Spent media was aspirated and replaced with 500 μ l of complete media containing 0.9 nM, 0.45 nM, 0.225 nM and 0.1125 nM of RuS12·AuNP20 and incubated for 24, 48 and 72 hours at 37°C. One hour before the end of the time points, positive control cells were treated with 0.15 % (v/v) Triton X-100. At the end of each time point, cells were rinsed with 500 μ l of PBS and stained with 1% crystal violet (w/v 5% ethanol in distilled water) for 30 minutes at room temperature. Stained cells were carefully washed three times with water and allowed to air dry for 3 hours at room temperature. Acetic acid (10%) 500 μ l was added to each well to solubilise the crystal violet and 100 μ l from each wells was

transferred to a fresh 96 well plate. Absorbance was read at 570 nm against a 10% acetic acid blank. The results were expressed as % control of (average mean- 10% acetic acid blank) \pm SEM.

2.8.3 Dichloro-dihydro-fluorescein Assay.

The dichloro-dihydro-fluorescein diacetate (H₂DCF-DA) assay is used for the detection of reactive oxygen species (ROS). 2',7'-dichlorodihydrofluorescein (H₂DCF) is sensitive to several ROS and is oxidised to a fluorescent 2',7'-dichlorofluorescein (DCF) (Chen *et al.*, 2010). DCFH-DA penetrates the membrane, and then it is hydrolysed by cellular esterases and converted via oxidation to DCF. Therefore, DCF fluorescent indicates the resultant oxidative stress due to overproduction of ROS. H₂DCF-DA powder was made to a stock solution of 10 mM in 100% ethanol and used at a final concentration of 10 μ M in media. Cells were seeded at a density of 8,000 cells per well in a white clear bottom 96 well plate and left overnight for attachment to occur. Spent media was aspirated and replaced with 100 μ l of complete media containing 0.9 nM, 0.45 nM 0.225 nM and 0.1125 nM of RuS12·AuNP20 and incubated for 24, 48 and 72 hours at 37⁰C. One hour before the end of the time points, positive control cells were incubated with 200 μ M H₂O₂. At the end of each time point, all cells were washed three times with PBS which was then replaced with media containing 10 μ M H₂DCF-DA and incubated for 45 minutes at 37⁰C. At the end of 45 minutes, cells were washed and fresh PBS added to each well and fluorescence intensity was measured at an excitation of 485 nm and emission of 535 nm in a plate reader (Infinite® 200 PRO, Tecan trading). Unstained cells were read to calculate background fluorescence. Result was expressed as % florescence intensity of control calculated by average mean -means of unstained cells \pm SEM.

2.8.4 Glutathione Assay.

Glutathione (GSH) assay measures the levels of intracellular glutathione. In healthy cells, glutathione exist more in its reduced form (GSH), a depletion of GSH indicates cellular stress. The levels of GSH was measured in cells treated with RuS12·AuNP20 and read against a GSH standard curve (Hissin & Hilf, 1976). Cells were seeded at a density of 100,000 cells per well in a 6-well plate and left overnight for attachment to occur. Spent media was aspirated and replaced with 3 ml of complete media containing 0.9 nM, 0.45 nM, 0.225 nM and 0.1125 nM of RuS12·AuNP20 and incubated for 24, 48 and 72 hours 37°C. At the end of each time point, spent media was removed and cells washed with 1 ml of PBS. Cells were scraped into 450 µl of ice-cold lysis buffer (0.1% Triton X-100 in PO₄-EDTA) and placed on ice. The ice-cold protein precipitation buffer (50% trichloroacetic acid in PO₄-EDTA) 50 µl was added to lysate placed on ice which was vortexed first before centrifuging with a bench-top centrifuge at 13,000 RPM for 5 minutes and the supernatant used to measure GSH levels. GSH levels obtained were read against the standard GSH standard curve (GSH standard curve is shown in appendix 5D1) described in section 2.8.4.1 below.

2.8.4.1. Glutathione Standard Curve.

PO₄-EDTA buffer 1.8 ml (100 mM NaH₂PO₄ and 5 mM Na₂EDTA pH 8.0) was added to a 3 ml fluorescence cuvettes (standard curve and samples). For standard curve, 0,1,2,4,6,8,10,12,14,16,18 & 20 µl of GSH (0.1 mg/ml of GSH in PO₄-EDTA) was added to cuvettes, followed by 100 µl of 5% TCA. To sample cuvette, 100µl of sample (supernatant) was added followed by 100 µl of o-phthalaldehyde (1 mg/ml of OPT in 100 % methanol) to all cuvettes. Cuvettes were gently mixed and covered for 15 minutes and fluorescence read at excitation of 350 nm, emission of 520 nm and slit width set at 5 nm using a PerkinElmer LS50B luminescence spectrometer. GSH levels in each sample was expressed as % control of reduced glutathione levels ± SEM.

2.8.5 Alkaline Comet Assay.

The alkaline comet assay is a sensitive and quantitative technique for detecting DNA strand breaks (Singh *et al.*, 1988). During DNA damage, the supercoiled structure of intact DNA is lost and when electrophoresis is applied, DNA damage is observed as a comet-like structure.

Cells were seeded at a density of 200,000 cells per well in a 6-well plate and incubated at 37°C overnight for attachment to occur. Spent media was aspirated and replaced with 3 ml of complete media containing 0.9 nM, 0.45nM, 0.225nM and 0.1125nM of RuS12·AuNP20 for 24, 48 and 72 hours and incubated at 37°C.

2.8.5.1. Slide Preparation.

Microscope slides were pre-coated with normal melting point agarose (NMPA; 0.5% w/v in PBS) and air dried for at least 48 hours. After incubation, media was aspirated and cells washed with PBS and trypsinised with 1ml of trypsin. Cell pellets were re-suspended in 150 µl of PBS and 10 µl was aliquoted into tubes containing 150 µl warm low melting point agarose (LMPA; 0.5% w/v in PBS). The resulting mixture (10 µl sample + 150 µl LMPA) was added to NMPA-coated slides and slides were chilled on metal tray on ice for about 20 minutes to enable solidification of the agar. Once the agar had set, coverslips were taken off and slides placed into a coplin jar containing lysis buffer (2.5 M NaCl, 0.1 M Na₂EDTA, 110 mM Tris Base and 33.3 ml sodium laurylsarcosinate, in 1 liter of dH₂O). The coplin jar was wrapped in foil and left at 4°C for 1 hour. Slides were transferred after an hour of lysis, to a large electrophoresis tank containing electrophoresis buffer (9 M NaOH and 20 mM Na₂EDTA) in a cold room and the DNA is allowed to unwind for 20 minutes. After the 20 minutes, slides were electrophoresed for 20 minutes at 300 mA and 32 V. Following electrophoresis, slides were washed three times with neutralization buffer (0.4 M Tris Base pH 7.4) for 5 minutes followed by distilled water for an additional 5 minutes. Slides were

stained with 50 μ l SYBR gold solution and covered with a coverslip. Slides were then stored overnight in moist box at 4⁰C. Slides were scored (100 cells per slides) and comet analysed by comet assay IV software. Results are expressed as % control of the mean of the median tail intensity \pm SEM as opposed to conventionally used mean of mean. This is so because of the unequally distribution of the damage in the tail.

2.9. Statistics

Raw data generated from experiments were analysed using IBM SPSS software version 21. First, was to test the normality of all data. Normally distributed datasets were subject to parametric testing: one-way analysis of variance (ANOVA) and Bonferroni Post Hoc analysis. Non-normal datasets were analysed with Kruskal-Wallis tests. All experiments were biological triplicate with a minimum of two technical duplicates. Data are expressed in graphs, graphs were prepared using Microsoft office excel 2016. The level of significance considered was $P \leq 0.05$ after respective Post Hoc analysis.

Chapter 3

Characterization of RuS12-AuNP20 and Uptake in A549 cells

3.1. Introduction

The potential biomedical applications of AuNPs are highly dependent on their physical and chemical properties. These properties of AuNPs need proper characterization to ensure continuous uniformity in synthesis. Therefore, establishing a proper characterization profile of particles is essential before any cellular studies. Characterization of AuNPs as well as functionalised AuNPs involves understanding features such as surface area, solubility, particle size distribution, aggregation, shape and size of the particles, which are all reliant on the surface plasmon resonance (SPR) properties of AuNPs.

SPR of AuNPs is a very important property because it determines the physical properties such as size and shape of AuNP. SPR has been demonstrated to occur between a wavelength of 500-550 nm in the visible region, and it varies based on the size and aggregation state of AuNP (Jain *et al.*, 2006; Philip, 2008; Zheng *et al.*, 2016). The SPR of AuNP arises from the interaction of specific wavelength of light with free oscillating electrons on the surface of AuNPs to produce an absorption peak measured by ultraviolet-visible (UV-Vis) Absorption Spectroscopy (Ghosh & Pal, 2007). The incorporation of additional surface coating onto AuNPs during functionalization causes a shift in absorption peak of SPR (Davies *et al.*, 2012; Engel *et al.*, 2017). Therefore, determination of SPR of both AuNPs and the functionalised AuNPs (RuS12·AuNP20) is critical for their characterization profile.

The dependency of the particle size on value of SPR makes size characterization equally important. For a particle to be classified as a nanoparticle, it must have a diameter of between 1 -100 nm as set by the international standard organization (ISO, 2008). TEM imaging and dynamic light scattering (DLS) are methods used for size characterization of AuNPs. The high electron density of gold makes it easily visible by TEM imaging which can be used to measure the diameter of AuNPs (Brust *et al.*, 1994).

DLS is a technique often used to measure the hydrodynamic radius of the inorganic core as well as additional surface coatings on the core of sub-micron particles present in colloids (AuNPs) when they move under the influence of Brownian motion (Mehtala & Wei, 2014). The principle behind DLS is measuring the light scattered from the laser that passes through the colloid, which is then used to estimate the hydrodynamic size (Berne & Pecora, 2000). Using DLS to measure particle size also measures the polydispersity index (PDI) which gives the homogeneity of the size distribution. Particles with high PDI (>0.5) consist of varying sizes of particles with broad distribution while particles with evenly sized particles have a lower PDI (Cho *et al.*, 2013; Lu *et al.*, 2011). The PDI is also a useful indicator for confirming the attachment of the ligand to particle and the colloidal stability of functionalised ENPs (Masarudin *et al.*, 2015). Colloidal stability is also measured by zeta potential. Zeta potential is the potential difference that exists between the particle surface and dispersing liquid. A particle with large negative or positive potential will electrostatically repel each other while particles with small negative or positive potential will attract each other with a tendency to aggregate (Cho *et al.*, 2013). So generally, a recommended zeta potential for a stable colloid should be larger than +30mV or less than -30mV so as to maintain the electrostatic repulsion between the colloid and avoid aggregation (Cho *et al.*, 2013).

AuNP has an intrinsic luminescent property owing to its SPR, which can be altered either positively or negatively upon surface functionalization and change in shape or size (Eustis & El-Sayed, 2006; Thomas & Kamat, 2003). The functionalization of AuNPs with a luminescent molecule such as transition metals specifically ruthenium used in this study enhances the overall luminescent property of AuNPs making them an ideal candidate as a nanoprobe. RuS12·AuNP20 would therefore bear a distinct optical signature of the

ruthenium metal complex, independent of the particle properties (Osborne & Pikramenou, 2015; Rogers *et al.*, 2014).

Only fully characterised RuS12·AuNP20 were used for cellular studies by first studying the kinetics of uptake in A549 cells in this chapter and trying to decipher the mechanism of uptake. Imaging as well as analytically using inductively coupled plasma mass spectrometry (ICP-MS) was used to study the uptake of RuS12·AuNP20 and this was done over a period of 2-72 hours. Study of uptake by imaging was by confocal, which involved both fixed and live cells and lastly TEM. Confocal microscopy of the uptake of RuS12·AuNP20 in A549 cells was possible because of its luminescent property as confocal microscopy works by excitation of light from a laser passing through a pinhole to reject out of focus light and producing images from a section of the sample (Sheppard & Shotton, 1997). The limiting low resolution of confocal imaging was the reason for supplementing the uptake study with TEM imaging. TEM enables detailed imaging of cells because of its high resolution and contrast of gold in biological samples. The contrast is possible because gold is a heavy metal.

ICP-MS is a sensitive technique capable of detecting very small quantity of metals in samples therefore making it ideal as a quantitative measurement of uptake of RuS12·AuNP20 in A549 cells. The work in this chapter presents a detailed characterization of RuS12·AuNP20 and the study of their uptake in A549 cells over 2-72 hours using various technique such as imaging and ICP-MS.

3.2. Results

3.2.1 Characterisation of RuS12·AuNP20

The protocols for preparation and functionalization of RuS12·AuNP20 were performed according to Osborne and Pikramenou (2015) and the characterization data generated are in agreement with published data.

The SPR of synthesised citrate stabilised AuNP colloid was measured first, followed by the concentrated AuNP. The concentrated AuNP showed an increase in SPR from 516 to 517 nm (table 3) indicating a more concentrated solution than the originally synthesised citrate-stabilised AuNP colloid (1.6 nM to 9 nM). The concentrated AuNP was first coated with zonyl, a fluorosurfactant and a SPR shift from 517 to 518 nm (Table 3 and Figure 12) was observed. The zonyl coated AuNP (Z.AuNP) was isolated by centrifugation and finally coated with RuS12 to give RuS12·AuNP20 and SPR shifted from 518 to 520 nm with no further shifting indicating a full loading of RuS12 onto AuNP surface. RuS12·AuNP20 was purified by size-exclusion chromatography to remove any excess and unbound ruthenium complex. The UV-Vis scan of the purified RuS12·AuNP20 gave the same SPR of 520 nm confirming the stability of the ruthenium complex on the AuNP surface even after chromatography. Purified RuS12·AuNP20 was further characterised for its size and luminescence property before use in cellular studies.

Dynamic light scattering (DLS) and TEM were used for particle size characterisation. DLS characterization data is summarised in table 4. The DLS result showed an increase in number and intensity distribution upon addition of zonyl and ruthenium complex onto the gold surface, indicating their attachment to surface of AuNP. Also the PDI values are quite low, indicating particles are monodispersed. All batch of particles used throughout this study had a final size (number distribution) of around 20 nm and a PDI of ≤ 0.4 .

The TEM analysis (Figure 13) of RuS12·AuNP20 showed monodispersed, spherical particles of about 20 nm, the TEM analysis was performed and published by Osborne and Pikramenou (2015). The TEM analysis and DLS result are in agreement about the size of the particle been about 20 nm with no evidence of aggregation.

The SPR band at about 520 nm observed by UV-vis spectroscopy is an indication of the luminescent ability of RuS12·AuNP20. To further, confirm this a luminescence emission spectrum of RuS12·AuNP20 excited at 488 nm is shown in Figure 14 with a peak of about 650 nm which is the red end of visible spectrum (red colour wavelength is between 620-750 nm). The emission spectra further proves the luminescence property of RuS12·AuNP20, which was useful in cellular studies.

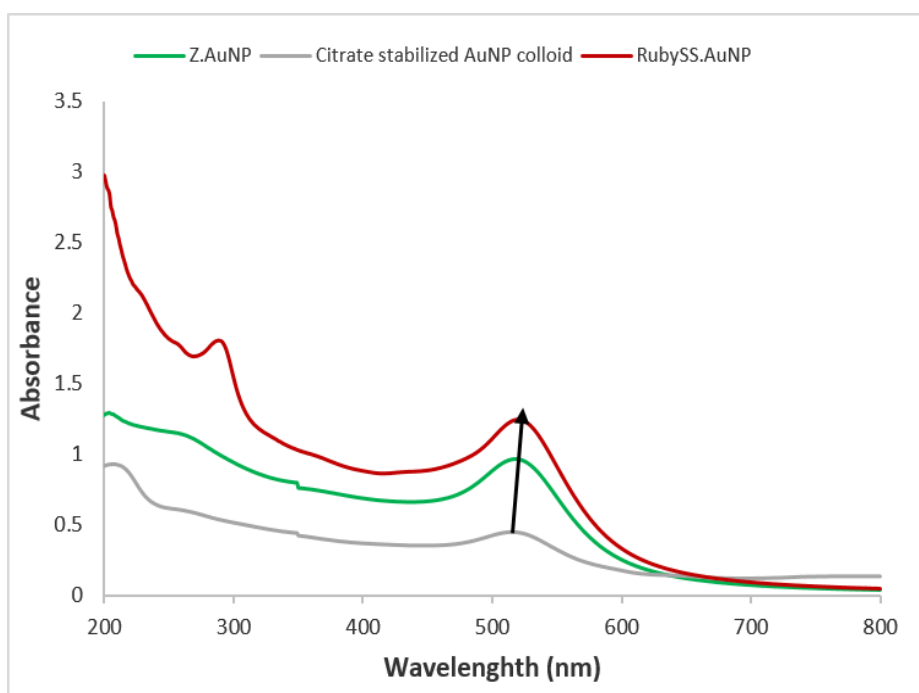


Figure 12: Uv-vis absorption spectra coating of citrate stabilised AuNP with RuS12.

1 ml of citrate stabilised AuNP colloid was coated with 10% zonyl and an increase in absorbance was observed. The observed increased in absorbance shows the increase in luminescence of AuNP colloid upon the attachment of RuS12. On further coating with RuS12 a further increase in absorbance is observed as a 4 nm shift compared to the AuNP colloid indicating the loading of the coatings onto the surface of AuNP. The exact shift in wavelength is shown in Table 3.

Sample	λ_{max} (nm)	Shift (nm)
Citrate stabilised AuNP colloid	516	0
Concentrated AuNP colloid	517	1
Z.AuNP	518	2
RuS12·AuNP20	520	4
Purified RuS12·AuNP20	520	4

Table 3: Summary of AuNP SPR shift upon coating.

Sample	Number Distribution (nm)	Intensity Distribution (nm)	P DI
Citrate stabilised AuNP colloid	12 ± 3	18±5	0.1
Concentrated AuNP colloid	13 ±3	19±5	0.1
Z.AuNP	16 ±5	31 ±13	0.3
Purified RuS12·AuNP20	22 ± 9	161 ± 110	0.3

Table 4: Dynamic light scattering (DLS) sizing data of AuNP in water.

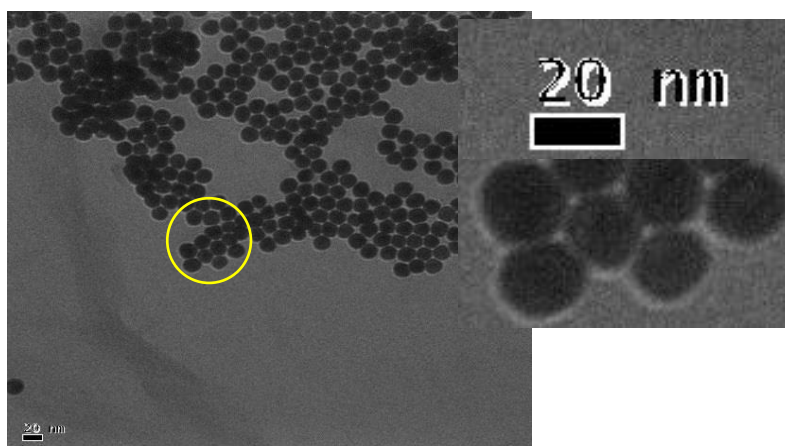


Figure 13: TEM image of RuS12·AuNP20 in water.

The result of the DLS shows the number distribution at 22 nm (Table 4), which is similar to the characterisation TEM data gotten and published by *Osborne & Pikramenou, 2015*, which shows the particles to be mono-dispersed and about 20nm.

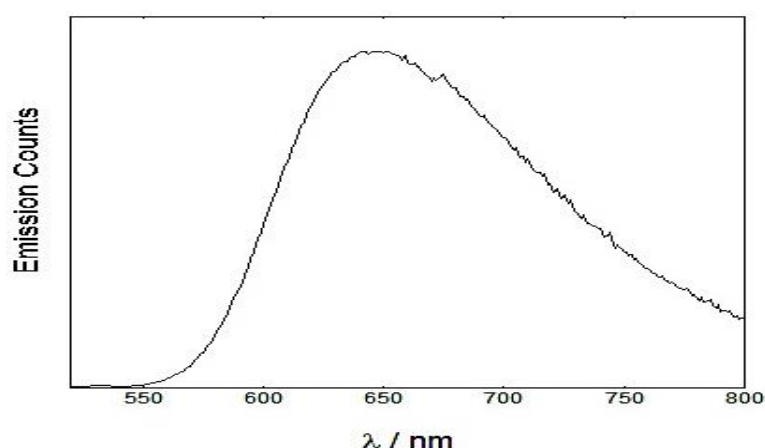


Figure 14: Luminescence emission spectra of RuS12·AuNP20 in water

1ml of RuS12·AuNP20 was excited at 488 nm to collect it emission scan, which was shown to be about 650. This result is also similar to published data by *Osborne & Pikramenou, 2015*. Confirming the reliability of the protocol used in the synthesise of **RuS12·AuNP20**

3.2.2. Uptake in A549 cells

Fully characterised RuS12·AuNP20 were used to study the cellular uptake in A549 cells by different imaging techniques. 0.9 nM of RuS12·AuNP20, which is equivalent to 1:10 dilution with media, was the concentration used for the study of uptake. This concentration was observed to be non-toxic to A549 cells by MTT Assay (detailed results in chapter 5) and from previous investigation in our lab (Rogers *et al.*, 2014) thereby making it a suitable concentration for use in cellular studies. The luminescence properties of RuS12·AuNP20 was exploited for this study especially in confocal imaging while the electron dense characteristic of gold was harnessed for TEM imaging.

3.2.2.1. Confocal Microscopy

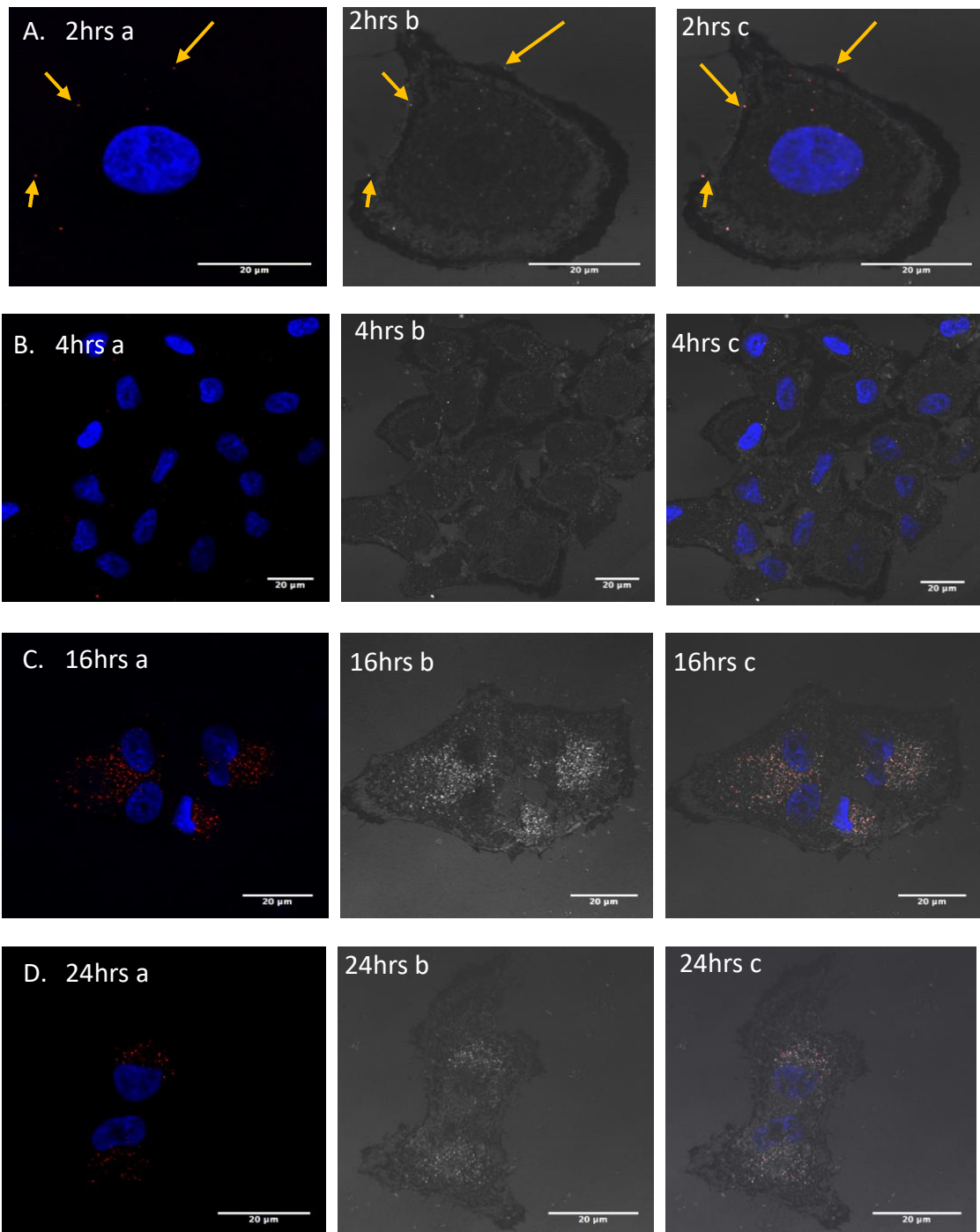
RuS12·AuNP20 uptake in A549 cells were studied over a period of 2-72 hours in fixed cells, supplemented with live cell imaging. Live cell imaging was used because the cells are in their normal physiological state and to remove possibility of artefact related to the fixation procedure. Representative images shown are from major time points: 2, 8, 16 and 48 hours (other time points are shown in appendix 3A). The images shown are fluorescence images of RuS12·AuNP20 with counterstained nuclei (blue, stained with Hoechst) and the corresponding reflection images showing the outline of the cells and RuS12·AuNP20 as bright spots. The bright spots of RuS12·AuNP20 in reflection images is as a result of the scattering signal of the gold while the luminescent ruthenium complex on the AuNP surface is responsible for the red signal on the fluorescence channel, which represents clusters of RuS12·AuNP20. Also, shown are overlay images of the fluorescence and reflection channels, which the red spot and the white dot overlap indicating the intracellular stability of RuS12·AuNP20. Ruthenium complex alone (RuS12) was also imaged in cells after 4 hours treatment (data in appendix 3B) and the imaging showed a very diffuse staining

compared to nanoparticle (RuS12·AuNP20) images further confirming the stability of RuS12 on the gold surface. Unless otherwise stated all scale bar are 20 μm .

The result of the images shows that at early time point of 2 hours, very few nanoparticles are observed in the fluorescence channel (Figure 15a; yellow arrows) and the corresponding reflection image shows the particle to be localised on the cell membrane suggesting the particles are taken up by the cells at about 2 hours post treatment. Similar observation of membrane associated particles at 2 hours was noticed in the live cell imaging (Figure 16) therefore, ruling out any chance of it been artefact. Over time, more nanoparticles are observed to be taken up by the cells in both fixed and live cell imaging (Figure 15 and 16) indicating that the uptake of particles into cells is time dependent. Also observed, the particles accumulated and localised in perinuclear region of the cells that is around the nucleus evident in both fluorescence and reflection channel irrespective of the time points.

Having established a time dependent uptake as observed in the confocal images, we aimed to quantify the uptake of RuS12·AuNP20 in A549 cells based on acquired images. For each time points, 10 different images were acquired and processed as described in Figure 17 with details in appendix 2C. The aim of the processing was to quantify the RuS12·AuNP20 by counting the number of dots from the red fluorescence channel, which is a representation of nanoparticle clusters. The count was done per field of view and the zoom were all corrected to one irrespective of zoom used to acquire image to makes the count comparable within time points. In addition, acquiring 10 different images helped to increase the precision and reduce error. The graph in Figure 18 shows various time points and the average count of 10 different acquired images. A time dependent increase in count is observed which is expected based on the confocal imaging Figure 15 and 16. The count remained almost constant at about 40 hours up to 72 hours suggesting a saturation of cells with RuS12·AuNP20 at about

40 hours. Therefore, confocal images show that the uptake of RuS12·AuNP20 into A549 increases in a time dependent manner that can be quantified.



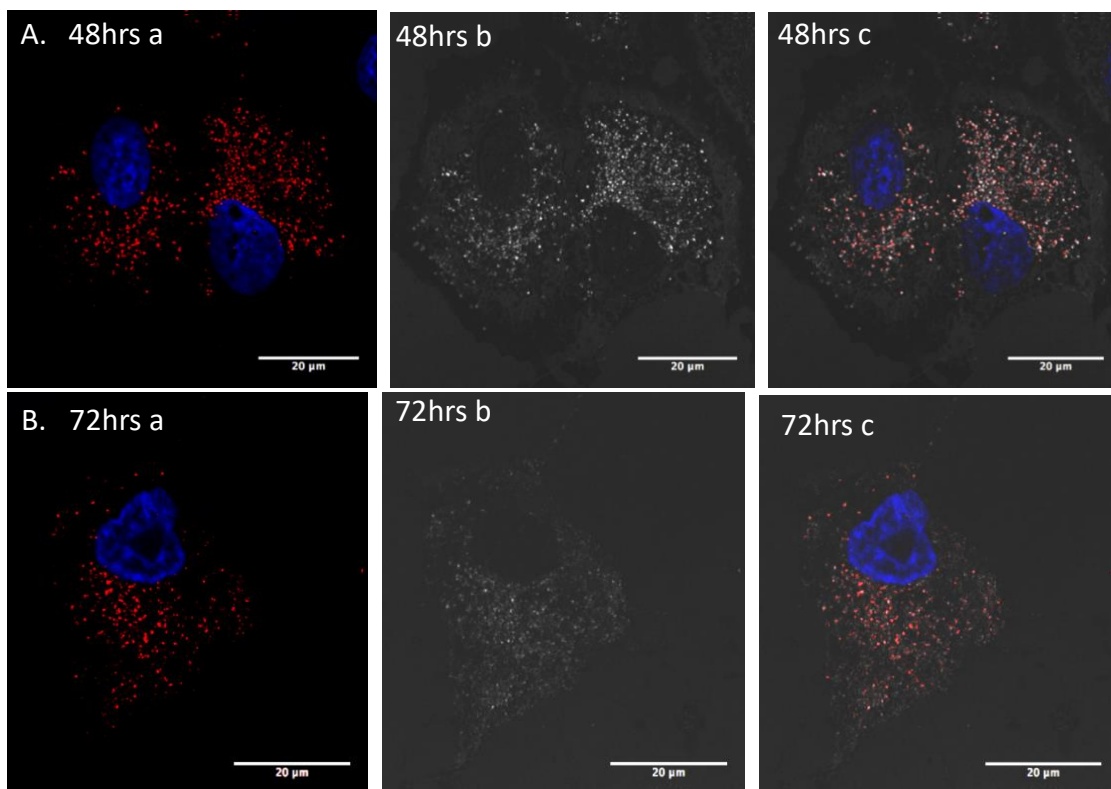


Figure 15: Representative merged confocal images of major time points of fixed A549 treated with 0.9 nM RuS12-AuNP20 and Hoechst.

A549 cells were treated with 0.9 nM RuS12-AuNP20 between 2-72 hours. The images shown are representative of 10 different images acquired per slide (for each time point). This experiment was done as a biological triplicate, the first two duplicate were used to optimize imaging conditions and showed similar result with the third replicate which are the images reported ($n=1$). An increase in uptake is observed over time and the yellow arrows are nanoparticles on the cell membrane (A 2hours c). Only major time points are shown here and other time points are in appendix 3A.

- a. Merged images of RuS12-AuNP20 and Hoechst
- b. Their corresponding reflection image ($\lambda_{exc} = 488 \text{ nm}$, $\lambda_{em} = 478-498 \text{ nm}$) a
- c. Merged fluorescence and reflection channel.

RuS12-AuNP20 emission form red channel ($\lambda_{exc} = 488 \text{ nm}$, $\lambda_{em} = 620-800 \text{ nm}$)

Hoechst emission form the blue channel ($\lambda_{exc} = 405 \text{ nm}$, $\lambda_{em} = 410-455 \text{ nm}$)

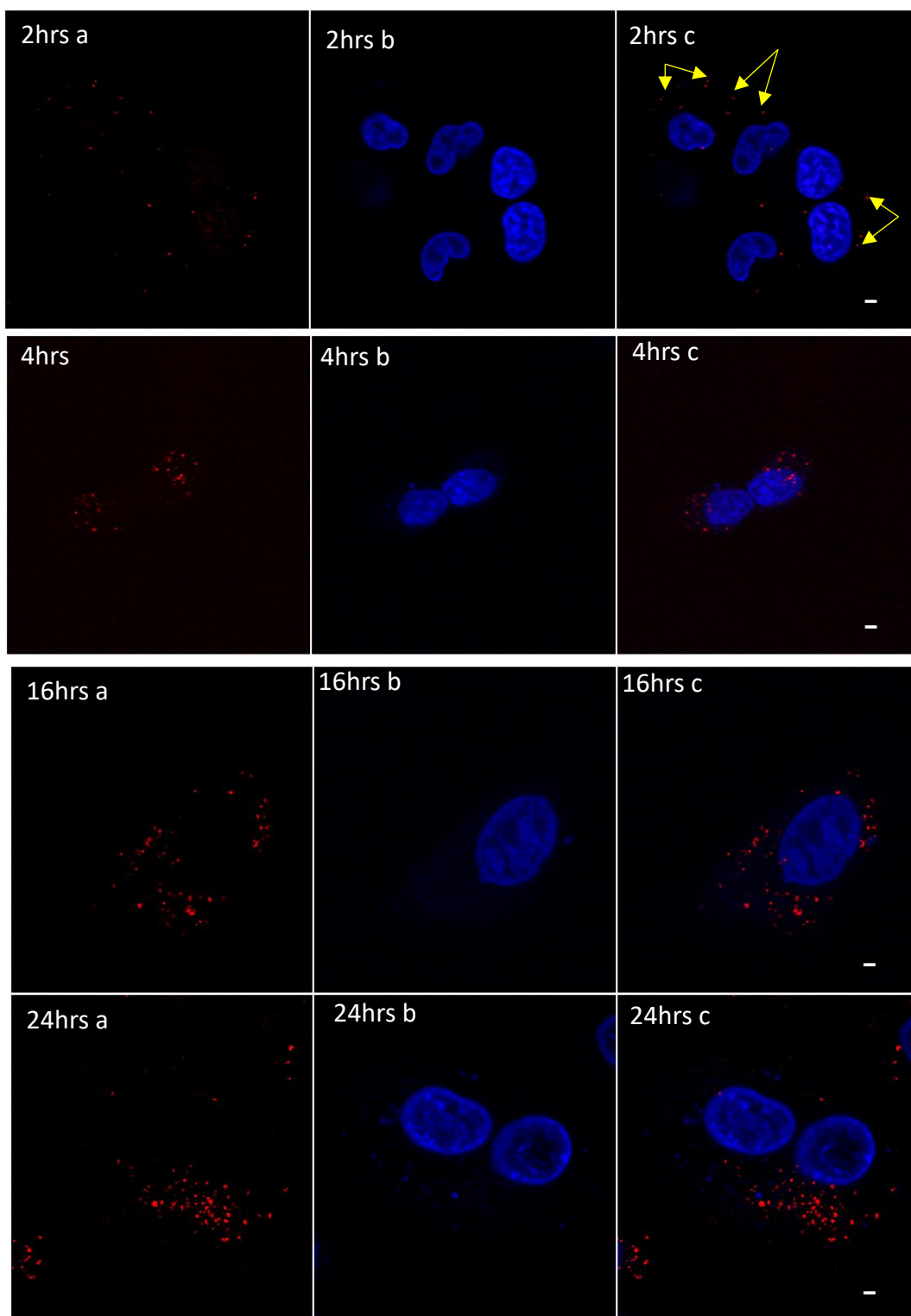
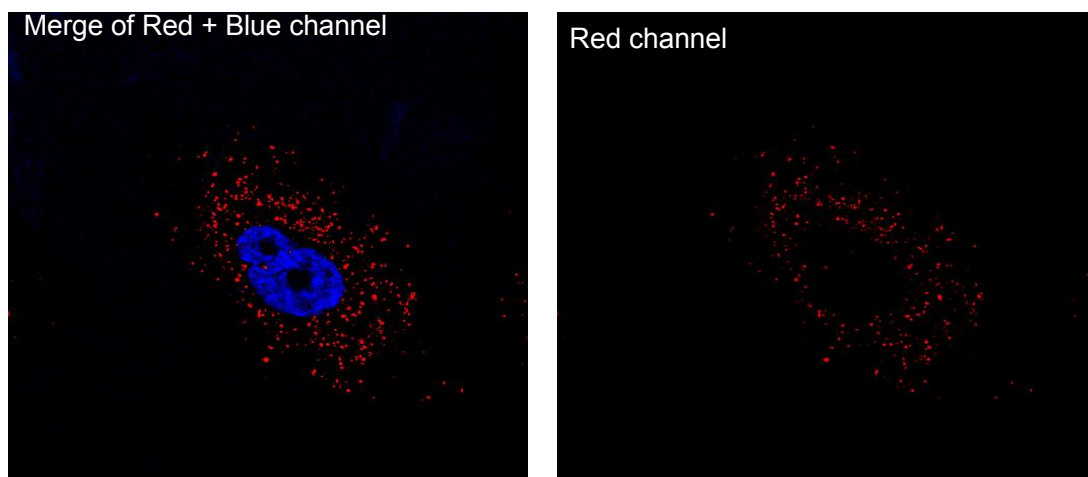


Figure 16: Representative confocal images of live cell imaging of A549 treated with 0.9 nM RuS12.AuNP20
 Live cell imaging was done to complement the fixed cell imaging. Imaging was done in live cell imaging solution. The experiment was done biological triplicate, the first two duplicate were used to optimize imaging conditions and showed similar result with the third replicate which are the images reported ($n=1$). Results were similar to fixed cell especially at 2 hours (yellow arrow) showing nanoparticles on the cell membrane and also the increase in uptake of time.

- a. RuS12.AuNP20 emission form red channel ($\lambda_{exc} = 488 \text{ nm}$, $\lambda_{em} 620\text{-}800 \text{ nm}$)
- b. Hoechst emission form the blue channel ($\lambda_{exc} = 405 \text{ nm}$, $\lambda_{em} = 410\text{-}455 \text{ nm}$)
- c. Merged images.



Binary image (b)



Outline of count (c)

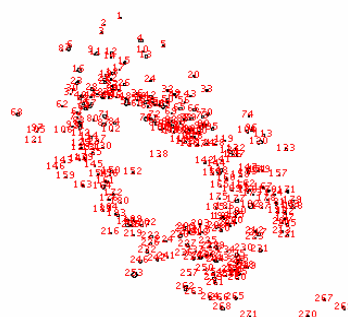


Figure 17: Steps in quantification of confocal images

Images acquired by confocal microscopy were subjected to analysis by ImageJ software (Image processing software). The red channel (nanoparticle luminescence) was converted to binary images (b), each of the dots represents clusters of RuS12.AuNP20 and was counted automatically, and (c) shows the outline of particles counted and the number details of procedure explained in appendix 2C.

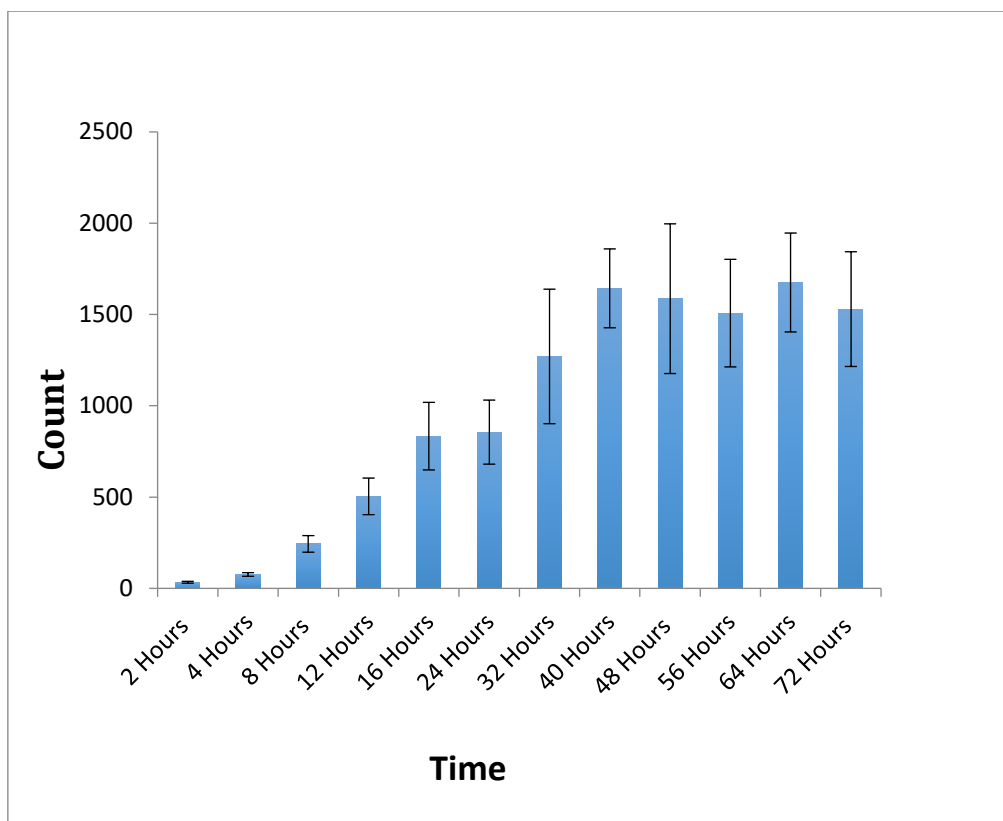


Figure 18: Quantification of acquired images of A549 cells treated with 0.9 nM RuS12-AuNP20

Each time point was represented by a slide, for each time point, 10 random images per slides were acquired and processed by counting the red dots, which represent clusters of RuS12-AuNP20. The A549 cells used for this imaging were treated with 0.9 nM of RuS12-AuNP20 between 2-72 hours and the result shown was from a single experiment with no technical replicate (n=1). The count was done with Image software. The result is expressed as average count \pm SEM and shows an increase over time.

3.2.2.2. Transmission Electron Microscopy Imaging

TEM utilises beams of electrons to create an image. The image is formed by the interaction of electrons with gold, which provides a good contrast against the biological medium that is the cell. In addition, the resolution of TEM is higher in comparison with confocal microscope, thereby enabling visualization of individual particles in respect to its cellular localisation and monitoring their uptake over time. The TEM images acquired at early time points of 2 hours showed the particles to be localised mainly on the membrane (Figure 19) which is in agreement with confocal imaging. The particles are observed to be spherical as expected based on the size characterisation in water by TEM (Figure 13). Also, noticed is a ruffling of the cell membrane at early time points of 2 hours and observed are particles adhering to parts of the fragmented cell membrane (Figure 19). The cell membrane undergoes conformational changes observed as fragments and protrusion as more evident in 4 hours compared to 2 hours because of the presence of more particles (Figure 20). The reshuffling and protrusion of the cell membrane seen is an indication of the involvement of macropinocytosis as a likely mechanism of uptake of RuS12·AuNP20 in A549 cells. Additionally, observed are small vesicles near the cell membrane (yellow dashed circles in Figure 19 and 20) that have most likely been recently formed from an inward budding of the cell membrane indicating the involvement of clathrin-mediated endocytosis, a receptor mediated form of endocytosis as another plausible mechanism of uptake. Interestingly at later time points (Figure 21), the cell membrane returns back to normal with no more observed reshuffling or protrusion and RuS12·AuNP20 is seen localised in vesicles. Both imaging techniques are in agreement with perinuclear localisation of particles. It is worth noting that irrespective of length of exposure, RuS12·AuNP20 is still observed as spherical, monodispersed particles further supporting its stability and reinforcing its lack of aggregation intracellularly.

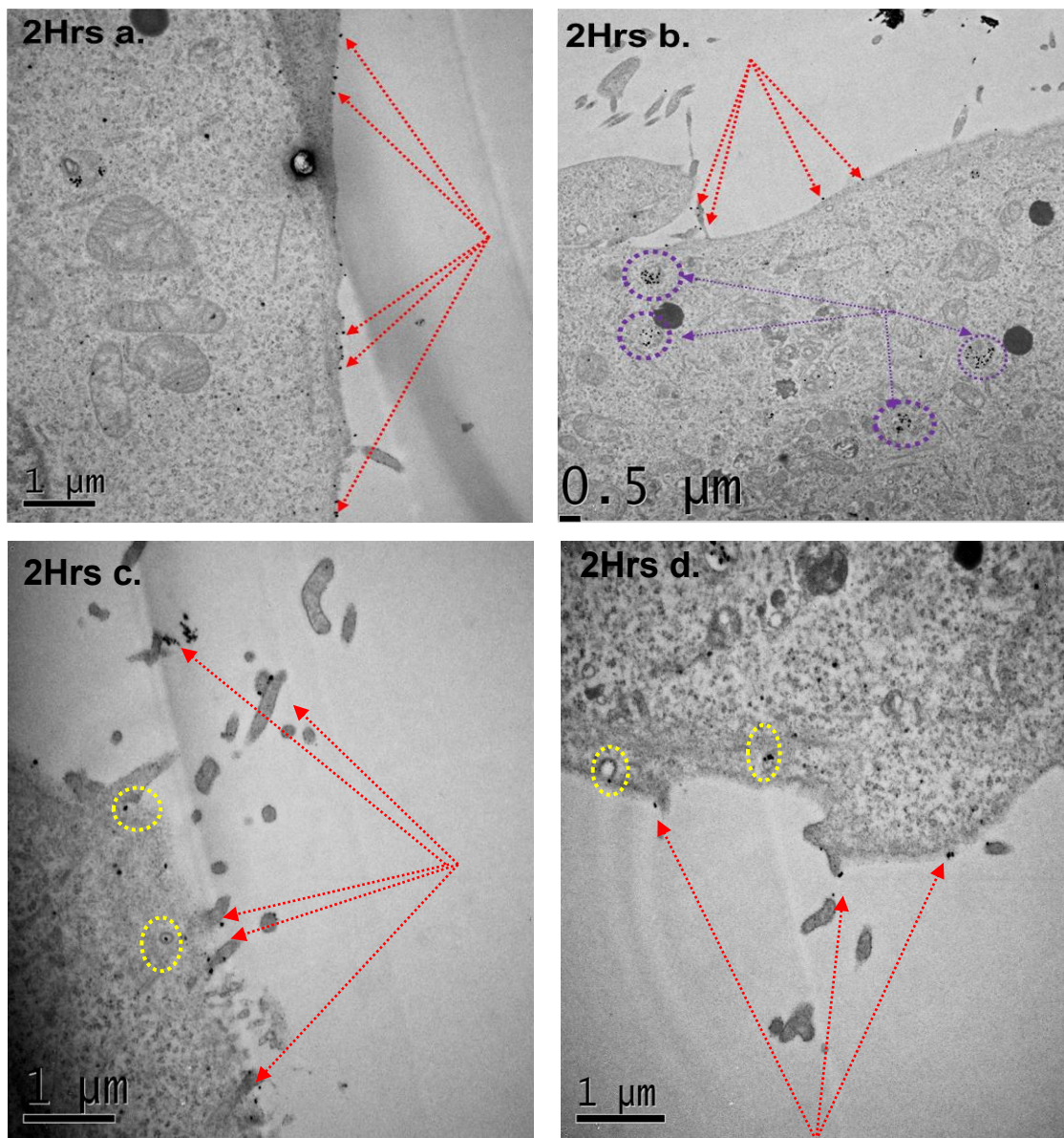


Figure 19: TEM image of A549 cells treated with 0.9 nM RuS12·AuNP20 for 2 hours.

Cells shown are from a single experiment, although the slides were prepared in duplicate. Images in both slides had similar observation but only one slide was shown. **a).** RuS12·AuNP20 localised majorly on the cell membrane (red arrow). **b).** Internalised RuS12·AuNP20 in vesicles (purple arrow). **c).** disruption of cell membrane and RuS12·AuNP20 attached to part of cell membrane and yellow circle shows likely recently formed vesicles from the cell membrane.

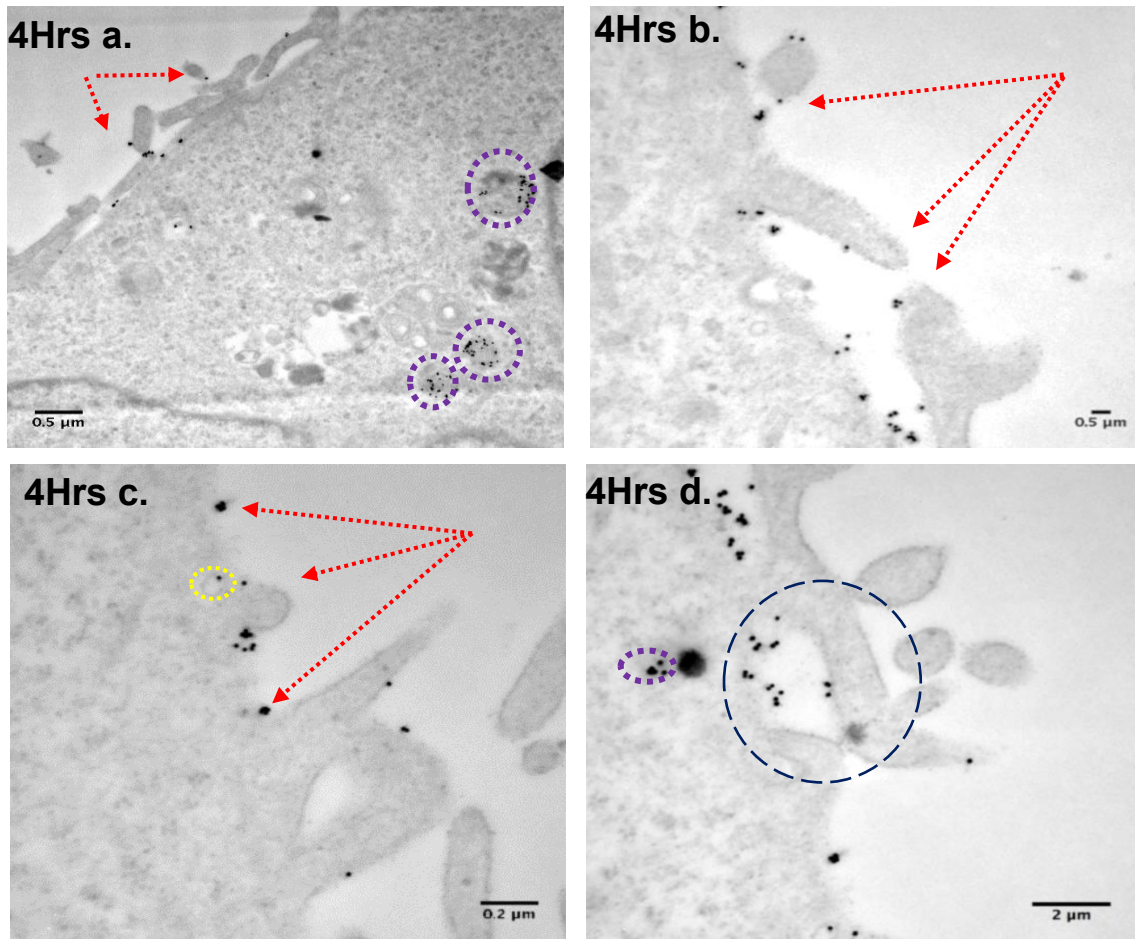


Figure 20: TEM image of A549 cells treated with 0.9 nM RuS12.AuNP20 for 4 hours. Cells shown are from a single experiment, although the slides were prepared in duplicate. Images in both slides had similar observation but only one slide was shown.
a). RuS12.AuNP20 localised majorly on the cell membrane (red arrow) and some internalised in vesicles (purple region). **b and c.** Membrane is protruding and RuS12.AuNP20 is being internalised in vesicles. **d.** the membrane closes up after reshuffling and RuS12.AuNP20 is then

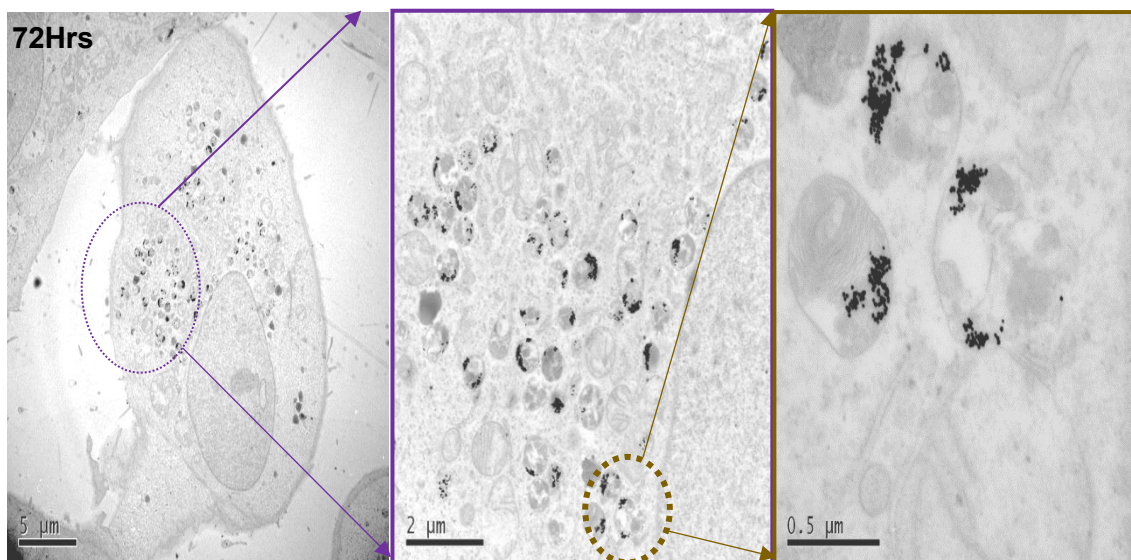


Figure 21: TEM image of A549 cells treated with RuS12.AuNP20 for 72 hours. A zoomed image into a vesicle at 24 hours shows the particles to be nicely spherically mono-dispersed with no evidence of aggregation and at 72 hours, more particles are observed all in vesicles with still no evidence of aggregation or nuclear localisation instead they are localised in perinuclear region.

3.2.2.3. Inductively coupled plasma mass spectrometry (ICP-MS)

To analytically quantify the uptake of RuS12·AuNP20 in A549 cells and compare it with the image quantification method, cells were subjected to same treatment as uptake study by imaging that is the same seeding density, length of exposure and concentration of particles were all similar for both. Cells were digested with freshly prepared aqua regia and concentration of gold taken up by the cells in each sample was measured by ICP-MS.

The ICP-MS result presented in Figure 22 is a graph showing an increase in gold (Au) concentration in a time dependent manner similar to image quantification. The uptake after 32 hours all the way to 72 hours became almost constant while for the image quantification showed no further uptake at about 40 hours all the way to 72 hours. This suggest from both methods of quantification of uptake that the cells begin to become saturated with RuS12·AuNP20 between 32-40 hours. Unfortunately, we found it was technically challenging to measure the concentration of ruthenium complex; the values were low in the samples (shown in appendix 3C2). Previous analysis of elemental composition of RuS12·AuNP20 in our lab reveals the Ru: Au ratio to be 1:180 (Osborne & Pikramenou, 2015) and we attributed this large ratio to a plausible reason for the difficulty in measuring the ruthenium composition in the samples. The results obtained from the ICP-MS analysis was linearly plotted against the counts obtained from the image qualification (Figure 23). This was done because both samples were treated in the same way and because ICP-MS is a well-known quantification method for measuring uptake of AuNP, so the image quantification was validated against it to see if the approach of image quantification is a logical way of quantification. The result of the plot of image quantification vs ICP-MS gave a R^2 value of 0.9285 indicating a high correlation between both techniques. Therefore, image quantification by counts can be used as a method for quantifying uptake of AuNP in cells. From the results (both imaging and ICP-MS) presented the summary of the quantification of

uptake of RuS12·AuNP20 in A549 are: its time dependent and cells are saturated with particles at about 32-40 hours after exposure at 37⁰C incubation.

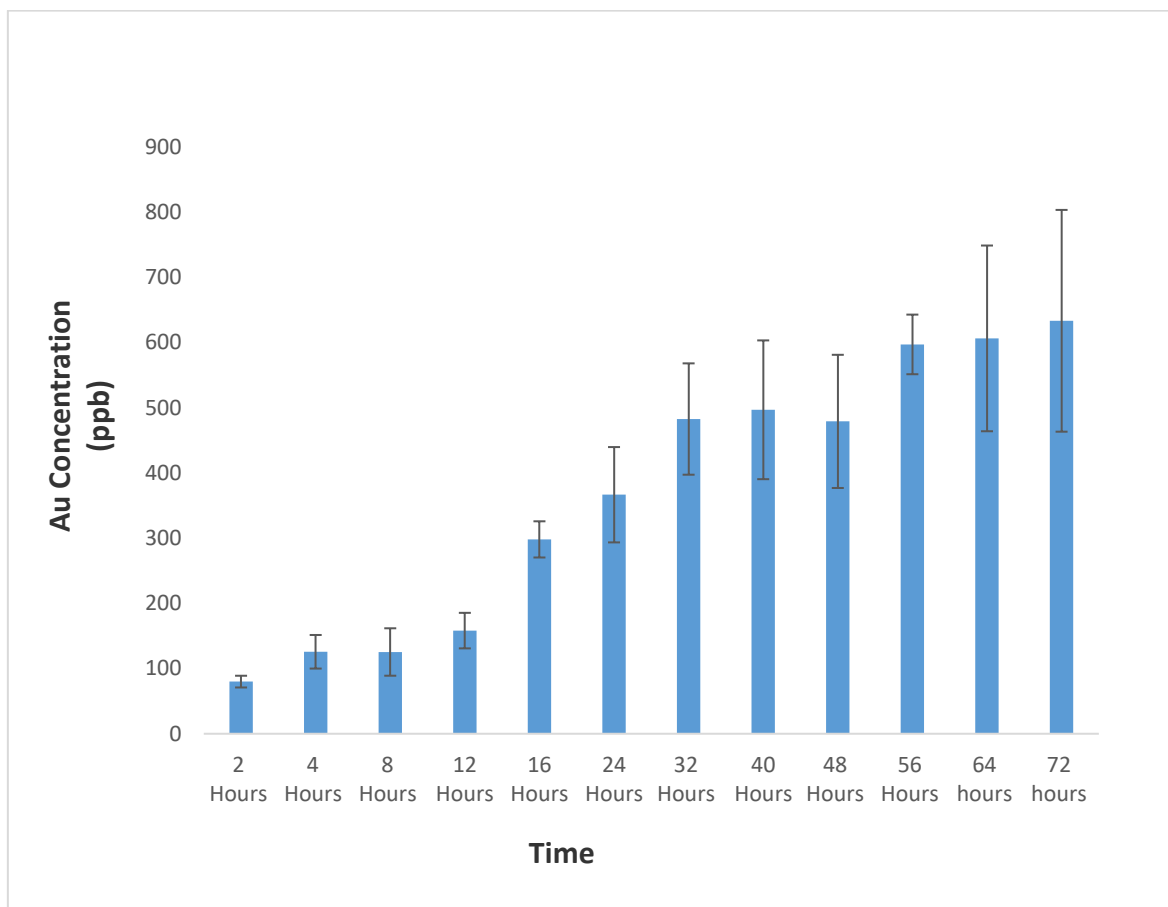


Figure 22: ICP-MS measurement of uptake of 0.9 nM RuS12·AuNP20 in A549 cells

Cells were treated with 0.9 nM RuS12·AuNP20 and at the end of each time points, cells were digested with aqua regia. The digested samples were used for ICP-MS analysis to determine intracellular concentration of gold. Result presented is biological triplicate each having a technical triplicate (n=3), which shows an increase in Au concentration over time.

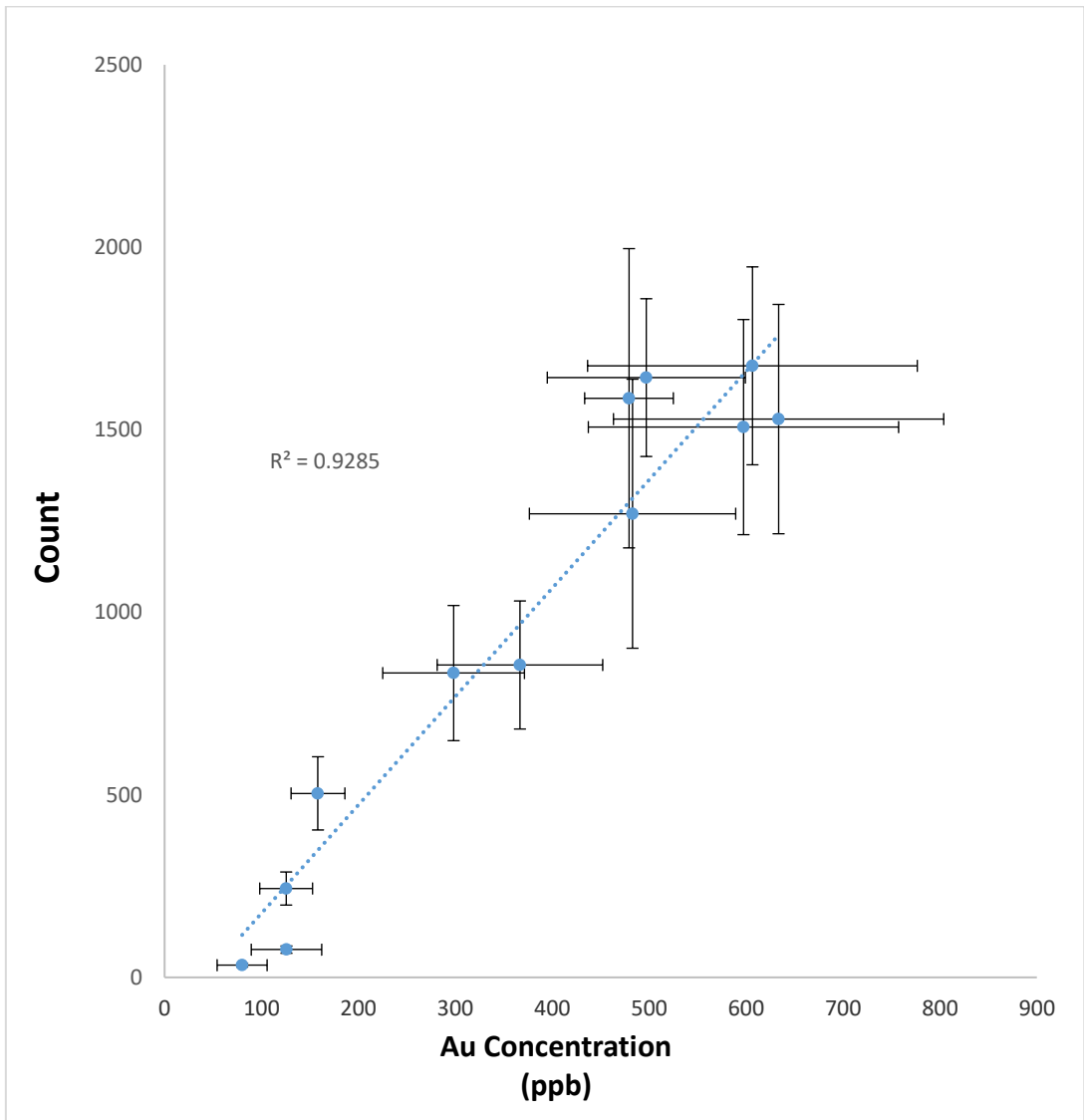


Figure 23: Linear fit of count by microscopy and concentration of Au by ICP-MS.
 Image quantification was done by quantifying the counts from acquired images by confocal microscopy and plotted against the concentration of Au measured. Results are expressed as values from each method with their corresponding standard error of mean.

3.3. Discussion

In biomedical field, the development of luminescent gold nanoprobe as a diagnostic and therapeutic agent is a promising alternative to molecular probes especially as an imaging agent (Panchapakesan *et al.*, 2011). RuS12·AuNP20 has great potential as an ideal nanoprobe, based on the results presented above. The aim of this chapter was to show the characterization profile of RuS12·AuNP20 used in the study and the cellular uptake into A549 cells. Understanding the cellular uptake helps in understanding subsequent cellular process (Alkilany & Murphy, 2010). Different factors affects the cellular uptake of AuNP such as size, shape, surface coatings, aggregation state (Chithrani *et al.*, 2006; Dykman & Khlebtsov, 2012; Kunzmann *et al.*, 2011; Nativo *et al.*, 2008). To avoid too many variances in this study, the characterization of AuNP used for this studied was properly done on each batch to ensure similarities in all batch of nanoparticles used.

The result of the characterization of RuS12·AuNP20 showed the particles to be stable, luminescent with an emission in the red region of visible spectrum, spherical uniformly shaped and size, mono-dispersed about 20 nm in size (confirmed by both sizing technique: DLS and TEM). The characterization data of RuS12·AuNP20 were reproducible making it very suitable for continuous cellular study. Imaging of cells exposed to AuNP is an established way of understanding their cellular uptake (Pernodet *et al.*, 2006). Most confocal images acquired from other studies are used as a qualitative method of assessing cellular uptake (Nativo *et al.*, 2008; Shah *et al.*, 2011; Shukla *et al.*, 2005) while image quantification is mostly done on TEM images since it enables visualization of individual particles as evident in our result and similar studies (Rothen-Rutishauser *et al.*, 2014). The decision to quantify the confocal images was to develop an alternative method to complement another quantification method such as ICP-MS (Chithrani *et al.*, 2006). Similar quantification of acquired confocal images from the cellular uptake study of AuNP using ImageJ to assess

the scattering intensity of AuNP has been performed by Kim *et al.* (2015). Although, their procedure is a bit different from ours because we counted the fluorescence based on RuS12·AuNP20, they created a list of pixel values based on the scattering intensity and set a threshold for collection and analysing five different images per experiment. However, both method shows that cellular uptake can be quantified by image analysis of confocal images. Interestingly, our result for the validation of our method of image quantification obtained by plotting a graph of image quantification vs quantification by ICP-MS gave a R^2 value of 0.92. This is similar to theirs, which was 0.94, and both showed a linear correlation, although the size of their AuNP was smaller (6 nm) than ours, the results were quite similar. Confocal image quantification can therefore be used as an additional method for quantifying cellular uptake. Having quantified and confirmed the cellular uptake of RuS12·AuNP20, establishing the exact mechanism involved is the next step.

Based on the TEM images, most of the internalised RuS12·AuNP20 were observed to be localised in vesicles in a perinuclear fashion (Figure 19, 20 and 21) with no evidence of cytoplasmic localisation suggesting that particles are internalised by endocytosis. This observed result of vesicular localisation is very similar to many previous studies (Brandenberger *et al.*, 2010; Chithrani & Chan, 2007; Nativo *et al.*, 2008; Rothen-Rutishauser *et al.*, 2014; Wang & Petersen, 2013). Endocytosis involves cells engulfing substance for internalization and there are two main types: macropinocytosis and receptor-mediated endocytosis (Conner & Schmid, 2003). Both have been implicated in the mechanism of uptake of AuNP in A549 cells (Brandenberger *et al.*, 2010; Kuhn *et al.*, 2014) and in other cell lines (Gunduz *et al.*, 2017; Ng *et al.*, 2015). Macropinocytosis is involved in the uptake of solute macromolecules with diameter of about 200 nm while smaller particles are internalised by clathrin-mediated endocytosis; the most studied and understood type of receptor-mediated endocytosis (Swanson & Watts, 1995; Xie *et al.*, 2017). To

ascertain the exact type of endocytosis involved, endocytic inhibitors can be used to specifically block these distinct pathways. EIPA inhibits macropinocytosis by blocking Na^+/H^+ exchange located on the membrane and lowering the pH of membrane (Lin *et al.*, 2014; Masereel *et al.*, 2003). While CPZ inhibits clathrin-dependent endocytosis by inhibiting the formation of clathrin coated pits budded from the membrane receptor thereby obstructing endosomal delivery (Wang *et al.*, 1993). Our cytotoxicity result of endocytic inhibitor for both pathways in A549 cells showed pronounced decreased cell viability especially with CPZ compared to EIPA (data in appendix 3D). It has been reported that endocytic inhibitors are capable of inducing cytotoxicity at high concentrations as well as having no effect on inhibiting pathway of interest (dos Santos *et al.*, 2011; Vercauteren *et al.*, 2010). Therefore, their use and conclusion should be reported cautiously. Interestingly, in A549 cells, AuNPs and other metallic ENPs have shown inhibition of either clathrin-mediated and/or macropinocytosis endocytosis using CPZ and/or EIPA without affecting cell viability (dos Santos *et al.*, 2011; Kuhn *et al.*, 2014; Rothen-Rutishauser *et al.*, 2014; Wang *et al.*, 2011). The inability to conclude using endocytic inhibitors to ascertain the type of endocytosis involved in RuS12·AuNP20 cellular uptake in A549 leaves us to qualitatively analyse the TEM images to propose the mechanism of uptake.

The TEM images (Figure 19 and 20) is suggesting that the most prominent form of endocytosis occurring is macropinocytosis. This is evident at early time points of 2 and 4 hours by the membrane ruffling and folding back onto into itself after the uptake of RuS12·AuNP20. The schematic in Figure 24 shows the pathway of macropinocytosis, which is very similar to what we observed in terms of protrusion, and ruffling of membrane. Similar TEM observation of plasma membrane protrusion and distortion on exposure to AuNP has been observed in other cell lines (Chithrani & Chan, 2007; Jiang *et al.*, 2008; Mustafa *et al.*, 2011) as well as in A549 cell line (Rothen-Rutishauser *et al.*, 2014).

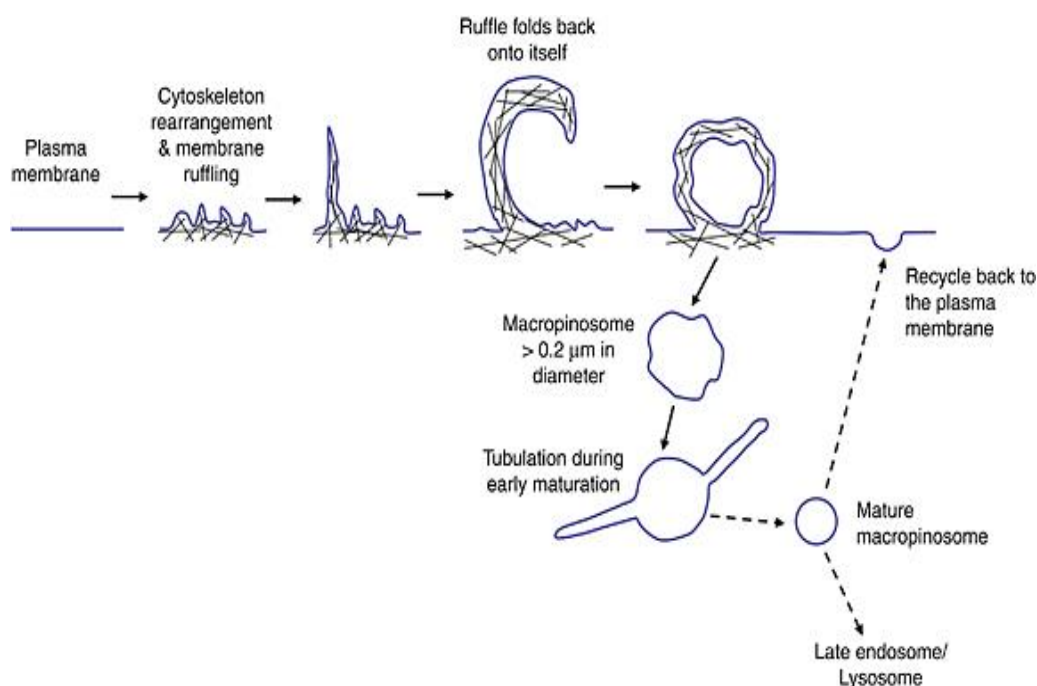


Figure 24: Pathway of macropinocytosis

Macropinocytosis involves the re-arrangement of plasma membrane to form ruffles that later re-joins to the plasma membrane by fusion and form a macropinosomes. The maturation process of macropinosomes involves extensive tubulation before forming a spherical mature macropinosomes. The content of the macropinosomes is usually trafficked to the lysosomes or sometimes recycled back to the plasma membrane. The black line represents the involvement of the cytoskeleton. Image was adapted from (Lim & Gleeson, 2011).

Interestingly, macropinocytosis is known to be associated with uptake of large molecule of about 200 nm but our TEM evidence suggests that the cellular uptake of 20 nm RuS12·AuNP20 is probably by macropinocytosis. This observation can be attributed to the fact that during the cellular uptake of particles, they do not get internalised as individual particles but as clusters accumulated on the membrane, similar observation of cellular uptake by membrane ruffling of clustered AuNPs has been observed (Yang *et al.*, 2013). They explained that clustered AuNPs on the membrane achieves a density that triggers cellular uptake and stated that both clathrin-mediated endocytosis and macropinocytosis were involved in the uptake of AuNPs cluster based on their result of endocytic inhibitors used.

It is likely that both types of endocytosis are involved in the cellular uptake of RuS12·AuNP20 as small invagination of plasma membrane (Figure 19d) synonymous with

clathrin-mediated endocytosis were also observed. A number of studies have also shown the cellular uptake of 12-25 nm AuNP to be by clathrin-dependent endocytosis (Ng *et al.*, 2015; Rattanapinyopituk *et al.*, 2014). Using 15 nm citrate capped AuNP the cellular uptake in A549 cells showed both macropinocytosis and clathrin-mediated endocytosis to be involved (Brandenberger *et al.*, 2010), this study is similar to ours in terms of size and cell line use. Therefore, this supports our observation of the involvement of both types of endocytosis in the cellular uptake of RuS12·AuNP20 in A549 cells.

In conclusion, we have demonstrated the cellular uptake of 20 nm RuS12·AuNP20 in A549 cells using various techniques and have been able to quantify the uptake, which was proven to increase in a time dependent manner and solely localised in vesicles indicating endocytosis as a route of uptake. In addition, we postulate the uptake mechanism to involve both macropinocytosis and clathrin-mediated endocytosis with strong evidence. The trafficking of RuS12·AuNP20 to identify vesicles and cellular fate is discussed in next chapter.

Chapter 4

Localisation and Cellular Fate of RuS12·AuNP20 in A549 cells

4.1 Introduction

The surface modification of engineered nanoparticles with fluorescence compounds such as transition metal complex can result in fluorescent nanoprobes. These nanoprobes have advantages in fluorescence imaging over conventional fluorescent probes such as such as rhodamine, fluorescein, and cyanine (Comby *et al.*, 2014; Zhang *et al.*, 2016)The surface modification of the AuNP used in this research with transition metal complex enables it to function as a nanoprobe in fluorescence imaging. For this function and other biomedical applications to be fully utilised, understanding the localisation and cellular fate in respect to its uptake is crucial. Already established from chapter 3, endocytosis specifically macropinocytosis and clathrin-mediated endocytosis is the most likely means of internalisation of RuS12·AuNP20 into A549 cells. Most of the internalised nanoparticles were localised in vesicles evident from TEM imaging in previous chapter (chapter 3). Therefore, it is logical to study co-localisation of RuS12·AuNP20 within organelles involved in the endocytic pathway as a means of identifying the intracellular fate of RuS12·AuNP20 in more details.

In-vitro localisation of AuNP is usually studied majorly by imaging: either fluorescence imaging using confocal microscopy or TEM. In addition, imaging gives an understanding of AuNP trafficking within the cell. To study the localisation of RuS12·AuNP20 by confocal microscopy, the luminescent properties of the RuS12·AuNP20 were utilised in combination with organelle specific stain or transfection of cells with fluorescent-tagged specific organelle markers. The emission wavelength of RuS12·AuNP20 is distinctive from the emission wavelength of fluorescent organelle markers therefore, for co-localisation to occur there must be a fluorescence overlap between the nanoparticle signal and the fluorescent organelle. The degree of overlap was measured by Pearson correlation coefficient (PCC). PCC has a range of +1 (perfect correlation) to -1 (perfect negative correlation) and 0 which

means no correlation (Adler & Parmryd, 2010). Details of the method used to calculate PCC is shown in the appendix 4G. TEM imaging supplemented the confocal imaging by identifying the specific organelles via their structure, which is a major limit in confocal imaging.

The ultimate aim of studying localisation is to follow the RuS12·AuNP20 in cells overtime and hence decipher their cellular fate. Further evaluation of their cellular fate involved studying, protein and gene changes in pathways implicated in their uptake and trafficking as well as their response. These responses, were studied using western blotting and RT-PCR. Western blotting is the most used technique for the identification of specific proteins while RT-PCR is a sensitive technique for quantifying gene expression.

All study was done with a concentration of 0.9 nM of RuS12·AuNP20. Localisation and cellular fate were studied on A549 cells treated with RuS12·AuNP20 between 4-72 hours, a mixture of transiently transfected A549 cells and A549 cells stained with specific organelle stains were used as model for fluorescent organelles. This chapter aims to understand the localisation of RuS12·AuNP20 in A549 by imaging and ultimately their cellular fate by western blotting and real time PCR.

4.2 Results

4.2.1. Co-localisation by Confocal Imaging

The result of co-localisation study presented using confocal imaging involved either fluorescent organelle stains or A549 cells that have been transiently transfected with tagged fluorescent markers to label the organelle of interest. All organelles studied were GFP tagged therefore they showed green fluorescence, while RuS12·AuNP20 has a red fluorescence. Co-localisation of RuS12·AuNP20 within an organelle is observed when there is an overlap of the green and red signal to produce a yellow signal. Also PCC number(measure of co-localisation) for at least 3 images for each time points was generated using an ImageJ plugin (Bolte & Cordelieres, 2006). All images presented are a representative of selected time point showing the individual red channel (nanoparticle luminescence), green channel (GFP-organelles), blue channel (Hoechst nuclear stain) and the merged channel. In some cases, the reflection channel is also shown to give an outline of the whole cell and show RuS12·AuNP20 internalisation within the cell. Control images are also shown. All scale bars are 20 μm , unless otherwise stated; refer to section 2.3.1 for microscope setting.

4.2.1.1. Golgi Apparatus

The images shown in Figure 25 are a representative of control cells without any particles but stained with Golgi ID dye, which is a dual detection dye that stains both nucleus and the golgi. Control A is the fluorescence channel showing the golgi organelle (green) and the nucleus (blue). Control B is the equivalent reflection images of A which shows the outline of the cells, in the absence of any nanoparticles.

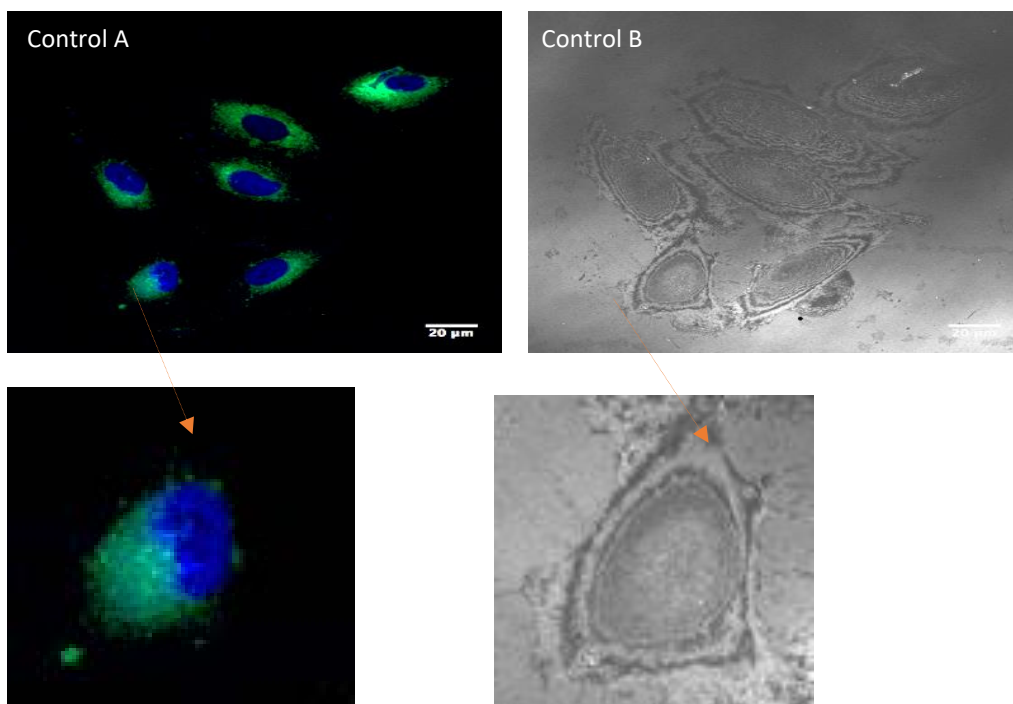


Figure 25: Representative image of fixed A549 control cells stained with Golgi ID

A. Merged image of green (GFP emission λ_{exc} = 488 nm, λ_{em} = 502 nm) and blue channel (Hoechst λ_{exc} = 405 nm, λ_{em} = 410-455 nm).

B. Corresponding Reflection image (λ_{exc} = 488 nm, λ_{em} = 478 -498 nm)
Zoomed images below emphasizing on just a cell.

When A549 cells are treated with RuS12·AuNP20 from 4 -24 hours, no co-localisation was observed with the golgi. The image in Figure 26 is a representative image of A549 cells treated with RuS12·AuNP20 for 24 hours to study the co-localisation within the golgi. As evident from the reflection and fluorescence images, the particles are clearly internalised and localised around the nucleus. The fluorescence images shows the particles to have no co-localisation with the golgi (green), this is evident in the merged picture (24 hrs M). This image is very similar across time points from 4 -24 hours (shown in appendix 4A) for A549 cells stained with Golgi-ID, therefore it can be concluded that in A549 cells over a period of 24 hours, RuS12·AuNP20 does not co-localise with the golgi as evident from confocal microscopy and PCC value of 0.2.

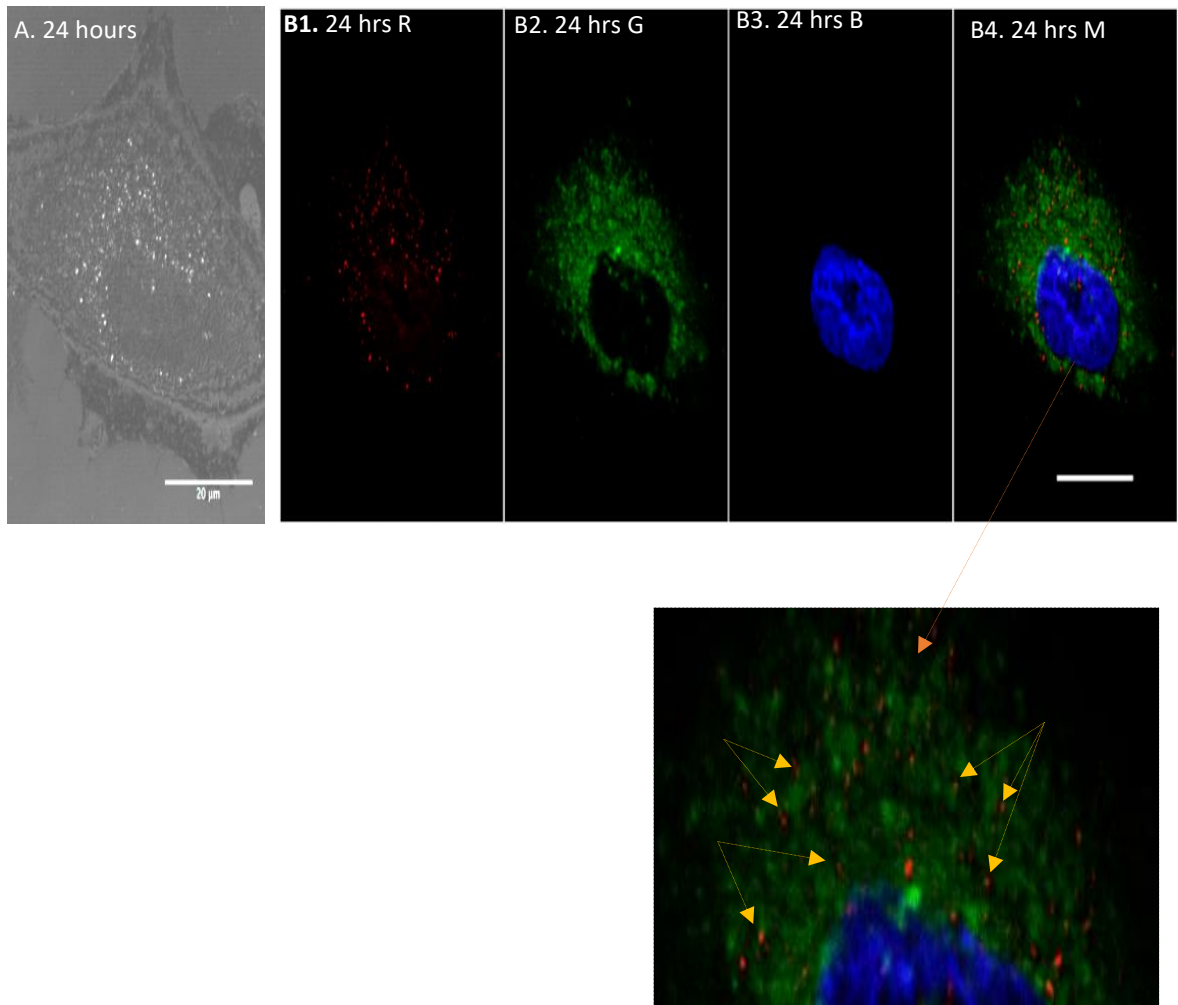


Figure 26 Representative image of fixed A549 treated with 0.9nM RuS12-AuNP20 for 24 hours and stained with Golgi ID

The image shown is a representative image of A549 cells treated with 0.9nM RuS12-AuNP20 for 24 hours. This experiment was done as a biological duplicate and images were all similar, showing no co-localisation.

A. Reflection image ($\lambda_{exc} = 488 \text{ nm}$, $\lambda_{em} = 478 - 498 \text{ nm}$)

B1. RuS12-AuNP20 emission from red channel ($\lambda_{exc} = 488 \text{ nm}$, $\lambda_{em} = 620 - 800 \text{ nm}$).

B2. GFP emission from green channel ($\lambda_{exc} = 488 \text{ nm}$, $\lambda_{em} = 502 \text{ nm}$)

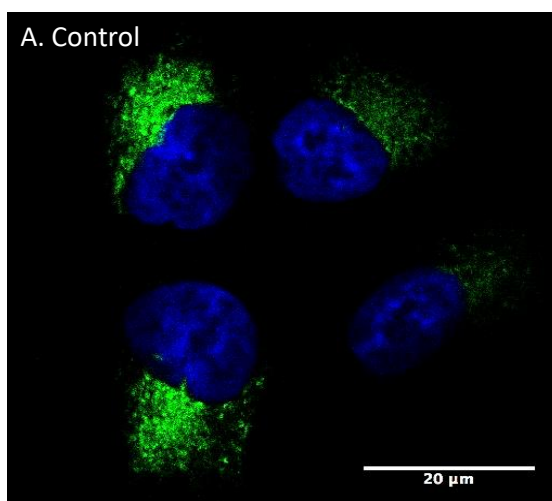
B3. Hoechst emission from the blue channel ($\lambda_{exc} = 405 \text{ nm}$, $\lambda_{em} = 410 - 455 \text{ nm}$)

B4. Merged image of red, green and blue channel.

Zoomed images showing localisation of particles in spaces between green channel (yellow arrow).

4.2.1.2. Mitochondria

The images shown in Figure 27 is a representative image of the study of co-localisation of RuS12·AuNP20 with the mitochondria. The mitochondria were stained with MitoGreen and the nucleus with Hoechst. Image A of Figure 27 is the control image of just A549 cells showing the mitochondria (green) and the nucleus (blue). A representative image of 24 hours treatment with RuS12·AuNP20 is shown in Figure 27 B-C4; the reflective image shows the outline of the cells and the internalised particles. The fluorescence images (Figure 27 R, G, B and M) show the particles, mitochondria, nucleus and the merged images respectively. Similar observed with the golgi, the particles do not show any co-localisation within the mitochondria evident from images and PCC value of 0.3. The particles appear to be located in spaces in between the mitochondria, evident from the yellow arrow. This observation was similar across all time points studied (4-24 hours shown in appendix 4B). Therefore, RuS12·AuNP20 does not co-localise with the mitochondria.



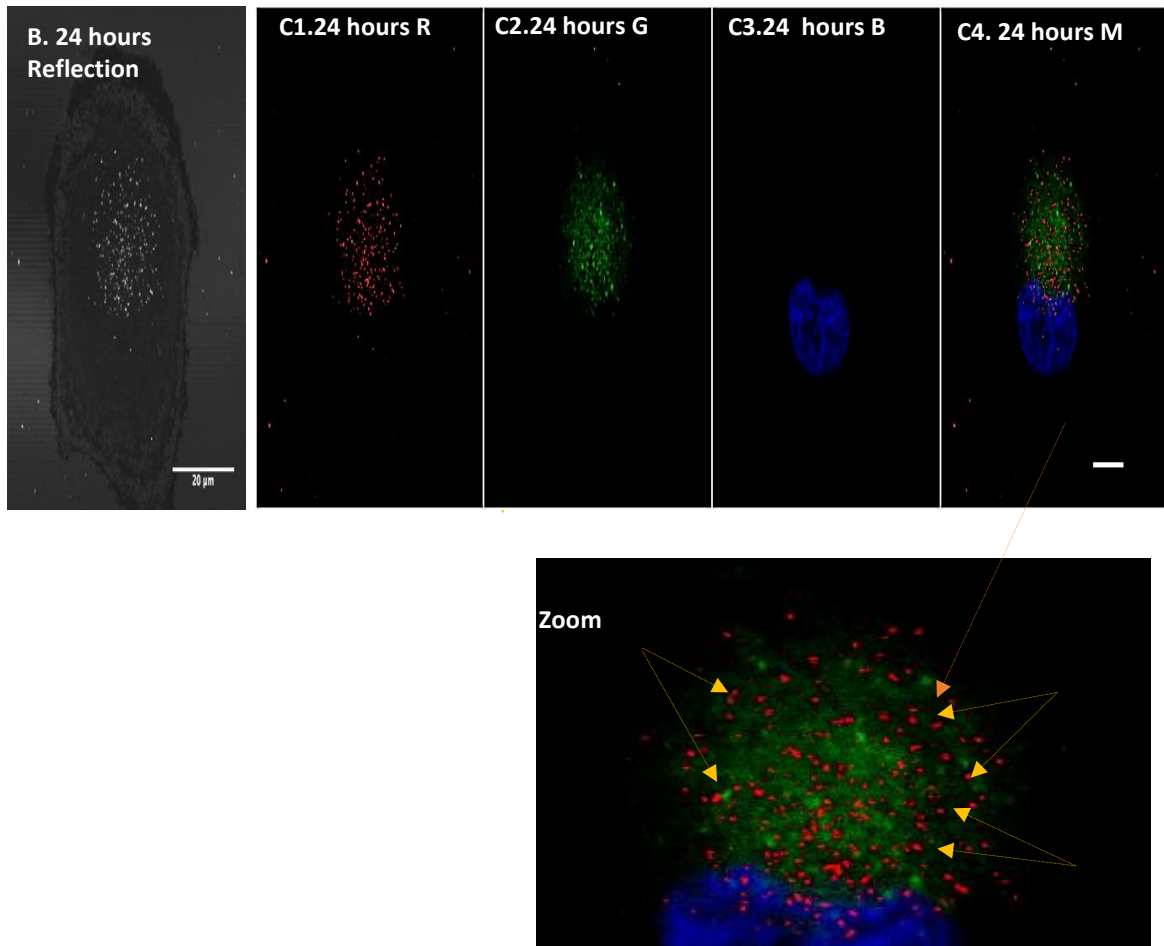


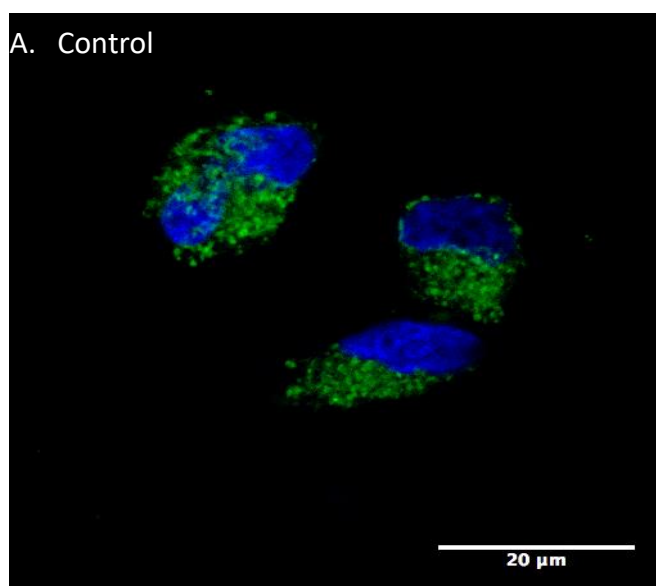
Figure 27: Representative image of fixed A549 treated with 0.9nM RuS12·AuNP20 for 24 hours and stained with MitoGreen

The image shown is a representative image of A549 cells treated with 0.9nM RuS12·AuNP20 for 24 hours. This experiment was done as a biological duplicate and images were all similar, showing no co-localisation.

- A. Control image of merged green and blue channel.
- B. Reflection image showing A549 cells treated with RuS12·AuNP20 for 24 hours. ($\lambda_{exc} = 488 \text{ nm}$, $\lambda_{em} = 478 - 498 \text{ nm}$)
- C. Corresponding fluorescence imaging of B.
 - C1. RuS12·AuNP20 emission form red channel ($\lambda_{exc} = 488 \text{ nm}$, $\lambda_{em} = 620 - 800 \text{ nm}$).
 - C2. GFP emission form green channel ($\lambda_{exc} = 488 \text{ nm}$, $\lambda_{em} = 502 \text{ nm}$)
 - C3. Hoechst emission form the blue channel ($\lambda_{exc} = 405 \text{ nm}$, $\lambda_{em} = 410 - 455 \text{ nm}$)
 - C4. Merged image of red, green and blue channel.
- Zoomed images showing localisation of particles in spaces between green channel (yellow

4.2.2.3. Endoplasmic reticulum

The images shown in Figure 28 is a representative image of the study of co-localisation of RuS12·AuNP20 with the endoplasmic reticulum (ER). The ER was stained with ER-tracker Green and the nucleus with Hoechst. Image A is the control image of just A549 cells showing the ER (green) and the nucleus (blue). A representative image of 24 hours treatment with RuS12·AuNP20 is shown in Figure 24 B-C4; the reflective image shows the outline of the cells and the internalised particles around the nucleus. The fluorescence images (Figure 28 C1-C4) shows the particles, ER, nucleus and the merged images respectively. As observed in previous images with organelle stains (mitochondria and golgi), the particles do not show any co-localisation with the ER evident from images and PCC value of 0.1. The particles appear to be located in spaces in between the ER similar to the mitochondria. This observation was very similar across all time points studied (shown in the appendix 4C). Therefore, RuS12·AuNP20 does not co-localise with the ER.



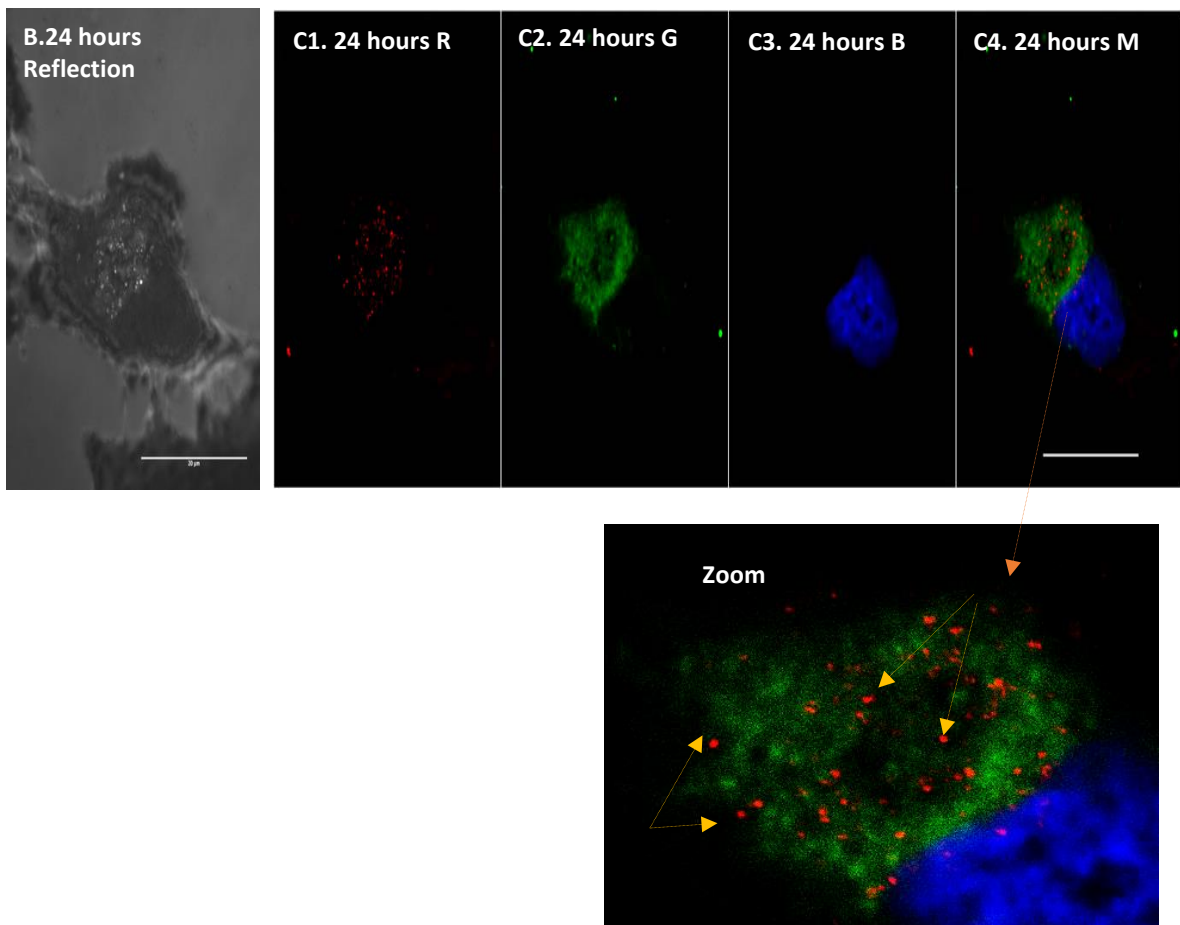


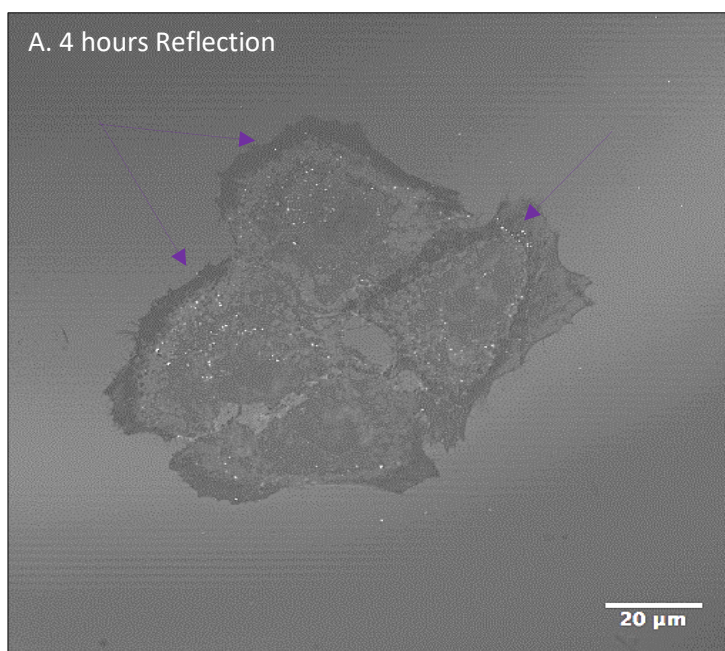
Figure 28: Representative image of fixed A549 treated with 0.9 nM RuS12·AuNP20 for 24 hours and stained with ER-tracker green.

The image shown is a representative image of A549 cells treated with 0.9nM RuS12·AuNP20 for 24 hours. This experiment was done as a biological duplicate and images were all similar, showing no co-localisation.

- A. Control image of merged green and blue channel.
 - B. Reflection image showing A549 cells treated with RuS12·AuNP20 for 24 hours ($\lambda_{exc} = 488 \text{ nm}$, $\lambda_{em} = 478 - 498 \text{ nm}$).
 - C. Corresponding fluorescence imaging of B.
 - C1. RuS12·AuNP20 emission form red channel ($\lambda_{exc} = 488 \text{ nm}$, $\lambda_{em} = 620-800 \text{ nm}$).
 - C2. GFP emission form green channel ($\lambda_{exc} = 488 \text{ nm}$, $\lambda_{em} = 502 \text{ nm}$)
 - C3. Hoechst emission form the blue channel ($\lambda_{exc} = 405 \text{ nm}$, $\lambda_{em} = 410-455 \text{ nm}$)
 - C4. Merged image of red, green and blue channel.
- Zoomed images showing localisation of particles in spaces between green channel (yellow arrow)

4.2.2.4. RAB4: Early endosomes

The images presented in Figure 29 are representative images of co-localisation of RuS12·AuNP20 with A549 cells transiently transfected with GFP-RAB4. RAB4 is an organelle marker for early endosome, an organelle that participates in endocytosis of AuNP. The co-localisation was studied over a period of (4-24 hours, images in appendix 4D). Interestingly, co-localisation was observed only at 4 and 8 hours close to be cell membrane (purple arrow) although they had low PCC values of 0.1 and 0.3 at 4 and 8 hours respectively. A likely reason for the low PCC despite evidence of correlation is as a result of the software designed to calculate the PCC values, which calculates the whole images and not specific location. No co-localisation was observed with later time points. Therefore, RuS12·AuNP20 is co-localised in the early endosomes at early time points (4 and 8 hours).



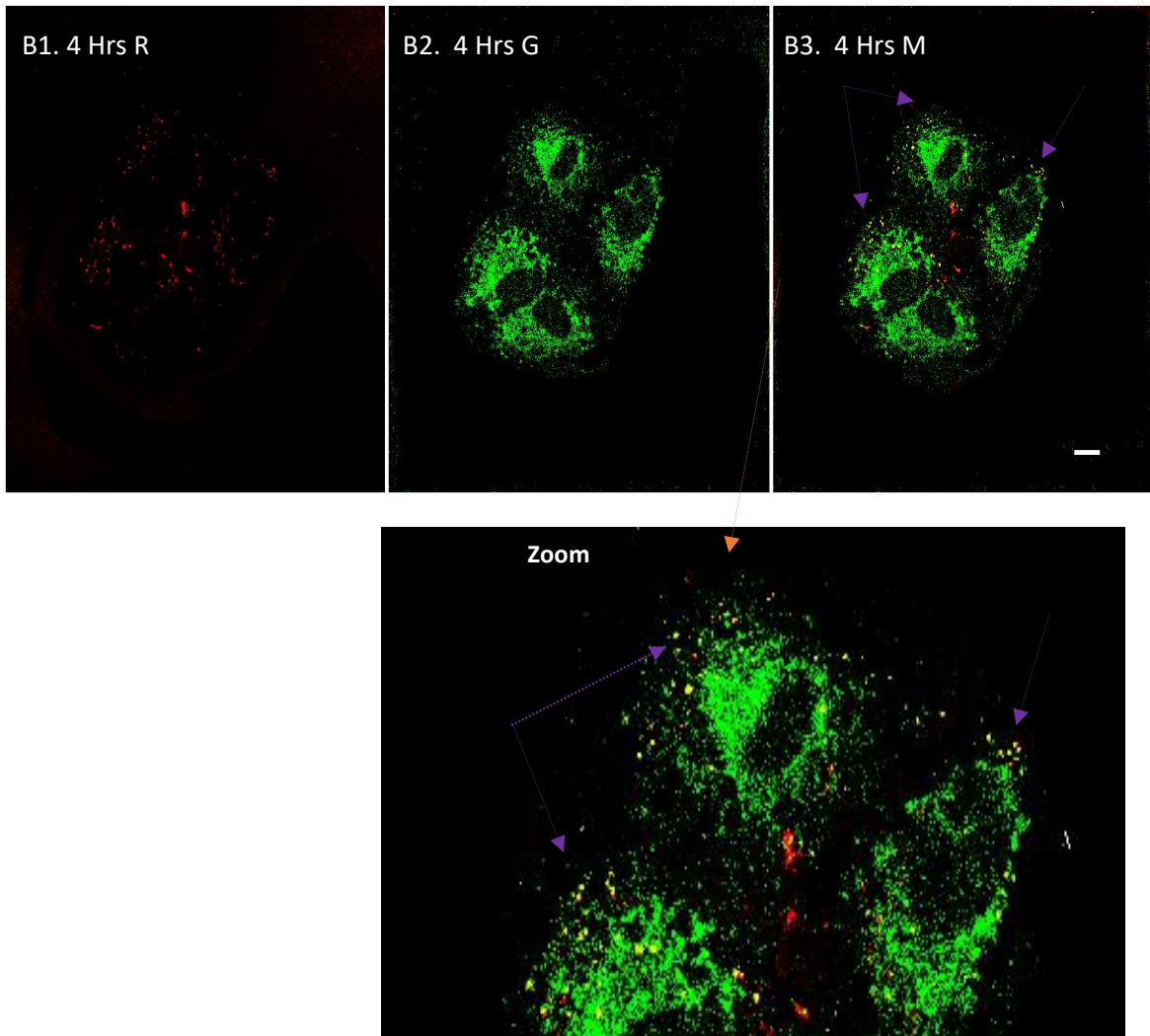


Figure 29: Representative image of fixed A549 transiently transfected with GFP-RAB4.

The image shown is a representative image of A549 cells treated with 0.9 nM RuS12·AuNP20 for 4 hours after 48 hours transfection with GFP-RAB4. This experiment was done as a biological duplicate and images were all similar within time points.

Reflection image showing A549 cells treated with RuS12·AuNP20 for 4 hours ($\lambda_{exc} = 488 \text{ nm}$, $\lambda_{em} = 478 - 498 \text{ nm}$).

Corresponding fluorescence imaging of A.

B1. RuS12·AuNP20 emission form red channel ($\lambda_{exc} = 488 \text{ nm}$, $\lambda_{em} = 620 - 800 \text{ nm}$).

B2. GFP emission form green channel ($\lambda_{exc} = 488 \text{ nm}$, $\lambda_{em} = 502 \text{ nm}$).

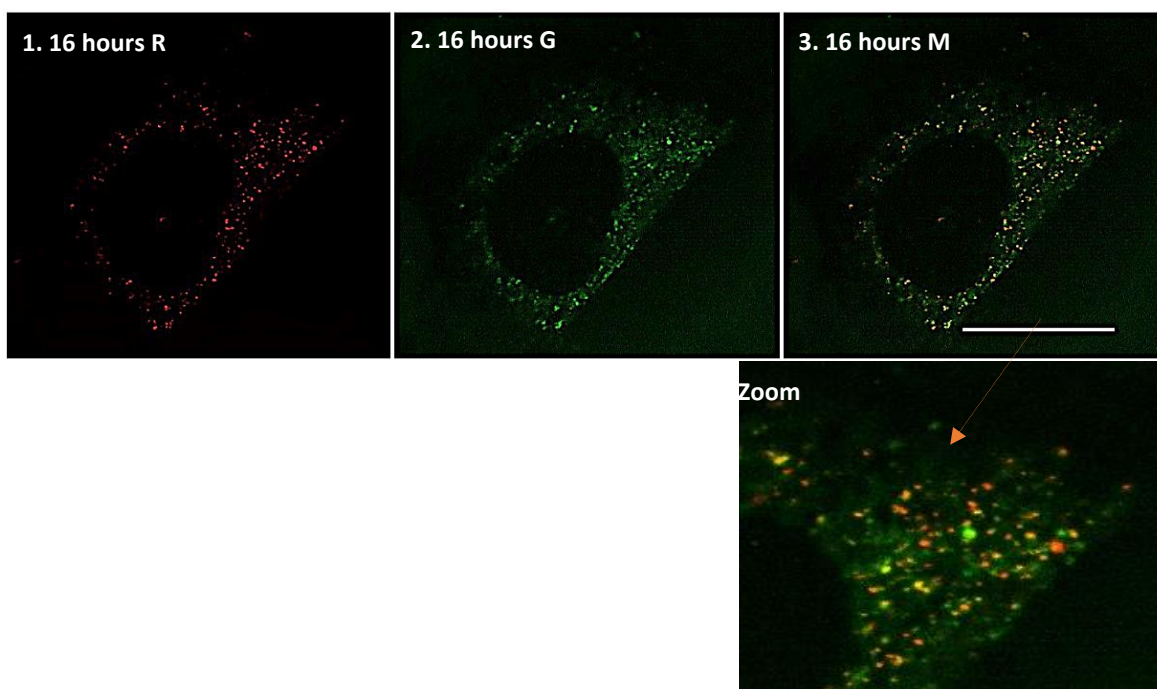
B3. Merged image of red and green channel.

Zoomed images showing co-localisation of particles with GFP-RAB4 majorly on the membrane (purple arrow)

4.2.2.5. LAMP1: Lysosomes

The images presented in Figure 30 are representative images of co-localisation of RuS12·AuNP20 with A549 cells transiently transfected with GFP-LAMP1, an organelle marker for lysosome. The co-localisation was studied over a period of (4-72 hours). Co-localisation (zoomed images) was observed to increase over time from 16 hours to 72 hours (other time points shown in appendix 4E) Therefore, RuS12·AuNP20 co-localises with the lysosomes, which increases in a time dependent manner and the PCC values also increased from 0.4 in Figure 31 b3 (16 hours) to 0.5 in Figure 31 c3 (48 hours).

A.



B.

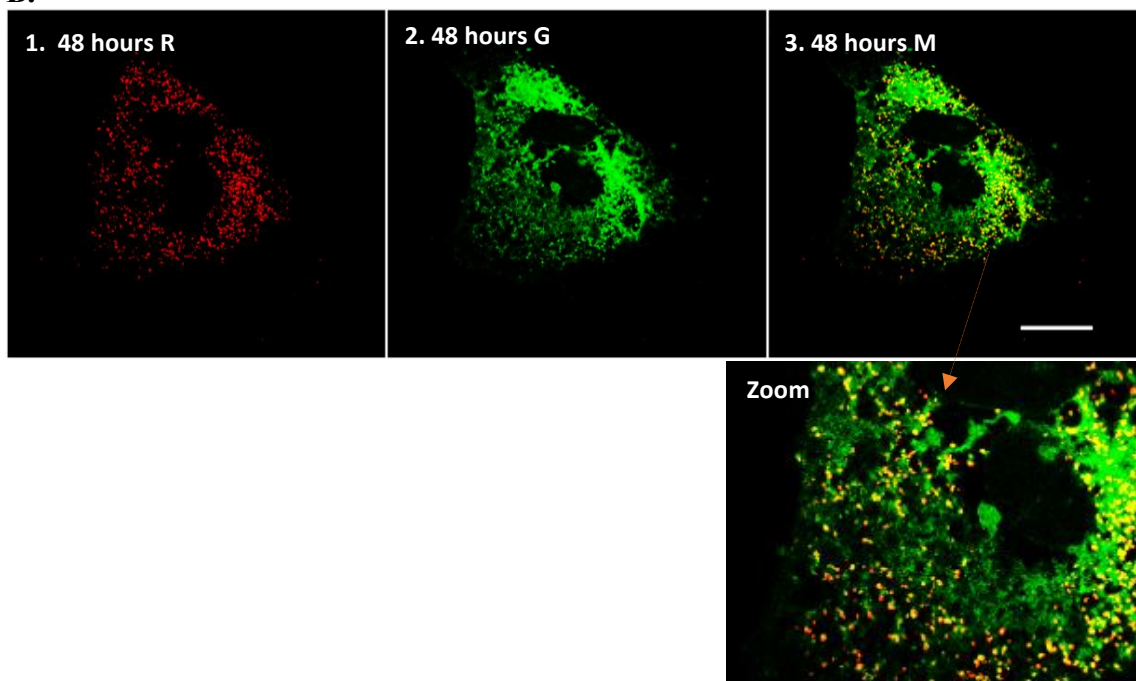


Figure 30: Representative image of fixed A549 transiently transfected with GFP- LAMP1.

The image shown is a representative image of A549 cells treated with 0.9 nM RuS12·AuNP20 for 16 and 48 hours after 48 hours transfection with GFP-LAMP1. This experiment was done as a biological duplicate and images were all similar within time points.

A. Fluorescence imaging of A549 cells treated with RuS12·AuNP20 for 16 hours.

B. Fluorescence imaging of A549 cells treated with RuS12·AuNP20 for 48 hours.

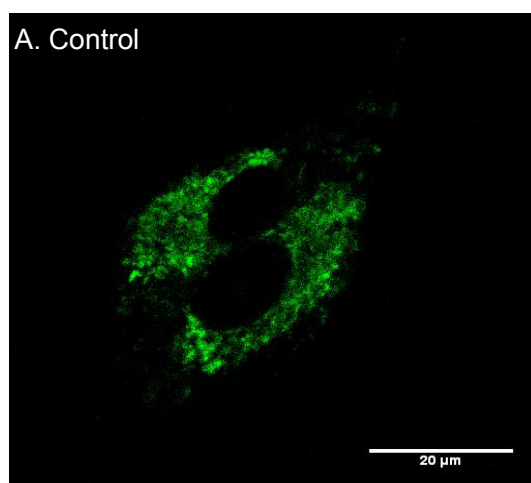
1. RuS12·AuNP20 emission form red channel (λ_{exc} = 488 nm, λ_{em} = 620-800 nm).

2. GFP emission form green channel (λ_{exc} = 488 nm, λ_{em} = 502 nm).

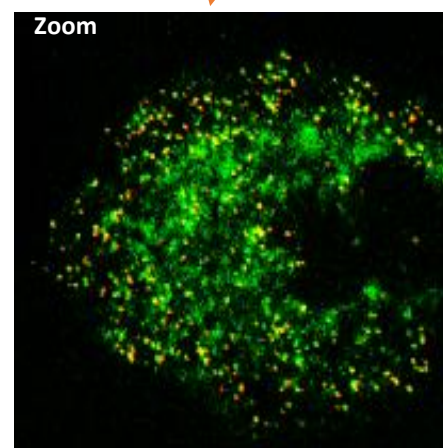
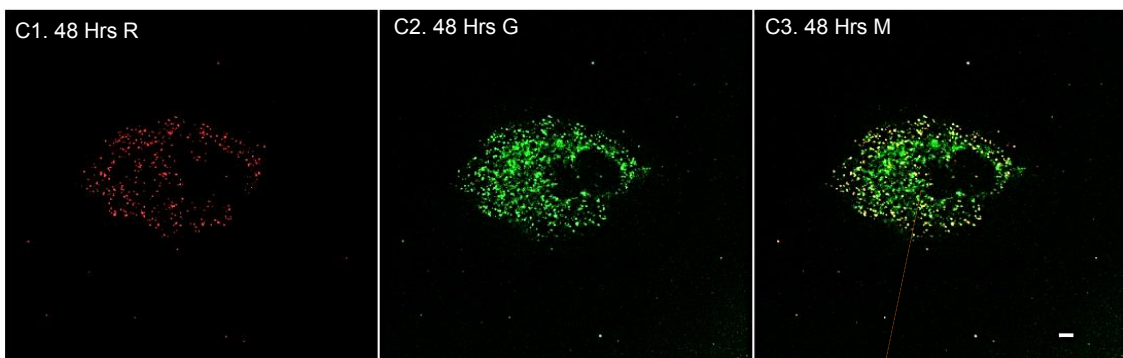
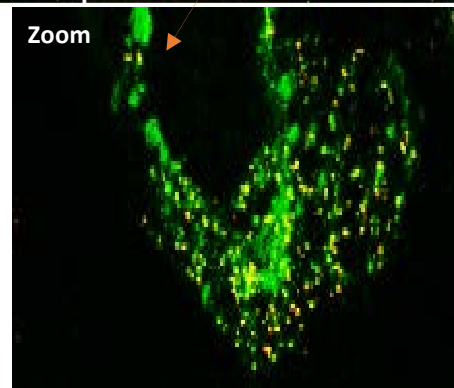
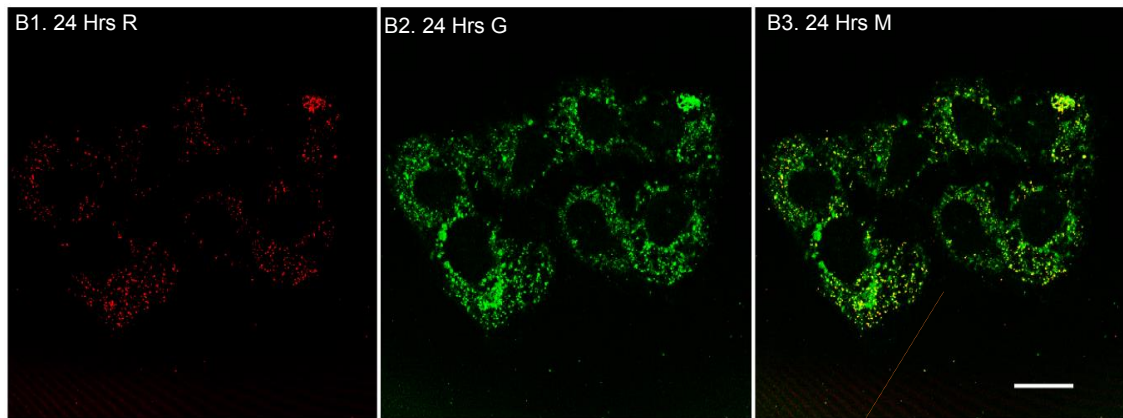
3. Merged image of red and green channel showing co-localisation more evident in zoomed images.

4.2.2.6. LC3: Autophagosome

Autophagosome is an organelle that is highly inducible during various conditions such as cellular stress and is believed to be assembled *de novo* in the cytosol when needed (Mizushima, 2007). Autophagosome was chosen as one of the organelles to study for co-localisation with RuS12·AuNP20 because it is involved in endocytic trafficking and plays a role in lysosomal degradation. A549 cells were transiently transfected with GFP-LC3 a marker for autophagosome. The image in Figure 31A shows a representative image of control cells that has been transfected and not treated with any particle. A diffuse GFP-LC3 staining is observed indicating the absence of active autophagosomes but on exposure to RuS12·AuNP20, a change in staining pattern is observed in time dependent manner. From 24 hours to 72 hours, the staining pattern changed from diffuse to become more punctuate indicating the formation of autophagosomes vesicles. A clear co-localisation (yellow signal) evident from the merged images and zoomed images is observed which increases in a time dependent manner similar to that observed in lysosome. The PCC values of images shown in Figure 31B-D are 0.6, 0.8 and 0.8, which corresponds to 24, 48 and 72 hours respectively. Both the images and the PCC show a time dependent increase of co-localisation in the autophagosomes. With these results, RuS12·AuNP20 is involved in the induction of autophagosomes in a time dependent manner.



LC3: Autophagosome



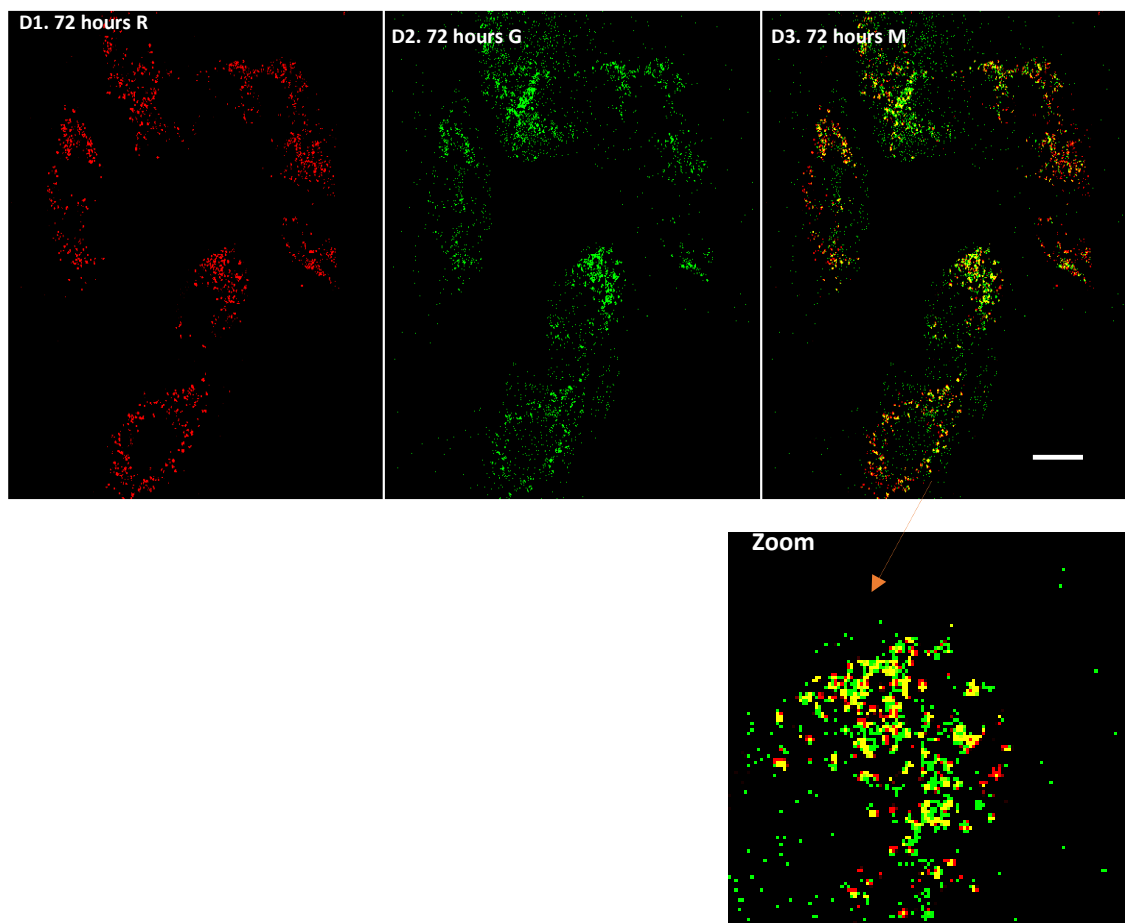


Figure 31: Representative image of fixed A549 transiently transfected with GFP-LC3.

The image shown is a representative image of A549 cells treated with 0.9 nM RuS12-AuNP20 for 24, 48 and 72 hours after 48 hours transfection with GFP-LC3. This experiment was done as a biological duplicate and images were all similar within time points.

A. Control cell: transiently transfected A549 cells with GFP-LC3.

B-D. Fluorescence imaging of A549 cells treated with RuS12.AuNP20 for 24, 48 and 72 hours.

1. RuS12.AuNP20 emission from red channel ($\lambda_{exc} = 488 \text{ nm}$, $\lambda_{em} = 620\text{-}800 \text{ nm}$).

2. GFP emission from green channel ($\lambda_{exc} = 488 \text{ nm}$, $\lambda_{em} = 502 \text{ nm}$).

3. Merged image of red and green channel showing co-localisation more evident in zoomed images. Yellow signal indicates co-localisation of RuS12-AuNP20 with autophagosomes, which increases over time.

4.2.2.7. Summary of the co-localisation by confocal imaging based on Pearson's Coefficient of Correlation.

All fluorescence images acquired by confocal microscopy were analysed to determine their PCC values as a quantitative measure of co-localisation by measuring the correlation between the red (RuS12·AuNP20) and green (GFP) signals. The graph in Figure 32 shows the summary of the analysis of all 6-organelles studied between 4-24 hours. For each time point and organelle, a minimum of three independent images were used for analysis (three random images per slide and each slide represents a time point and a specific organelle). Time points later than 24 hours were not included in this analysis because only two organelles were studied at later time points of 24 hours.

PCC values typical ranges from 0-1, the closer the value is to one, the higher the correlation, hence the greater the co-localisation with the organelle. Based on the fluorescence images above, co-localisation was only observed with the lysosomes (GFP-LAMP1) and autophagosomes (GFP-LC3) in a time dependent manner. This time dependent increase is also observed with the LAMP1 and LC3 in the graph, which shows LC3 having the greatest correlation value of 0.7 at 24 hours. The summary based on the confocal imaging is RuS12·AuNP20 co-localises with the lysosomes and autophagosomes in a time dependent manner.

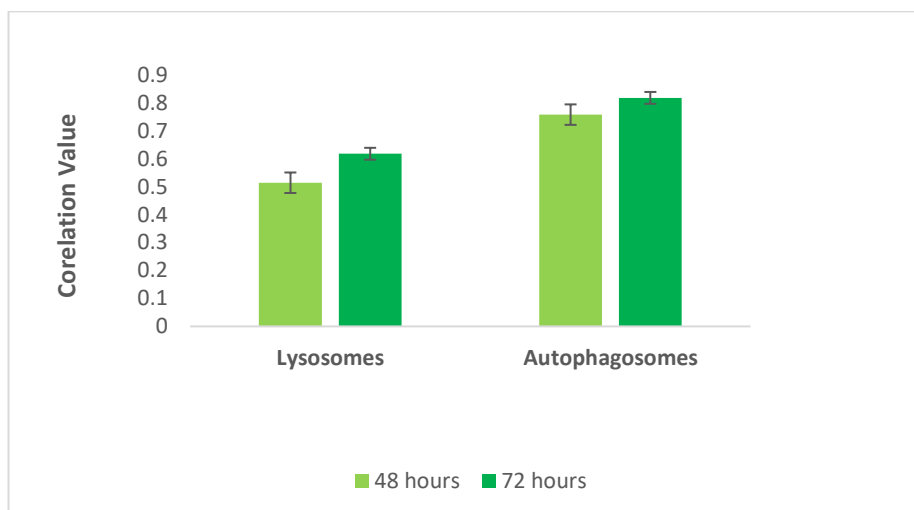
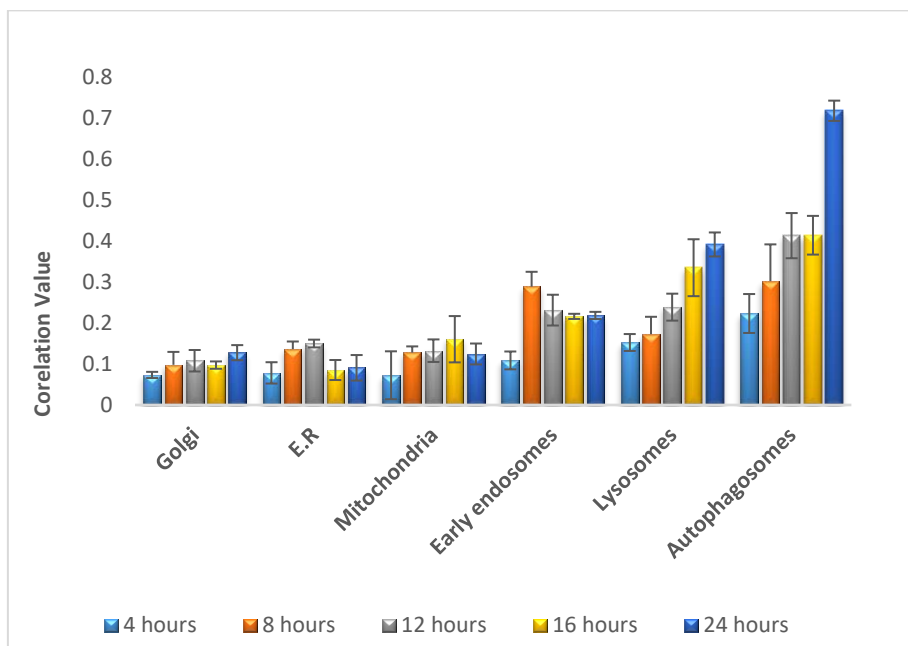


Figure 32: Pearson's Coefficient of Correlation value of A549 organelles treated with 0.9nM RuS12·AuNP20 at 37°C

The figure shows A549 cells treated with 0.9nM RuS12·AuNP20 for 4, 8, 12, 16 and 24 hours for each organelle studied. One slide was prepared to represent a time-point and an organelle. For each slide, three random images were acquired and the PCC values gotten for those images. These values were plotted to quantitatively measure the degree of co-localization between RuS12·AuNP20 and the organelle. The value shown is the PCC mean value of co-localisation \pm SEM. Values are from an experiment with no replicate. Organelles studied beyond 24 hours were lysosomes and autophagosomes at 24, 48 and 72 hours, their PCC values were between 0.5-0.8 (shown in lower panel).

4.2.2. Cellular Localisation by Transmission Electron Microscopy Imaging

TEM imaging was used to study the trafficking and localisation of RuS12·AuNP20 at higher resolution, which overcomes the limit of confocal imaging but support the result of confocal imaging. A549 cells studied was treated with 0.9 nM RuS12·AuNP20 between 4-72 hours similar to confocal imaging study. The result presented shows images at 4, 24 and 48 hours. At 4 hours, RuS12·AuNP20 were observed to be localised majorly on the cell membrane with evidence of internalization occurring by the protrusion of the cell membrane and particularly what appears to be an early endosome (Figure 33b) is observed. This is similar to confocal imaging of GFP-RAB4 at 4 hours (Figure 29), where co-localisation with the early endosomes (GFP-RAB4) is observed at 4 hours and nanoparticles where localised majorly on the membrane. At later time points, TEM images showed more particles are internalised as expected and are all localised in vesicles with no evidence of either cytoplasmic, golgi, mitochondria or nuclear co-localisation. The representative image at 24 hours shows interestingly, the co-localisation of RuS12·AuNP20 within the lysosomes (Figure 34). The lysosome is identifiable by its high electron density and single membrane. Zooming into the lysosomes (Figure 34c), RuS12·AuNP20 is observed to be still mono-dispersed, spherical, non-aggregated (20 nm) and undigested. The undigested particle observed is contrary to what was expected based on the role of the lysosome been the digestive organelle of cells. At later time points (48-72 hours), all internalised RuS12·AuNP20 were localised in a mix of vesicles. These vesicles were either: multi vesicular bodies (MVB), lysosome, and double membrane structure believed to be an autophagosome enclosing a lamella body (Figure 35). The result of TEM imaging is in agreement with the result of confocal imaging. Consequently, the summary of the localisation and trafficking of RuS12·AuNP20 in A549 cells is RuS12·AuNP20 is capable of modulating autophagy in A549 cells in a time dependent manner.

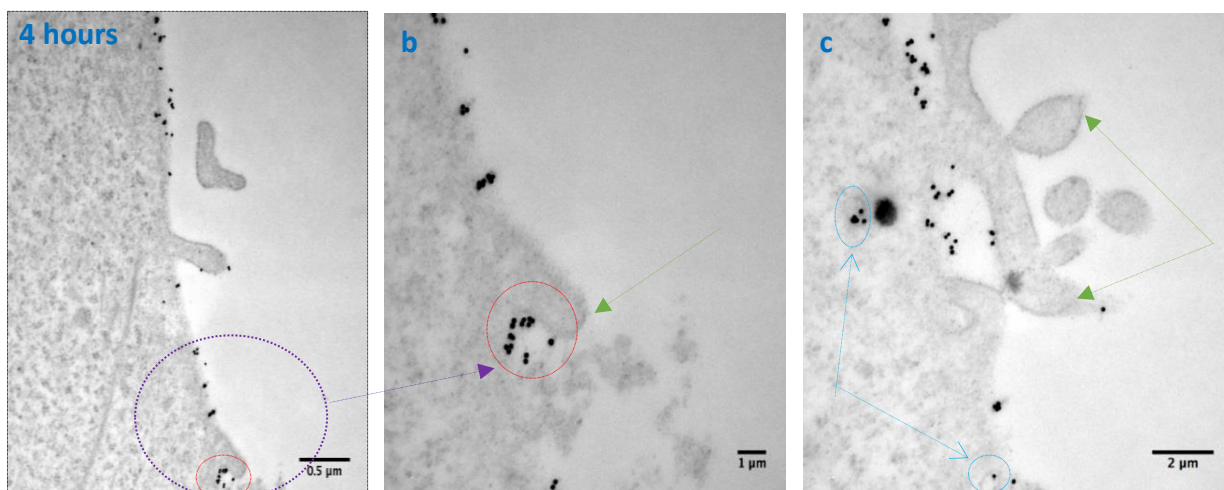


Figure 33: TEM image of A549 cells treated with 0.9nM RuS12·AuNP20 for 4 hours at 37°C
 RuS12·AuNP20 is observed as spherical black dot, which are roughly same size. They are observed to be attached to the cell membrane and part of the membrane is found to be disintegrated (green arrow).

- RuS12·AuNP20 localised majorly on the cell membrane.
- RuS12·AuNP20 getting internalised, blue arrow showing a likely early endosomes shown as blue circle.
- Zoomed in image of a) to show the cell membrane protruding to internalise RuS12·AuNP20 and forming a likely vesicle shown as red circle.

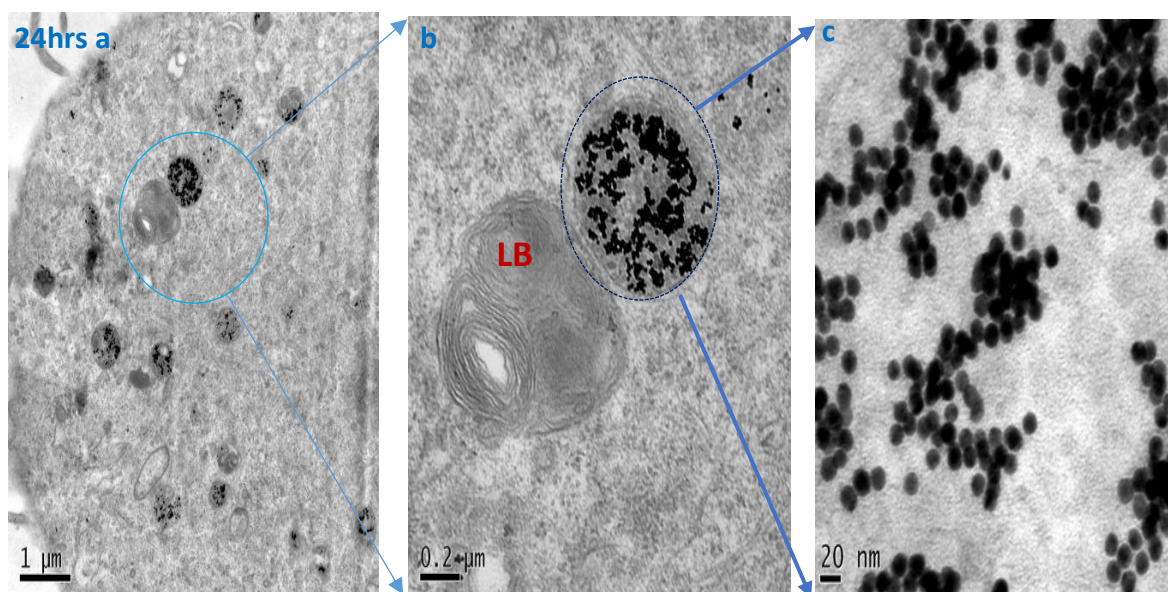


Figure 34: TEM image of A549 cells treated with 0.9nM RuS12·AuNP20 for 24 hours at 37°C

- Most of RuS12·AuNP20 are co-localised in the lysosomes.
- Mag of a). to view the lysosome and the lamella body (LB).
- RuS12·AuNP20 co-localised in the lysosomes and still mono-dispersed and undigested.

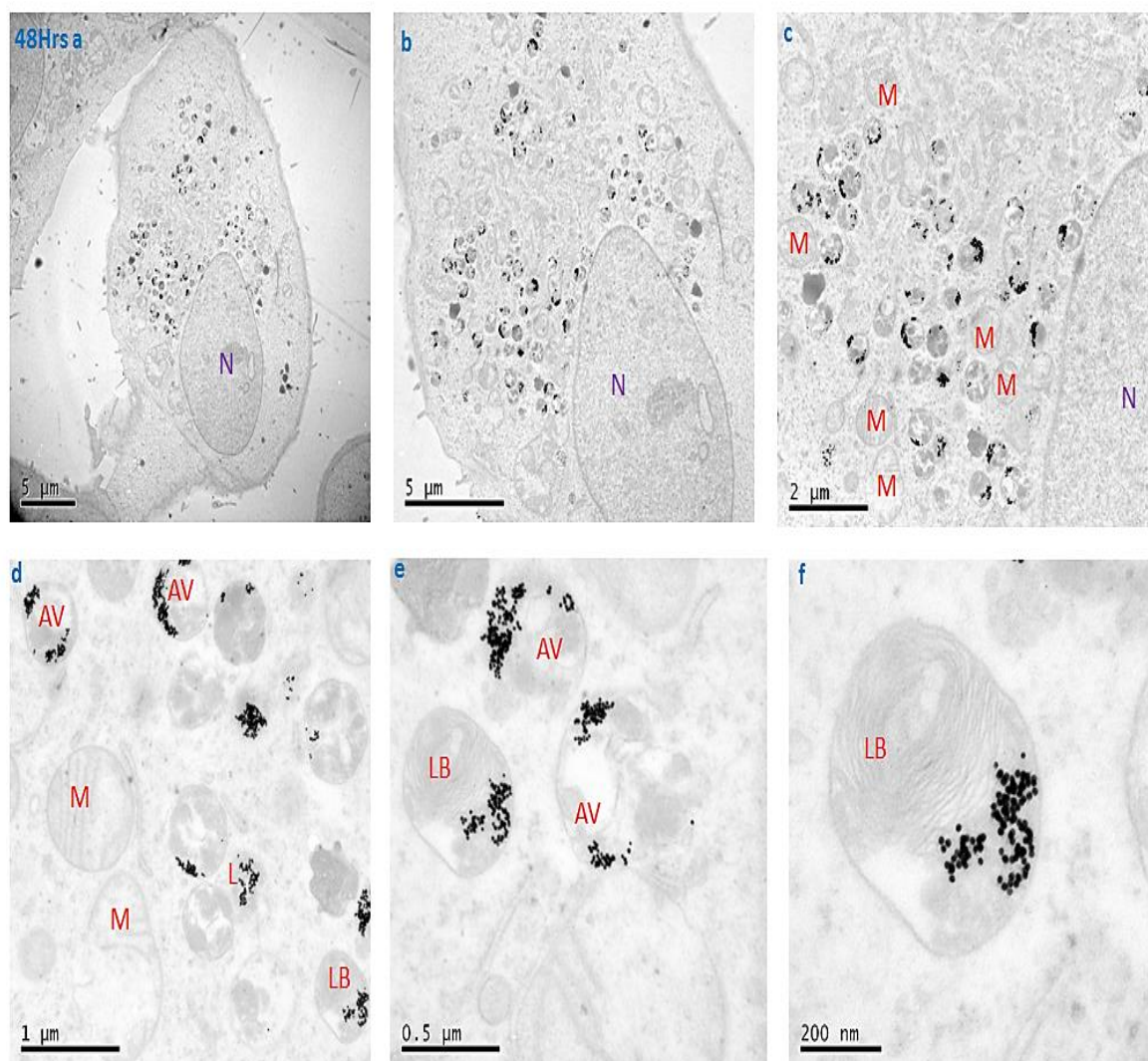


Figure 35: TEM image of A549 cells treated with 0.9 nM RuS12-AuNP20 for 48 hours at 37°C

- a. wide view
- b. Mag of a
- c. Mag of b showing the perinuclear region and particles all localised in vesicles.
- d-e. No co-localisation within the mitochondria (M) but co-localised in the lysosome (L) and a double membrane structures (AV) and one enclosing a lamella body (LB)
- f. Mag of e to show the co-localisation within a double membrane structure containing the lamella bodies (LB).

The experiment was done as a technical duplicate, the images were from a single
M= Mitochondria, N= Nucleus, AV= Autophagic Vacuole, L= lysosomes, LB= Lamella Body.

4.2.3. Western blotting of Microtubule-associated proteins 1A/1B light chain 3 (LC3)

Western blotting was done to detect autophagic vacuoles and this was based on the imaging results (confocal and TEM) particularly co-localisation with the LC3 (autophagosomes), it appears that RuS12·AuNP20 are trafficked to the autophagosomes and induces autophagy. To support this evidence and establish if RuS12·AuNP20 activate the autophagy pathway in A549 cells, western blotting of LC3 (autophagy marker light chain 3) protein was conducted on A549 cells treated with RuS12·AuNP20 for 2-24 hours (Figure 36). LC3 protein was chosen because during the formation of the autophagosomal membrane, cytosolic LC3 (LC3-I 18 kDa) is conjugated to phosphatidylethanolamine to form LC3-II by lipidation and LC3-II becomes associated with active autophagic vesicles. The presence of LC3-II band of about 16 kDa indicates the presence of autophagosomes. β -actin (a reference) was used to normalise the protein expression in this western blotting and its expression remained constant irrespective of treatment. As a positive control, cells were serum starved 24 hours.

The result showed the control cells (no treatment) and early time points (2-4hours) expressed LC3-I (cytosolic form) and later time points of (8-12 hours) expressed LC3-II indicating the presence/formation of autophagosomes in a time dependent manner. Therefore, this result validates the imaging result of the formation of autophagosome vesicles.

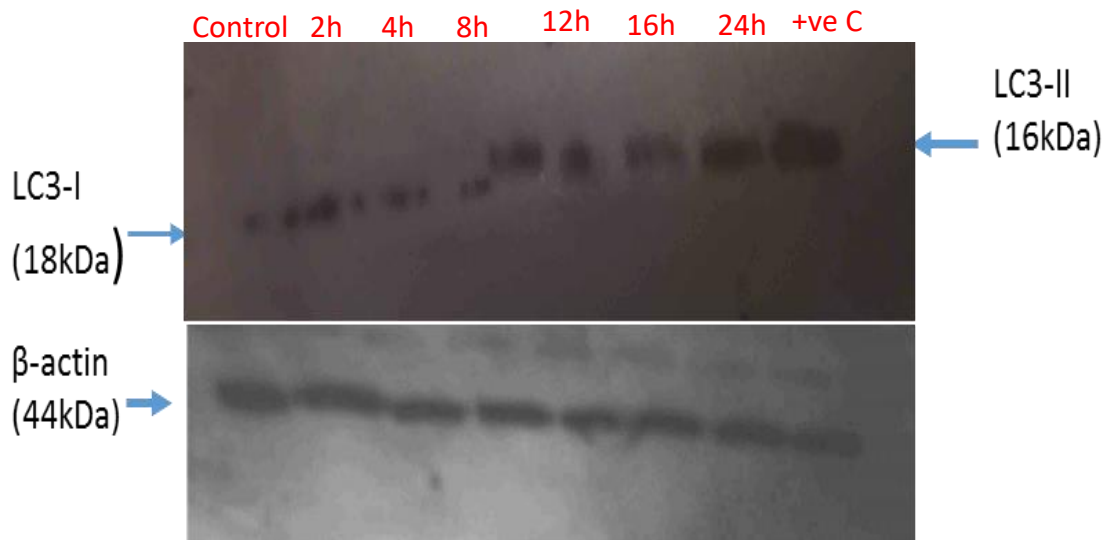


Figure 36: Detection of LC3 protein by western blotting.

A549 cells were treated with RuS12-AuNP20 for 2-24 hours (h). Protein was extracted and used for detection of lc3 and β-actin. Detection of protein was by chemiluminescent reagent and x-ray film exposed for 5minutes. LC3-II is detected at later points, while LC3-1 is detected at early time points of 2 and 4 hours, gradually by 8 hours LC3-II is been detected all the way to 24 hours. Positive control used was 24hours serum starved A549 cells. A number of trial experiments were done to ascertain the sensitivity of the antibody. The evidence of autophagy was confirmed once and could not be repeated because of lack of primary antibody.

4.2.4. Quantitative real-time PCR (RT-PCR)

With the established link between internalization of RuS12·AuNP20 in A549 and activation of autophagy, it is important to begin to understand the mechanism of action of AuNPs. In most cases, induction of autophagy is linked to cellular stress, hence the study of genes involved in autophagy and oxidative stress. Figure 37 summarises the changes in gene expression in the following genes: LC3, heat shock 70kDa protein A (HSP70), glutathione reductase (GSR) and catalase (CAT). The results are expressed as $2^{-\Delta\Delta Ct}$, this is fold change difference between control and treated samples normalised to a reference gene (β -actin based on western blot).

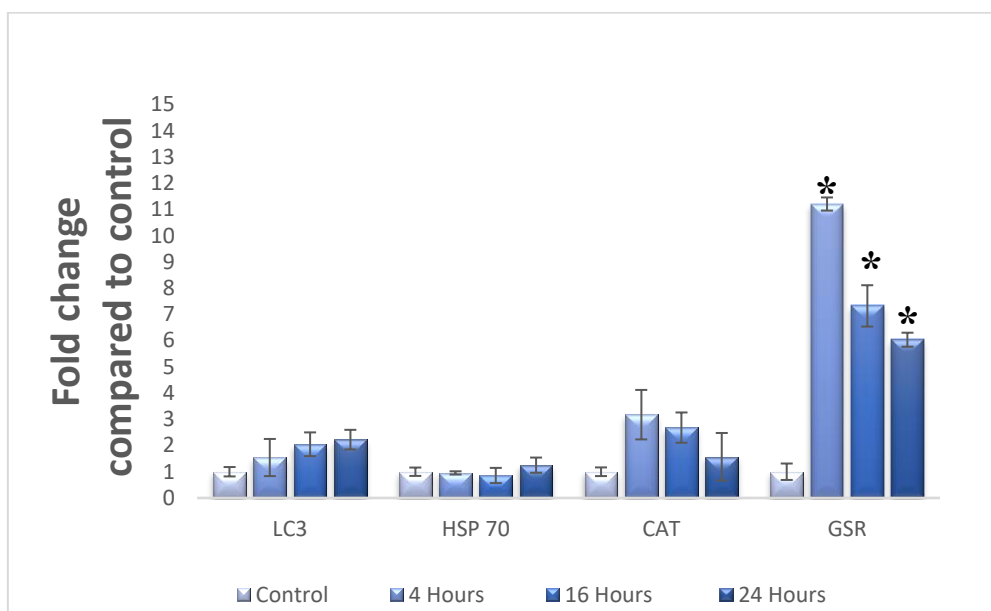


Figure 37: RT-PCR of A549 cells treated with 0.9 nM RuS12·AuNP20 over 0-24 hours

A549 cells were treated with 0.9 nM RuS12·AuNP20 for 0, 4, 16 and 24 hours. At the end of each time point, RNA was extracted and reverse transcribed to cDNA. cDNA was used for RT-PCR with taqMan gene expression. The experiment is a biological triplicate (n=3) for each time point with three technical replicates and presented as mean value \pm SEM of fold change compared to control. The result showed a statistically significant * ($p \leq 0.05$) difference in GSR by one-anova between treated and control cells at all time points.

Surprisingly, HSP remained unchanged between treated and control. LC3 as expected had a time-dependent increase in fold change in a time dependent manner. This implies the formation of autophagosome over time, further validating the imaging and western blot results. CAT shows a 3-fold increase at 4 hours compared to the control, which decreases, by half at 24 hours. The GSR gave an interesting result, a 10-fold increase at 4 hours compared to the control was observed which decreases over time by 4-fold at 24 hours. Based on the results in this chapter, it is evident that RuS12·AuNP20 is modulating autophagy via the formation of autophagosomes in a time-dependent manner. However, the observed autophagosome induction shows no direct link to stress based on the unchanged level in HSP but causes the induction of genes involved in detoxification especially at early time points.

4.3 Discussion

The aim of this chapter is to establish the intracellular fate of RuS12·AuNP20 in A549 cells. The internalization starts with the protrusion of cell membrane that leads to the RuS12·AuNP20 localisation in membrane bound vesicles. This observation is similar to other studies on trafficking AuNP in mammalian cells (Chithrani & Chan, 2007; Huang *et al.*, 2015b; Jiang *et al.*, 2008; Nativo *et al.*, 2008; Uboldi *et al.*, 2009). From the previous chapter on uptake (chapter 3), two routes of internalization of RuS12·AuNP20 in A549 cells were suggested to be macropinocytosis and clathrin-mediated endocytosis (clathrin and caveolae). Macropinocytosis leads to the formation of a large endocytic vesicles called macropinosomes (Panariti *et al.*, 2012). Macropinosomes over time fuses with acidic organelles such as lysosome (Hillaireau & Couvreur, 2009). The clathrin-mediated endocytosis on the other hand causes an invagination of cell membrane, which pinches off and forms a vesicle that becomes an early endosomes (Doherty & McMahon, 2009; McMahon & Boucrot, 2011).

Early endosomes are heterogeneous in terms of morphology, function and localisation (Huotari & Helenius, 2011; Lakadamyali *et al.*, 2006). They are small and mostly found close to the plasma membrane (Pascua-Maestro *et al.*, 2017). They receive most of their cargo from receptor-mediated endocytosis (clathrin and caveolin-mediated endocytosis), which is highly suggested to be one of the routes of uptake of RuS12·AuNP20 into A549 cells (chapter 3). We observed at early time points the first endocytic vesicles for internalised RuS12·AuNP20 was the early endosomes evident from both confocal (co-localisation with RAB4 Figure 29) and TEM imaging (localisation in small vesicles close to the membrane). Early endosomes is the main sorting station of internalised AuNP and is identifiable by the time it takes the AuNP to be localised within it usually few hours after exposure (Jovic *et al.*, 2010; Maxfield & McGraw, 2004). Therefore,

trafficking of RuS12·AuNP20 in A549 cells starts from, the plasma membrane to early endosomes. AuNP in the early endosomes can be sorted to one of three possible pathways:

1. Degradation pathway *en route* to the lysosome,
2. Connecting pathway that is delivery to golgi
3. Recycling pathway (Huotari & Helenius, 2011; Weisz & Rodriguez-Boulan, 2009).

Since our result showed RuS12·AuNP20 localised mostly in vesicles located around the nucleus and no evidence of golgi co-localisation with golgi (Figure 26), this suggests that RuS12·AuNP20 in A549 cells is trafficked to degradation pathway *en route* to the lysosomes. Similarly, AuNP uptake by macropinocytosis are also trafficked to the lysosomes and based on our observation at early time points showing protrusion of cell membrane, it is implied that internalised RuS12·AuNP20 is trafficked to the lysosome via the endo-lysosomal pathway. The main function of endo-lysosomal pathway is the bulk degradation or recycling of internalised material (Repnik *et al.*, 2013). The endo-lysosomal pathway involves the movement of internalised particles via vesicular trafficking until it gets to the lysosomes. The early endosome is dynamic and undergoes maturation by luminal acidification during endocytic trafficking, to become a late endosome (Hillaireau & Couvreur, 2009; Huotari & Helenius, 2011) as depicted in Figure 38. Multi vesicular bodies (MVB) are a special type of late endosomes, they are called MVB because they constitute of membrane-bound intraluminal vesicles i.e. different vesicles within them (Gruenberg & Stenmark, 2004). AuNP *en route* to the degradative route is trafficked to the late endosome/MVB first before the lysosomes. Our evidence that RuS12·AuNP20 is trafficked to the lysosomal degradation pathway is supported by our TEM images (Figure 33) that shows co-localisation within late endosomes. The late endosomes over time moves to perinuclear region and is capable of fusion with a primary lysosomes that originates from

the golgi (heterotypic fusion) (Piper & Luzio, 2001). The fusion with the lysosome creates a transient hybrid organelle called an endolysosome that matures to become a secondary lysosome which is electron dense and can easily be observed by TEM (Luzio *et al.*, 2007).

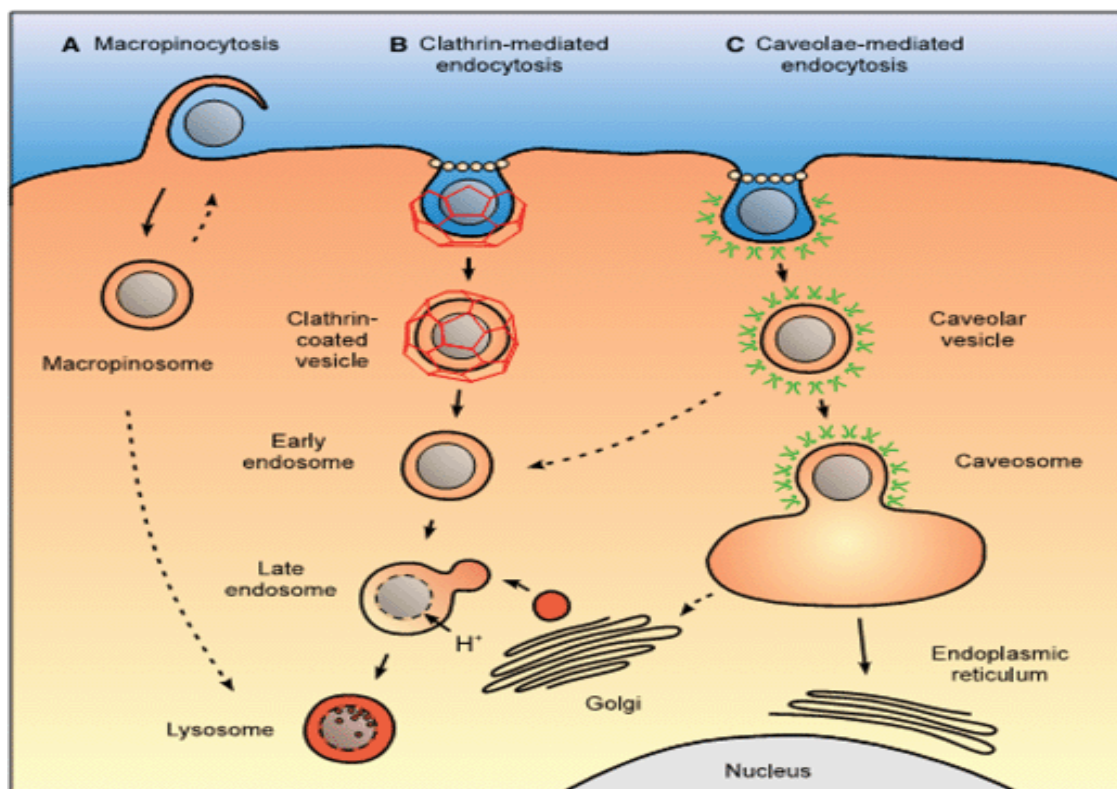


Figure 38: Intracellular trafficking of ENPs

A. Macropinocytosis: ENPs are internalised first into the macropinosome, which later fuses with lysosomes. B & C. Receptor-mediated endocytosis: ENPs internalization leads to the formation of early endosomes, which undergoes maturation and acidification by fusing with primary lysosome to become a late endosomes. Image adapted from (Hillaireau & Couvreur, 2009).

The late endosome contains lysosomal membrane protein such as LAMP1 (Huotari & Helenius, 2011) which is also abundant in the lysosome (Griffiths *et al.*, 1988). Our result of LAMP1 co-localisation with RuS12·AuNP20 (Figure 30) which increased over time as expected and localisation in electron dense structure further supports the lysosomal degradation pathway. The lysosome is the meeting point of all internalised AuNP as the site of degradation irrespective of route of uptake (Panariti *et al.*, 2012) and our result is in agreement with this.

Similar observation with mammalian cells treated with AuNP shows an increase in co-localisation with acidic compartments or lysosome in a time dependent manner and no co-localisation with the nucleus, mitochondria, endoplasmic reticulum, or Golgi (Brandenberger *et al.*, 2010; Mironava *et al.*, 2010; Wang & Petersen, 2013; Zarska *et al.*, 2016). Also observed were localisation of RuS12·AuNP20 in lamella bodies of A549 cells. Lamella bodies in A549 cells are membrane bound organelles involved in storage and secretion of lung surfactant (Mulugeta *et al.*, 2002; Schmitz & Muller, 1991). They contain lysosomal enzymes such as LAMP1 and are linked by vesicular exchange to MVB (Wasano & Hirakawa, 1994; Weaver *et al.*, 2002), hence the observed localisation of RuS12·AuNP20 with the lamella body. Due to their link with MVB, they are capable of binding with the lysosome (heterotypic fusion) as was observed at later time points of 48 hours (Figure 35). Similar observation of localisation of AuNP with the lamella bodies in A549 cells have been reported (Wang & Petersen, 2013) as well as other types of ENPs (Schumann *et al.*, 2012) in A549 cells. Although, RuS12·AuNP20 is trafficked to the lysosome for degradation, it is not degraded in the lysosomes. Similar observation of retention of AuNP in lysosome without degradation has been reported *in vitro* (Kreyling *et al.*, 2015) as well as *in vivo* which gradually degraded after months of internalization (Sadauskas *et al.*, 2009).

Generally, materials to be degraded are trafficked to the lysosome in two ways: either through the late endosomes; usually exogenous materials or autophagosome; usually endogenous materials (Eskelinen & Saftig, 2009; Liou *et al.*, 1997). Autophagosomes are double membrane vesicles that are formed around intracellular substrate such as part of the cytoplasm or organelles in a non-specific manner and targets its content for lysosomal degradation by lysosomal hydrolases in a process called autophagy as depicted in Figure 39 (Panariti *et al.*, 2012).

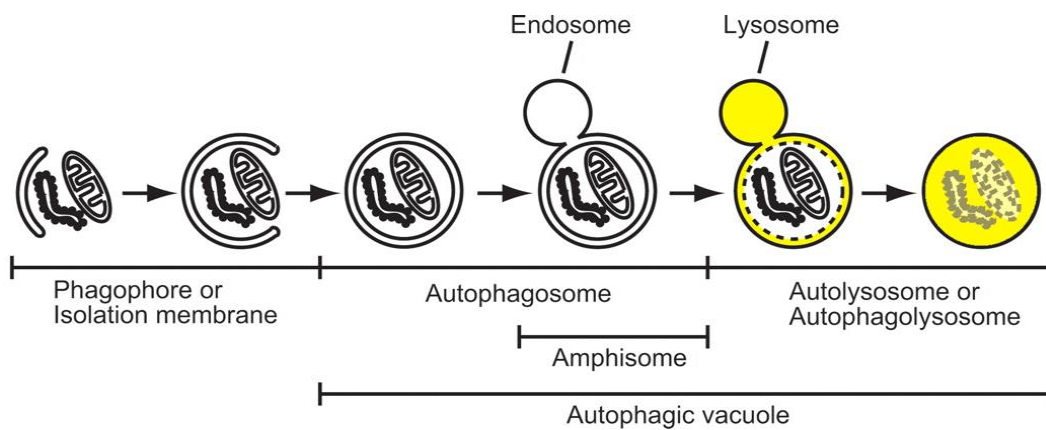


Figure 39: Process of Autophagy

Autophagosomes are formed from a phagophore/isolation membrane sequestering part of cytoplasm or organelles. Autophagosomes can subsequently fuse with the endosome or lysosome to form amphisome or autolysosome. In TEM imaging, it is difficult to distinguish between autophagosome, amphisome or autolysosome, so they are collectively referred to as autophagic vacuole. Images adapted from (Mizushima, 2007).

The formation of autophagosomes causes it to receive lysosomal constituents such as lysosomal membrane proteins (LAMP1) either by fusing with late endosomes and forming an amphisome or fusing with a lysosome and forming an autolysosomes (Eskelinen, 2005; Eskelinen & Saftig, 2009). Autophagosomes, amphisome and autolysosomes are collectively referred to as a autophagic vacuoles and are very similar in their structure and function (Mizushima, 2007). Lysosomal enzymes degrade contents of both amphisome and autolysosomes. Autophagy and endo-lysosomal pathway both converges at the lysosomes for degradation as well (Gordon & Seglen, 1988; Hoyvik *et al.*, 1987; Liou *et al.*, 1997; Yi & Tang, 1999). This also explains the increasing co-localisation over time of RuS12·AuNP20 with LAMP1 (Figure 30). The result in Figure 35e shows RuS12·AuNP20 co-localisation in a double membrane structure that either has an organelle or part of a cytoplasm, these characteristic are synonymous with autophagosomes/autophagic vacuoles and this co-localisation is observed at later time points.

Further supporting the evidence of formation of autophagosomes are the increasing co-localisation of RuS12·AuNP20 with GFP-LC3 (Figure 31) which also increases over time

as well as the western blot of LC3-II protein (Figure 36) which shows formation of autophagosomes over time because LC3-II is localised on autophagosomes and autolysosomes. Various ENPs including AuNP have been reported to induce autophagosomes accumulation. They are viewed as autophagy activators, which can be further harnessed for its therapeutic potential by inducing autophagy as a treatment in some metabolic diseases (Huang *et al.*, 2015a; Li *et al.*, 2010; Ma *et al.*, 2011; Peynshaert *et al.*, 2014; Stern *et al.*, 2012; Wei *et al.*, 2010; Zahirnyk *et al.*, 2007). Autophagy activation by AuNP is a means of degradation of particles since it involves the lysosome, while ensuring cell survival. However, RuS12·AuNP20 was not degraded. Ma *et al.* (2011) observed AuNP altered autophagic activity by impairment of lysosomes degradation activity, which caused lysosomal enlargement and alkalinisation, resulting in accumulation of autophagosomes and upregulation of LC3-II, which is similar to our RT-PCR result of LC3 protein. This helps explain a plausible reason for the observed intact RuS12·AuNP20 in autophagic vacuoles even at 72 hours. Interestingly, they attributed their observation of accumulated autophagosomes to a blockage of autophagy rather an activation of autophagy. Autophagy occurs at a basal level when there is a surplus supply of nutrient (autophagosomes are quickly turned over by lysosomes, so no autophagosome accumulation is observed) or under stress condition such as starvation which causes accumulation of autophagosomes (Codogno & Meijer, 2005; Degenhardt *et al.*, 2006; Ma *et al.*, 2011). Based on this, Ma *et al.* (2011) does not attribute their observation of autophagosome accumulation to stress, although oxidative stress is linked to the triggering of autophagy after exposure to AuNP (Ding *et al.*, 2014; Li *et al.*, 2010).

We hypothesize based on our result that the accumulation of autophagosome could be because of cellular stress; hence, the measurement in changes in gene expression on stress related genes by RT-PCR. The result of HSP 70 expression remaining almost constant is

similar to Hauck *et al.* (2008) that showed no significant up or down regulation changes in HSP 70 after exposure to AuNP or silica nanoparticles (Petrache Voicu *et al.*, 2015). This observation is opposite to what we expected, because HSPs especially HSP 27 and HSP 70 are induced on exposure to cellular and oxidative stress to resist subsequent cellular damage (Fulda *et al.*, 2010; Samali & Orrenius, 1998). This suggests that stress might not be directly linked to the modulation of autophagy observed. Interestingly, an elevated level of CAT and GSR observed especially at early time point of 4 hours is an indication of response to either ROS/hydrogen peroxide or cellular oxidant detoxification. CAT converts ROS (hydrogen peroxide) to water. An enzyme not studied glutathione peroxidase reduce lipid hydroperoxides to their corresponding alcohol and reduces free hydrogen peroxide to water, while GSR reduces oxidised glutathione (product of glutathione peroxidase) to glutathione. CAT and GSR are enzymatic antioxidant defensive mechanism of the cells (Birben *et al.*, 2012). We propose A549 cells perceives RuS12·AuNP20 especially at an early time point as a xenobiotic and causes significant induction of these genes to defend itself as an adaptive measure rather than an adverse measure which on more internalization reduces the induction of these genes.

This chapter has studied in details the trafficking of RuS12·AuNP20 from the cell membrane to autophagic vacuoles, which appears to be the last vesicles of localisation of particle and has proven the involvement of autophagy as a cellular fate of RuS12·AuNP20 in A549 cells. In addition, A549 cells strongly perceives RuS12·AuNP20 as foreign once it is beginning to get internalised and sets up a defensive/adaptive mechanism which decreases over time but does not cause a change in heat shock proteins. Therefore, autophagy is likely not mediated by stress but the presence of RuS12·AuNP20. In the next chapter, a proposed mechanism of toxicity especially involving the generation of ROS is discussed.

Chapter 5

Cytotoxicity of RuS12-AuNP20 on A549 cells

5.1. Introduction

Quantification of cellular functions usually forms the basis for cytotoxicity testing. Examples of such cellular functions include; cell adhesion, membrane integrity, DNA stability and metabolic enzyme activities. Using these endpoints, various assays have been developed to measure their changes as a way of assessing cytotoxicity (Hussain *et al.*, 2005).

Cytotoxicity of RuS12·AuNP20 on A549 cells was measured by two different methods because more than one assay is more informative in determining nanoparticle toxicity (Monteiro-Riviere *et al.*, 2009). Cytotoxicity was determined by using two colorimetric assays that involve the measurement of absorbance at 590 nm. First assay was MTT assay, which is a widely used endpoint for toxicity testing including nanoparticles because of its ease of performance and reproducibility (Kroll *et al.*, 2009; Marquis *et al.*, 2009). Second assay was CVS assay, which quantifies cell viability based on detachment of adherent cells from the culture flask. The principle behind the MTT is: viable cells with active mitochondria reduce MTT into a purple coloured formazan with an absorbance of around 570 nm (Riss *et al.*, 2004). While, the principle behind CVS for cytotoxicity testing is that, adherent cells detach from cell culture plates during cell death while staining the remaining cells and can be used as an indirect qualification of cell death as well as proliferation (Feoktistova *et al.*, 2016). Therefore, a reduction of values in absorbance in both assays means a decrease in cell viability. In this current study, these colorimetric methods of cell viability were used on A549 cells treated with various concentrations of RuS12·AuNP20 up to 72 hours.

Another indicator of cell viability is the changes in levels of protective factors within the cells; an example of such is glutathione. Glutathione is a small intracellular protein thiol molecule in the cell, which prevents cellular damage by scavenging ROS (Dickinson &

Forman, 2002). In healthy cells, most of glutathione present is in its reduced form (GSH); a major cellular antioxidant. In the presence of ROS, GSH is oxidised to GSSG and an increasing ratio of GSSG to GSH is an indication of oxidative stress and the health of the cells (Birben *et al.*, 2012). Also, the presence of ROS in the cell, can damage the DNA (Fang *et al.*, 2015; Green *et al.*, 2006; Jena, 2012) and damage to DNA such as strand breaks can be detected by comet Assay (Collins, 2004). The comet assay is a sensitive and quantitative technique for detecting DNA strand breaks in eukaryotic cells. Therefore, the measurement of ROS, glutathione and DNA strand break is essential in understanding the cytotoxicity potential of RuS12·AuNP20 on A549 cells.

All cytotoxicity assay was done on A549 cells treated with 0.9 nM of RuS12·AuNP20 serially diluted to 0.45, 0.225 and 0.1123 nM and incubated for 24, 48 and 72 hours and this data was used to establish a non-cytotoxic concentrations and time-points of treatment of cells for the uptake and cellular fate described in chapters 3 and 4. Assays were all done as biological triplicate with technical triplicate.

5.2. Results

5.2.1. MTT Assay.

The result presented in Figure 40 is the cytotoxic potential based on mitochondria activity of A549 cells treated with RuS12·AuNP20 for 24, 48 and 72 hours. A decrease in absorbance is directly proportional to a decrease in cell viability, which is an indication of cells with inactive mitochondria. The positive control used was 0.15% (v/v) Triton X-100 with media, which resulted in about 90% cell death (shown in appendix 5A). The result shows no statistical difference ($P \leq 0.05$) between treated and the control cells irrespective of length of exposure to particle or the concentration used. However, at 24 and 48 hours, a non-significant trend in decrease of about 10% in cell viability was observed following treatment of A549 cells with increasing concentration of particles. Although not significantly different RuS12·AuNP20 may be marginally toxic in A549 cells under these conditions. Overall this result suggests that although RuS12·AuNP20 at a concentration of 0.9 nM had no significant cytotoxic effect based on MTT assay on A549 cells even up to 72 hours exposure (98% cell viability), a slight potential exist for cytotoxicity at less exposure time of 24 hours (88% cell viability).

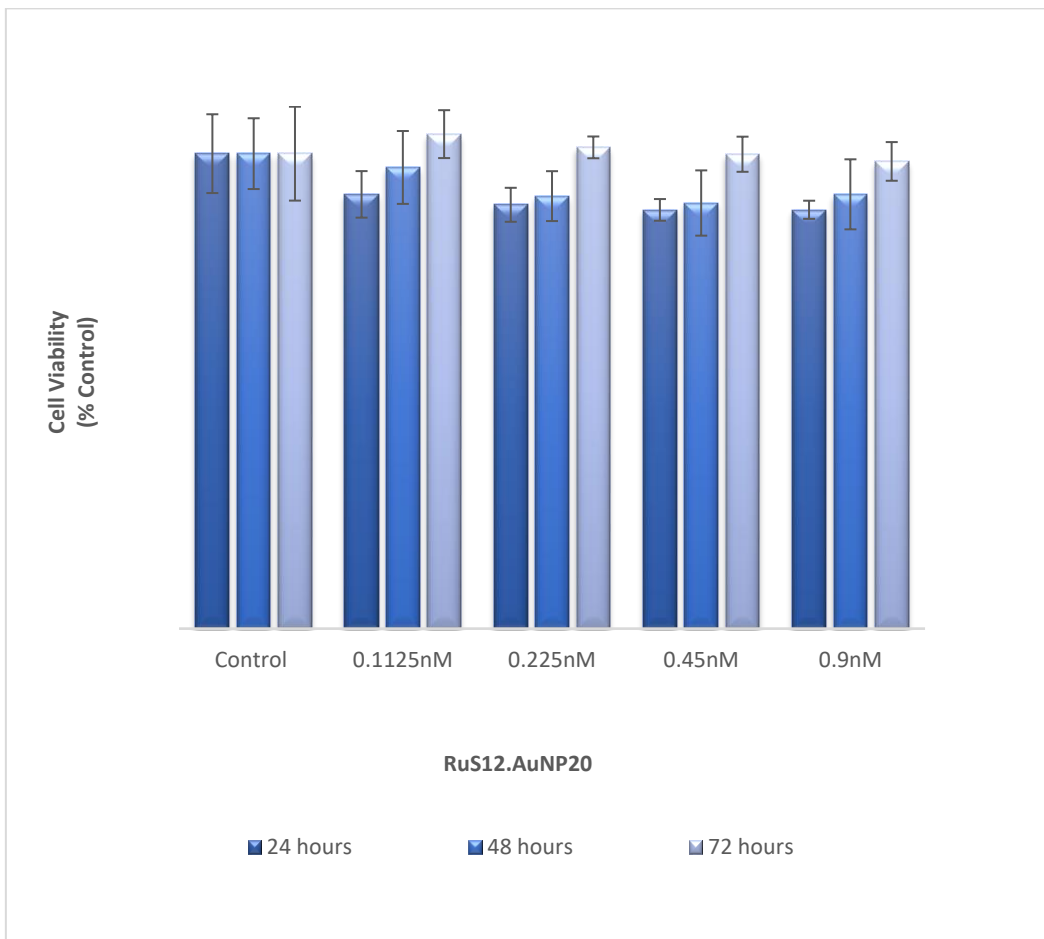


Figure 40: MTT Assay on A549 treated with RuS12·AuNP20 for 24, 48 and 72 hours
A549 cells were seeded at a density of 8,000 cells per well in 96 well plate and treated with RuS12·AuNP20 for 24, 48 and 72 hours. At the end of each time point, spent media was replaced with media containing MTT for 3 hours, and absorbance read at 590 nm was used to calculate cell viability. The experiment is a biological triplicate ($n=3$) and presented as % control of mean value \pm SEM. The result showed no statistically significant ($p \leq 0.05$) difference by one-anova and Bonferroni Post Hoc analysis between treated and control cells irrespective of length of exposure

5.2.2. Crystal Violet Assay.

The measurement of cytotoxic potential of RuS12·AuNP20 treated with A549 cells up for 24, 48 and 72 hours as assessed by the crystal violet assay is presented in Figure 41. The positive control used was 0.15% (v/v) Triton X-100 with media, which resulted in about 60% cell death (shown in appendix 5B). Cells treated with RuS12·AuNP20 for 24 hours, irrespective of concentration, showed a statistically significant ($P \leq 0.05$) decrease in cell viability of about 20% when compared to the untreated control. This significant decrease was not observed at later time points of 48 and 72 hours. Overall, this result suggests that RuS12·AuNP20 has a significant cytotoxic effect measured by CVS on A549 cells after 24 hours exposure.

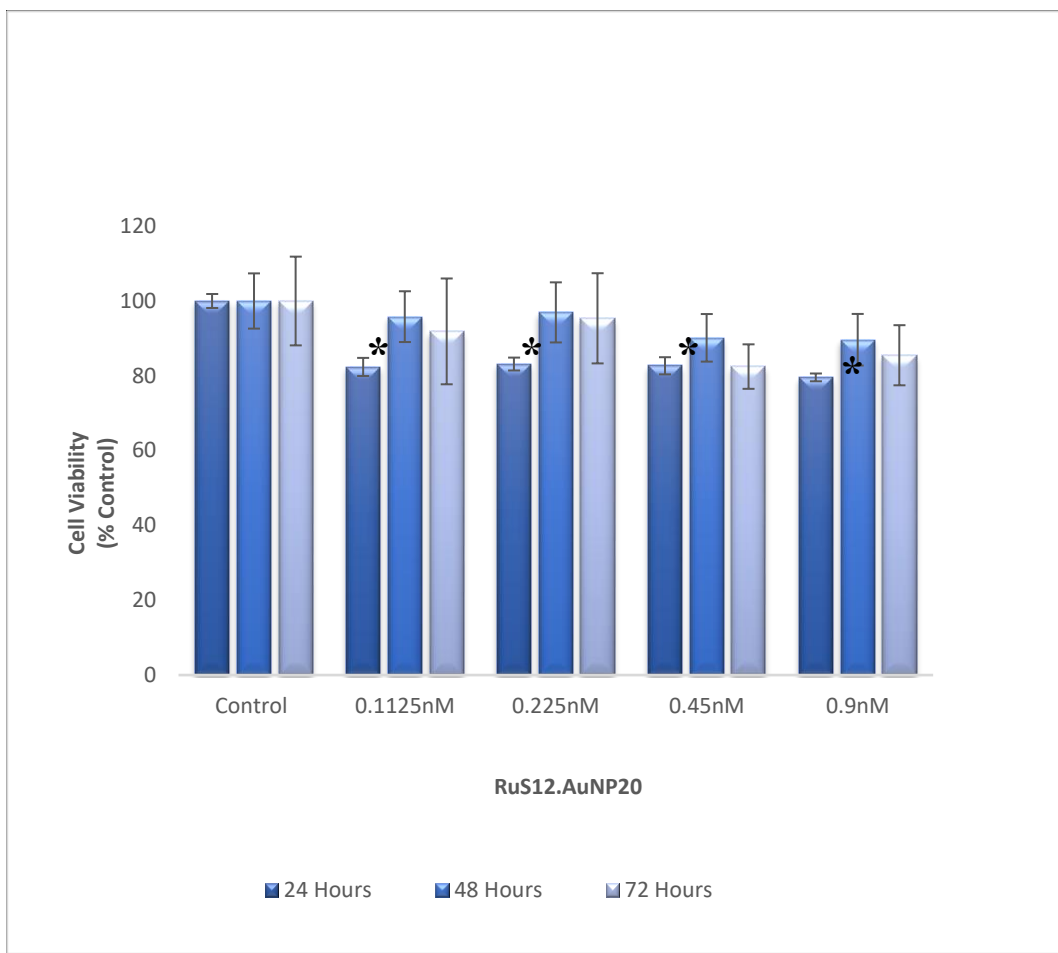


Figure 41: CVS on A549 treated with RuS12·AuNP20 for 24, 48 and 72 hours

A549 cells were seeded at a density of 15,000 cells per well in a 24 well plate and treated with RuS12·AuNP20 for 24, 48 and 72 hours. At the end of each time point, cells were stained with 1% crystal violet solution for 30 minutes and absorbance was read at 590nm. The experiment is a biological triplicate (n=3) and presented as % control of mean value \pm SEM. The result showed a statistically significant $*$ ($p \leq 0.05$) difference by one-anova and Bonferroni Post Hoc analysis between treated and non-treated control at 24 hours irrespective of concentration.

5.2.3. Dichloro-dihydro-fluorescein diacetate (H₂DCFDA Assay)

The level of ROS in A549 cells treated with RuS12·AuNP20 for 24, 48 and 72 hours was assessed by the oxidation of H₂DCFDA to fluorescent DCF is presented in

Figure 42. A549 cells treated with hydrogen peroxide (200 μ m) were used as positive control and showed 60% increase in fluorescence intensity (data shown in appendix 5C). No statistically significant difference was observed between the fluorescence intensity of treated cells and non-treated control up to 72 hours period irrespective of concentration of RuS12·AuNP20 used. An observable trend was a time dependent increase. Overall, this result suggests that the production of ROS in A549 cells treated with RuS12·AuNP20 is not significant.

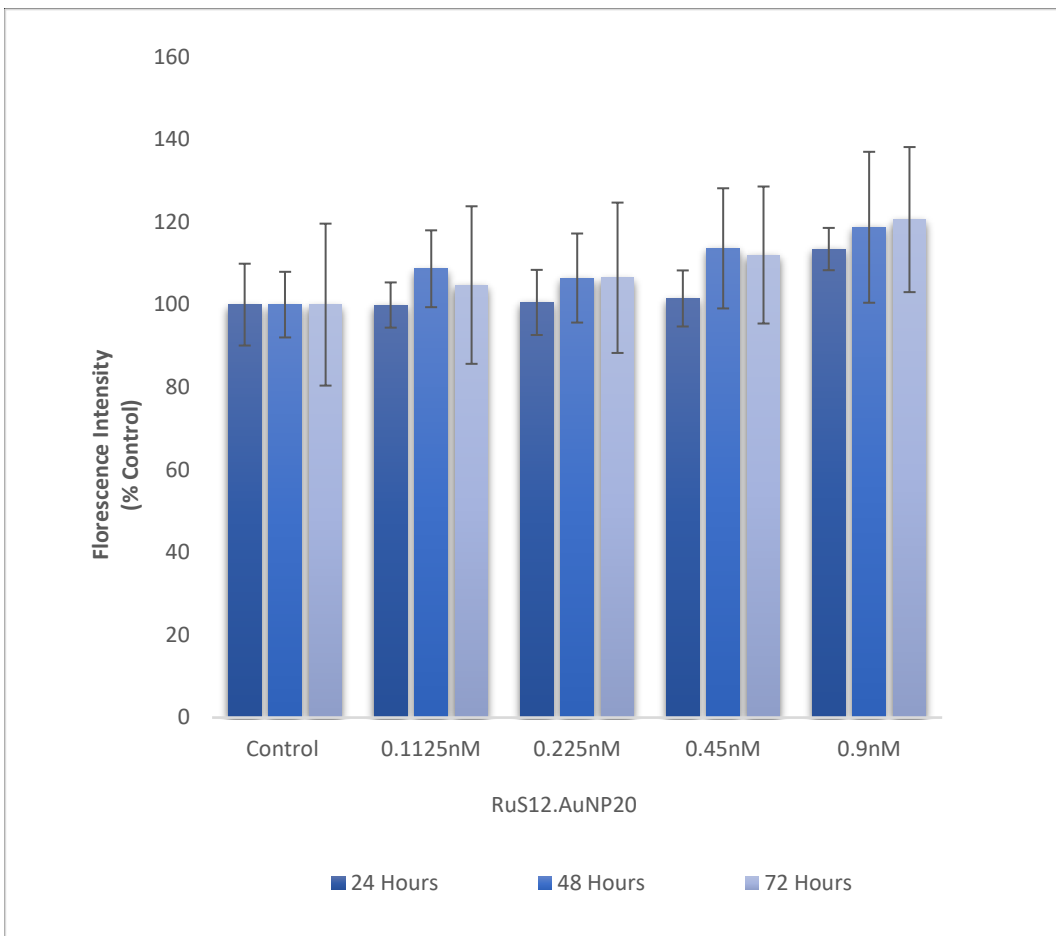


Figure 42: DCFH-DA Assay on A549 treated with RuS12·AuNP20 for 24, 48 and 72 hours

A549 cells were seeded at a density of 8,000 cells per well in a white-wall clear bottom 96 well plate and treated with RuS12·AuNP20 for 24, 48 and 72 hours. At the end of each time point, spent media was replaced with media containing DCFH-DA for 45 mins and fluorescence intensity was read at $\lambda_{exc} = 485\text{nm}$ and $\lambda_{em} = 545\text{nm}$. The experiment is a biological triplicate ($n=3$) and presented as % control of mean value \pm SEM. The result showed an increasing trend in a concentration and time-dependent manner that leads to ROS generation but this was not statistically significant by one-anova and Bonferroni Post Hoc analysis between treated and non-treated controls.

5.2.4. Glutathione Assay

The levels of reduced glutathione (GSH) in A549 cells treated with RuS12·AuNP20 was quantified over 24-72 hours and the result is presented in Figure 43 (Representative GSH standard curves are shown in the appendix 5D1). A decrease in reduced glutathione level would be consistent with the occurrence of oxidative stress. A549 cells treated with hydrogen peroxide (200 μ m) was used as positive control and a 50% difference decrease of glutathione is observed when compared to the non-treated control (shown in appendix 5D2). Generally, a time-dependent decrease in glutathione levels was observed irrespective of concentrations following treatment with RuS12·AuNP20 when compared to the non-treated control. However, this was only statistically significant ($P \leq 0.05$) following treatment with 0.9 nM and 0.45 nM of RuS12·AuNP20 and 0.9 nM of RuS12·AuNP20 at 72 and 48 hours respectively. This result indicates that treatment with RuS12·AuNP20 causes reduced GSH levels in A549 cells, which is statistically significant at longer treatment times and higher concentrations.

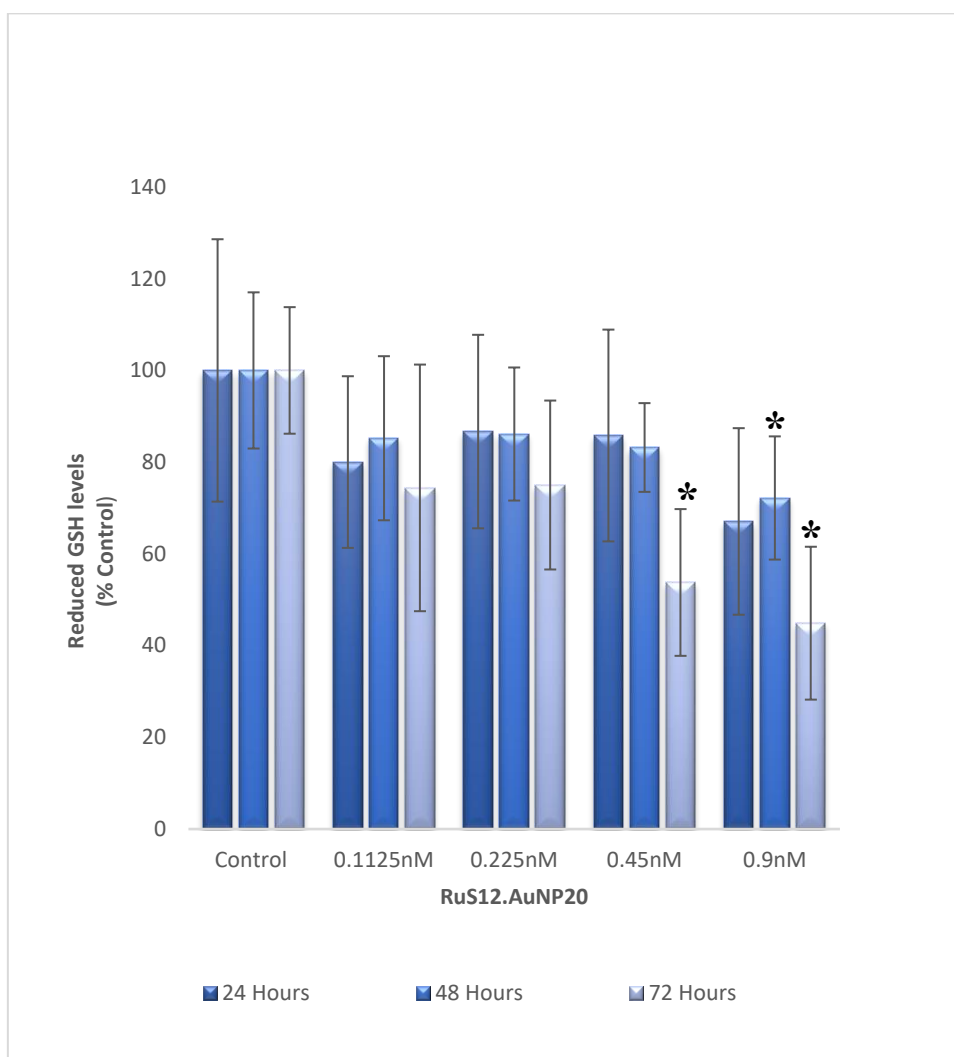


Figure 43: GSH Assay on A549 treated with RuS12·AuNP20 for 24, 48 and 72 hours

A549 cells were seeded at a density of 100,000 cells per well in 6 well plate and treated with RuS12·AuNP20 for 24, 48 and 72 hours. At the end of each time point, protein was precipitated by TCA, and fluorescence intensity was read at $\lambda_{exc} = 350\text{nm}$ and $\lambda_{emi} = 520\text{nm}$. The experiment is a biological triplicate ($n=3$) and presented as % control of mean value \pm SEM. The result showed a statistically significant * ($p \leq 0.05$) difference by one-anova between treated and control cells at 72 and 48 hours at highest concentrations of 0.9 nM and 0.45 nM.

5.2.5. Alkaline Comet Assay

Cells used for comet assay are embedded in agarose gel and are first lysed to reveal the nucleoid containing negative supercoiled DNA, which then undergo electrophoresis. Electrophoresis causes an unwinding of the DNA, only unwound DNA with strand breaks would migrate to the anode resulting in a comet-like structure; i.e. the comet 'head' which is undamaged and the tail which is damaged DNA (Zainol et al., 2009). Representative images illustrating the alkaline comet are shown in Figure 44A-D. Figure 44A shows control cell (untreated A549 cells) with minimal damage. While Figure 44 B shows A549 cells treated with 200 μ m of hydrogen peroxide (positive control) for 1 hour, all cells have extreme unwinds indicating the formation of DNA-strand break. Figure 44 C and D are A549 cells treated with 0.225 and 0.9 nM of RuS12·AuNP20 respectively for 24 hours. The result presented in Figure 45 is mean of the median tail intensity, against the conventional mean of mean of tail length. This is so because the measurement of the damage is often not normally distributed (Olive & Banath, 2006).

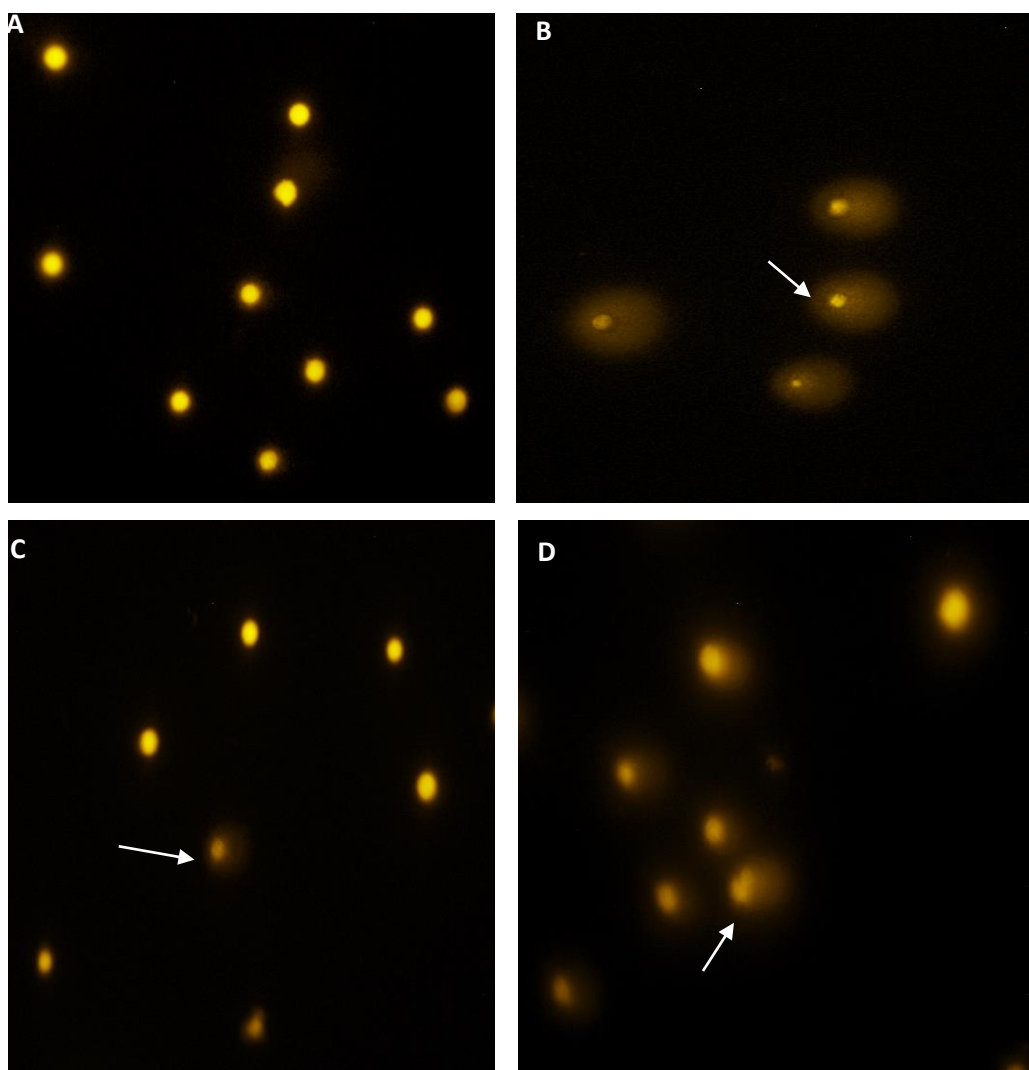


Figure 44: Representative images of cell nuclei of A549 assessed for DNA strand break by Comet Assay. Arrows indicate comet-like structure.

- A. Control A549 cells.
- B. Positively treated cells; 200 μ M of hydrogen peroxide for 1 hour
- C. A549 cells treated with 0.225 nM of RuS12·AuNP20 for 24 hours.

After 24-hour treatment of A549 cells with RuS12·AuNP20, a concentration dependent increase in median tail intensity was observed, which was statistically significant ($P \leq 0.05$) at the highest concentration of 0.9 nM when compared to untreated control. Although, an increase of 123% and 134% was observed at later time points of 48 and 72 hours respectively when compared to the control, these differences were not statistically significant.

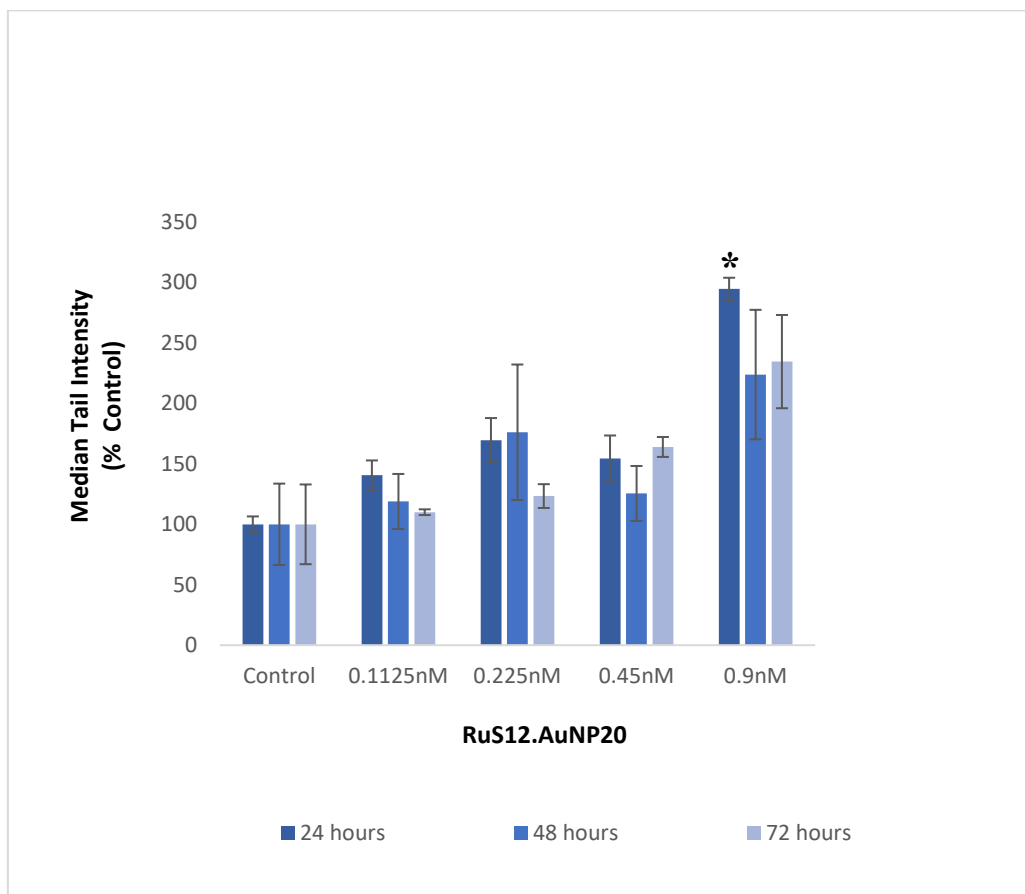


Figure 45: Median Tail intensity of A549 cells treated with RuS12-AuNP20

A549 cells were seeded at a density of 200,000 cells per well in six well plate and treated with RuS12-AuNP20 for 24, 48 and 72 hours. At the end of each time point. Cell suspension was used to prepare slides for comet assay. The experiment is a biological triplicate and presented as % control of mean value \pm SEM. The result showed a statistically significant * ($p \leq 0.05$) difference by one-anova and Bonferroni Post Hoc analysis between treated and non-treated control cells at 24 hours at highest concentration of 0.9 nM.

5.3 Discussion

The study of the toxic potential of AuNP to cell is important in its safety assessment. Previous studies have reported contradictory findings about their toxicity *in vitro* (Murphy *et al.*, 2008; Nel *et al.*, 2006; Pan *et al.*, 2009). Previous published data from our lab with same functionalised AuNPs demonstrated that at concentrations up to 0.9 nM, particles are not toxic after 24 hour treatments (Rogers *et al.*, 2014). This chapter aimed to establish the cytotoxic effect of internalised RuS12·AuNP20 in A549 cells following longer treatment up to 72 hours.

Cells in culture that undergo cell death lose their adherence properties which is measured by CVS, CVS can be comprised by proliferative response that occur at the same time as cell death response (Feoktistova *et al.*, 2016). Therefore, it is important that the data is validated using an additional independent method to assess cell viability. The MTT is an enzymatic assay that relies on capacity of succinate dehydrogenase, a mitochondrial dehydrogenase to reduce the tetrazolium salt to a formazan in the mitochondria (Slater *et al.*, 1963). Besides the mitochondria, the reduction of tetrazolium salt has been reported to occur in other places such as cytoplasm, surface of non-mitochondria membrane (endosome/lysosome) and the plasma membrane (Berridge *et al.*, 2005; Sliwka *et al.*, 2016).

Our MTT data showed RuS12·AuNP20 had no statistically significant effect on the viability of A549 cells, which is similar to previous studies on AuNPs in A549 cell (Rogers *et al.*, 2014), other cancer cell lines (Connor *et al.*, 2005) but contradictory to some previous studies in A549 cells (Patra *et al.*, 2007; Uboldi *et al.*, 2009). Interestingly, CVS showed a significant decrease in cell viability only after 24 hours treatment similar to the MTT (decrease in cell viability at 24 hours) although not significant. Taken together, both assays

suggests that the effect of RuS12·AuNP20 on A549 on cell viability is greatest at 24 hours compared to later time points of 48 and 72 hours and furthermore RuS12·AuNP20 does not inhibit the growth of A549 cells.

In contrast, Uboldi *et al.* (2009) found that citrate coated AuNPs were toxic to A549 cells treated for similar times (24, 48 and 72 hours) at 0.7 mM. They attributed the observed decrease in cell viability to the presence of contaminants such as excess sodium citrate used during the synthesis of AuNP and suggested dialysed and purified AuNP would be less cytotoxic. The free ruthenium complex on RuS12·AuNP20 is non-toxic in A549 cells by MTT (appendix data 5A2) and RuS12·AuNP20 is purified by size exclusion before treating with cells. This purification step could help explain the lack of toxicity observed by MTT in this current study. It has been reported that MTT assay is not capable of differentiating between dead cells and dormant or inactive cells (Berridge *et al.*, 2005). In contrast, most researchers agree that CVS stains only live cells, which is attributed to the measurement of DNA mass of viable cells (Sliwka *et al.*, 2016) implying that the observed cell viability by CVS could be more reliable than cell viability by MTT. Further evidence to back up the lack of toxicity observed by MTT was suggested by Hauck *et al.* (2008). They attributed lack of toxicity of AuNP to its localisation in membrane bound vesicles, making the particles directly unavailable to nuclei and other organelles such as mitochondria. This suggestion was evident in this study where RuS12·AuNP20 were localised in endocytic vesicles (chapter 3 and 4) with no evidence of nuclei or mitochondria localisation and lack of toxicity by MTT.

Cellular internalization of AuNP has been linked to oxidative stress as reviewed above. Oxidative stress is the result of the disruption to the balance of oxidant and anti-oxidant levels in the cells. Most oxidant results from the increased production of ROS causing a depletion of antioxidant to detoxify the ROS (Manke *et al.*, 2013). In this current study,

only a slight non-significant increase in ROS production in A549 cells was observed, which is in agreement with Fan *et al.* (2012). This is in contrast with other studies that has shown significant increase in ROS production in cells treated with AuNPs (Dayem *et al.*, 2017; Li *et al.*, 2008; Pan *et al.*, 2009; Zhang *et al.*, 2013). ROS production has been linked to damage/localisation in mitochondria (Wang *et al.*, 2011) and/or ER stress (Tsai *et al.*, 2011) which was not observed in this study (no-localisation in mitochondria or ER). Mitochondria is the major intrinsic source of intracellular ROS generation via the electron transport chain. The lumen of the ER. is a suitable oxidizing environment (high ratio of oxidised-to-reduced forms of GSH) for protein folding and formation of disulphide bonds (Van Der Vlies *et al.*, 2003). For this reason, localisation of particles within these two organelles (mitochondria and ER) contributes to increase production of ROS. As established in chapter 4, RuS12·AuNP20 do not localise within the mitochondria or the ER of A549 cells, hence a likely reason for an insignificant effect on the production of ROS even up to 72 hours.

Asides, oxidative stress, AuNP internalization has been linked to DNA damage (Chompoosor *et al.*, 2010; Li *et al.*, 2010; Manke *et al.*, 2013; Pan *et al.*, 2009). Although there was no significant increase in the level of ROS as assessed by H₂DCFDA assay, there was evidence of redox changes in A549 cells following treatment with RuS12·AuNP20. The significantly decreased level of GSH observed at later time points (48 and 72 hours) in a concentration dependent manner. This is similar to a number of studies that showed depletion of GSH in cells following AuNP treatment (Chen & Chang, 2004; Gao *et al.*, 2011). Therefore, following treatment of A549 cells with RuS12·AuNP20, the possibility of oxidative stress occurring exist. Interference of nanoparticles or the components of nanoparticles such as thiols with H₂DCF assay have been reported to either enhance or quench fluorescence signals leading to inaccurate measurement of generated ROS (Huang

et al., 2005; Kroll *et al.*, 2012; Roesslein *et al.*, 2013). This observation could be a plausible reason for the observed ROS data by H₂DCF assay. Tan *et al.* (1998) concluded that GSH depletion should not only be linked to ROS production, but other factors such as protease activation and Ca²⁺ mobilization should be studied before concluding ROS production leads to cytotoxicity.

In addition to depleted GSH levels observed, comet assays showed a positive result for DNA damage by strand breaks and similar observation has been made in other studies (George *et al.*, 2017; Li *et al.*, 2011). The DNA strand break was statistically significant at highest concentration of 0.9 nM at 24 hours (although there was an increase at other time points) which corresponds to the decreased cell viability by CVS and MTT at 24 hours. This observation is interesting because CVS measurement is based on DNA mass, and if DNA undergoes a significant amount of DNA damage, this possibly explains the correlation in results of comet assay and cell viability especially at 24 hours. It is interesting, that cell viability and DNA strand break effects in contrast to GSH depletion and increased ROS production effect in A549 cells treated with RuS12·AuNP20 is pronounced at 24 hours compared to later time points of 48-72 hours. An explanation of this observation is the ability of cells to adapt to stress following treatment. For example by inducing the synthesis of GSH as an adaptive response to internalised ENPs (Neibert & Maysinger, 2012) and this was evident from the RT-PCR result that showed a marked increase in glutathione reductase discussed in chapter 4. A possibility for the reduction of GSH level over time may be attributed to the ability of the particle binding to GSH. This is feasible because GSH is a thiol compounds and is capable of binding to metallic nanoparticles (Tauran *et al.*, 2013).

It is unclear how RuS12·AuNP20 can cause DNA damage in A549 cells, as it showed zero co-localisation with the nucleus evident from TEM images in chapter 3 and 4. An indirect

mechanism of DNA damage proposed irrespective of localisation in membrane bound structure could be from a nonspecific interaction with proteins leading to abnormal protein production (Li *et al.*, 2008; Pernodet *et al.*, 2006).

This chapter has demonstrated that RuS12·AuNP20 treatment in A549 cells is capable of inducing slight toxicity at 24 hours, which does not inhibit cell growth even up to 72 hours, and the formation of ROS was not statistically significant as assessed by H₂DCFDA. In contrast to GSH depletion and DNA damage after prolonged period of treatment. An indirect interaction of particles with proteins is suggested as a means of oxidative stress and DNA damage, which is subject to further investigation. In a recent study by George *et al.* (2017), they reported that AuNP is capable of interfering with comet assay to generate overestimated false positive they recommend additional genotoxicity testing such as micronucleus and chromosomal aberration before making definite claim about the genotoxicity of AuNPs. Additional work investigating the cytotoxicity of RuS12·AuNP20 in A549 cells is recommended, as this would enable a more detailed understanding of the mechanism of toxicity of this functionalised AuNP in A549 cells.

Chapter 6

General Discussion and Conclusion

6.1. General Discussion

ENPs especially metallic nanoparticles and specifically AuNP has been extensively reviewed at the beginning of this thesis with an emphasis on their bio-medical importance as diagnostic and therapeutic agents. The unique characteristic of AuNP particularly their SPR is heavily exploited during their synthesis and design of functionalised AuNP with biomedical application aimed to be clinically translated. This therefore led to the design of functionalised AuNP used in this thesis; RuS12·AuNP20 a functionalised AuNP with ruthenium bipyridine SS (a luminescent transition metal complex) which has great potential as a nanoprobe. Nanoprobes can be used as contrast agents during imaging and as drug delivery vehicles for targeted therapeutics (Panchapakesan *et al.*, 2011). This thesis focused and has presented an extensive *in vitro* cellular study of RuS12·AuNP20 in A549 cells by trying to elucidate the mechanism of uptake, trafficking the particles to determine their sub-cellular localisation and cellular fate and lastly their mechanism of toxicity. The characterization of RuS12·AuNP20 was done first to ascertain the physiochemical properties of the particles before any cellular studies, which was done between 2-72 hours after exposure to nanoparticles. The characterization result of particles showed RuS12·AuNP20 to be 20 nm in size, spherical in shape and have an emission peak at the red channel wavelength. A non-toxic concentration of 0.9 nM in A549 cells was obtained by MTT assay after 72 hours exposure and used for cellular study.

The cellular uptake of RuS12·AuNP20 in A549 increased in a time dependent manner, evident from both imaging (confocal and TEM) and analytically result by ICP-MS. TEM imaging enables visualisation of individual particles which can then be monitored over time but labour intensive when it comes to be quantification, which led to the use of ICP-MS and developing a method to quantify the images acquired from confocal microscopy. Quantification of cellular uptake by both technique confirmed the time dependent increase,

which has been similarly observed in other *in vitro* study where functionalised AuNP cellular uptake increased over time (Chithrani *et al.*, 2006; Huefner *et al.*, 2014; Patra *et al.*, 2007; Xie *et al.*, 2017). Both imaging method showed the particles to be localised majorly on the cell membrane and ruffling of the cell membrane at early time between 2-4 hours after treatment indicating the start of internalization by endocytosis. Endocytosis is an established mechanism of cellular uptake of AuNP that involves either the membrane protruding or invagination to engulf particles leaving the particles trapped in vesicles (Levy *et al.*, 2010). Although we were unable to directly prove the type of endocytosis involved, we present strong evidence that macropinocytosis and clathrin-mediated endocytosis were the major routes of cellular uptake. Those evidence were from the TEM imaging (Figure 19 and 20). The possibility of having two forms of endocytosis has been reported (Brandenberger *et al.*, 2010; Yang *et al.*, 2013) and interestingly they both reported the involvement of both macropinocytosis and clathrin-mediated endocytosis and the localisation of AuNP in vesicles which is similar to our observation of localisation in vesicles in perinuclear region.

To identify these vesicles, RuS12·AuNP20 were trafficked and cellular fate monitored. Trafficking of RuS12·AuNP20 was achieved by co-localisation study of organelles involved in the endocytic pathway either by using molecular probe or transiently by transfecting A549 cells to express organelle specific markers. Co-localisation was quantified by measuring the Pearson coefficient of correlation (PCC) between RuS12·AuNP20 (red) and organelle of interest (green) and the closer the value is to 1, the higher the co-localisation. The trafficking results showed no co-localisation of RuS12·AuNP20 within the golgi, endoplasmic reticulum and mitochondria with their PCC values all below 0.3. Co-localisation of RuS12·AuNP20 was observed with the early endosomes at early time points and a time dependent increase in co-localisation within the lysosomes and autophagosomes was observed with PCC values of 0.7. The organelles that demonstrated co-localisation: early

endosomes, lysosomes and autophagosomes are all involved in the endo-lysosomal pathway, which is a degradative pathway via the lysosome irrespective of type of endocytosis (Stern *et al.*, 2012). Our result of time dependent increase in co-localisation in the endo-lysosomal pathway is summarised in table 5 and is consistent with similar studies that have observed co-localisation of functionalised AuNP with lysosomes and other acidic organelles in an increasing time dependent manner (Mironava *et al.*, 2010; Wang & Petersen, 2013; Zarska *et al.*, 2016).

Time (hours)	Cell membrane	Early endosomes	Lysosomes	Autophagosome
2	+ (TEM, CM)			
4	+ (TEM,CM)	+ (TEM,CM)		
12			+(TEM, CM)	+ (TEM, CM)
24			+(TEM, CM)	+ (TEM, CM)
48			+(TEM, CM)	+ (TEM, CM)
72			+(TEM, CM)	+ (TEM, CM)

Table 5: Summary of the trafficking of RuS12·AuNP20 in A549 cell from 2-72hrs.

Based on imaging results, RuS12·AuNP20 once internalised is localised within the lysosome and autophagosome, in a time dependent manner. **CM**; confocal imaging, **TEM**; transmission electron microscopy.

One unanticipated findings was the intactness of RuS12·AuNP20 within the lysosomes because the role of the lysosome is degradation usually via autophagy and the main function of endo-lysosomal pathway is bulk degradation of internalised materials (Panariti *et al.*, 2012; Repnik *et al.*, 2013). Autophagosomes are autophagic vacuoles involved in autophagy. The presence of autophagosomes at later time points and increase in gene expression of LC3

proteins on the inner membrane of autophagosomes indicates the involvement of autophagy as a cellular fate of RuS12·AuNP20 in A549 cells. Autophagy activation has been reported on exposure to AuNP (Li *et al.*, 2010; Zabirnyk *et al.*, 2007). However, in our case there is a possibility that RuS12·AuNP20 is altering the degradation activity of the lysosome, which then alters autophagy and prevents RuS12·AuNP20 degradation. The rationale behind this possibility is justified by a study that showed internalization of AuNP and co-localisation within the lysosome caused alkalinisation of the lysosome resulting in lysosomal impairment yet upregulating gene expression of LC3-II indicating co-localisation in autophagosomes (Ma *et al.*, 2011). Interestingly, this study suggested a blockage of autophagy rather than an activation of autophagy as a basis of observed increased autophagosomes, which could be a similar occurrence in this study.

Having established that RuS12·AuNP20 modulates autophagy, we investigated if the internalization of RuS12·AuNP20 in A549 results in cellular stress, because stress is a known activator of autophagy (Li *et al.*, 2010) and AuNP mechanism of toxicity is potentially via production of ROS which leads to oxidative stress (Alkilany & Murphy, 2010). Although there was no change in gene expression of HSP (stress related gene), there was a marked increase in CAT and GSR at early time points of 4 hours which is when active cellular uptake was observed as membrane ruffling. The GSR results suggests an increase in the conversion of oxidised glutathione to reduced glutathione (GSH) to maintain the level of cellular GSH a major antioxidant involved in cell protection and neutralization of free radicals especially ROS (Gao *et al.*, 2011). Similar to GSR, CAT protects the cells from oxidative stress caused by ROS. Interestingly, over time the GSR and CAT gene expression reduced, this observation is probably due to an adaptive mechanism by A549 cells by producing CAT and GSR, which upon more internalization over time causes a reduction of CAT, and GSR. Interestingly, the ROS data showed no significant production of ROS even

up to 72 hours but showed a significant depletion of GSH enzyme at 72 hours likely due to the more internalised RuS12·AuNP20 and also observed is a significant increase in DNA single strand break by comet assay at 24 hours, which reduced over time. The depleted GSH is an indication of oxidative stress majorly linked to over-production of ROS.

The production of ROS is usually associated with co-localisation within the mitochondria, ER or nucleus (Tsai *et al.*, 2011; Wang *et al.*, 2011), which was absent in this study. However, pathways and processes involving ROS such as DNA damage, increased CAT and GSR, depleted GSH all observed is suggestive of an indirect mechanism of toxicity of RuS12·AuNP20 in A549 cells that does not involve co-localisation within these organelles. Although by MTT assay, RuS12·AuNP20 showed no toxicity, but unexpectedly the cell viability measured by CVS decreased significantly at 24 hours. This outcome might be attributed to MTT assay measuring mitochondria activity while CVS recognises viable cells by measurement of DNA mass (Berridge *et al.*, 2005; Sliwka *et al.*, 2016) and because RuS12·AuNP20 showed no co-localisation within the mitochondria, so it is expected for MTT result to show no significant difference in cell viability. However, the result of the comet assay and CVS are similar because they both have to do with measurement of DNA although RuS12·AuNP20 showed no evidence of nuclear localisation further affirming the evidence of an indirect mechanism of toxicity. Table 7 shows a summary of data generated from studying the uptake, cellular fate and toxicity of A549 cells treated with 0.9 nM RuS12·AuNP20.

A.

	24 hours	48 hours	72 hours
MTT Assay	-	-	-
Crystal Violet Assay	0.1125 nM * 0.225 nM* 0.45 nM* 0.9 nM*	-	-
H₂DCFDA Assay	-	-	-
Glutathione Assay	-	0.45 nM*	0.45 nM* 0.9 nM*
Comet Assay	0.9 nM*	-	-

B.

	Control	4 hours	16 hours	24 hours	Summary Note
LC3	1	1.5	2.0	2.2	Slight increase compared to the control.
HSP70	1	1	1	1	No change in gene expression
CAT	1	3.1	2.7	2.6	Increase in treated which decreases over time
GSR	1	11	7.3	6.0	Significant increase at early time point, which decreases over time.

Table 6: Summary of intracellular fate and toxicity of A549 treated with RuS12·AuNP20

- a. Summary of toxicity data showing treatment with different concentrations at various time points. Only statistically significant (*) treatment compared to the control was shown. At 24 hours, crystal violet assay and comet assay showed statistical significant difference between the treated and controlled. At later time points, glutathione assay showed a decreased in glutathione level.
- b. Summary of changes in gene expressions of genes tested at various time points compared to the control. All experiment were done with the same concentration of 0.9nM of RuS12·AuNP20. The GSR and CAT showed increase at early time points, which decreased over time.

6.2 Conclusion

This thesis has demonstrated and proven the cellular uptake of RuS12·AuNP20 in A549 cells. The cellular uptake was quantified using image quantification of acquired confocal images and analytically by ICP-MS. Both methods showed a similar trend of increase over time in cellular uptake. Also established is that the cellular uptake occurs by endocytosis specifically macropinocytosis and clathrin-mediated endocytosis evident from TEM imaging. The endocytosis increased in a time dependent manner and RuS12·AuNP20 were solely localised in vesicles with no evidence of nuclear or cytoplasmic co-localisation. The trafficking of RuS12·AuNP20 over the period of 2-72 hours identified the endo-lysosomal pathway as the route of internalisation. This pathway led to a final co-localisation within lysosome and/or autophagic vesicles, which was found to modulate autophagy. Modulation of autophagy was evident from the accumulation of autophagosomes. Finally, RuS12·AuNP20 is probable of causing toxicity by an indirect mechanism of action with DNA to cause single strand break and depletion of GSH over time. Overall RuS12·AuNP20 has proven to be a stable intracellular nanoprobe in A549 cells as it does not show any evidence of degradation or losing its luminescence however, RuS12·AuNP20 modulates cellular activities capable of inducing toxicity.

6.3 Future Work/ Recommendations

This study has shown with imaging evidence macropinocytosis and clathrin-mediated endocytosis is involved in the cellular uptake of RuS12·AuNP20 in A549 cells but without direct confirmation. To confirm the exact mechanism of cellular uptake without the use of endocytic inhibitors, it would be better to study the signalling pathways involved in this process possibly by monitoring changes in gene expression of actin and other proteins such as EGFR15 present in clathrin-coated pits.

To confirm if RuS12·AuNP20 co-localisation at later time points in the lysosome is causing an increase in pH; cells could be treated with substances known to alkalinise the lysosome and compare it with cells treated with nanoparticle. This would help understand why RuS12·AuNP20 is not degraded in the lysosome. To fully understand the cellular fate of RuS12·AuNP20 in A549 cells, a study of the possibility of exocytosis would be an advantage because exocytosis of AuNP has not been documented as much as endocytosis. It could be done by splitting the cells after 72 hours exposure and seeding them without exposure to any particles but imaging the cells over the next 72 hours to see if the particles are still internalized.

Finally, because of the marked increase in CAT and GSR gene expression at early time points, ROS measurement at early time point of less than 24 hours would be recommended as well as looking at other markers of oxidative stress. Also, an in-depth study of the membrane potential and permeabilization of the mitochondria as a means of trying to proffer an insight to the indirect mechanism by which RuS12·AuNP20 induces toxicity.

References

- Adams, S. J., Lewis, D. J., Preece, J. A., & Pikramenou, Z. (2014). Luminescent gold surfaces for sensing and imaging: Patterning of transition metal probes. *Acs Applied Materials & Interfaces*, 6(14), 11598-11608.
- Adler, J., & Parmryd, I. (2010). Quantifying colocalization by correlation: The Pearson correlation coefficient is superior to the Mander's overlap coefficient. *Cytometry Part A*, 77a(8), 733-742.
- Aillon, K. L., Xie, Y. M., El-Gendy, N., Berkland, C. J., & Forrest, M. L. (2009). Effects of nanomaterial physicochemical properties on in vivo toxicity. *Advanced Drug Delivery Reviews*, 61(6), 457-466.
- Albanese, A., & Chan, W. C. W. (2011). Effect of gold nanoparticle aggregation on cell uptake and toxicity. *Acs Nano*, 5(7), 5478-5489.
- Alharbi, K. K., & Al-Sheikh, Y. A. (2014). Role and implications of nanodiagnosics in the changing trends of clinical diagnosis. *Saudi J Biol Sci*, 21(2), 109-117.
- Alkilany, A. M., & Murphy, C. J. (2010). Toxicity and cellular uptake of gold nanoparticles: What we have learned so far? *Journal of Nanoparticle Research*, 12(7), 2313-2333.
- Alkilany, A. M., Nagaria, P. K., Hexel, C. R., Shaw, T. J., Murphy, C. J., & Wyatt, M. D. (2009). Cellular uptake and cytotoxicity of gold nanorods: Molecular origin of cytotoxicity and surface effects. *Small*, 5(6), 701-708.
- Amendola, V., Pilot, R., Frascioni, M., Marago, O. M., & Iati, M. A. (2017). Surface plasmon resonance in gold nanoparticles: A review. *Journal of Physics-Condensed Matter*, 29(20).
- Andrews, N. W., Almeida, P. E., & Corrotte, M. (2014). Damage control: Cellular mechanisms of plasma membrane repair. *Trends in Cell Biology*, 24(12), 734-742.
- Appenzeller, T. (1991). The man who dared to think small. *Science*, 254(5036), 1300.
- Arrowsmith, R. L., Pascu, S. I., & Smugowski, H. (2012). New developments in the biomedical chemistry of metal complexes: From small molecules to nanotheranostic design. *Organometallic Chemistry*, Vol 38, 38, 1-35.
- Arvizo, R., Bhattacharya, R., & Mukherjee, P. (2010). Gold nanoparticles: Opportunities and challenges in nanomedicine. *Expert Opinion on Drug Delivery*, 7(6), 753-763.
- Auffan, M., Rose, J., Wiesner, M. R., & Bottero, J.-Y. (2009). Chemical stability of metallic nanoparticles: A parameter controlling their potential cellular toxicity in vitro. *Environmental Pollution*, 157(4), 1127-1133.
- Babu, K., & Dhamodharan, R. (2009). Synthesis of polymer grafted magnetite nanoparticle with the highest grafting density via controlled radical polymerization. *Nanoscale Research Letters*, 4(9), 1090-1102.
- Bazak, R., Houri, M., Achy, S. E., Hussein, W., & Refaat, T. (2014). Passive targeting of nanoparticles to cancer: A comprehensive review of the literature. *Mol Clin Oncol*, 2(6), 904-908.
- Berne, B. J., & Pecora, R. (2000). *Dynamic light scattering: With applications to chemistry, biology, and physics*: Courier Corporation.
- Berridge, M. V., Herst, P. M., & Tan, A. S. (2005). Tetrazolium dyes as tools in cell biology: New insights into their cellular reduction. *Biotechnology Annual Review*, 11, 127-152.
- Bertoncello, P., Kefalas, E. T., Pikramenou, Z., Unwin, P. R., & Forster, R. J. (2006). Adsorption dynamics and electrochemical and photophysical properties of thiolated ruthenium 2,2'-bipyridine monolayers. *J Phys Chem B*, 110(20), 10063-10069.
- Bhatt, I., & Tripathi, B. N. (2011). Interaction of engineered nanoparticles with various components of the environment and possible strategies for their risk assessment. *Chemosphere*, 82(3), 308-317.

- Biju, V., Itoh, T., Anas, A., Sujith, A., & Ishikawa, M. (2008). Semiconductor quantum dots and metal nanoparticles: Syntheses, optical properties, and biological applications. *Analytical and Bioanalytical Chemistry*, 391(7), 2469-2495.
- Birben, E., Sahiner, U. M., Sackesen, C., Erzurum, S., & Kalayci, O. (2012). Oxidative stress and antioxidant defense. *World Allergy Organ J*, 5(1), 9-19.
- Boisselier, E., & Astruc, D. (2009). Gold nanoparticles in nanomedicine: Preparations, imaging, diagnostics, therapies and toxicity. *Chemical Society Reviews*, 38(6), 1759-1782.
- Bolisetty, S., & Jaimes, E. A. (2013). Mitochondria and reactive oxygen species: Physiology and pathophysiology. *International Journal of Molecular Sciences*, 14(3), 6306-6344.
- Bolte, S., & Cordelieres, F. P. (2006). A guided tour into subcellular colocalization analysis in light microscopy. *Journal of Microscopy-Oxford*, 224, 213-232.
- Botchway, S. W., Charnley, M., Haycock, J. W., Parker, A. W., Rochester, D. L., Weinstein, J. A., & Williams, J. A. G. (2008). Time-resolved and two-photon emission imaging microscopy of live cells with inert platinum complexes. *Proceedings of the National Academy of Sciences of the United States of America*, 105(42), 16071-16076.
- Brandenberger, C., Muhlfeld, C., Ali, Z., Lenz, A. G., Schmid, O., Parak, W. J., Gehr, P., & Rothen-Rutishauser, B. (2010). Quantitative evaluation of cellular uptake and trafficking of plain and polyethylene glycol-coated gold nanoparticles. *Small*, 6(15), 1669-1678.
- Brown, M. A., Abbas, Z., Kleibert, A., Green, R. G., Goel, A., May, S., & Squires, T. M. (2016). Determination of surface potential and electrical double-layer structure at the aqueous electrolyte-nanoparticle interface. *Physical Review X*, 6(1).
- Brust, M., Walker, M., Bethell, D., Schiffrin, D. J., & Whyman, R. (1994). Synthesis of thiol-derivatised gold nanoparticles in a two-phase liquid-liquid system. *Journal of the Chemical Society, Chemical Communications*(7), 801-802.
- Burgess, P., Hutt, P. B., Farokhzad, O. C., Langer, R., Minick, S., & Zale, S. (2010). On firm ground: Ip protection of therapeutic nanoparticles. *Nat Biotechnol*, 28(12), 1267-1270.
- Byrne, J. D., Betancourt, T., & Brannon-Peppas, L. (2008). Active targeting schemes for nanoparticle systems in cancer therapeutics. *Adv Drug Deliv Rev*, 60(15), 1615-1626.
- Camacho, A. S. (2015). Focusing nanoplasmonics. *J Nano Sc Tech*, 3, 10-17.
- Cao, Y. C., Jin, R., Nam, J. M., Thaxton, C. S., & Mirkin, C. A. (2003). Raman dye-labeled nanoparticle probes for proteins. *J Am Chem Soc*, 125(48), 14676-14677.
- Capel, V., Vllasaliu, D., Watts, P., & Stolnik, S. (2016). Insight into the relationship between the cell culture model, cell trafficking and sirna silencing efficiency. *Biochemical and Biophysical Research Communications*, 477(2), 260-265.
- Caruthers, S. D., Wickline, S. A., & Lanza, G. M. (2007). Nanotechnological applications in medicine. *Curr Opin Biotechnol*, 18(1), 26-30.
- Castro, E., & Kumar, A. (2013). Nanoparticles in drug delivery systems. *Nanomedicine in drug delivery*, 1-22.
- Chang, Y. L., Yang, S. T., Liu, J. H., Dong, E., Wang, Y. W., Cao, A. N., Liu, Y. F., & Wang, H. F. (2011). In vitro toxicity evaluation of graphene oxide on a549 cells. *Toxicology Letters*, 200(3), 201-210.
- Chapman, J., Sullivan, T., & Regan, F. (2012). Nanoparticles in anti-microbial materials use and characterisation conclusions. *Nanoparticles in Anti-Microbial Materials: Use and Characterisation*(23), 228-230.
- Chapman, S., Dobrovolskai, M., Farahani, K., Goodwin, A., Joshi, A., Lee, H., Meade, T., Pomper, M., Ptak, K., Rao, J., Singh, R., Sridhar, S., Stern, S., Wang, A., Weaver, J. B., Woloschak, G., & Yang, L. (2013). Nanoparticles for cancer imaging: The good, the bad, and the promise. *Nano Today*, 8(5), 454-460.
- Chen, S. J., & Chang, H. T. (2004). Nile red-adsorbed gold nanoparticles for selective determination of thiols based on energy transfer and aggregation. *Analytical Chemistry*, 76(13), 3727-3734.

- Chen, X., Chen, C. B., Udalagama, C. N. B., Ren, M. Q., Fong, K. E., Yung, L. Y. L., Giorgia, P., Bettiol, A. A., & Watt, F. (2013). High-resolution 3d imaging and quantification of gold nanoparticles in a whole cell using scanning transmission ion microscopy. *Biophysical Journal*, *104*(7), 1419-1425.
- Chen, X. P., Zhong, Z. F., Xu, Z. T., Chen, L. D., & Wang, Y. T. (2010). 2',7'-dichlorodihydrofluorescein as a fluorescent probe for reactive oxygen species measurement: Forty years of application and controversy. *Free Radical Research*, *44*(6), 587-604.
- Chithrani, B. D., & Chan, W. C. (2007). Elucidating the mechanism of cellular uptake and removal of protein-coated gold nanoparticles of different sizes and shapes. *Nano Letters*, *7*(6), 1542-1550.
- Chithrani, B. D., Ghazani, A. A., & Chan, W. C. W. (2006). Determining the size and shape dependence of gold nanoparticle uptake into mammalian cells. *Nano Letters*, *6*(4), 662-668.
- Chithrani, D. B. (2011). Optimization of bio-nano interface using gold nanostructures as a model nanoparticle system. *Insciences J.*, *1*(3), 115-135.
- Cho, E. J., Holback, H., Liu, K. C., Abouelmagd, S. A., Park, J., & Yeo, Y. (2013). Nanoparticle characterization: State of the art, challenges, and emerging technologies. *Mol Pharm*, *10*(6), 2093-2110.
- Chompoosor, A., Saha, K., Ghosh, P. S., Macarthy, D. J., Miranda, O. R., Zhu, Z. J., Arcaro, K. F., & Rotello, V. M. (2010). The role of surface functionality on acute cytotoxicity, ros generation and DNA damage by cationic gold nanoparticles. *Small*, *6*(20), 2246-2249.
- Chow, M. K., & Zukoski, C. F. (1994). Gold sol formation mechanisms - role of colloidal stability. *Journal of Colloid and Interface Science*, *165*(1), 97-109.
- Chueh, P. J., Liang, R. Y., Lee, Y. H., Zeng, Z. M., & Chuang, S. M. (2014). Differential cytotoxic effects of gold nanoparticles in different mammalian cell lines. *J Hazard Mater*, *264*, 303-312.
- Codogno, P., & Meijer, A. J. (2005). Autophagy and signaling: Their role in cell survival and cell death. *Cell Death and Differentiation*, *12*, 1509-1518.
- Collins, A. R. (2004). The comet assay for DNA damage and repair - principles, applications, and limitations. *Molecular Biotechnology*, *26*(3), 249-261.
- Colomban, P., Tournie, A., & Ricciardi, P. (2009). Raman spectroscopy of copper nanoparticle-containing glass matrices: Ancient red stained-glass windows. *Journal of Raman Spectroscopy*, *40*(12), 1949-1955.
- Comby, S., Surender, E. M., Kotova, O., Truman, L. K., Molloy, J. K., & Gunnlaugsson, T. (2014). Lanthanide-functionalized nanoparticles as mri and luminescent probes for sensing and/or imaging applications. *Inorg. Chem*, *53*(4), 1867-1879.
- Conner, S. D., & Schmid, S. L. (2003). Regulated portals of entry into the cell. *Nature*, *422*(6927), 37-44.
- Connor, E. E., Mwamuka, J., Gole, A., Murphy, C. J., & Wyatt, M. D. (2005). Gold nanoparticles are taken up by human cells but do not cause acute cytotoxicity. *Small*, *1*(3), 325-327.
- Contado, C. (2015). Nanomaterials in consumer products: A challenging analytical problem. *Frontiers in Chemistry*, *3*.
- Damm, E. M., Pelkmans, L., Kartenbeck, J., Mezzacasa, A., Kurzckalia, T., & Helenius, A. (2005). Clathrin- and caveolin-1-independent endocytosis: Entry of simian virus 40 into cells devoid of caveolae. *Journal of Cell Biology*, *168*(3), 477-488.
- Davies, A., Lewis, D. J., Watson, S. P., Thomas, S. G., & Pikramenou, Z. (2012). Ph-controlled delivery of luminescent europium coated nanoparticles into platelets. *Proceedings of the National Academy of Sciences of the United States of America*, *109*(6), 1862-1867.
- Davis, M. E., Chen, Z., & Shin, D. M. (2008). Nanoparticle therapeutics: An emerging treatment modality for cancer. *Nature Reviews Drug Discovery*, *7*(9), 771-782.

- Dayem, A. A., Hossain, M. K., Lee, S. B., Kim, K., Saha, S. K., Yang, G. M., Choi, H. Y., & Cho, S. G. (2017). The role of reactive oxygen species (ros) in the biological activities of metallic nanoparticles. *International Journal of Molecular Sciences*, *18*(1).
- De Jong, W. H., & Borm, P. J. A. (2008). Drug delivery and nanoparticles: Applications and hazards. *International Journal of Nanomedicine*, *3*(2), 133-149.
- De Marzi, L., Ottaviano, L., Perrozzi, F., Nardone, M., Santucci, S., De Lapuente, J., Borrás, M., Treossi, E., Palermo, V., & Poma, A. (2014). Flake size-dependent cyto and genotoxic evaluation of graphene oxide on in vitro a549, caco2 and vero cell lines. *Journal of Biological Regulators and Homeostatic Agents*, *28*(2), 281-289.
- Degenhardt, K., Mathew, R., Beaudoin, B., Bray, K., Anderson, D., Chen, G., Mukherjee, C., Shi, Y., Gélinas, C., Fan, Y., Nelson, D. A., Jin, S., & White, E. (2006). Autophagy promotes tumor cell survival and restricts necrosis, inflammation, and tumorigenesis. *Cancer Cell*, *10*(1), 51-64.
- Demas, J. N., & DeGraff, B. A. (2001). Applications of luminescent transition platinum group metal complexes to sensor technology and molecular probes. *Coordination Chemistry Reviews*, *211*, 317-351.
- des Rieux, A., Pourcelle, V., Cani, P. D., Marchand-Brynaert, J., & Preat, V. (2013). Targeted nanoparticles with novel non-peptidic ligands for oral delivery. *Adv Drug Deliv Rev*, *65*(6), 833-844.
- Dickinson, D. A., & Forman, H. J. (2002). Cellular glutathione and thiols metabolism. *Biochemical Pharmacology*, *64*(5-6), 1019-1026.
- Ding, F. A., Li, Y. P., Liu, J., Liu, L., Yu, W. M., Wang, Z., Ni, H. F., Liu, B. C., & Chen, P. S. (2014). Overendocytosis of gold nanoparticles increases autophagy and apoptosis in hypoxic human renal proximal tubular cells. *International Journal of Nanomedicine*, *9*, 4317-4330.
- Doherty, G. J., & McMahon, H. T. (2009). Mechanisms of endocytosis. *Annual Review of Biochemistry*, *78*, 857-902.
- dos Santos, T., Varela, J., Lynch, I., Salvati, A., & Dawson, K. A. (2011). Effects of transport inhibitors on the cellular uptake of carboxylated polystyrene nanoparticles in different cell lines. *PLoS One*, *6*(9), e24438.
- Duncan, B., Kim, C., & Rotello, V. M. (2010). Gold nanoparticle platforms as drug and biomacromolecule delivery systems. *Journal of Controlled Release*, *148*(1), 122-127.
- Dykman, L., & Khlebtsov, N. (2012). Gold nanoparticles in biomedical applications: Recent advances and perspectives. *Chemical Society Reviews*, *41*(6), 2256-2282.
- Edmundson, M. C., Capeness, M., & Horsfall, L. (2014). Exploring the potential of metallic nanoparticles within synthetic biology. *New Biotechnology*, *31*(6), 572-578.
- Elkin, S. R., Lakoduk, A. M., & Schmid, S. L. (2016). Endocytic pathways and endosomal trafficking: A primer. *Wiener Medizinische Wochenschrift*, *166*(7-8), 196-204.
- Elmes, R. B. P., Orange, K. N., Cloonan, S. M., Williams, D. C., & Gunnlaugsson, T. (2011). Luminescent ruthenium(ii) polypyridyl functionalized gold nanoparticles; their DNA binding abilities and application as cellular imaging agents. *Journal of the American Chemical Society*, *133*(40), 15862-15865.
- Engel, S., Fritz, E.-C., & Ravoo, B. J. (2017). New trends in the functionalization of metallic gold: From organosulfur ligands to n-heterocyclic carbenes. *Chemical Society Reviews*, *46*(8), 2057-2075.
- Eskelinen, E. L. (2005). Maturation of autophagic vacuoles in mammalian cells. *Autophagy*, *1*(1), 1-10.
- Eskelinen, E. L., & Saftig, P. (2009). Autophagy: A lysosomal degradation pathway with a central role in health and disease. *Biochim Biophys Acta*, *1793*(4), 664-673.
- Eustis, S., & El-Sayed, M. A. (2006). Why gold nanoparticles are more precious than pretty gold: Noble metal surface plasmon resonance and its enhancement of the radiative and nonradiative properties of nanocrystals of different shapes. *Chemical Society Reviews*, *35*(3), 209-217.

- Fan, Z. L., Yang, X., Li, Y. Y., Li, S. P., Niu, S. W., Wu, X. C., Wei, J. Y., & Nie, G. J. (2012). Deciphering an underlying mechanism of differential cellular effects of nanoparticles: An example of hsp-70 dependent induction of hsp-70 expression by gold nanorod. *Biointerphases*, 7(1-4).
- Fang, L., Neutzner, A., Turtschi, S., Flammer, J., & Mozaffarieh, M. (2015). Comet assay as an indirect measure of systemic oxidative stress. *Journal of Visualized Experiments*(99).
- Faraday, M. (1857). The bakerian lecture: Experimental relations of gold (and other metals) to light. *Philosophical Transactions of the Royal Society of London*, 147, 145-181.
- Fard, J. K., Jafari, S., & Eghbal, M. A. (2015). A review of molecular mechanisms involved in toxicity of nanoparticles. *Advanced Pharmaceutical Bulletin*, 5(4), 447-454.
- Feng, X. L., Chen, A. J., Zhang, Y. L., Wang, J. F., Shao, L. Q., & Wei, L. M. (2015). Central nervous system toxicity of metallic nanoparticles. *International Journal of Nanomedicine*, 10, 4321-4340.
- Feoktistova, M., Geserick, P., & Leverkus, M. (2016). Crystal violet assay for determining viability of cultured cells. *Cold Spring Harb Protoc*, 2016(4), pdb prot087379.
- Fernandez-Moreira, V., Thorp-Greenwood, F. L., & Coogan, M. P. (2010). Application of d(6) transition metal complexes in fluorescence cell imaging. *Chemical Communications*, 46(2), 186-202.
- Fitzpatrick, J. A. J., Inouye, Y., Manley, S., & Moerner, W. E. (2014). From "there's plenty of room at the bottom" to seeing what is actually there. *Chemphyschem*, 15(4), 547-549.
- Fleischer, C. C., & Payne, C. K. (2014). Nanoparticle-cell interactions: Molecular structure of the protein corona and cellular outcomes. *Acc Chem Res*, 47(8), 2651-2659.
- Foster, K. A., Oster, C. G., Mayer, M. M., Avery, M. L., & Audus, K. L. (1998). Characterization of the A549 cell line as a type II pulmonary epithelial cell model for drug metabolism. *Experimental Cell Research*, 243(2), 359-366.
- Frens, G. (1973). Controlled nucleation for the regulation of the particle size in monodisperse gold suspensions. *Nature*, 241(105), 20-22.
- Fulda, S., Gorman, A. M., Hori, O., & Samali, A. (2010). Cellular stress responses: Cell survival and cell death. *Int J Cell Biol*, 2010, 214074.
- Gao, H. J., Shi, W. D., & Freund, L. B. (2005). Mechanics of receptor-mediated endocytosis. *Proceedings of the National Academy of Sciences of the United States of America*, 102(27), 9469-9474.
- Gao, W., Xu, K. H., Ji, L. F., & Tang, B. (2011). Effect of gold nanoparticles on glutathione depletion-induced hydrogen peroxide generation and apoptosis in H17702 cells. *Toxicology Letters*, 205(1), 86-95.
- George, J. M., Magogotya, M., Vetten, M. A., Buys, A. V., & Gulumian, M. (2017). An investigation of the genotoxicity and interference of gold nanoparticles in commonly used in vitro mutagenicity and genotoxicity assays. *Toxicological sciences: an official journal of the Society of Toxicology*.
- Ghosh, S. K., & Pal, T. (2007). Interparticle coupling effect on the surface plasmon resonance of gold nanoparticles: From theory to applications. *Chem Rev*, 107(11), 4797-4862.
- Giard, D. J., Aaronson, S. A., Todaro, G. J., Arnstein, P., Kersey, J. H., Dosik, H., & Parks, W. P. (1973). In vitro cultivation of human tumors: Establishment of cell lines derived from a series of solid tumors. *Journal of the National Cancer Institute*, 51(5), 1417-1423.
- Gibson, J. D., Khanal, B. P., & Zubarev, E. R. (2007). Paclitaxel-functionalized gold nanoparticles. *Journal of the American Chemical Society*, 129(37), 11653-11661.
- Giljohann, D. A., Seferos, D. S., Daniel, W. L., Massich, M. D., Patel, P. C., & Mirkin, C. A. (2010). Gold nanoparticles for biology and medicine. *Angew Chem Int Ed Engl*, 49(19), 3280-3294.
- Glomm, W. R., Moses, S. J., Brennaman, M. K., Papanikolas, J. M., & Franzen, S. (2005). Detection of adsorption of Ru(II) and Os(II) polypyridyl complexes on gold and silver nanoparticles by single-photon counting emission measurements. *Journal of Physical Chemistry B*, 109(2), 804-810.

- Gong, N., Chen, S., Jin, S., Zhang, J., Wang, P. C., & Liang, X. J. (2015). Effects of the physicochemical properties of gold nanostructures on cellular internalization. *Regen Biomater*, 2(4), 273-280.
- Goodman, C. M., McCusker, C. D., Yilmaz, T., & Rotello, V. M. (2004). Toxicity of gold nanoparticles functionalized with cationic and anionic side chains. *Bioconjugate Chemistry*, 15(4), 897-900.
- Gordon, P. B., & Seglen, P. O. (1988). Prelysosomal convergence of autophagic and endocytic pathways. *Biochemical and Biophysical Research Communications*, 151(1), 40-47.
- Green, R. M., Graham, M., O'Donovan, M. R., Chipman, J. K., & Hodges, N. J. (2006). Subcellular compartmentalization of glutathione: Correlations with parameters of oxidative stress related to genotoxicity. *Mutagenesis*, 21(6), 383-390.
- Griffiths, G., Hoflack, B., Simons, K., Mellman, I., & Kornfeld, S. (1988). The mannose 6-phosphate receptor and the biogenesis of lysosomes. *Cell*, 52(3), 329-341.
- Gruenberg, J., & Stenmark, H. (2004). The biogenesis of multivesicular endosomes. *Nat Rev Mol Cell Biol*, 5(4), 317-323.
- Gu, Y. J., Cheng, J., Lin, C. C., Lam, Y. W., Cheng, S. H., & Wong, W. T. (2009). Nuclear penetration of surface functionalized gold nanoparticles. *Toxicol Appl Pharmacol*, 237(2), 196-204.
- Gual, A., Godard, C., Castillon, S., & Claver, C. (2010). Soluble transition-metal nanoparticles-catalysed hydrogenation of arenes. *Dalton Transactions*, 39(48), 11499-11512.
- Gunduz, N., Ceylan, H., Guler, M. O., & Tekinay, A. B. (2017). Intracellular accumulation of gold nanoparticles leads to inhibition of macropinocytosis to reduce the endoplasmic reticulum stress. *Scientific Reports*, 7.
- Hamad-Schifferli, K. (2015). Exploiting the novel properties of protein coronas: Emerging applications in nanomedicine. *Nanomedicine (Lond)*, 10(10), 1663-1674.
- Handy, R. D., & Shaw, B. J. (2007). Toxic effects of nanoparticles and nanomaterials: Implications for public health, risk assessment and the public perception of nanotechnology. *Health Risk & Society*, 9(2), 125-144.
- Hauck, T. S., Ghazani, A. A., & Chan, W. C. W. (2008). Assessing the effect of surface chemistry on gold nanorod uptake, toxicity, and gene expression in mammalian cells. *Small*, 4(1), 153-159.
- Heiligtag, F. J., & Niederberger, M. (2013). The fascinating world of nanoparticle research. *Materials Today*, 16(7-8), 262-271.
- Hillaireau, H., & Couvreur, P. (2009). Nanocarriers' entry into the cell: Relevance to drug delivery. *Cellular and Molecular Life Sciences*, 66(17), 2873-2896.
- Hissin, P. J., & Hilf, R. (1976). A fluorometric method for determination of oxidized and reduced glutathione in tissues. *Anal Biochem*, 74(1), 214-226.
- Hochella, M. F., Spencer, M. G., & Jones, K. L. (2015). Nanotechnology: Nature's gift or scientists' brainchild? *Environmental Science-Nano*, 2(2), 114-119.
- Hoet, P. H., Bruske-Hohlfeld, I., & Salata, O. V. (2004). Nanoparticles - known and unknown health risks. *J Nanobiotechnology*, 2(1), 12.
- Horikoshi, S., & Serpone, N. (2013). Introduction to nanoparticles *Microwaves in nanoparticle synthesis* (pp. 1-24): Wiley-VCH Verlag GmbH & Co. KGaA.
- Hotze, E. M., Phenrat, T., & Lowry, G. V. (2010). Nanoparticle aggregation: Challenges to understanding transport and reactivity in the environment. *Journal of Environmental Quality*, 39(6), 1909-1924.
- Hoyvik, H., Gordon, P. B., & Seglen, P. O. (1987). Convergence of autophagic and endocytic pathways at the level of the lysosome. *Biochemical Society Transactions*, 15(5), 964-965.
- Hu, M., Chen, J. Y., Li, Z. Y., Au, L., Hartland, G. V., Li, X. D., Marquez, M., & Xia, Y. N. (2006). Gold nanostructures: Engineering their plasmonic properties for biomedical applications. *Chemical Society Reviews*, 35(11), 1084-1094.
- Huang, D. T., Zhou, H. L., & Gao, J. H. (2015a). Nanoparticles modulate autophagic effect in a dispersity-dependent manner. *Scientific Reports*, 5.

- Huang, D. T., Zhou, H. L., Liu, H. Y., & Gao, J. H. (2015b). The cytotoxicity of gold nanoparticles is dispersity-dependent. *Dalton Transactions*, 44(41), 17911-17915.
- Huang, T., & Murray, R. W. (2002). Quenching of [ru(bpy)(3)](2+) fluorescence by binding to au nanoparticles. *Langmuir*, 18(18), 7077-7081.
- Huang, X., & El-Sayed, M. A. (2010). Gold nanoparticles: Optical properties and implementations in cancer diagnosis and photothermal therapy. *Journal of Advanced Research*, 1(1), 13-28.
- Huang, X. H., El-Sayed, I. H., Yi, X. B., & El-Sayed, M. A. (2005). Gold nanoparticles: Catalyst for the oxidation of nadh to nad(+). *Journal of Photochemistry and Photobiology B-Biology*, 81(2), 76-83.
- Huang, X. H., Jain, P. K., El-Sayed, I. H., & El-Sayed, M. A. (2007). Gold nanoparticles: Interesting optical properties and recent applications in cancer diagnostic and therapy. *Nanomedicine*, 2(5), 681-693.
- Huefner, A., Septiadi, D., Wilts, B. D., Patel, I. I., Kuan, W. L., Fragniere, A., Barker, R. A., & Mahajan, S. (2014). Gold nanoparticles explore cells: Cellular uptake and their use as intracellular probes. *Methods*, 68(2), 354-363.
- Huotari, J., & Helenius, A. (2011). Endosome maturation. *EMBO J*, 30(17), 3481-3500.
- Hussain, S. M., Hess, K. L., Gearhart, J. M., Geiss, K. T., & Schlager, J. J. (2005). In vitro toxicity of nanoparticles in brl 3a rat liver cells. *Toxicology in Vitro*, 19(7), 975-983.
- Hutter, E., Boridy, S., Labrecque, S., Lalancette-Hebert, M., Kriz, J., Winnik, F. M., & Maysinger, D. (2010). Microglial response to gold nanoparticles. *Acs Nano*, 4(5), 2595-2606.
- ISO, N. (2008). Terminology and definitions for nano-objects—nanoparticle, nanofibre and nanoplate. *ISO/TS*, 27687.
- Iversen, T. G., Skotland, T., & Sandvig, K. (2011). Endocytosis and intracellular transport of nanoparticles: Present knowledge and need for future studies. *Nano Today*, 6(2), 176-185.
- Jain, K. K. (2008). Nanomedicine: Application of nanobiotechnology in medical practice. *Med Princ Pract*, 17(2), 89-101.
- Jain, P. K., Huang, X. H., El-Sayed, I. H., & El-Sayed, M. A. (2008). Noble metals on the nanoscale: Optical and photothermal properties and some applications in imaging, sensing, biology, and medicine. *Accounts of Chemical Research*, 41(12), 1578-1586.
- Jain, P. K., Lee, K. S., El-Sayed, I. H., & El-Sayed, M. A. (2006). Calculated absorption and scattering properties of gold nanoparticles of different size, shape, and composition: Applications in biological imaging and biomedicine. *Journal of Physical Chemistry B*, 110(14), 7238-7248.
- Jebb, M., Sudeep, P. K., Pramod, P., Thomas, K. G., & Kamat, P. V. (2007). Ruthenium(ii) trisbipyridine functionalized gold nanorods. Morphological changes and excited-state interactions. *Journal of Physical Chemistry B*, 111(24), 6839-6844.
- Jena, N. R. (2012). DNA damage by reactive species: Mechanisms, mutation and repair. *J Biosci*, 37(3), 503-517.
- Jiang, W., Kim, B. Y. S., Rutka, J. T., & Chan, W. C. W. (2008). Nanoparticle-mediated cellular response is size-dependent. *Nature Nanotechnology*, 3(3), 145-150.
- Jin, R. C., Cao, Y. W., Mirkin, C. A., Kelly, K. L., Schatz, G. C., & Zheng, J. G. (2001). Photoinduced conversion of silver nanospheres to nanoprisms. *Science*, 294(5548), 1901-1903.
- Jo, S. D., Ku, S. H., Won, Y. Y., Kim, S. H., & Kwon, I. C. (2016). Targeted nanotheranostics for future personalized medicine: Recent progress in cancer therapy. *Theranostics*, 6(9), 1362-1377.
- Johannes, L., Parton, R. G., Bassereau, P., & Mayor, S. (2015). Building endocytic pits without clathrin. *Nature Reviews Molecular Cell Biology*, 16(5), 311-321.
- Jovic, M., Sharma, M., Rahajeng, J., & Caplan, S. (2010). The early endosome: A busy sorting station for proteins at the crossroads. *Histology and Histopathology*, 25(1), 99-112.
- Juris, A., Balzani, V., Barigelletti, F., Campagna, S., Belsler, P. I., & Von Zelewsky, A. (1988). Ru (ii) polypyridine complexes: Photophysics, photochemistry, eletrochemistry, and chemiluminescence. *Coordination Chemistry Reviews*, 84, 85-277.

- Kamaly, N., Xiao, Z., Valencia, P. M., Radovic-Moreno, A. F., & Farokhzad, O. C. (2012). Targeted polymeric therapeutic nanoparticles: Design, development and clinical translation. *Chem Soc Rev*, *41*(7), 2971-3010.
- Karatas, O. F., Sezgin, E., Aydin, O., & Culha, M. (2009). Interaction of gold nanoparticles with mitochondria. *Colloids and Surfaces B-Biointerfaces*, *71*(2), 315-318.
- Kessler, R. (2011a). Engineered nanoparticles in consumer products understanding a new ingredient. *Environmental Health Perspectives*, *119*(3), 121-125.
- Kessler, R. (2011b). Engineered nanoparticles in consumer products: Understanding a new ingredient. *Environ Health Perspect*, *119*(3), a120-125.
- Khan, J. A., Pillai, B., Das, T. K., Singh, Y., & Maiti, S. (2007). Molecular effects of uptake of gold nanoparticles in hela cells. *Chembiochem*, *8*(11), 1237-1240.
- Kim, C. S., Li, X. N., Jiang, Y., Yan, B., Tonga, G. Y., Ray, M., Solfiell, D. J., & Rotello, V. M. (2015). Cellular imaging of endosome entrapped small gold nanoparticles. *Methodsx*, *2*, 306-315.
- Kim, J. A., Aberg, C., Salvati, A., & Dawson, K. A. (2012). Role of cell cycle on the cellular uptake and dilution of nanoparticles in a cell population. *Nature Nanotechnology*, *7*(1), 62-68.
- Kim, T., & Hyeon, T. (2014). Applications of inorganic nanoparticles as therapeutic agents. *Nanotechnology*, *25*(1).
- Kirkham, M., & Parton, R. G. (2005). Clathrin-independent endocytosis: New insights into caveolae and non-caveolar lipid raft carriers (vol 1744, pg 273, 2005). *Biochimica Et Biophysica Acta-Molecular Cell Research*, *1746*(3), 349-363.
- Kobayashi, H., Watanabe, R., & Choyke, P. L. (2013). Improving conventional enhanced permeability and retention (EPR) effects; what is the appropriate target? *Theranostics*, *4*(1), 81-89.
- Kodiha, M., Wang, Y. M., Hutter, E., Maysinger, D., & Stochaj, U. (2015). Off to the organelles - killing cancer cells with targeted gold nanoparticles. *Theranostics*, *5*(4), 357-370.
- Kou, L., Sun, J., Zhai, Y., & He, Z. (2013). The endocytosis and intracellular fate of nanomedicines: Implication for rational design. *Asian Journal of Pharmaceutical Sciences*, *8*(1), 1-10.
- Kovacic, P., & Somanathan, R. (2013). Nanoparticles: Toxicity, radicals, electron transfer, and antioxidants. *Oxidative Stress and Nanotechnology: Methods and Protocols*, 15-35.
- Kraynov, A., & Müller, T. E. (2011). Concepts for the stabilization of metal nanoparticles in ionic liquids *Applications of ionic liquids in science and technology*: InTech.
- Kreyling, W. G., Abdelmonem, A. M., Ali, Z., Alves, F., Geiser, M., Haberl, N., Hartmann, R., Hirn, S., de Aberasturi, D. J., Kantner, K., Khadem-Saba, G., Montenegro, J. M., Rejman, J., Rojo, T., de Larramendi, I. R., Ufartes, R., Wenk, A., & Parak, W. J. (2015). In vivo integrity of polymer-coated gold nanoparticles. *Nature Nanotechnology*, *10*(7), 619-+.
- Kroll, A., Pillukat, M. H., Hahn, D., & Schneckeburger, J. (2009). Current in vitro methods in nanoparticle risk assessment: Limitations and challenges. *European Journal of Pharmaceutics and Biopharmaceutics*, *72*(2), 370-377.
- Kroll, A., Pillukat, M. H., Hahn, D., & Schneckeburger, J. (2012). Interference of engineered nanoparticles with in vitro toxicity assays. *Archives of Toxicology*, *86*(7), 1123-1136.
- Kuhn, D. A., Vanhecke, D., Michen, B., Blank, F., Gehr, P., Petri-Fink, A., & Rothen-Rutishauser, B. (2014). Different endocytotic uptake mechanisms for nanoparticles in epithelial cells and macrophages. *Beilstein Journal of Nanotechnology*, *5*, 1625-1636.
- Kunzmann, A., Andersson, B., Thurnherr, T., Krug, H., Scheynius, A., & Fadeel, B. (2011). Toxicology of engineered nanomaterials: Focus on biocompatibility, biodistribution and biodegradation. *Biochimica Et Biophysica Acta-General Subjects*, *1810*(3), 361-373.
- Lakadamyali, M., Rust, M. J., & Zhuang, X. (2006). Ligands for clathrin-mediated endocytosis are differentially sorted into distinct populations of early endosomes. *Cell*, *124*(5), 997-1009.
- Levy, R., Shaheen, U., Cesbron, Y., & See, V. (2010). Gold nanoparticles delivery in mammalian live cells: A critical review. *Nano Rev*, *1*.
- Lewis, D. J., & Pikramenou, Z. (2014). Lanthanide-coated gold nanoparticles for biomedical applications. *Coordination Chemistry Reviews*, *273*, 213-225.

- Li, J. J., Hartono, D., Ong, C. N., Bay, B. H., & Yung, L. Y. L. (2010). Autophagy and oxidative stress associated with gold nanoparticles. *Biomaterials*, *31*(23), 5996-6003.
- Li, J. J., Lo, S. L., Ng, C. T., Gurung, R. L., Hartono, D., Hande, M. P., Ong, C. N., Bay, B. H., & Yung, L. Y. L. (2011). Genomic instability of gold nanoparticle treated human lung fibroblast cells. *Biomaterials*, *32*(23), 5515-5523.
- Li, J. J., Zou, L., Hartono, D., Ong, C. N., Bay, B. H., & Yung, L. Y. L. (2008). Gold nanoparticles induce oxidative damage in lung fibroblasts in vitro. *Advanced Materials*, *20*(1), 138-+.
- Lim, J. P., & Gleeson, P. A. (2011). Macropinocytosis: An endocytic pathway for internalising large gulps. *Immunology and Cell Biology*, *89*(8), 836-843.
- Limbach, L. K., Wick, P., Manser, P., Grass, R. N., Bruinink, A., & Stark, W. J. (2007). Exposure of engineered nanoparticles to human lung epithelial cells: Influence of chemical composition and catalytic activity on oxidative stress. *Environmental Science & Technology*, *41*(11), 4158-4163.
- Lin, Q. Y., Chen, J., Ng, K. K., Cao, W. G., Zhang, Z. H., & Zheng, G. (2014). Imaging the cytosolic drug delivery mechanism of hdl-like nanoparticles. *Pharmaceutical Research*, *31*(6), 1438-1449.
- Lin, S. Y., Tsai, Y. T., Chen, C. C., Lin, C. M., & Chen, C. H. (2004). Two-step functionalization of neutral and positively charged thiols onto citrate-stabilized au nanoparticles. *Journal of Physical Chemistry B*, *108*(7), 2134-2139.
- Linkov, I., Steevens, J., Adlakha-Hutcheon, G., Bennett, E., Chappell, M., Colvin, V., Davis, J. M., Davis, T., Elder, A., Hansen, S., Hakkinen, P. B., Hussain, S. M., Karkan, D., Korenstein, R., Lynch, I., Metcalfe, C., Ramadan, A. B., & Satterstrom, F. K. (2009). Emerging methods and tools for environmental risk assessment, decision-making, and policy for nanomaterials: Summary of nato advanced research workshop. *Journal of Nanoparticle Research*, *11*(3), 513-527.
- Liou, W., Geuze, H. J., Geelen, M. J. H., & Slot, J. W. (1997). The autophagic and endocytic pathways converge at the nascent autophagic vacuoles. *Journal of Cell Biology*, *136*(1), 61-70.
- Liu, B. R., Lo, S. Y., Liu, C. C., Chyan, C. L., Huang, Y. W., Aronstam, R. S., & Lee, H. J. (2013). Endocytic trafficking of nanoparticles delivered by cell-penetrating peptides comprised of nona-arginine and a penetration accelerating sequence. *PLoS One*, *8*(6), e67100.
- Lo, K. K. W., Choi, A. W. T., & Law, W. H. T. (2012). Applications of luminescent inorganic and organometallic transition metal complexes as biomolecular and cellular probes. *Dalton Transactions*, *41*(20), 6021-6047.
- Lu, X. Y., Wu, D. C., Li, Z. J., & Chen, G. Q. (2011). Polymer nanoparticles. *Prog Mol Biol Transl Sci*, *104*, 299-323.
- Luzio, J. P., Pryor, P. R., & Bright, N. A. (2007). Lysosomes: Fusion and function. *Nat Rev Mol Cell Biol*, *8*(8), 622-632.
- Ma, D. L., He, H. Z., Leung, K. H., Chan, D. S., & Leung, C. H. (2013a). Bioactive luminescent transition-metal complexes for biomedical applications. *Angew Chem Int Ed Engl*, *52*(30), 7666-7682.
- Ma, D. L., He, H. Z., Leung, K. H., Chan, D. S. H., & Leung, C. H. (2013b). Bioactive luminescent transition-metal complexes for biomedical applications. *Angewandte Chemie-International Edition*, *52*(30), 7666-7682.
- Ma, X. W., Wu, Y. Y., Jin, S. B., Tian, Y., Zhang, X. N., Zhao, Y. L., Yu, L., & Liang, X. J. (2011). Gold nanoparticles induce autophagosome accumulation through size-dependent nanoparticle uptake and lysosome impairment. *ACS Nano*, *5*(11), 8629-8639.
- Madl, A. K., Plummer, L. E., Carosino, C., & Pinkerton, K. E. (2014). Nanoparticles, lung injury, and the role of oxidant stress. *Annual Review of Physiology*, Vol 76, *76*, 447-465.
- Maiorano, G., Sabella, S., Sorce, B., Brunetti, V., Malvindi, M. A., Cingolani, R., & Pompa, P. P. (2010). Effects of cell culture media on the dynamic formation of protein-nanoparticle complexes and influence on the cellular response. *ACS Nano*, *4*(12), 7481-7491.

- Manke, A., Wang, L. Y., & Rojanasakul, Y. (2013). Mechanisms of nanoparticle-induced oxidative stress and toxicity. *Biomed Research International*.
- Marquis, B. J., Love, S. A., Braun, K. L., & Haynes, C. L. (2009). Analytical methods to assess nanoparticle toxicity. *Analyst*, *134*(3), 425-439.
- Marzbali, M. Y., Khosroushahi, A. Y., Movassaghpour, A., & Yeganeh, H. (2016). Polyurethane dispersion containing quaternized ammonium groups: An efficient nanosize gene delivery carrier for a549 cancer cell line transfection. *Chemico-Biological Interactions*, *244*, 27-36.
- Masarudin, M. J., Cutts, S. M., Evison, B. J., Phillips, D. R., & Pigram, P. J. (2015). Factors determining the stability, size distribution, and cellular accumulation of small, monodisperse chitosan nanoparticles as candidate vectors for anticancer drug delivery: Application to the passive encapsulation of [14c]-doxorubicin. *Nanotechnology, science and applications*, *8*, 67-80.
- Masereel, B., Pochet, L., & Laeckmann, D. (2003). An overview of inhibitors of na⁺/h⁺ exchanger. *European Journal of Medicinal Chemistry*, *38*(6), 547-554.
- Maurer-Jones, M. A., Gunsolus, I. L., Murphy, C. J., & Haynes, C. L. (2013). Toxicity of engineered nanoparticles in the environment. *Analytical Chemistry*, *85*(6), 3036-3049.
- Maxfield, F. R., & McGraw, T. E. (2004). Endocytic recycling. *Nat Rev Mol Cell Biol*, *5*(2), 121-132.
- Mayor, S., & Pagano, R. E. (2007). Pathways of clathrin-independent endocytosis. *Nature Reviews Molecular Cell Biology*, *8*(8), 603-612.
- Mazzola, L. (2003). Commercializing nanotechnology. *Nat Biotechnol*, *21*(10), 1137-1143.
- McCusker, J. K. (2003). Femtosecond absorption spectroscopy of transition metal charge-transfer complexes. *Accounts of Chemical Research*, *36*(12), 876-887.
- McMahon, H. T., & Boucrot, E. (2011). Molecular mechanism and physiological functions of clathrin-mediated endocytosis. *Nature Reviews Molecular Cell Biology*, *12*(8), 517-533.
- Mehtala, J. G., & Wei, A. (2014). Nanometric resolution in the hydrodynamic size analysis of ligand-stabilized gold nanorods. *Langmuir*, *30*(46), 13737-13743.
- Mieszawska, A. J., Mulder, W. J. M., Fayad, Z. A., & Cormode, D. P. (2013). Multifunctional gold nanoparticles for diagnosis and therapy of disease. *Molecular Pharmaceutics*, *10*(3), 831-847.
- Minai, L., Yeheskely-Hayon, D., & Yelin, D. (2013). High levels of reactive oxygen species in gold nanoparticle-targeted cancer cells following femtosecond pulse irradiation. *Scientific Reports*, *3*.
- Mirabello, V., Calatayud, D. G., Arrowsmith, R. L., Ge, H., & Pascu, S. I. (2015). Metallic nanoparticles as synthetic building blocks for cancer diagnostics: From materials design to molecular imaging applications. *Journal of Materials Chemistry B*, *3*(28), 5657-5672.
- Mironava, T., Hadjiargyrou, M., Simon, M., Jurukovski, V., & Rafailovich, M. H. (2010). Gold nanoparticles cellular toxicity and recovery: Effect of size, concentration and exposure time. *Nanotoxicology*, *4*(1), 120-137.
- Mizushima, N. (2007). Autophagy: Process and function. *Genes & Development*, *21*(22), 2861-2873.
- Mody, V. V., Siwale, R., Singh, A., & Mody, H. R. (2010). Introduction to metallic nanoparticles. *J Pharm Bioallied Sci*, *2*(4), 282-289.
- Monteiro-Riviere, N. A., Inman, A. O., & Zhang, L. W. (2009). Limitations and relative utility of screening assays to assess engineered nanoparticle toxicity in a human cell line. *Toxicology and Applied Pharmacology*, *234*(2), 222-235.
- Moore, T. L., Rodriguez-Lorenzo, L., Hirsch, V., Balog, S., Urban, D., Jud, C., Rothen-Rutishauser, B., Lattuada, M., & Petri-Fink, A. (2015). Nanoparticle colloidal stability in cell culture media and impact on cellular interactions. *Chemical Society Reviews*, *44*(17), 6287-6305.
- Mu, H. B., Liu, Q. J., Niu, H., Wang, D. D., Tang, J. J., & Duan, J. Y. (2016). Autophagy promotes DNA-protein crosslink clearance. *Mutation Research-Genetic Toxicology and Environmental Mutagenesis*, *797*, 21-25.

- Mulugeta, S., Gray, J. M., Notarfrancesco, K. L., Gonzales, L. W., Koval, M., Feinstein, S. I., Ballard, P. L., Fisher, A. B., & Shuman, H. (2002). Identification of Ibm180, a lamellar body limiting membrane protein of alveolar type ii cells, as the abc transporter protein abca3. *Journal of Biological Chemistry*, 277(25), 22147-22155.
- Murphy, C. J., Gole, A. M., Stone, J. W., Sisco, P. N., Alkilany, A. M., Goldsmith, E. C., & Baxter, S. C. (2008). Gold nanoparticles in biology: Beyond toxicity to cellular imaging. *Accounts of Chemical Research*, 41(12), 1721-1730.
- Murphy, C. J., & Jana, N. R. (2002). Controlling the aspect ratio of inorganic nanorods and nanowires. *Advanced Materials*, 14(1), 80-82.
- Murthy, S. K. (2007). Nanoparticles in modern medicine: State of the art and future challenges. *Int J Nanomedicine*, 2(2), 129-141.
- Mustafa, T., Watanabe, F., Monroe, W., Mahmood, M., Xu, Y., Saeed, L., Karmakar, A., Casciano, D., All, S., & Biris, A. (2011). Impact of gold nanoparticle concentration on their cellular uptake by mc3t3-e1 mouse osteoblastic cells as analyzed by transmission electron microscopy. *J. Nanomed. Nanotechnol*, 2(6), 1000118.
- Nativo, P., Prior, I. A., & Brust, M. (2008). Uptake and intracellular fate of surface-modified gold nanoparticles. *Acs Nano*, 2(8), 1639-1644.
- Neibert, K. D., & Maysinger, D. (2012). Mechanisms of cellular adaptation to quantum dots--the role of glutathione and transcription factor eb. *Nanotoxicology*, 6(3), 249-262.
- Nel, A., Xia, T., Madler, L., & Li, N. (2006). Toxic potential of materials at the nanolevel. *Science*, 311(5761), 622-627.
- Ng, C. T., Tang, F. M. A., Li, J. J., Ong, C., Yung, L. L. Y., & Bay, B. H. (2015). Clathrin-mediated endocytosis of gold nanoparticles in vitro. *Anatomical Record-Advances in Integrative Anatomy and Evolutionary Biology*, 298(2), 418-427.
- Nordberg, J., & Arner, E. S. J. (2001). Reactive oxygen species, antioxidants, and the mammalian thioredoxin system. *Free Radical Biology and Medicine*, 31(11), 1287-1312.
- Oberdorster, G., Oberdorster, E., & Oberdorster, J. (2005). Nanotoxicology: An emerging discipline evolving from studies of ultrafine particles. *Environmental Health Perspectives*, 113(7), 823-839.
- Oh, N., & Park, J. H. (2014). Endocytosis and exocytosis of nanoparticles in mammalian cells. *International Journal of Nanomedicine*, 9, 51-63.
- Olive, P. L., & Banath, J. P. (2006). The comet assay: A method to measure DNA damage in individual cells. *Nature Protocols*, 1(1), 23-29.
- Oo, M. K. K., Yang, Y. M., Hu, Y., Gomez, M., Du, H., & Wang, H. J. (2012). Gold nanoparticle-enhanced and size-dependent generation of reactive oxygen species from protoporphyrin ix. *Acs Nano*, 6(3), 1939-1947.
- Osborne, S., & Pikramenou, Z. (2015). Highly luminescent gold nanoparticles: Effect of ruthenium distance for nanoprobe with enhanced lifetimes. *Faraday Discussions*.
- Ott, M., Gogvadze, V., Orrenius, S., & Zhivotovsky, B. (2007). Mitochondria, oxidative stress and cell death. *Apoptosis*, 12(5), 913-922.
- Paciotti, G. F., Kingston, D. G. I., & Tamarkin, L. (2006). Colloidal gold nanoparticles: A novel nanoparticle platform for developing multifunctional tumor-targeted drug delivery vectors. *Drug Development Research*, 67(1), 47-54.
- Pan, Y., Leifert, A., Ruau, D., Neuss, S., Bornemann, J., Schmid, G., Brandau, W., Simon, U., & Jahnke-Dechent, W. (2009). Gold nanoparticles of diameter 1.4 nm trigger necrosis by oxidative stress and mitochondrial damage. *Small*, 5(18), 2067-2076.
- Panariti, A., Misericocchi, G., & Rivolta, I. (2012). The effect of nanoparticle uptake on cellular behavior: Disrupting or enabling functions? *Nanotechnol Sci Appl*, 5, 87-100.
- Panchapakesan, B., Book-Newell, B., Sethu, P., Rao, M., & Irudayaraj, J. (2011). Gold nanoprobe for theranostics. *Nanomedicine*, 6(10), 1787-1811.
- Pantarotto, D., Briand, J. P., Prato, M., & Bianco, A. (2004). Translocation of bioactive peptides across cell membranes by carbon nanotubes. *Chemical Communications*(1), 16-17.

- Panyam, J., & Labhasetwar, V. (2003). Biodegradable nanoparticles for drug and gene delivery to cells and tissue. *Advanced Drug Delivery Reviews*, 55(3), 329-347.
- Park, C., Youn, H., Kim, H., Noh, T., Kook, Y. H., Oh, E. T., Park, H. J., & Kim, C. (2009). Cyclodextrin-covered gold nanoparticles for targeted delivery of an anti-cancer drug. *Journal of Materials Chemistry*, 19(16), 2310-2315.
- Pascua-Maestro, R., Diez-Hermano, S., Lillo, C., Ganfornina, M. D., & Sanchez, D. (2017). Protecting cells by protecting their vulnerable lysosomes: Identification of a new mechanism for preserving lysosomal functional integrity upon oxidative stress. *Plos Genetics*, 13(2).
- Patel, V., Papineni, R. V., Gupta, S., Stoyanova, R., & Ahmed, M. M. (2012). A realistic utilization of nanotechnology in molecular imaging and targeted radiotherapy of solid tumors. *Radiat Res*, 177(4), 483-495.
- Patra, H. K., Banerjee, S., Chaudhuri, U., Lahiri, P., & Dasgupta, A. K. (2007). Cell selective response to gold nanoparticles. *Nanomedicine-Nanotechnology Biology and Medicine*, 3(2), 111-119.
- Peer, D., Karp, J. M., Hong, S., Farokhzad, O. C., Margalit, R., & Langer, R. (2007). Nanocarriers as an emerging platform for cancer therapy. *Nature Nanotechnology*, 2(12), 751-760.
- Pernodet, N., Fang, X. H., Sun, Y., Bakhtina, A., Ramakrishnan, A., Sokolov, J., Ulman, A., & Rafailovich, M. (2006). Adverse effects of citrate/gold nanoparticles on human dermal fibroblasts. *Small*, 2(6), 766-773.
- Petrache Voicu, S. N., Dinu, D., Sima, C., Hermenean, A., Ardelean, A., Codrici, E., Stan, M. S., Zărnescu, O., & Dinischiotu, A. (2015). Silica nanoparticles induce oxidative stress and autophagy but not apoptosis in the mrc-5 cell line. *International Journal of Molecular Sciences*, 16(12), 29398-29416.
- Peynshaert, K., Manshian, B. B., Joris, F., Braeckmans, K., De Smedt, S. C., Demeester, J., & Soenen, S. J. (2014). Exploiting intrinsic nanoparticle toxicity: The pros and cons of nanoparticle-induced autophagy in biomedical research. *Chemical Reviews*, 114(15), 7581-7609.
- Pfaffl, M. W. (2001). A new mathematical model for relative quantification in real-time rt-pcr. *Nucleic Acids Research*, 29(9).
- Philip, D. (2008). Synthesis and spectroscopic characterization of gold nanoparticles. *Spectrochimica Acta Part a-Molecular and Biomolecular Spectroscopy*, 71(1), 80-85.
- Piella, J., Bastus, N. G., & Puntès, V. (2017). Size-dependent protein-nanoparticle interactions in citrate-stabilized gold nanoparticles: The emergence of the protein corona. *Bioconjug Chem*, 28(1), 88-97.
- Piper, R. C., & Luzio, J. P. (2001). Late endosomes: Sorting and partitioning in multivesicular bodies. *Traffic*, 2(9), 612-621.
- Polte, J. (2015). Fundamental growth principles of colloidal metal nanoparticles - a new perspective. *Crystengcomm*, 17(36), 6809-6830.
- Provenzale, J. M., & Silva, G. A. (2009). Uses of nanoparticles for central nervous system imaging and therapy. *American Journal of Neuroradiology*, 30(7), 1293-1301.
- Rahman, M., Laurent, S., Tawil, N., Yahia, L., & Mahmoudi, M. (2013). *Protein-nanoparticle interactions*: Springer.
- Rattanapinyopituk, K., Shimada, A., Morita, T., Sakurai, M., Asano, A., Hasegawa, T., Inoue, K., & Takano, H. (2014). Demonstration of the clathrin- and caveolin-mediated endocytosis at the maternal-fetal barrier in mouse placenta after intravenous administration of gold nanoparticles. *Journal of Veterinary Medical Science*, 76(3), 377-387.
- Reibold, M., Paufler, P., Levin, A. A., Kochmann, W., Patzke, N., & Meyer, D. C. (2006). Materials - carbon nanotubes in an ancient damascus sabre. *Nature*, 444(7117), 286-286.
- Reinert, K., Andrews, L., & Keenan, R. (2006). Nanotechnology nexus - intersection of research, science, technology, and regulation. *Human and Ecological Risk Assessment*, 12(5), 811-818.

- Repnik, U., Cesen, M. H., & Turk, B. (2013). The endolysosomal system in cell death and survival. *Cold Spring Harb Perspect Biol*, 5(1), a008755.
- Rim, K. T., Song, S. W., & Kim, H. Y. (2013). Oxidative DNA damage from nanoparticle exposure and its application to workers' health: A literature review. *Saf Health Work*, 4(4), 177-186.
- Riss, T. L., Moravec, R. A., Niles, A. L., Duellman, S., Benink, H. A., Worzella, T. J., & Minor, L. (2004). Cell viability assays. In G. S. Sittampalam, N. P. Coussens, K. Brimacombe, A. Grossman, M. Arkin, D. Auld, C. Austin, B. Bejcek, M. Glicksman, J. Inglese, P. W. Iversen, Z. Li, J. McGee, O. McManus, L. Minor, A. Napper, J. M. Peltier, T. Riss, O. J. Trask, Jr., & J. Weidner (Eds.), *Assay guidance manual*. Bethesda (MD).
- Roesslein, M., Hirsch, C., Kaiser, J. P., Krug, H. F., & Wick, P. (2013). Comparability of in vitro tests for bioactive nanoparticles: A common assay to detect reactive oxygen species as an example. *International Journal of Molecular Sciences*, 14(12), 24320-24337.
- Rogers, N. J., Claire, S., Harris, R. M., Farabi, S., Zikeli, G., Styles, I. B., Hodges, N. J., & Pikramenou, Z. (2014). High coating of ru(ii) complexes on gold nanoparticles for single particle luminescence imaging in cells. *Chemical Communications*, 50(5), 617-619.
- Rosi, N. L., & Mirkin, C. A. (2005). Nanostructures in biodiagnostics. *Chem Rev*, 105(4), 1547-1562.
- Rothen-Rutishauser, B., Kuhn, D. A., Ali, Z., Gasser, M., Amin, F., Parak, W. J., Vanhecke, D., Fink, A., Gehr, P., & Brandenberger, C. (2014). Quantification of gold nanoparticle cell uptake under controlled biological conditions and adequate resolution. *Nanomedicine*, 9(5), 607-621.
- Roux, S., Garcia, B., Bridot, J. L., Salome, M., Marquette, C., Lemelle, L., Gillet, P., Blum, L., Perriat, P., & Tillement, O. (2005). Synthesis, characterization of dihydrolipoic acid capped gold nanoparticles, and functionalization by the electroluminescent luminol. *Langmuir*, 21(6), 2526-2536.
- Sabella, S., Carney, R. P., Brunetti, V., Malvindi, M. A., Al-Juffali, N., Vecchio, G., Janes, S. M., Bakr, O. M., Cingolani, R., Stellacci, F., & Pompa, P. P. (2014). A general mechanism for intracellular toxicity of metal-containing nanoparticles. *Nanoscale*, 6(12), 7052-7061.
- Sadauskas, E., Danscher, G., Stoltenberg, M., Vogel, U., Larsen, A., & Wallin, H. (2009). Protracted elimination of gold nanoparticles from mouse liver. *Nanomedicine*, 5(2), 162-169.
- Saha, R. N., Vasanthakumar, S., Bende, G., & Snehalatha, M. (2010). Nanoparticulate drug delivery systems for cancer chemotherapy. *Mol Membr Biol*, 27(7), 215-231.
- Sahoo, S. K., & Labhasetwar, V. (2003). Nanotech approaches to delivery and imaging drug. *Drug Discovery Today*, 8(24), 1112-1120.
- Salata, O. (2004). Applications of nanoparticles in biology and medicine. *J Nanobiotechnology*, 2(1), 3.
- Samali, A., & Orrenius, S. (1998). Heat shock proteins: Regulators of stress response and apoptosis. *Cell stress & chaperones*, 3(4), 228.
- Sanvicens, N., & Marco, M. P. (2008). Multifunctional nanoparticles - properties and prospects for their use in human medicine. *Trends in Biotechnology*, 26(8), 425-433.
- Schaeublin, N. M., Braydich-Stolle, L. K., Schrand, A. M., Miller, J. M., Hutchison, J., Schlager, J. J., & Hussain, S. M. (2011). Surface charge of gold nanoparticles mediates mechanism of toxicity. *Nanoscale*, 3(2), 410-420.
- Schmitz, G., & Muller, G. (1991). Structure and function of lamellar bodies, lipid-protein complexes involved in storage and secretion of cellular lipids. *J Lipid Res*, 32(10), 1539-1570.
- Schulz, F., Homolka, T., Bastus, N. G., Puentes, V., Weller, H., & Vossmeier, T. (2014). Little adjustments significantly improve the turkevich synthesis of gold nanoparticles. *Langmuir*, 30(35), 10779-10784.
- Schumann, C., Schubbe, S., Cavalius, C., & Kraegeloh, A. (2012). A correlative approach at characterizing nanoparticle mobility and interactions after cellular uptake. *Journal of Biophotonics*, 5(2), 117-127.

- Shah, N. B., Dong, J. P., & Bischof, J. C. (2011). Cellular uptake and nanoscale localization of gold nanoparticles in cancer using label-free confocal raman microscopy. *Molecular Pharmaceutics*, *8*(1), 176-184.
- Sharma, V. K., Filip, J., Zboril, R., & Varma, R. S. (2015). Natural inorganic nanoparticles - formation, fate, and toxicity in the environment. *Chemical Society Reviews*, *44*(23), 8410-8423.
- Sheppard, C., & Shotton, D. (1997). Confocal fluorescence microscopy. *Confocal Laser Scanning Microscopy; Springer-Verlag New York Inc.: New York*, 61-70.
- Shukla, R., Bansal, V., Chaudhary, M., Basu, A., Bhonde, R. R., & Sastry, M. (2005). Biocompatibility of gold nanoparticles and their endocytotic fate inside the cellular compartment: A microscopic overview. *Langmuir*, *21*(23), 10644-10654.
- Singh, N. P., McCoy, M. T., Tice, R. R., & Schneider, E. L. (1988). A simple technique for quantitation of low-levels of DNA damage in individual cells. *Experimental Cell Research*, *175*(1), 184-191.
- Singh, R., & Lillard, J. W. (2009). Nanoparticle-based targeted drug delivery. *Experimental and Molecular Pathology*, *86*(3), 215-223.
- Slater, T. F., Sawyer, B., & Straeuli, U. (1963). Studies on succinate-tetrazolium reductase systems. Ii. Points of coupling of four different tetrazolium salts. *Biochim Biophys Acta*, *77*, 383-393.
- Sliwka, L., Wiktorska, K., Suchocki, P., Milczarek, M., Mielczarek, S., Lubelska, K., Cierpial, T., Lyzwa, P., Kielbasinski, P., Jaromin, A., Flis, A., & Chilmonczyk, Z. (2016). The comparison of mtt and cvs assays for the assessment of anticancer agent interactions. *PLoS One*, *11*(5).
- Soenen, S. J., Rivera-Gil, P., Montenegro, J. M., Parak, W. J., De Smedt, S. C., & Braeckmans, K. (2011). Cellular toxicity of inorganic nanoparticles: Common aspects and guidelines for improved nanotoxicity evaluation. *Nano Today*, *6*(5), 446-465.
- Sokolov, K., Follen, M., Aaron, J., Pavlova, I., Malpica, A., Lotan, R., & Richards-Kortum, R. (2003). Real-time vital optical imaging of precancer using anti-epidermal growth factor receptor antibodies conjugated to gold nanoparticles. *Cancer Research*, *63*(9), 1999-2004.
- Solano-Umaña, V., Vega-Baudrit, J. R., & González-Paz, R. (2015). The new field of the nanomedicine. *International Journal of Applied*, *5*(1).
- Stefancikova, L., Porcel, E., Eustache, P., Li, S., Salado, D., Marco, S., Guerquin-Kern, J. L., Refregiers, M., Tillement, O., Lux, F., & Lacombe, S. (2014). Cell localisation of gadolinium-based nanoparticles and related radiosensitising efficacy in glioblastoma cells. *Cancer Nanotechnol*, *5*(1), 6.
- Steinman, R. M., Mellman, I. S., Muller, W. A., & Cohn, Z. A. (1983). Endocytosis and the recycling of plasma membrane. *Journal of Cell Biology*, *96*(1), 1-27.
- Stern, S. T., Adiseshiah, P. P., & Crist, R. M. (2012). Autophagy and lysosomal dysfunction as emerging mechanisms of nanomaterial toxicity. *Particle and Fibre Toxicology*, *9*.
- Stow, J. L., & Condon, N. D. (2016). The cell surface environment for pathogen recognition and entry. *Clinical & Translational Immunology*, *5*.
- Strojan, K., Leonardi, A., Bregar, V. B., Krizaj, I., Svete, J., & Pavlin, M. (2017). Dispersion of nanoparticles in different media importantly determines the composition of their protein corona. *PLoS One*, *12*(1).
- Subbiah, R., Veerapandian, M., & Yun, K. S. (2010). Nanoparticles: Functionalization and multifunctional applications in biomedical sciences. *Curr Med Chem*, *17*(36), 4559-4577.
- Sung, J. C., Pulliam, B. L., & Edwards, D. A. (2007). Nanoparticles for drug delivery to the lungs. *Trends in Biotechnology*, *25*(12), 563-570.
- Svensson, F. R., Abrahamsson, M., Stromberg, N., Ewing, A. G., & Lincoln, P. (2011). Ruthenium(ii) complex enantiomers as cellular probes for diastereomeric interactions in confocal and fluorescence lifetime imaging microscopy. *Journal of Physical Chemistry Letters*, *2*(5), 397-401.

- Swanson, J. A., & Watts, C. (1995). Macropinocytosis. *Trends in cell biology*, 5(11), 424-428.
- Takahashi, H., Niidome, Y., Niidome, T., Kaneko, K., Kawasaki, H., & Yamada, S. (2006). Modification of gold nanorods using phosphatidylcholine to reduce cytotoxicity. *Langmuir*, 22(1), 2-5.
- Tan, S. L., Sagara, Y., Lin, Y. B., Maher, P., & Schubert, D. (1998). The regulation of reactive oxygen species production during programmed cell death. *Journal of Cell Biology*, 141(6), 1423-1432.
- Tanaka, K., & Fukase, K. (2008). Pet (positron emission tomography) imaging of biomolecules using metal-dota complexes: A new collaborative challenge by chemists, biologists, and physicians for future diagnostics and exploration of in vivo dynamics. *Organic & Biomolecular Chemistry*, 6(5), 815-828.
- Tang, Y., Shen, Y., Huang, L., Lv, G., Lei, C., Fan, X., Lin, F., Zhang, Y., Wu, L., & Yang, Y. (2015). In vitro cytotoxicity of gold nanorods in a549 cells. *Environ Toxicol Pharmacol*, 39(2), 871-878.
- Tauran, Y., Brioude, A., Coleman, A. W., Rhimi, M., & Kim, B. (2013). Molecular recognition by gold, silver and copper nanoparticles. *World J Biol Chem*, 4(3), 35-63.
- Taylor, J., Huefner, A., Li, L., Wingfield, J., & Mahajan, S. (2016). Nanoparticles and intracellular applications of surface-enhanced raman spectroscopy. *Analyst*, 141(17), 5037-5055.
- Thomas, K. G., & Kamat, P. V. (2003). Chromophore-functionalized gold nanoparticles. *Accounts of Chemical Research*, 36(12), 888-898.
- Tiede, K., Boxall, A. B. A., Tear, S. P., Lewis, J., David, H., & Hasselov, M. (2008). Detection and characterization of engineered nanoparticles in food and the environment. *Food Additives and Contaminants Part a-Chemistry Analysis Control Exposure & Risk Assessment*, 25(7), 795-821.
- Tkachenko, A. G., Xie, H., Coleman, D., Glomm, W., Ryan, J., Anderson, M. F., Franzen, S., & Feldheim, D. L. (2003). Multifunctional gold nanoparticle-peptide complexes for nuclear targeting. *Journal of the American Chemical Society*, 125(16), 4700-4701.
- Tlotleng, N., Vetten, M. A., Keter, F. K., Skepu, A., Tshikhudo, R., & Gulumian, M. (2016). Cytotoxicity, intracellular localization and exocytosis of citrate capped and peg functionalized gold nanoparticles in human hepatocyte and kidney cells. *Cell Biol Toxicol*, 32(4), 305-321.
- Tonga, G. Y., Saha, K., & Rotello, V. M. (2014). 25th anniversary article: Interfacing nanoparticles and biology: New strategies for biomedicine. *Advanced Materials*, 26(3), 359-370.
- Treuel, L., Jiang, X., & Nienhaus, G. U. (2013). New views on cellular uptake and trafficking of manufactured nanoparticles. *J R Soc Interface*, 10(82), 20120939.
- Tsai, Y. Y., Huang, Y. H., Chao, Y. L., Hu, K. Y., Chin, L. T., Chou, S. H., Hour, A. L., Yao, Y. D., Tu, C. S., Liang, Y. J., Tsai, C. Y., Wu, H. Y., Tan, S. W., & Chen, H. M. (2011). Identification of the nanogold particle-induced endoplasmic reticulum stress by omic techniques and systems biology analysis. *Acs Nano*, 5(12), 9354-9369.
- Tsuji, J. S., Maynard, A. D., Howard, P. C., James, J. T., Lam, C. W., Warheit, D. B., & Santamaria, A. B. (2006). Research strategies for safety evaluation of nanomaterials, part iv: Risk assessment of nanoparticles. *Toxicological Sciences*, 89(1), 42-50.
- Turkevich, J., Stevenson, P. C., & Hillier, J. (1951). A study of the nucleation and growth processes in the synthesis of colloidal gold. *Discussions of the Faraday Society*(11), 55-&.
- Uboldi, C., Bonacchi, D., Lorenzi, G., Hermanns, M. I., Pohl, C., Baldi, G., Unger, R. E., & Kirkpatrick, C. J. (2009). Gold nanoparticles induce cytotoxicity in the alveolar type-ii cell lines a549 and ncih441. *Particle and Fibre Toxicology*, 6.
- Unfried, K., Albrecht, C., Klotz, L. O., Von Mikecz, A., Grether-Beck, S., & Schins, R. P. F. (2007). Cellular responses to nanoparticles: Target structures and mechanisms. *Nanotoxicology*, 1(1), 52-71.
- Upadhyay, R. K. (2014). Drug delivery systems, cns protection, and the blood brain barrier. *Biomed Research International*.

- Valko, M., Rhodes, C. J., Moncol, J., Izakovic, M., & Mazur, M. (2006). Free radicals, metals and antioxidants in oxidative stress-induced cancer. *Chemico-Biological Interactions*, *160*(1), 1-40.
- Van Der Vlies, D., Makkinje, M., Jansens, A., Braakman, I., Verkleij, A. J., Wirtz, K. W. A., & Post, J. A. (2003). Oxidation of er resident proteins upon oxidative stress: Effects of altering cellular redox/antioxidant status and implications for protein maturation. *Antioxidants & Redox Signaling*, *5*(4), 381-387.
- Vercauteren, D., Vandenbroucke, R. E., Jones, A. T., Rejman, J., Demeester, J., De Smedt, S. C., Sanders, N. N., & Braeckmans, K. (2010). The use of inhibitors to study endocytic pathways of gene carriers: Optimization and pitfalls. *Molecular Therapy*, *18*(3), 561-569.
- Verma, A., & Stellacci, F. (2010). Effect of surface properties on nanoparticle-cell interactions. *Small*, *6*(1), 12-21.
- Verma, A., Uzun, O., Hu, Y., Hu, Y., Han, H. S., Watson, N., Chen, S., Irvine, D. J., & Stellacci, F. (2008). Surface-structure-regulated cell-membrane penetration by monolayer-protected nanoparticles. *Nat Mater*, *7*(7), 588-595.
- Voigt, J., Christensen, J., & Shastri, V. P. (2014). Differential uptake of nanoparticles by endothelial cells through polyelectrolytes with affinity for caveolae. *Proceedings of the National Academy of Sciences of the United States of America*, *111*(8), 2942-2947.
- Wang, L. H., Rothberg, K. G., & Anderson, R. G. W. (1993). Mis-assembly of clathrin lattices on endosomes reveals a regulatory switch for coated pit formation. *Journal of Cell Biology*, *123*(5), 1107-1117.
- Wang, L. M., Liu, Y., Li, W., Jiang, X. M., Ji, Y. L., Wu, X. C., Xu, L. G., Qiu, Y., Zhao, K., Wei, T. T., Li, Y. F., Zhao, Y. L., & Chen, C. Y. (2011). Selective targeting of gold nanorods at the mitochondria of cancer cells: Implications for cancer therapy. *Nano Letters*, *11*(2), 772-780.
- Wang, M. J., & Petersen, N. O. (2013). Lipid-coated gold nanoparticles promote lamellar body formation in a549 cells. *Biochimica Et Biophysica Acta-Molecular and Cell Biology of Lipids*, *1831*(6), 1089-1097.
- Wang, P. Y., Wang, X., Wang, L. M., Hou, X. Y., Liu, W., & Chen, C. Y. (2015). Interaction of gold nanoparticles with proteins and cells. *Science and Technology of Advanced Materials*, *16*(3).
- Wang, Y. Z., Sun, L. M., Yi, S. J., Huang, Y. J., Lenaghan, S. C., & Zhang, M. J. (2013). Naturally occurring nanoparticles from arthrotrypis oligospora as a potential immunostimulatory and antitumor agent. *Advanced Functional Materials*, *23*(17), 2175-2184.
- Ward, C. J., Tronndorf, R., Eustes, A. S., Auad, M. L., & Davis, E. W. (2014). Seed-mediated growth of gold nanorods: Limits of length to diameter ratio control. *Journal of Nanomaterials*.
- Wasano, K., & Hirakawa, Y. (1994). Lamellar bodies of rat alveolar type-2 cells have late endosomal marker proteins on their limiting membranes. *Histochemistry*, *102*(5), 329-335.
- Weaver, T. E., Na, C. L., & Stahlman, M. (2002). Biogenesis of lamellar bodies, lysosome-related organelles involved in storage and secretion of pulmonary surfactant. *Seminars in Cell & Developmental Biology*, *13*(4), 263-270.
- Wei, P., Zhang, L., Lu, Y., Man, N., & Wen, L. (2010). C60(nd) nanoparticles enhance chemotherapeutic susceptibility of cancer cells by modulation of autophagy. *Nanotechnology*, *21*(49), 495101.
- Wei, X. L., Mo, Z. H., Li, B., & Wei, J. M. (2007). Disruption of hepg2 cell adhesion by gold nanoparticle and paclitaxel disclosed by in situ qcm measurement. *Colloids and Surfaces B-Biointerfaces*, *59*(1), 100-104.
- Weir, E., Lawlor, A., Whelan, A., & Regan, F. (2008). The use of nanoparticles in anti-microbial materials and their characterization. *Analyst*, *133*(7), 835-845.
- Weissleder, R. (2006). Molecular imaging in cancer. *Science*, *312*(5777), 1168-1171.

- Weisz, O. A., & Rodriguez-Boulan, E. (2009). Apical trafficking in epithelial cells: Signals, clusters and motors. *J Cell Sci*, 122(Pt 23), 4253-4266.
- Wilczewska, A. Z., Niemirowicz, K., Markiewicz, K. H., & Car, H. (2012). Nanoparticles as drug delivery systems. *Pharmacological Reports*, 64(5), 1020-1037.
- Woehrle, G. H., & Hutchison, J. E. (2005). Thiol-functionalized undecagold clusters by ligand exchange: Synthesis, mechanism, and properties. *Inorganic Chemistry*, 44(18), 6149-6158.
- Xie, X., Liao, J., Shao, X., Li, Q., & Lin, Y. (2017). The effect of shape on cellular uptake of gold nanoparticles in the forms of stars, rods, and triangles. *Sci Rep*, 7(1), 3827.
- Xu, S., Olenyuk, B. Z., Okamoto, C. T., & Hamm-Alvarez, S. F. (2013). Targeting receptor-mediated endocytotic pathways with nanoparticles: Rationale and advances. *Advanced Drug Delivery Reviews*, 65(1), 121-138.
- Yameen, B., Choi, W. I., Vilos, C., Swami, A., Shi, J. J., & Farokhzad, O. C. (2014). Insight into nanoparticle cellular uptake and intracellular targeting. *Journal of Controlled Release*, 190, 485-499.
- Yang, L. X., Shang, L., & Nienhaus, G. U. (2013). Mechanistic aspects of fluorescent gold nanocluster internalization by live hela cells. *Nanoscale*, 5(4), 1537-1543.
- Yi, J., & Tang, X. M. (1999). The convergent point of the endocytic and autophagic pathways in leydig cells. *Cell Research*, 9(4), 243-253.
- Yu, B., Tai, H. C., Xue, W., Lee, L. J., & Lee, R. J. (2010). Receptor-targeted nanocarriers for therapeutic delivery to cancer. *Mol Membr Biol*, 27(7), 286-298.
- Zabirnyk, O., Yezhelyev, M., & Seleverstov, O. (2007). Nanoparticles as a novel class of autophagy activators. *Autophagy*, 3(3), 278-281.
- Zainol, M., Stoute, J., Almeida, G. M., Rapp, A., Bowman, K. J., Jones, G. D. D., & Ecvag. (2009). Introducing a true internal standard for the comet assay to minimize intra- and inter-experiment variability in measures of DNA damage and repair. *Nucleic Acids Research*, 37(22).
- Zarska, M., Novotny, F., Havel, F., Sramek, M., Babelova, A., Benada, O., Novotny, M., Saran, H., Kuca, K., Musilek, K., Hvezdova, Z., Dzajak, R., Vancurova, M., Krejcikova, K., Gabajova, B., Hanzlikova, H., Kyjaco,va, L., Bartek, J., Proska, J., & Hodny, Z. (2016). Two-step mechanism of cellular uptake of cationic gold nanoparticles modified by (16-mercaptohexadecyl)trimethylammonium bromide. *Bioconjugate Chemistry*, 27(10), 2558-2574.
- Zhang, J., Cheng, F., Li, J., Zhu, J. J., & Lu, Y. (2016). Fluorescent nanoprobe for sensing and imaging of metal ions: Recent advances and future perspectives. *Nano Today*, 11(3), 309-329.
- Zhang, L., Gu, F. X., Chan, J. M., Wang, A. Z., Langer, R. S., & Farokhzad, O. C. (2008). Nanoparticles in medicine: Therapeutic applications and developments. *Clin Pharmacol Ther*, 83(5), 761-769.
- Zhang, L. M., Wang, L. M., Hu, Y. L., Liu, Z. G., Tian, Y., Wu, X. C., Zhao, Y. L., Tang, H. R., Chen, C. Y., & Wang, Y. L. (2013). Selective metabolic effects of gold nanorods on normal and cancer cells and their application in anticancer drug screening. *Biomaterials*, 34(29), 7117-7126.
- Zhang, Y. A., Xu, D., Li, W. Q., Yu, J., & Chen, Y. (2012). Effect of size, shape, and surface modification on cytotoxicity of gold nanoparticles to human hep-2 and canine mdck cells. *Journal of Nanomaterials*.
- Zhang, Y. Y., Leu, Y. R., Aitken, R. J., & Riediker, M. (2015). Inventory of engineered nanoparticle-containing consumer products available in the singapore retail market and likelihood of release into the aquatic environment. *International Journal of Environmental Research and Public Health*, 12(8), 8717-8743.
- Zheng, T. Y., Bott, S., & Huo, Q. (2016). Techniques for accurate sizing of gold nanoparticles using dynamic light scattering with particular application to chemical and biological sensing based on aggregate formation. *Acs Applied Materials & Interfaces*, 8(33), 21585-21594.

- Zhou, J. F., Beattie, D. A., Ralston, J., & Sedev, R. (2007). Colloid stability of thymine-functionalized gold nanoparticles. *Langmuir*, 23(24), 12096-12103.
- Zhou, J. F., Ralston, J., Sedev, R., & Beattie, D. A. (2009). Functionalized gold nanoparticles: Synthesis, structure and colloid stability. *Journal of Colloid and Interface Science*, 331(2), 251-262.

Appendix

Chapter 2: Materials and Method

Calculation of concentration of gold nanoparticles used in this thesis (AuNP)

Mass of $\text{HAuCl}_4 \cdot 3\text{H}_2\text{O}$ = 0.008g (amount weighed)

$$\begin{aligned} 49 \% \text{ Au by assay} &= \text{Mass of Au} \\ &= 0.49 \times 0.008 \\ &= 3.92 \times 10^{-3} \text{ g} \end{aligned}$$

$$\begin{aligned} \text{No of moles of Au} &= (3.92 \times 10^{-3} \text{ g}) / (197) \\ &= 1.98 \times 10^{-5} \text{ moles} \end{aligned}$$

$$\begin{aligned} [\text{Au}] &= 1.98 \times 10^{-5} \text{ moles} / 0.125 \text{ dm}^3 \text{ (total volume in flask)} \\ &= 1.59 \times 10^{-4} \text{ M} \end{aligned}$$

Number of Atoms per 13nm AuNP (Assuming that particles are spherical and estimated atomic radius of gold = 140 pm)

$$\begin{aligned} &= (6.5 \times 10^{-9})^3 / (140 \times 10^{-12})^3 \\ &= 100081.9971 \end{aligned}$$

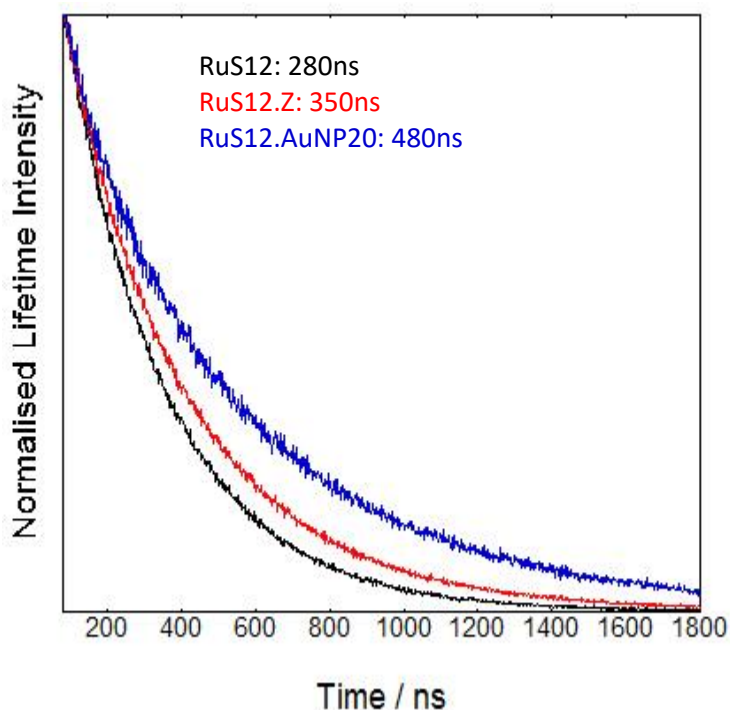
$$\begin{aligned} \text{Concentration of AuNP} &= 1.59 \times 10^{-4} / 100081.9971 \\ &= 1.6 \times 10^{-9} \end{aligned}$$

$$= 1.6 \text{ nM}$$

A. Ruthenium (RuS12) Synthesis

RuS12 was prepared by Shani Osborne (Osborne & Pikramenou, 2015) using published data (Adams *et al.*, 2014; Bertoncello *et al.*, 2006; Rogers *et al.*, 2014). The counter ion was exchanged using Dowex® 1X8 ion exchange chromatography and the final solutions to be used for coating were prepared in methanol, 0.95 mM. This was followed by sonication with NH_4OH to produce a 0.63 mM solution, which was the final concentration used.

B. Lifetime decay



Luminescence lifetime decay of RuS12·AuNP20: increase in 71% is observed on the addition of AuNP to probe.

This experiment was done by Shani Osbourne and published in Osbourne (Osbourne & Pikramenou, 2015).

C. Steps in quantification of confocal images by ImageJ

1. Images acquired from the Red Channel are converted to 16-bit image to remove colour.
2. The 16-bit image undergoes thresholding, which is done using the threshold function of imageJ. This is done automatically using the default setting which aims to get a close resemblance of the initially fluorescent image from the red channel to the binary images.
3. The binary image is analysed using the analyse particle tools on Image J
4. This counts the black dots on the binary images that has a circularity of 0-1 and shows the outline of the count.
5. A summary table is obtained that shows the count, total area, average size, % area and mean. Only the count was used because the aim was to quantify cellular uptake of time.

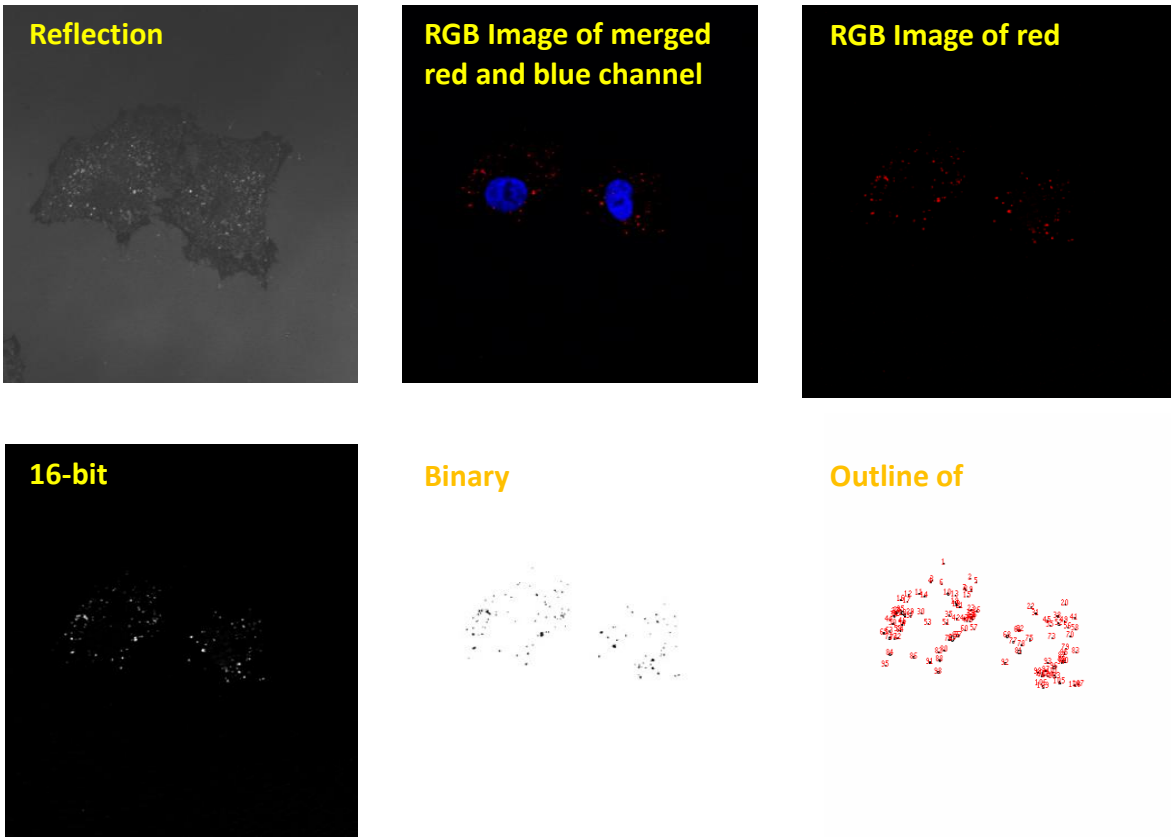
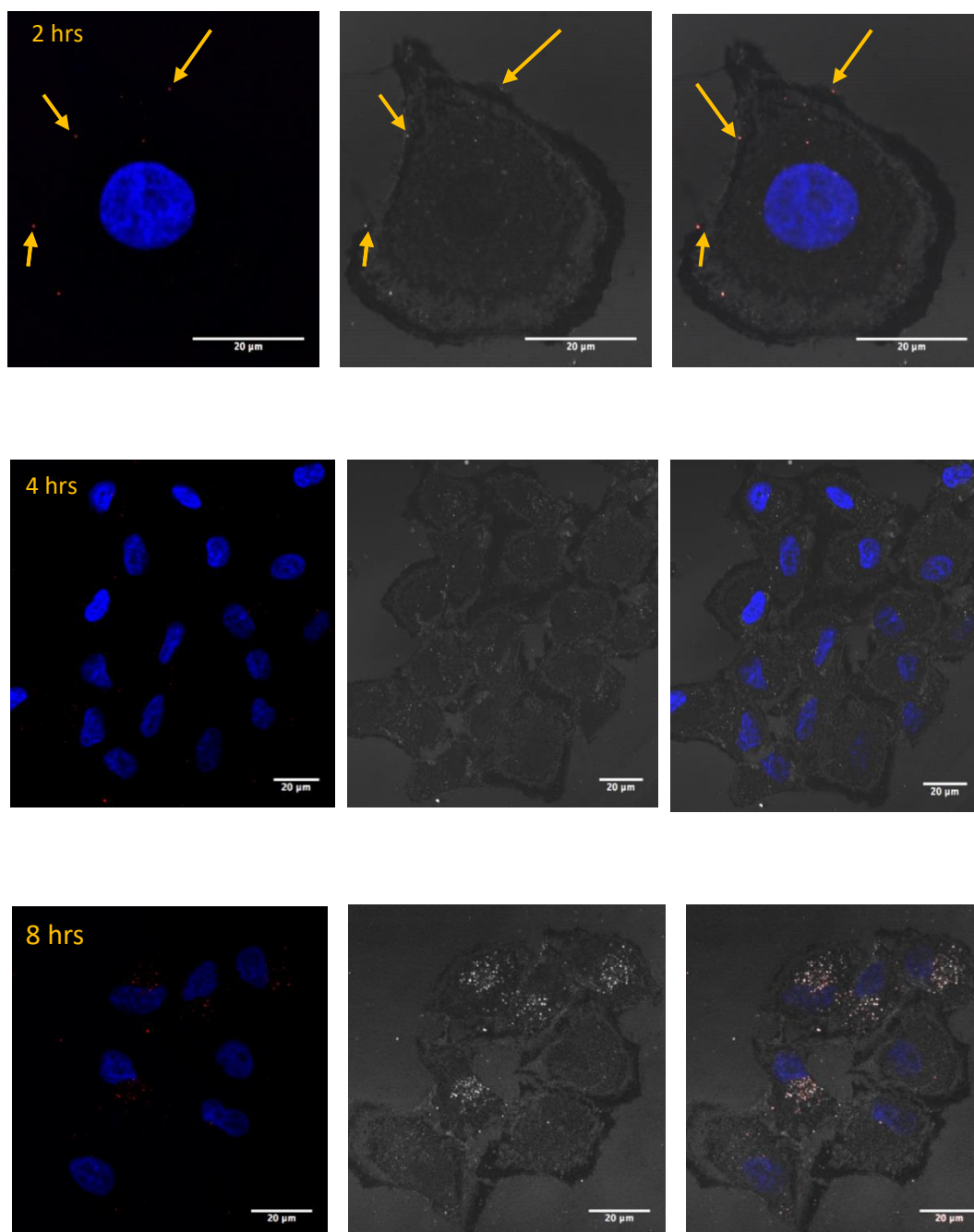
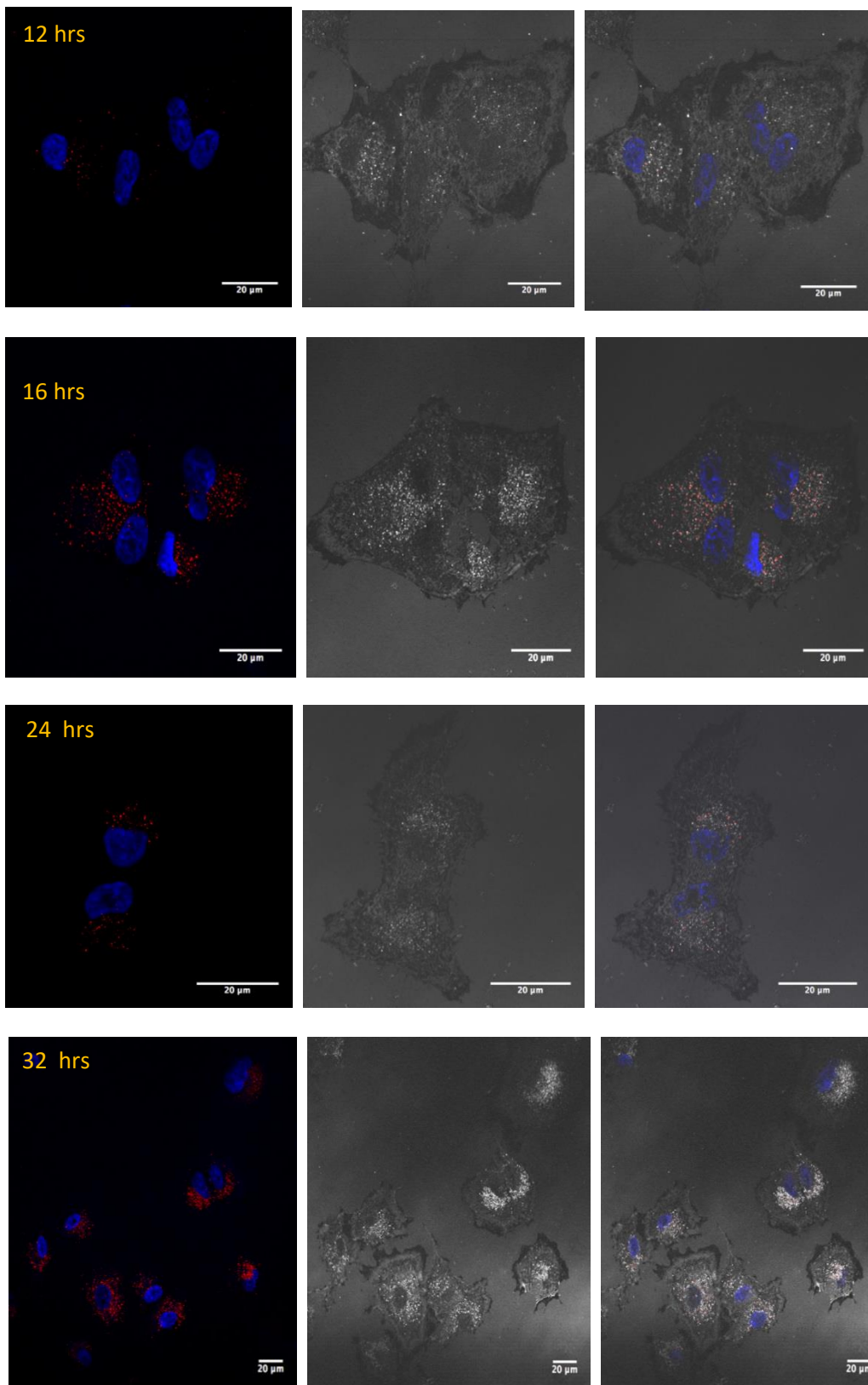


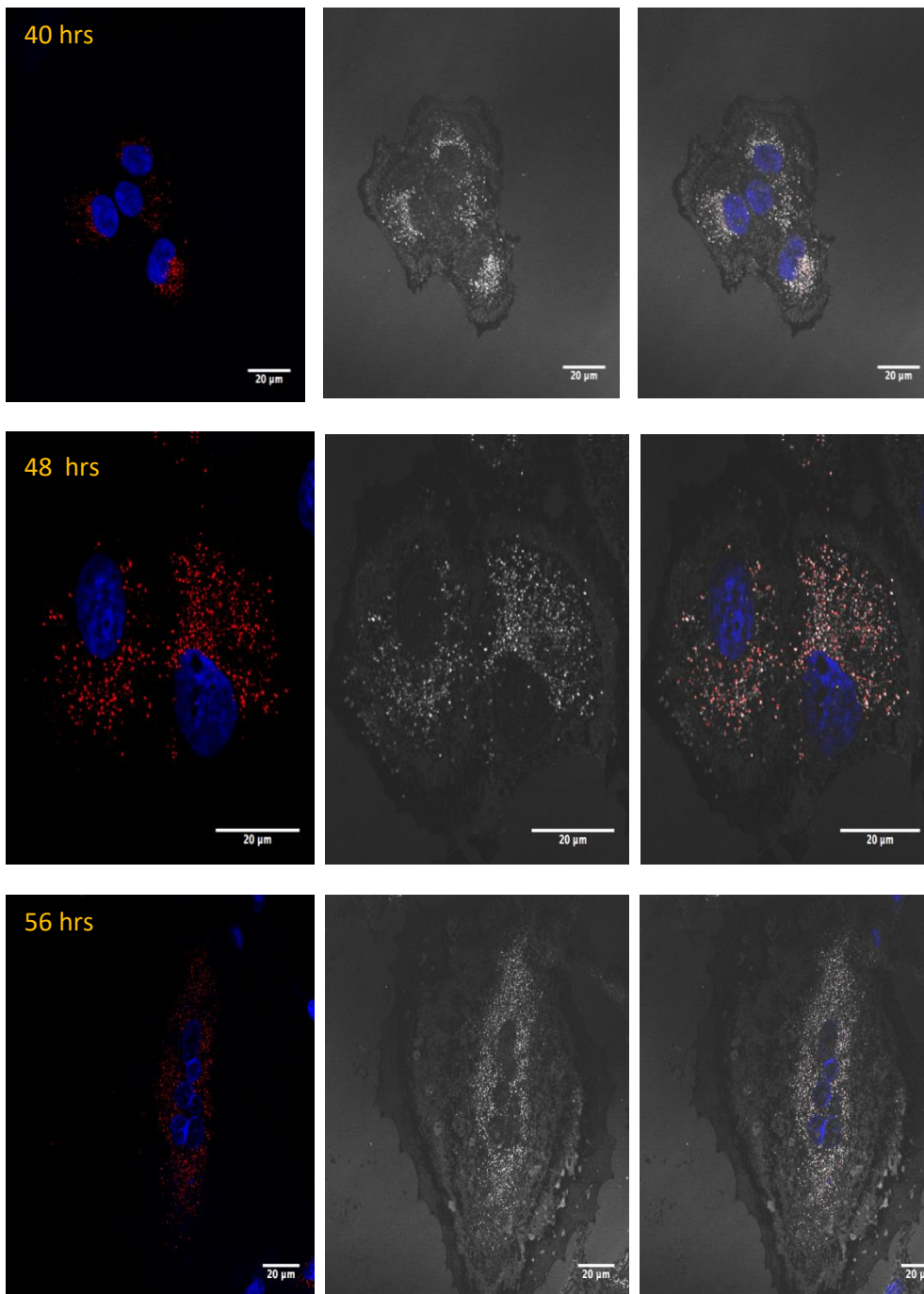
Figure 46: Steps in quantification of confocal images by ImageJ

Chapter 3: Characterization of RuS12·AuNP20 and Uptake in A549 cells

A. Representative time points used for quantitative measurement of uptake







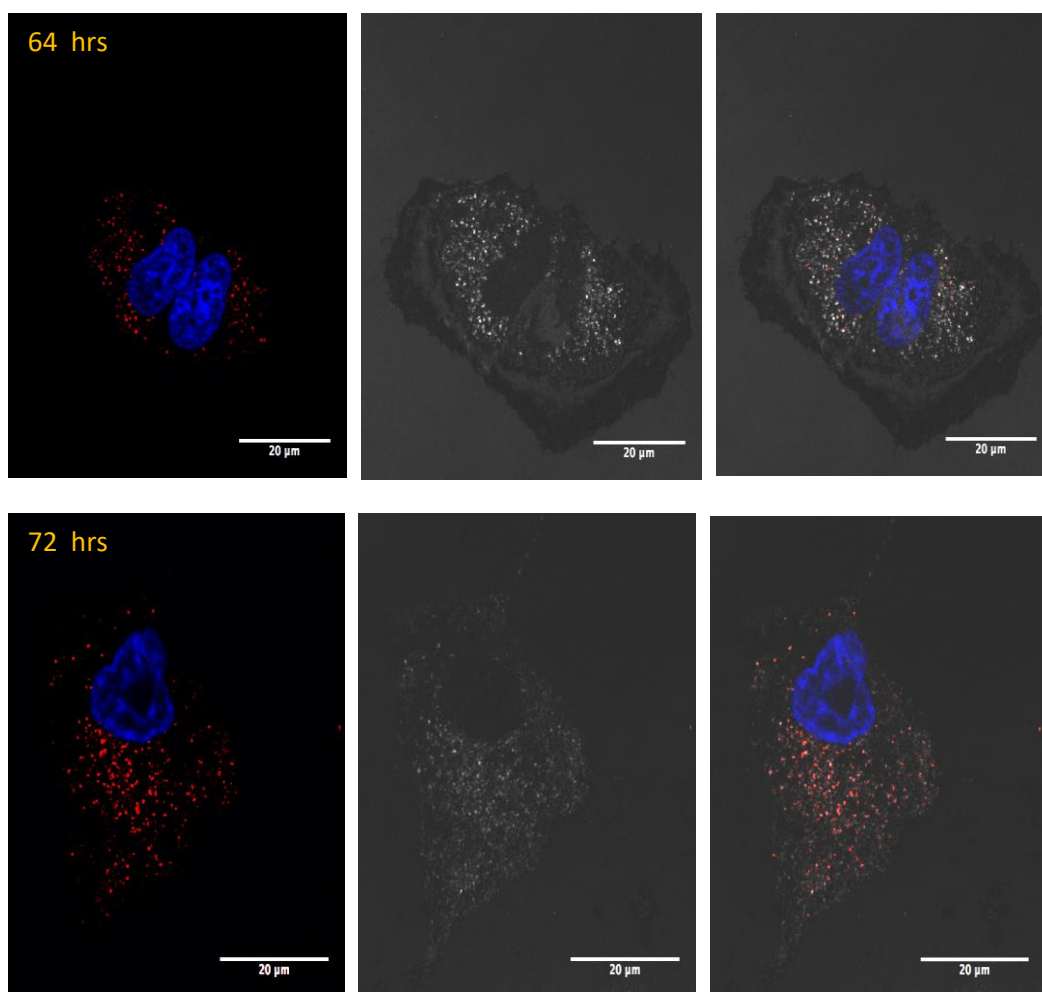


Figure 47: Representative merged confocal images of major time points of fixed A549 treated with 0.9 nM RuS12·AuNP20 and Hoechst.

A549 cells were treated with 0.9 nM RuS12·AuNP20 between 2-72 hours. The images shown are representative of all time points. This experiment was done as a biological triplicate, the first two duplicate were used to optimize imaging conditions and showed similar result with the third replicate which are the images reported.

- c. Merged images of RuS12·AuNP20 and Hoechst
- d. Their corresponding reflection image ($\lambda_{exc} = 488 \text{ nm}$, $\lambda_{em} = 478-498 \text{ nm}$)
- e. Merged fluorescence and reflection channel.

RuS12·AuNP20 emission form red channel ($\lambda_{exc} = 488 \text{ nm}$, $\lambda_{em} = 620-800 \text{ nm}$)

Hoechst emission form the blue channel ($\lambda_{exc} = 405 \text{ nm}$, $\lambda_{em} = 410-455 \text{ nm}$)

B. RuS12 alone in cells

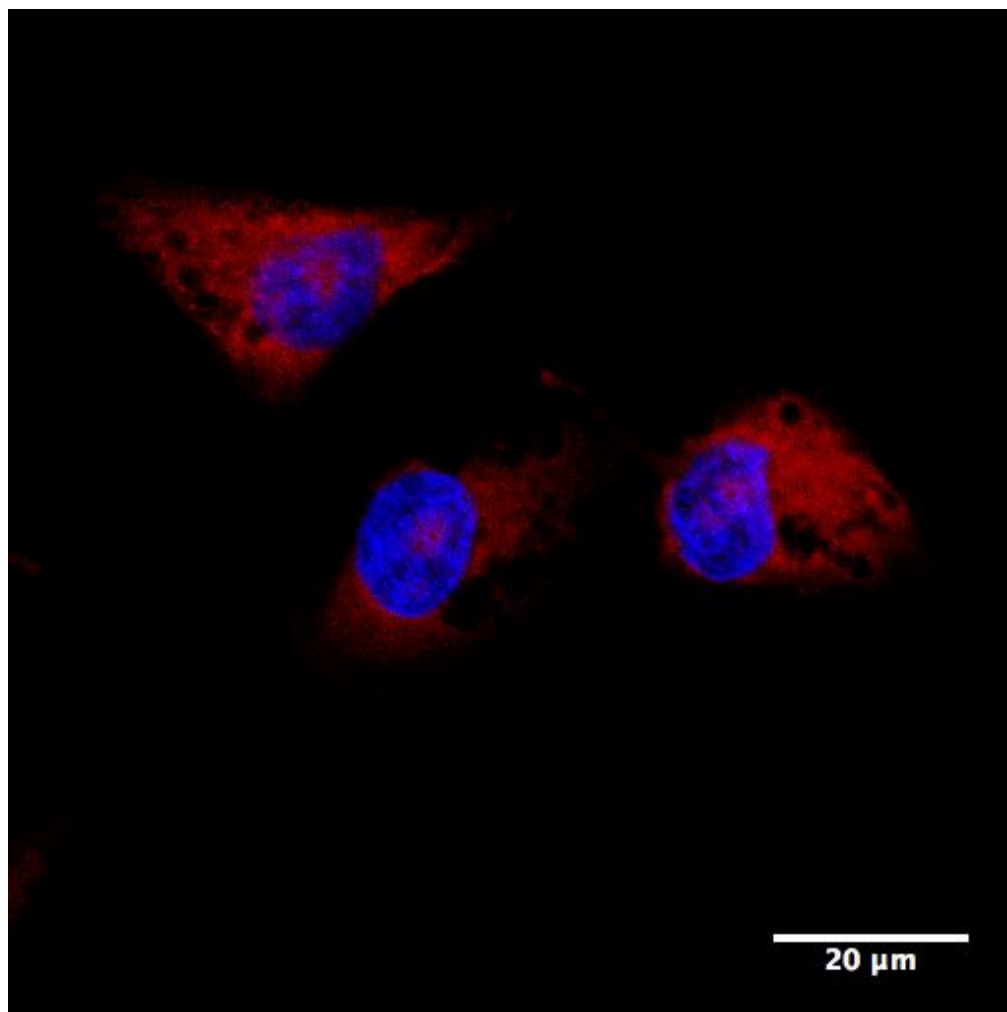


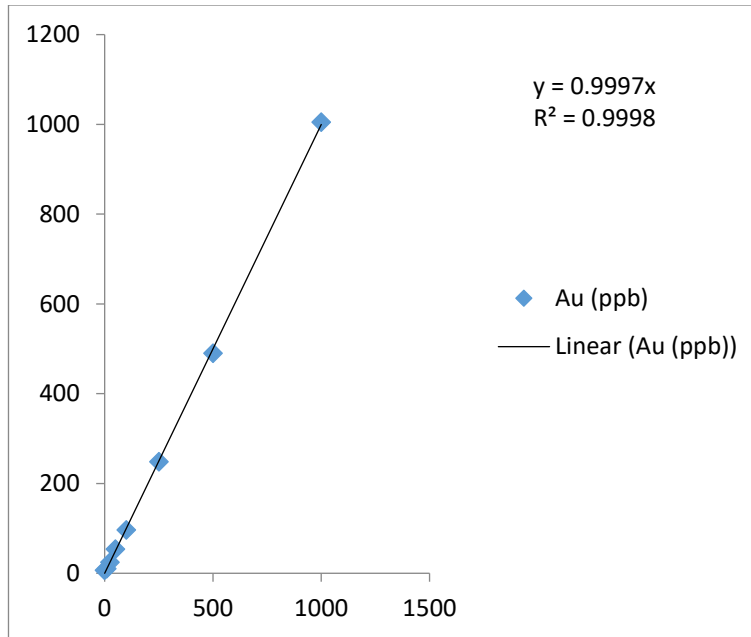
Figure 48: A549 cells treated with 0. 63 nM RuS12 alone for 4 hours

RuS12 emission form red channel ($\lambda_{exc} = 458 \text{ nm}$, $\lambda_{em} = 620\text{-}800 \text{ nm}$)

Hoechst emission form the blue channel ($\lambda_{exc} = 405\text{nm}$, $\lambda_{em} = 410\text{-}455 \text{ nm}$)

C. ICP-MS Standard curve

A. Gold standard curve



B. Ruthenium Standard curve

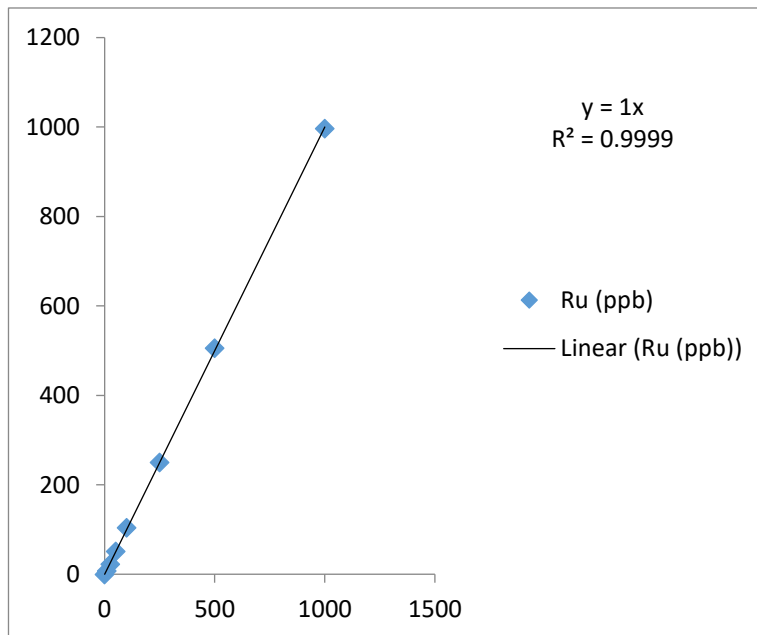


Figure 49: Standard curve of Au and Ru used for ICP-MS

The standard curve were prepared using a series of standard solutions (0, 0.2, 0.5, 1, 2, 5, 10, 20 ppb) containing metals to be detected (A. gold and B. ruthenium). Standard was used for calibration and determining metal content taken up by cells in each sample.

C2.

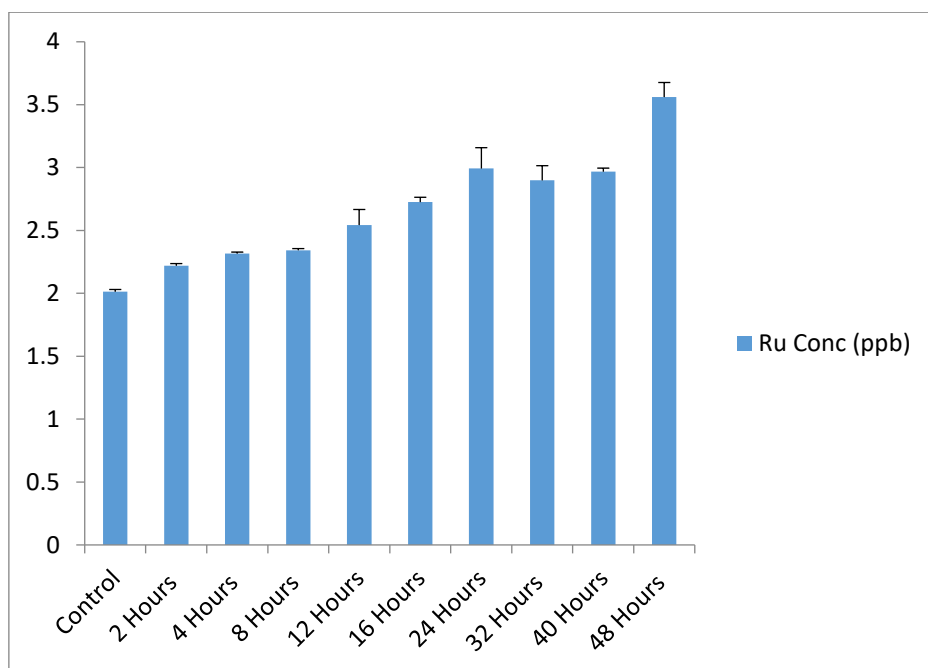


Figure 50: ICP-MS measurement of uptake of 0.9 nM RuS12·AuNP20 in A549 cells
Cells were treated with 0.9 nM RuS12·AuNP20 and at the end of each time points, cells were digested with aqua regia. The digested samples were used for ICP-MS analysis to determine intracellular concentration of ruthenium. Result presented is biological triplicate with three technical triplicate.

D. Inhibition of Endocytic Uptake

Method

Two endocytosis inhibitors were employed namely: Chlorpromazine and 5-(N-Ethyl-N-isopropyl) amiloride (EIPA) to study inhibition of endocytic uptake. Firstly, the cytotoxicity potential of both drugs on A549 cells were assessed using MTT assay. Chlorpromazine (5 mM) and EIPA (5 mM) stock solutions cytotoxic potential on A549 cells was tested by treating cells for 30 minutes with concentrations ranging from 10 μ M -10 0 μ M to obtain a non-toxic concentration for further studies.

Alexa Fluor® 488 conjugated transferrin from human serum (hTF-488) from Molecular probes and fluorescein-conjugated dextran (FITC-dextran 70 kDa) were used as positive control for clathrin dependent and macropinocytosis endocytosis respectively. Titrations of different dilutions (1:250, 1:500, 1:1000, 1:2000, 1:4000, 1:8000 and 1:10000) and concentrations (0.1 mg/ml, 0.2 mg/ml, 0.5 mg/ml, 1 mg/ml and 2 mg/ml) of stock solution of hTF-488 and FITC-dextran70 respectively were treated with A549 cells for 30 minutes for hTF-488 and 60 minutes for FITC-dextran 70 kDa. This was done to optimize condition that showed suitable cellular uptake in A549 cells without been saturated. Optimization was done by flow cytometry. Briefly, cells were seeded at a density of 100,000 cells per well in a 6-well plate and left overnight for attachment to occur. Spent media was aspirated and cell pre-treated with 3ml of a media containing either 1.25 μ g/ml of hTF-488 or 2mg/ml of FITC-dextran70 for 30 minutes followed by the addition of 50 μ M Chlorpromazine and 50 μ M EIPA for a further 30 minutes.

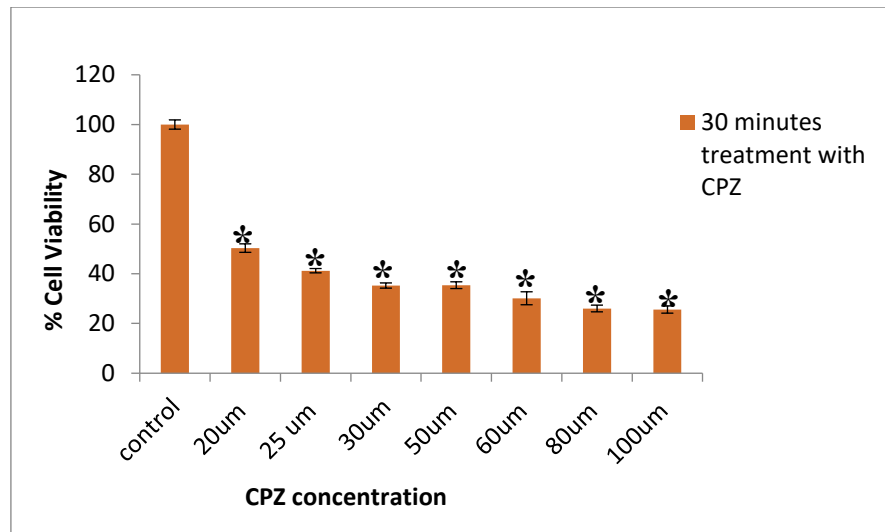
At the end of each time point, spent media was removed and cells washed three times with 1ml of PBS. Cells were detached by treating with 1ml of trypsin for 10 minutes and centrifuged for 10 minutes at 1500g. Cell pellets were re-suspended in fresh 1ml of PBS and transferred to flow cytometry tubes for analysis (FACScalibur, BD Biosciences USA).

Forward scatter, side scatter and fitc fluorescence ($\lambda_{exc}=488$ nm with light collected through a 670 nm band pass filter) of 10,000 cells were collected and Weasel freeware 3.2.1 software was used for data analysis.

Result

The result presented is 30 minutes treatment of A549 cells with CPZ and EIPA, 30 minutes was chosen as a suitable time of treating cells based on published evidence (Brandenberger *et al.*, 2010; Kuhn *et al.*, 2014). Both inhibitor showed a concentration dependent decrease in cell viability, which was more pronounced in cells treated with CPZ, compared to cell treated with EIPA. With these result in mind, we aimed to test the ability of these inhibitors (although they showed evidence of cytotoxicity Figure 51) to inhibit the positive controls. The FITC florescence of positive controls were measured by flow cytometry after 30 minutes treatment, which is suitable for cellular uptake. The mean fluorescence shown in was obtained from the FITC histogram (Figure 52). The result showed that FITC-dextran showed very little fluorescence which increased in a concentration dependent. The unexpected result obtained was not conclusive enough to establish optimization inhibition study. Therefore, the inhibition of RuS12·AuNP20 in A549 cells could not be studied.

A.



B.

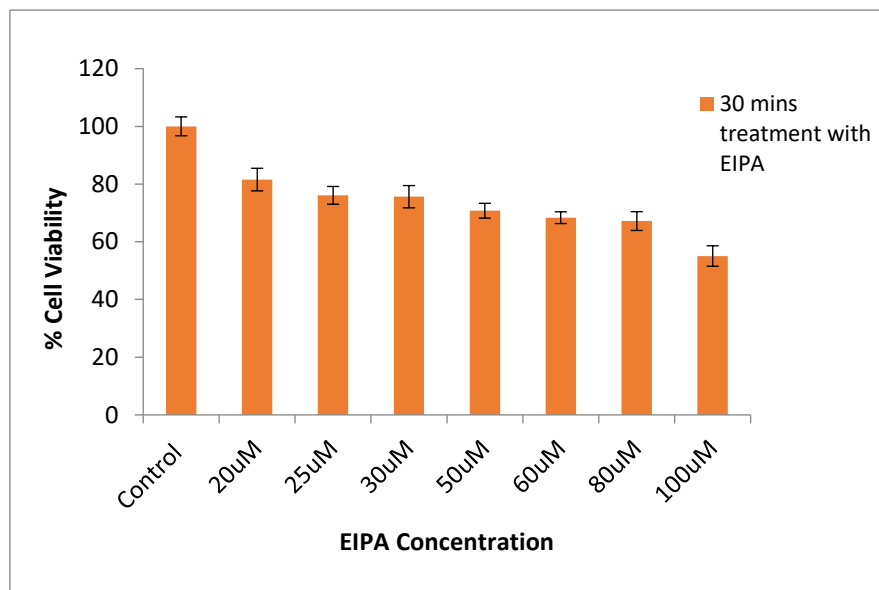


Figure 51: Cell viability of A549 cells treated with endocytic inhibitors

Both inhibitors were treated with different concentration for 30 minutes and cell viability was measured by MTT assay. The experiment was biological triplicate ($n=3$) and result was presented as % control of mean absorbance \pm SEM. The result showed a statistically significant $*(p \leq 0.05)$ difference by one-anova and Bonferroni Post Hoc analysis between treated and non-treated control in A. (CPZ)

A.

A.

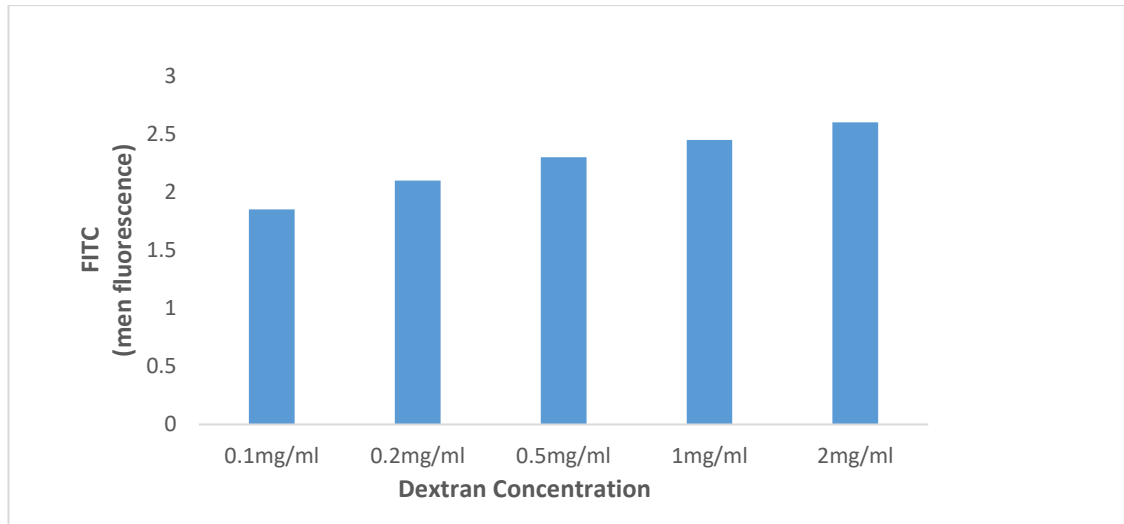


Figure 52: FITC fluorescence of positive control of endocytic inhibitors

A549 cells were treated with various concentration of GFP-tagged transferrin and FITC-tagged dextran for 30 minutes. The fluorescence was gotten from the histogram plot by FACS Aria, the result is expressed as mean fluorescence of treated-mean fluorescence of control. Number of replicate =1. A. Dextran.

Chapter 4: Localisation and Cellular Fate of RuS12·AuNP20 in A549 cells

Representative images for all time points used in studying co-localisation in all six organelles.

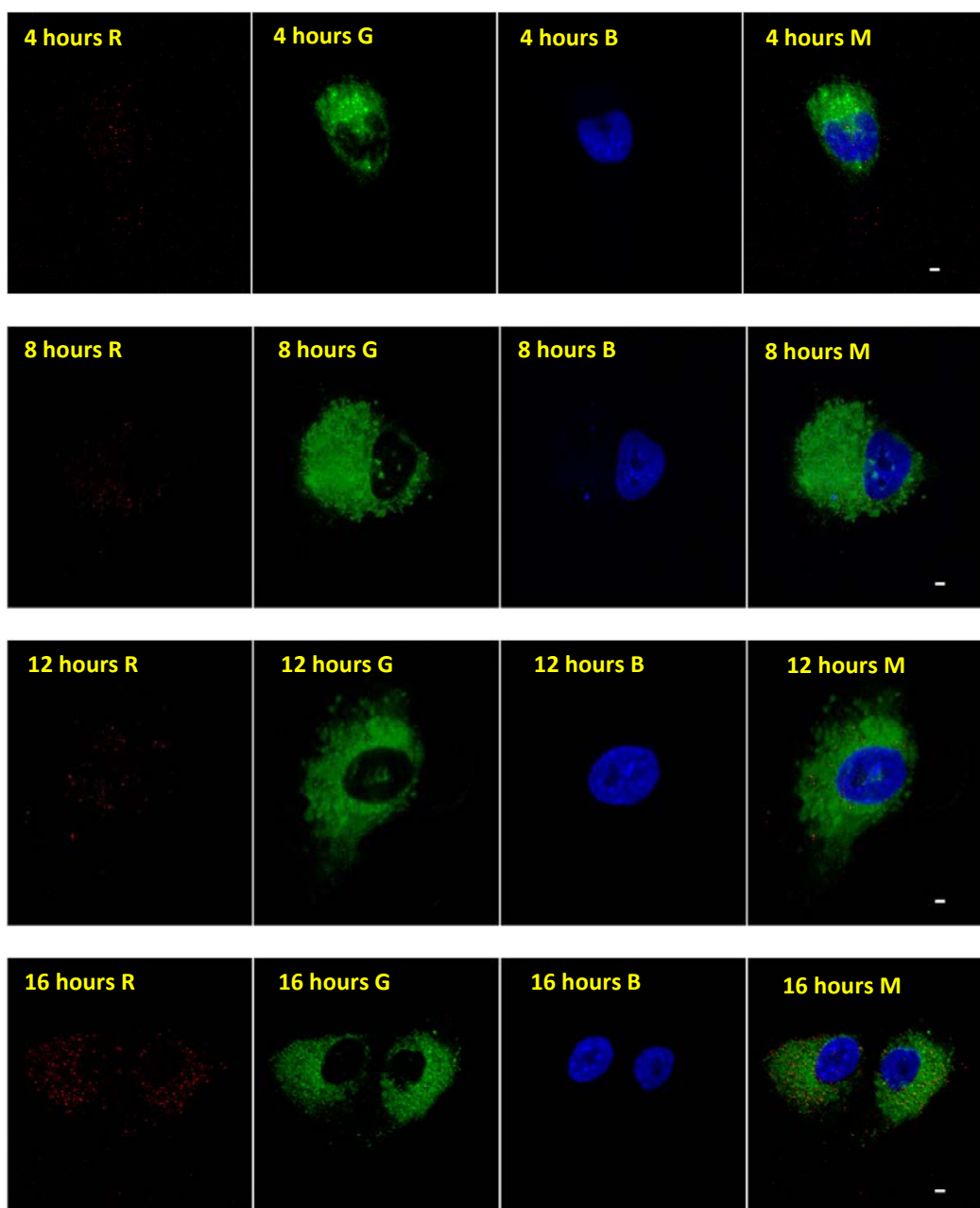
R. RuS12·AuNP20 emission form red channel ($\lambda_{exc}= 488 \text{ nm}$, $\lambda_{em} = 620\text{-}800 \text{ nm}$).

G. GFP emission form green channel ($\lambda_{exc}= 488 \text{ nm}$, $\lambda_{em}= 502 \text{ nm}$)

B. Hoechst emission form the blue channel ($\lambda_{exc}= 405 \text{ nm}$, $\lambda_{em}= 410\text{-}455 \text{ nm}$)

M. Merged image of red, green and blue channel

A. Golgi



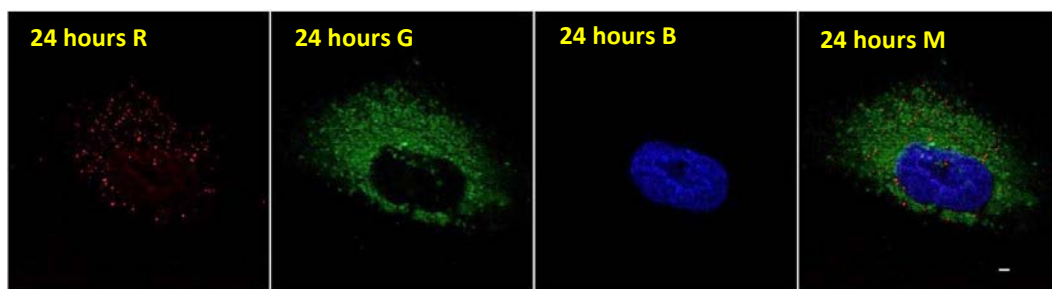


Figure 53: Representative image of fixed A549 treated with 0.9 nM RuS12·AuNP20 and stained with Golgi ID

The image shown is a representative image of A549 cells treated with 0.9 nM RuS12·AuNP20 between 4-24 hours. This experiment was done as a biological duplicate and images were all similar, showing no co-localisation between the particle and the golgi at any time point.

B. Mitochondria.

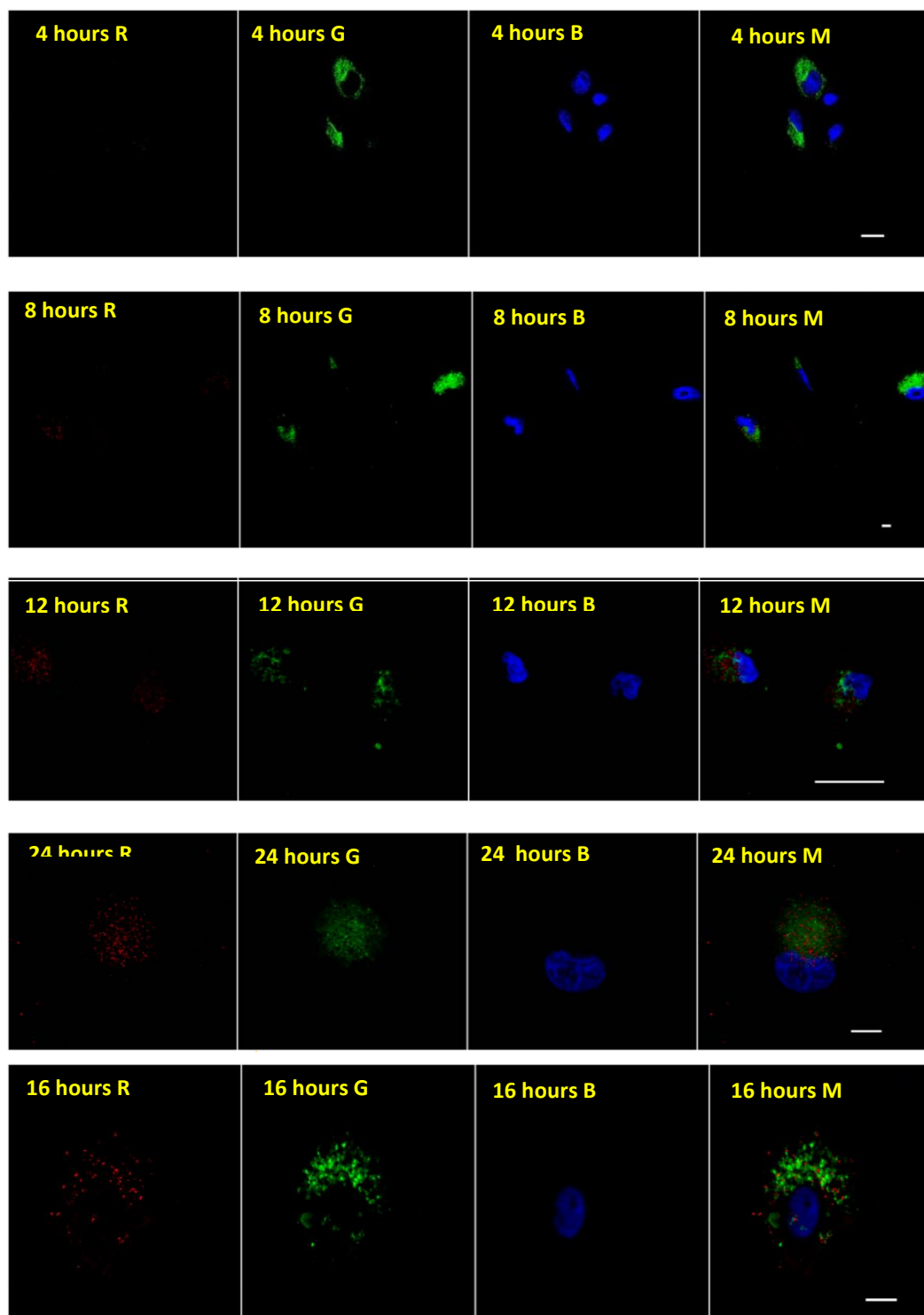


Figure 54: Representative image of fixed A549 treated with 0.9nM RuS12-AuNP20 and stained with MitoGreen

The image shown is a representative image of A549 cells treated with 0.9nM RuS12-AuNP20 between 4-24 hours. This experiment was done as a biological duplicate and images were all similar, showing no co-localisation between the particles and the mitochondria at any time point.

C. Endoplasmic Reticulum

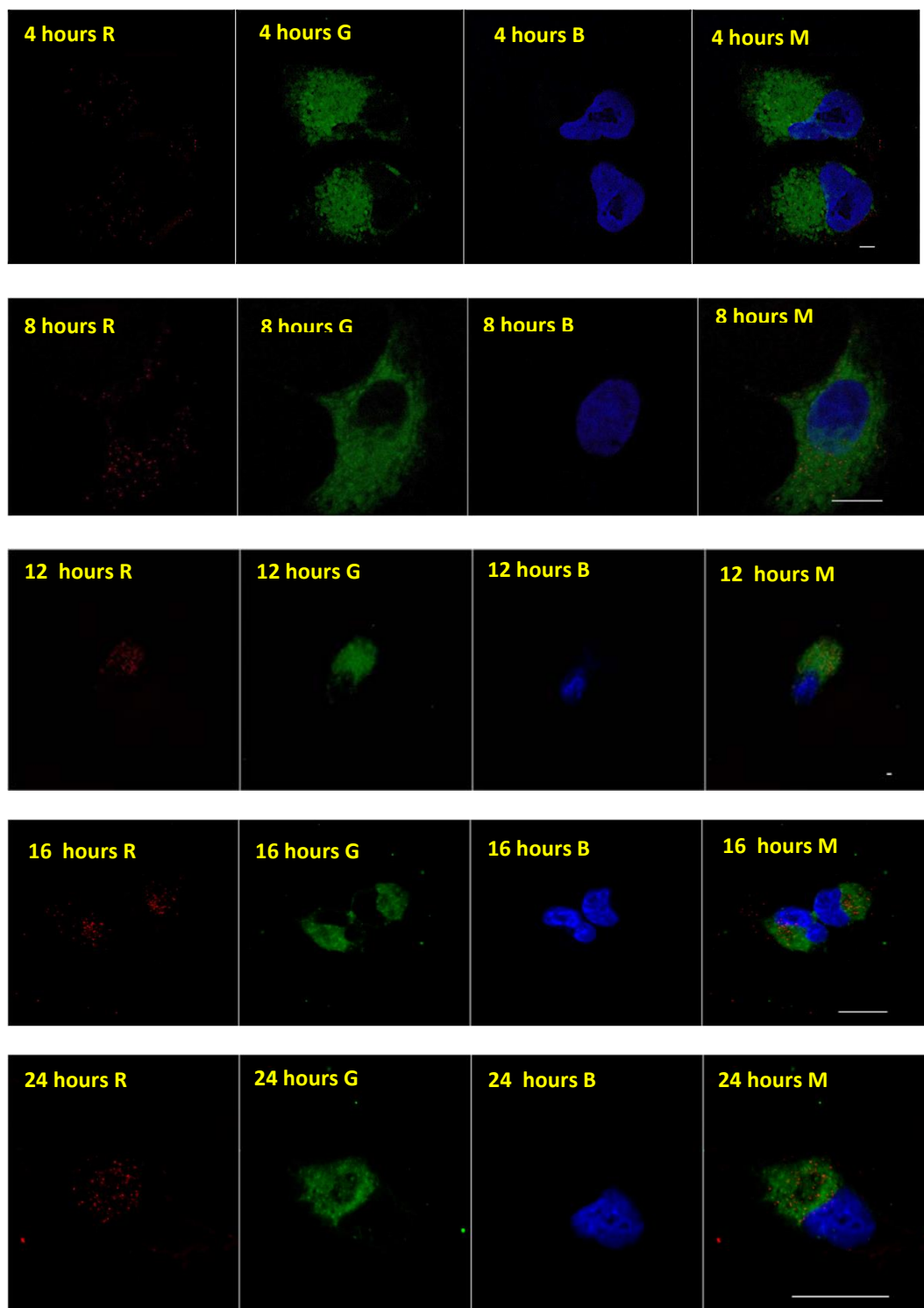


Figure 55: Representative image of fixed A549 treated with 0.9nM RuS12·AuNP20 and stained with ER-tracker green.

The image shown is a representative image of A549 cells treated with 0.9nM RuS12·AuNP20 for 24 hours. This experiment was done as a biological duplicate and images were all similar, showing no co-localisation between the particle and the ER at any time point.

E. Early endosomes

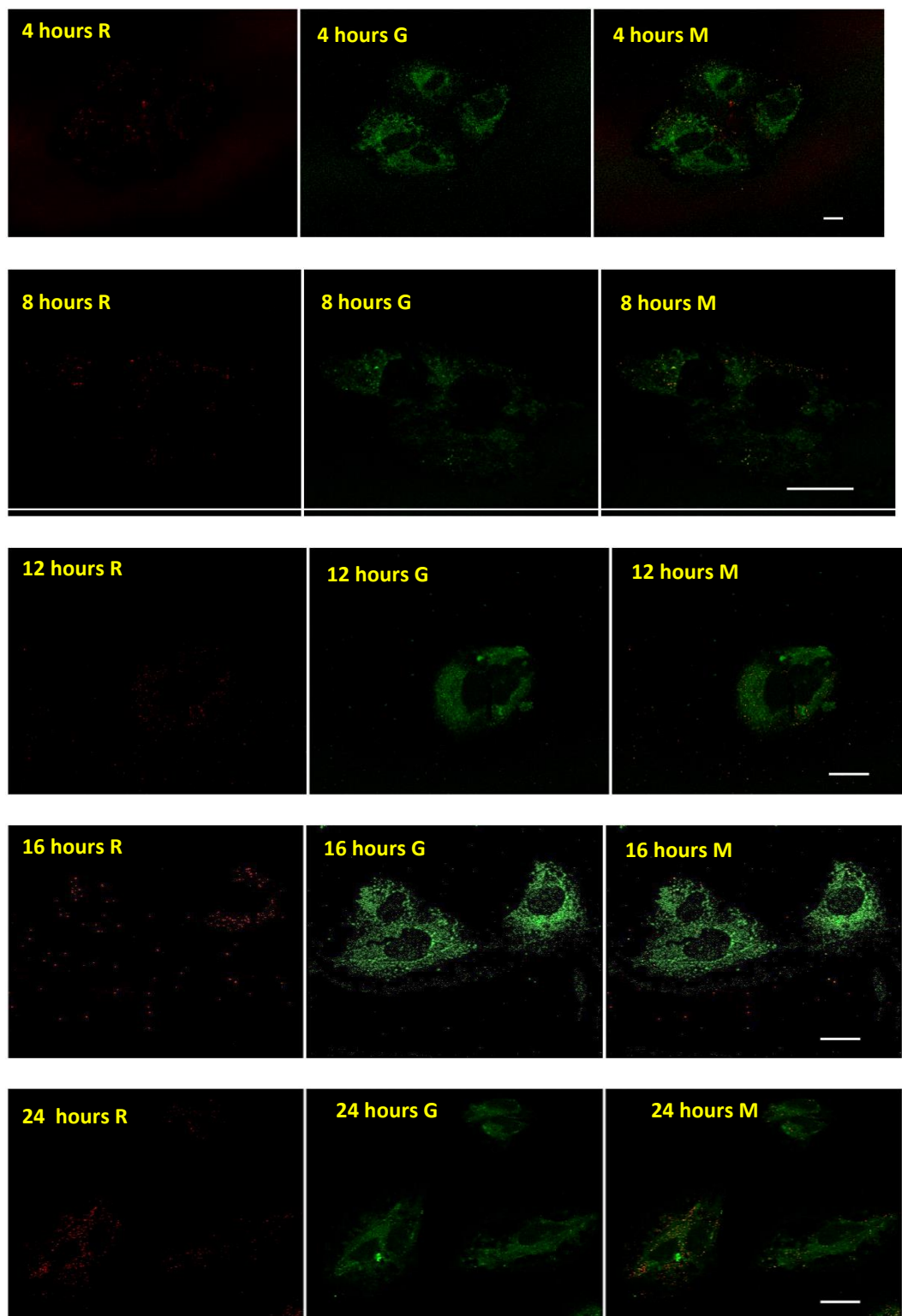
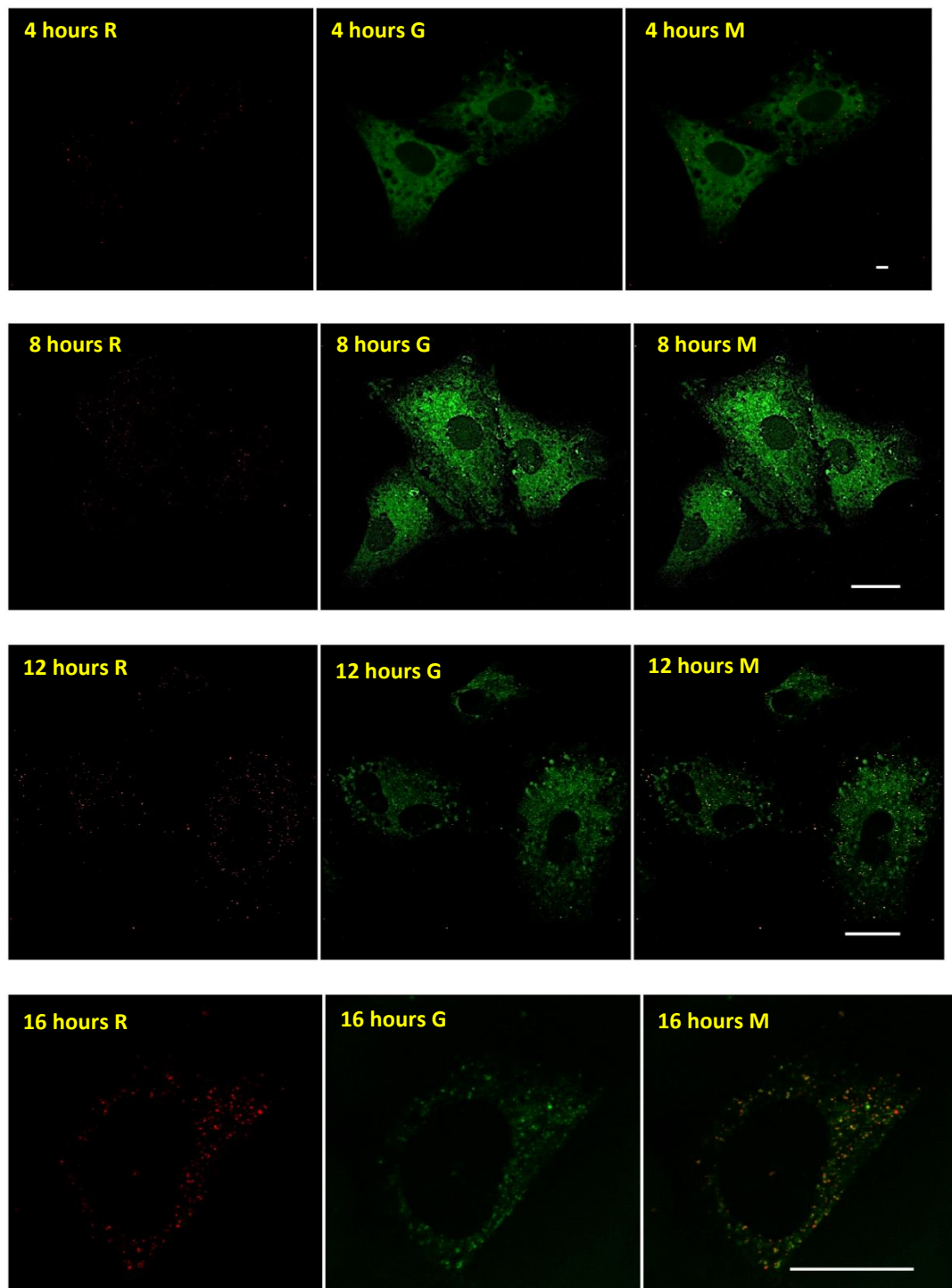


Figure 56 Representative image of fixed A549 transiently transfected with GFP-RAB4 and treated with 0.9 nm of RuS12·AuNP20.

The image shown is a representative image of A549 cells treated with 0.9nM RuS12·AuNP20 between 4-24 hours after 48 hours post-transfection with GFP-RAB4. This experiment was done as a biological duplicate and images were all similar within time point.

F. Lysosomes



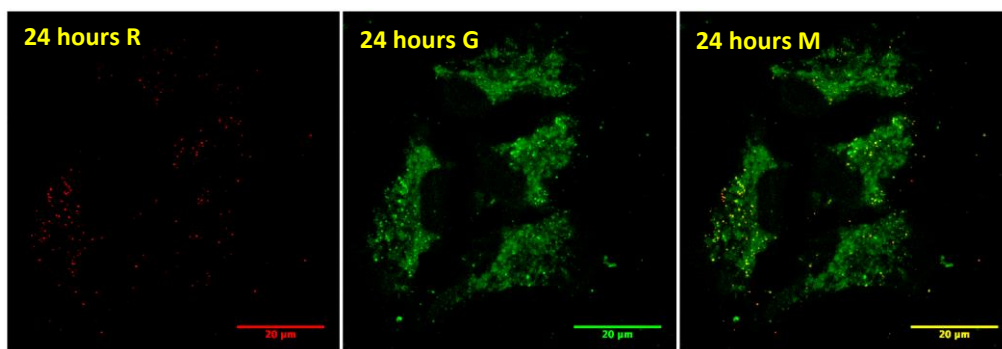
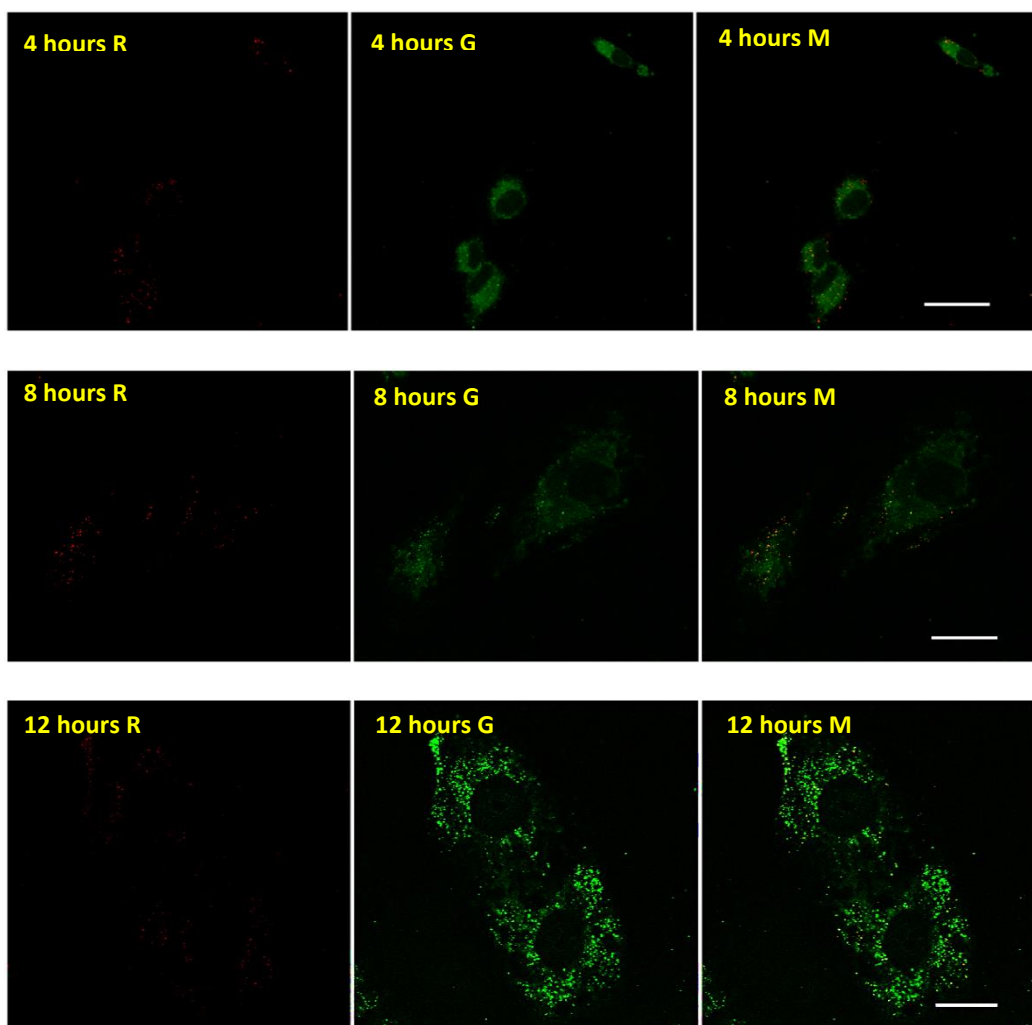


Figure 57: Representative image of fixed A549 transiently transfected with GFP- LAMP1. The image shown is a representative image of A549 cells treated with 0.9 nM RuS12-AuNP20 between 4-24 hours after 48 hours post-transfection with GFP-LAMP1. This experiment was done as a biological duplicate and images were all similar within time points. Increases time dependent co-localisation of particles with the lysosome is observed.

F. Autophagosomes



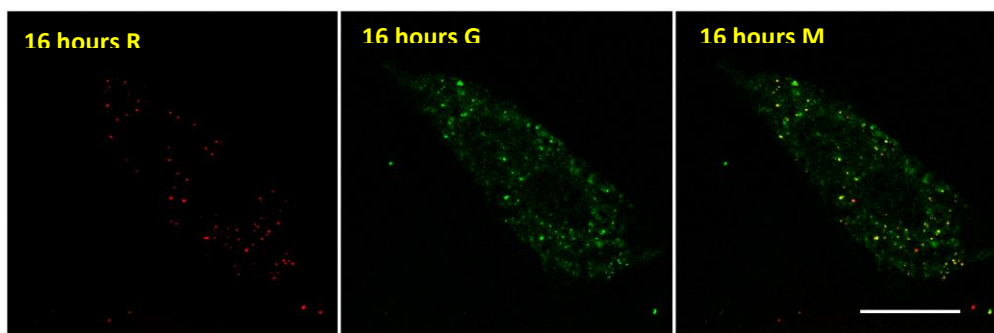


Figure 58: Representative image of fixed A549 transiently transfected with GFP-LC3.
The image shown is a representative image of A549 cells treated with 0.9 nM RuS12·AuNP20 between 4-24 hours, after 48 hours post-transfection with GFP-LC3. This experiment was done as a biological duplicate and images were all similar within time points. Result showed increase in co-localisation over time.

G. Steps in co-localisation study by ImageJ to find the PCC.

RGB images is spilt to individual channel and ready for co-localisation study using the Just Another Co-Localisation Plugin (JaCOP) on image.

This plugin is capable of analysis images and getting the Pearson's coefficient. This is done by comparing two different fluorescent channels. Which in our case was the red and green channel.

Images from both channels is first threshold before analyzing. This is done automatically A summary data is obtained that shows the Pearson's Coefficient. An example of the summary is shown below with the Pearson's Coefficient

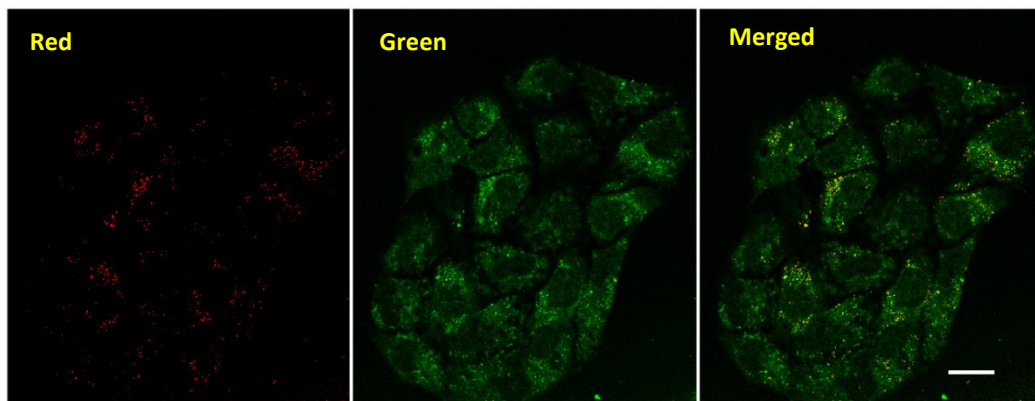


Image A: 16hours threshold (red).tif

Image B: 16hours threshold (green).tif

Pearson's Coefficient: $r=0.328$

Chapter 5: Cytotoxicity of RuS12·AuNP20 on A549 cells.

All graphs shown in this section have been previously shown in chapter 5 without the positive control. The positive control was added here to validate the experiment. The positive control was not shown previously because it makes it difficult to see the difference between the treated and the control.

A. MTT Assay

i. RuS12·AuNP20 with positive Control

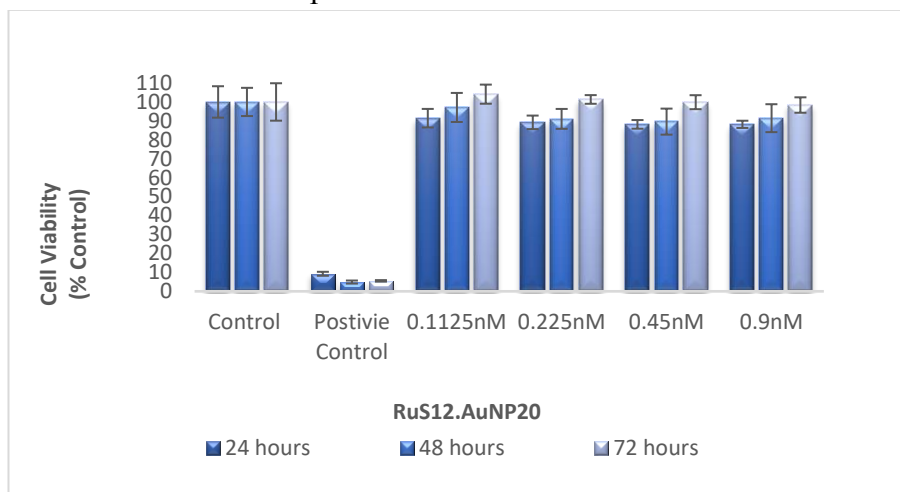


Figure 59: MTT Assay on A549 treated with RuS12·AuNP20 for 24, 48 and 72 hours

The experiment is a biological triplicate ($n=3$) and presented as % control of mean value \pm SEM. The positive control was 0.15% (v/v) Triton X-100 with media, which resulted in about 90% cell death. The result showed no statistically significant ($p \leq 0.05$) difference by one-anova and Bonferroni Post Hoc analysis between treated and control cells irrespective of length of exposure.

ii. RuS12 alone

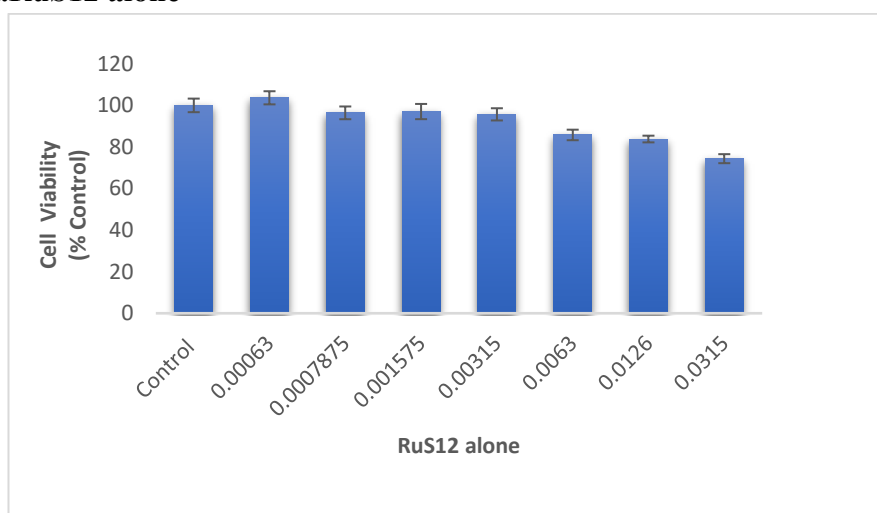


Figure 60: MTT Assay on A549 treated with RuS12 alone for 24 hours

The experiment is a biological triplicate ($n=3$) and presented as % control of mean value \pm SEM. The result showed no statistically significant ($p \leq 0.05$) difference by one-anova and Bonferroni Post Hoc analysis between treated and control cells.

B. CVS Assay of RuS12·AuNP20 with positive Control

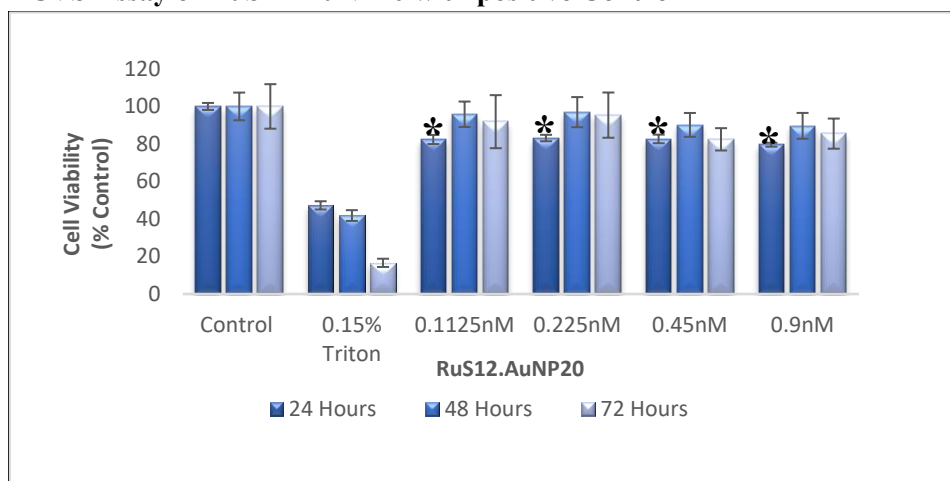


Figure 61: CVS on A549 treated with RuS12·AuNP20 for 24, 48 and 72 hours

The experiment is a biological triplicate ($n=3$) and presented as % control of mean value \pm SEM. The positive control used was 0.15% (v/v) Triton X-100 with media, which resulted in about 60% cell death. The result showed a statistically significant $*(p \leq 0.05)$ difference by one-anova and Bonferroni Post Hoc analysis between treated and non-treated control at 24 hours irrespective of concentration.

C. H₂DCF-DA Assay of RuS12·AuNP20 with positive Control

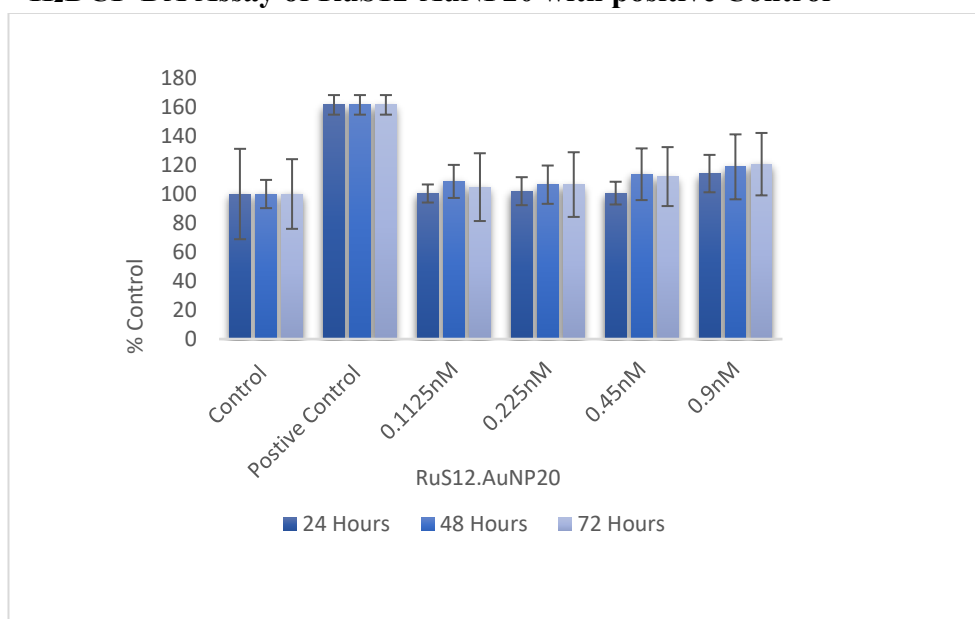


Figure 62: DCFH-DA Assay on A549 treated with RuS12·AuNP20 for 24, 48 and 72 hours

The experiment is a biological triplicate ($n=3$) and presented as % control of mean value \pm SEM. A549 cells treated with hydrogen peroxide (200 μ m) were used as positive control and showed 60% increase in fluorescence intensity. The result showed an increasing trend in a concentration and time-dependent manner that leads to ROS generation but this was not statistically significant by one-anova and Bonferroni Post Hoc analysis between treated and non-treated controls.

D. GSH ASSAY

i) Standard Curve

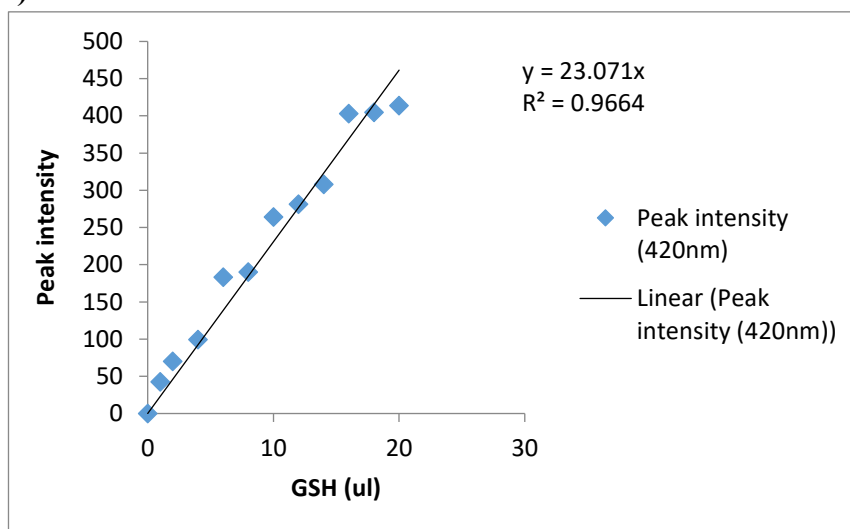


Figure 63: Standard curve of GSH used for GSH Assay.

ii) Result of RuS12·AuNP20 with positive Control

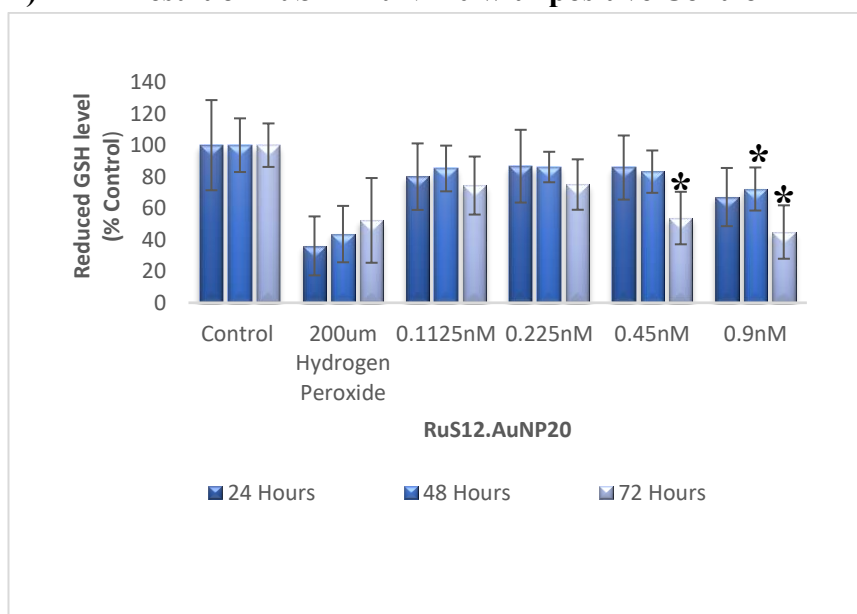


Figure 64: GSH Assay on A549 treated with RuS12·AuNP20 for 24, 48 and 72 hours

The experiment is a biological triplicate (n=3) and presented as % control of mean value \pm SEM. A549 cells treated with hydrogen peroxide (200 μ m) was used as positive control and a 50% difference decrease of glutathione is observed when compared to the non-treated control. Generally, a time-dependent decrease in glutathione levels was observed irrespective of concentrations following treatment with RuS12·AuNP20 when compared to the non-treated control. However, this was only statistically significant $*$ ($P \leq 0.05$) following treatment with 0.9 nM and 0.45 nM of RuS12·AuNP20 and 0.9 nM of RuS12·AuNP20 at 72 and 48 hours respectively.

E. Alkaline Comet Assay of RuS12·AuNP20 with positive Control

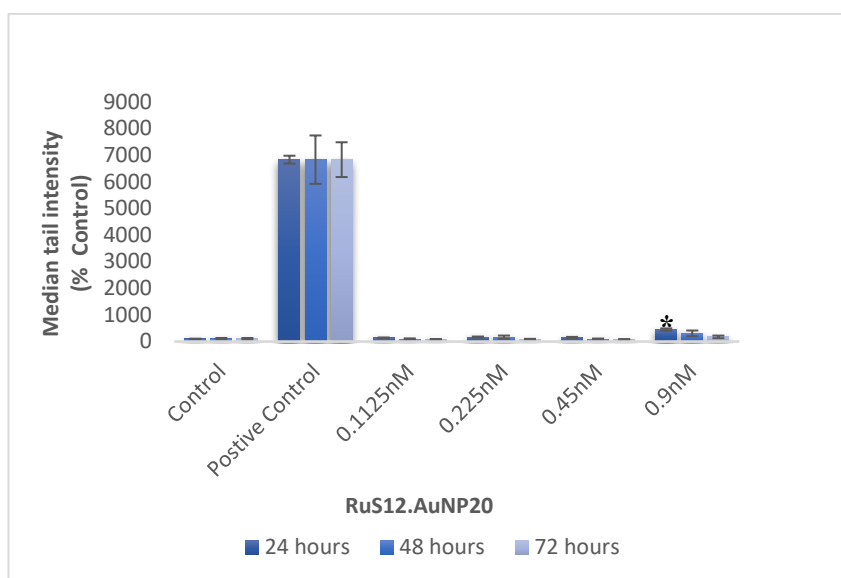


Figure 65: Median Tail intensity of A549 cells on exposure to RuS12·AuNP20

The experiment is a biological triplicate ($n=3$) and presented as % control of mean value \pm SEM. A549 cells treated with 200 μ m of hydrogen peroxide (positive control) for 1 hour, showed extreme unwinds indicating the formation of DNA-strand break. The result showed a statistically significant * ($p \leq 0.05$) difference by one-anova and Bonferroni Post Hoc analysis between treated and non-treated control cells at 24 hours at highest concentration of 0.9 nM.